Fakultät für Physik

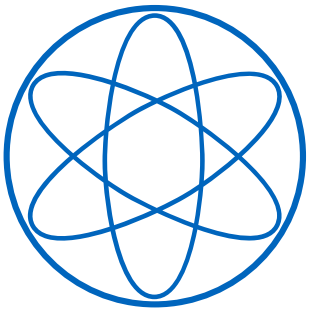

The Immersion Scanning Tunneling Microscope: Development and First Long-Term Variable-Temperature Studies at Liquid-Solid Interfaces

Dissertation

von

Oliver Michael Ochs

Technische Universität München

Technische Universität München
Fakultät für Physik
Oskar-von-Miller Lehrstuhl für Wissenschaftskommunikation

The Immersion Scanning Tunneling Microscope: Development and First Long-Term Variable-Temperature Studies at Liquid-Solid Interfaces

Oliver Michael Ochs

Vollständiger Abdruck der von der Fakultät für Physik der Technischen Universität München zur Erlangung des akademischen Grades eines

Doktors der Naturwissenschaften
(Dr. rer. nat.)

genehmigten Dissertation.

Vorsitzender: Prof. Dr. Björn Garbrecht
Prüfer der Dissertation:
1. Priv.-Doz. Dr. Markus Lackinger
2. Prof. Dr. Katharina Krischer

Die Dissertation wurde am 14.10.2020 bei der Technischen Universität München eingereicht und durch die Fakultät für Physik am 25.01.2021 angenommen.

Abstract

This thesis describes the realization of a new type of scanning tunneling microscope dedicated to long-term variable-temperature studies at liquid-solid interfaces: The Immersion Scanning Tunneling Microscope. This new instrument was applied in two fundamental studies investigating solvent and temperature-induced effects that influence the evolution of self-assembled molecular monolayers in liquids by affecting the underlying thermodynamics and kinetics.

In a comprehensive description, the development of the immersion scanning tunneling microscope is presented in detail. The key concept of this new instrument is the complete immersion of the microscope body into solution. The temperature of the solution, and thus also of the microscope, is precisely controlled inside a heatable and hermetically sealed container. Fast thermal equilibration after a temperature change is promoted through the choice of materials, a highly symmetric design and the introduction of heat-bridges. At steady state, temperatures are stabilized by feedback-control, hence reducing thermal drift to a minimum. Furthermore, owing to the hermetic isolation of the microscope and solution, solvent evaporation is completely eliminated, thereby removing any principal limitation for the duration of experiments at liquid-solid interfaces. Elaborate corrosion tests revealed the vulnerability of less noble metals and epoxy glues against corrosive solvents. Yet, the implementation of an effective corrosion protection concept using gold and a fluoroelastomeric coating material enables the usage of the highly appropriate but rather reactive fatty acid solvents. First test-experiments proved the low-drift and high-resolution imaging capability of the instrument at variable-temperatures between room temperature and 100 $^{\circ}C$. Even over the course of days, stable imaging can be achieved without any corrosion-induced contamination of the solution.

The immersion scanning tunneling microscope was used for two scientific case studies. In the first study, the origin of solvent-induced polymorphism of trimesic acid monolayers self-assembled at the solution-graphite interface was studied. Using fatty acids, trimesic acid assembles in two polymorphs: The porous chickenwire and denser flower structure for longer and shorter fatty acids, respectively (heptanoic acid = chickenwire, hexanoic acid = flower). In contrast to experimental findings, thermodynamic evaluations point towards a superior stabilization of the chickenwire polymorph for both solvents. In the end, stereochemically specific coadsorption of solvent molecules in a unique feature of the flower polymorph, i.e. additional elongated small pores, was identified to be the structure determining factor. This was revealed by variable-temperature experiments using the immersion scanning

tunneling microscope, which showed a reversible phase transition from the flower polymorph to the chickenwire polymorph at 110 $^{\circ}C$ (solvent = hexanoic acid).

A second study is presented, where in novel experiments the monolayer coverage of 2,6-naphthalenedicarboxylix acid at the nonanoic acid-graphite interface was tracked at temperatures between 57.5 and 65.0 $^{\circ}C$. The coverages decreased slowly over the course of days with a time dependence described by single exponential decays. From the individual rate constants a surprisingly high energy barrier for desorption of 208 $kJ\ mol^{-1}$ was derived. In vast discrepancy to this findings, an adapted Born-Haber cycle resulted in a desorption enthalpy of 16.4 $kJ\ mol^{-1}$, indicating the existence of a high-energy transition state.

Zusammenfassung

Diese Dissertation beschreibt die Realisierung eines neuen Typs von Rastertunnelmikroskop, das auf temperaturabhängige Langzeitstudien an Flüssig-Fest Grenzflächen spezialisiert ist: das Immersions-Rastertunnelmikroskop. Dieses neue Instrument wurde in zwei grundlegenden Studien angewandt. In diesen Studien wurden lösungsmittel- und temperaturinduzierte Effekte untersucht, welche die Entwicklung von selbstassemblierten molekularen Monolagen in Flüssigkeiten durch ihren Einfluss auf die dabei zugrunde liegende Thermodynamik und Kinetik verändern.

In einer umfassenden Beschreibung wird die Entwicklung des Immersions-Rastertunnelmikroskops detailliert vorgestellt. Das Schlüsselkonzept dieses neuen Instruments ist das vollständige Eintauchen des Mikroskopkörpers in Lösung. Die Temperatur der Lösung, und damit die des Mikroskops, wird in einem beheizbaren und hermetisch verschlossenen Behälter präzise geregelt. Ein schnelles Erreichen des thermischen Gleichgewichts nach einer Temperaturänderung wird durch die Wahl der Materialien, eines hochsymmetrischen Aufbaus und die Integrierung von Wärmebrücken gefördert. Im stationären Zustand werden die Temperaturen durch einen Regelkreis stabilisiert, wodurch die thermische Drift auf ein Minimum reduziert wird. Darüber hinaus wird durch die hermetische Isolierung von Mikroskop und Lösung die Verdampfung des Lösungsmittels vollständig eliminiert, wodurch jedwede prinzipielle Begrenzung der Dauer für Experimente an der flüssig-fest Grenzfläche entfällt. Ausführliche Korrosionstests zeigten die Anfälligkeit von halb- und unedlen Metallen sowie Epoxidklebern gegenüber korrosiven Lösungsmitteln. Die Umsetzung eines effektiven Konzepts zum Korrosionsschutz unter der Verwendung von Gold und einem fluorelastomeren Beschichtungsmaterial ermöglicht jedoch den Einsatz der besonders geeigneten aber korrosiv wirkenden Fettsäuren als Lösungsmittel. Erste Testexperimente bewiesen die geringe Drift und das hochauflösende Abbildungsvermögen des Instruments in einem Temperaturbereich zwischen Raumtemperatur und 100 $^{\circ}C$. Selbst über Tage hinweg kann eine stabile Bildgebung ohne korrosionsbedingte Kontamination der Lösung erreicht werden.

Das Immersions-Rastertunnelmikroskop wurde für zwei wissenschaftliche Fallstudien eingesetzt. In der ersten Studie wird der Ursprung des lösungsmittelbedingten Polymorphismus von Trimesinsäure-Monolagen, welche sich an der Lösungs-Graphit Grenzfläche selbstassemblieren, untersucht und vorgestellt. Unter der Verwendung von Fettsäuren assembliert Trimesinsäure zu zwei Polymorphen: der porösen Chickenwire- und der dichteren Flower-Struktur für jeweils längere bzw. kürzere Fettsäuren (Heptansäure = Chickenwire, Hexansäure = Flower). Im Gegen-

satz zu experimentellen Ergebnissen deuten thermodynamische Analysen auf eine überlegene Stabilisierung des Chickenwire-Polymorphs in beide Lösungsmittel hin. Als strukturbestimmender Faktor wurde schließlich die stereochemisch spezifische Koadsorption von Lösungsmittelmolekülen in einem Alleinstellungsmerkmal des Flower-Polymorphs, d. h. in dessen länglichen kleinen Poren, identifiziert. Dies wurde in temperaturabhängigen Experimente unter Verwendung des Immersions-Rastertunnelmikroskops festgestellt, welche einen reversiblen Phasenübergang vom Flower-Polymorph zum Chickenwire-Polymorph bei 110 $°C$ zeigten (Lösungsmittel = Hexansäure).

Eine zweite Studie wird vorgestellt, bei der in neuartigen Experimenten die Monolagenbedeckung von 2,6-Naphthalindicarbonsäure an der Grenzfläche zwischen Nonansäure und Graphit in einem Temperaturbereich von 57,5 bis 65,0 $°C$ verfolgt wurde. Die Bedeckungen nahmen langsam über Tage hinweg ab und ihre Zeitabhängigkeit konnte als einfacher exponentieller Abfall beschrieben werden. Aus den einzelnen Geschwindigkeitskonstanten wurde eine überraschend hohe Energiebarriere für die Desorption von 208 $kJ\ mol^{-1}$ abgeleitet. In großer Diskrepanz zu diesem Ergebnis ergab ein adaptierter Born-Haber-Zyklus eine Desorptionsenthalpie von 16,4 $kJ\ mol^{-1}$, was auf die Existenz eines hochenergetischen Übergangszustands hinweist.

Contents

List of Abbreviations

1D	=	one dimensional
2D	=	two dimensional
3D	=	three dimensional
6A	=	hexanoic acid
7A	=	heptanoic acid
9A	=	nonanoic acid
AWG	=	**a**merican **w**ire **g**auge
BPDA	=	4,4'-biphenyldicarboxylic acid
BTB	=	1,3,5-benzenetribenzoic acid
CTLB	=	**c**ontainer for the **t**hermostatic **l**iquid-**b**ath
CVD	=	**c**hemical **v**apour **d**eposition
DFT	=	**d**ensity-**f**unctional **t**heory
DOS	=	**d**ensity **o**f **s**tate
ethyl-6A	=	2-ethylhexanoic acid
HOPG	=	**h**ighly **o**riented **p**yrolytic **g**raphite
HPD	=	**h**igher **p**acking **d**ensity
I-STM	=	**i**mmersion **s**canning **t**unneling **m**icroscope
LDOS	=	**l**ocal **d**ensity **o**f **s**tate
LPD	=	**l**ower **p**acking **d**ensity
methyl-6A	=	2-methylhexanoic acid
MD	=	**m**olecular **d**ynamics
MM	=	**m**olecular **m**echanics
NDA	=	2,6-naphthalenedicarboxlic acid
OFHC-copper	=	**o**xygen **f**ree **h**igh **c**onductivity copper
PEEK	=	**p**oly**e**ther **e**ther **k**etone
PREN-Index	=	**p**itting **r**esistance **e**quivalent **n**umber - index
PZT	=	lead zirconate titanate
QCMB	=	**q**uartz **c**rystal **m**icro**b**alance
RAHB	=	**r**esonance **a**ssisted **h**ydrogen **b**ounds
RT	=	**r**oom-**t**emperature
SDA	=	4,4'-stilbenedicarboxylix acid
SNR	=	**s**ignal-to-**n**oise **r**atio
STM	=	**s**canning **t**unneling **m**icroscope/**m**icroscopy
TMA	=	benzene-1,3,5-tricarboxylic acid (trimesic acid)
TOC	=	**t**able **o**f **c**ontent
TPD	=	**t**emperature **p**rogrammed **d**esorption
TPA	=	benzene-1,4-dicarboxylic acid (terephthalic)
TTL	=	**t**ransistor **t**ransistor **l**ogic
UHV	=	**u**ltra-**h**igh **v**acuum
UV	=	**u**ltra **v**iolet
UV-vis	=	**u**ltra **v**iolet-**vis**ible

Chapter 1

Introduction

In the 1980s, Jean-Marie Lehn proposed his idea of supramolecular chemistry as a new discipline in the field of chemistry.[1] Rewarded with the Nobel Prize in 1987,[2] Lehn changed the focus of chemistry from structures and properties of single molecules to the non-covalent interaction between them. In this respect, a particularly interesting phenomenon is intermolecular self-assembly, as it describes the spontaneous organisation of molecules to non-covalently bounded supramolecular structures reaching from 3D crystals to highly ordered 2D and 1D structures on surfaces.[3,4] Self-assembly experienced a tremendous growth in interest, studies and discoveries over the last decades, not at least through its importance in biology[5,6] and in material science as a bottom-up approach for the fabrication of nano-materials.[7–9]

Around the same time when Lehn stated his proposal, Gerhard Binning and Heinrich Rohrer presented the first Scanning Tunneling Microscope (STM) in 1981, an instrument with unprecedented resolution capability beyond the diffraction limit.[10,11] Enabling real space imaging of structures at the atomic scale and even the controlled manipulation of single atoms,[12] STM played a pivotal role in studying self-assembly processes and contributed greatly to the advent of nano-science. For their pioneering work, Binnig and Rohrer received the Nobel Prize in Physics in the year 1986.[13] Since then, the development of more sophisticated STMs took place. Apart from the original application in vacuum[10,14,15], contemporary state-of-the-art STMs are capable to operate at ambient conditions,[16,17] at high pressure[18] and even in liquids[19–21].

Liquids, particularly the liquid-solid interfaces, are proved to be ideal environments to study the phenomenon of supramolecular self-assembly, not least because of an enhanced mobility of the molecules, modest preparational efforts and straightforward experimental approaches using STM.[22,23] In this field, many studies aim to establish an enhanced fundamental understanding of the driving forces behind supramolecular self-assembly. In general, self-assembly at the liquid-solid interface evolves under equilibrium conditions controlled by thermodynamic forces but, also kinetic effects can play a fundamental role in monolayer formation. Yet, the final structure is rarely already predefined by the molecular building blocks themselves, as environmental conditions can drastically influence the equilibrium conditions. In this respect, the interplay of parameters like molecular structure, type of solvent, the

surface, solute concentration as well as temperature are crucially important in liquid environments. A particularly interesting and relevant parameter is temperature as it affects both, thermodynamics through the entropic contribution to the free energy and kinetics by providing activation energy to overcome barriers. Surprisingly, and in stark contrast to its importance, only a few studies focus on temperature. Presumably, technical limitations are the main reason for the low number of studies as variable-temperature STM experiments in liquids imply additional complications. So far, the majority of variable-temperature STM experiments are performed using locally heated sample holders.[24–26] Unfortunately, the usage of liquid solvents with relatively high vapour pressure, e.g. the highly appropriate homologues series of fatty acids, inevitably results in a continuous loss of solvent over the course of the experiment. The accompanied change in concentration distorts the final results and with ongoing time, samples can even completely dry out. Since this effect is even enhanced at elevated temperatures, variable-temperature liquid-solid STM experiments are strongly restricted in duration or in the choice of solvent, i.e. are limited to solvents with low vapour pressure. Furthermore, locally heated sample holders induce substantial thermal drift over the entire instrument. Generally, thermal drift is reduced over the course of time as thermal equilibration proceeds, but progressive evaporation of volatile solvents prohibit extended waiting times. At the end, a trade-off between settling thermal drift and keeping solvent evaporation at a minimum is dictating the duration of STM experiments with locally heated samples, while scientific interests come often secondary.

In 2014, Hipps and co-workers took a novel approach to overcome this dilemma by suppressing solvent evaporation through a saturated solvent atmosphere inside of a temperature controlled closed chamber.[27] Therefore, a reservoir of pure solvent is placed next to a home-built STM. By suppressing solvent evaporation, extended waiting times for thermal equilibration are affordable while heating of the entire STM avoids substantial thermal drift from the start. The great potential of the instrument was proven by first long-term STM experiments over 24 h at temperatures up to 75 $^{\circ}C$ to evaluate the temperature dependency of porphyrin monolayers adsorbed at the toluene-Au(111) interface.[27] Even though this approach represented a milestone for long-term variable-temperature STM experiments at the liquid-solid interface, points for improvement can be identified. The original system features a high thermal mass and a non-optimal heat transport through the instrument, resulting in ineffective thermal equilibration. The creation of a saturated solvent atmosphere is limiting the instrument to less corrosive solvents as all STM components are exposed to the vapour. Moreover, minor concentration changes through solvent evaporation from the sample cannot be fully excluded during heating.

The ongoing efforts to realize long-term variable-temperature STM experiments underpin their high potential to gain enhanced fundamental knowledge and to clarify the reasons for phenomena observed in self-assembly at liquid-solid interfaces. In this respect, observations in two earlier studied model systems, trimesic acid (TMA) and 2,6-naphtahlendicarboxylix acid (NDA), require further evaluation.[28,29] Using fatty acids as solvents, TMA self-assembles on graphite into two different polymorphs,

i.e. the flower and chickenwire polymorph for shorter and longer solvent alkyl chain length, respectively. The origin of this experimentally observed solvent-induced polymorphism is so far not fully understood.[28] The other model system, NDA, features an uncommonly low degree of structural quality of its monolayers for a self-assembly at the liquid-solid interface. A kinetic inhibition in the desorption process might be the reason for that effect, limiting the normally enhanced self-healing ability of monolayers in liquid environments.[29] In both cases, variable-temperature experiments could contribute to further insights in the underlying reasons.

Motivated by the ground-breaking work of Hipps *et al.* and to clarify open questions of previous research, we tackle the development of a new type of STM: The Immersion Scanning Tunneling Microscope (I-STM). In a completely novel approach, we propose the immersion of a dedicated STM in solution while both, STM and solution, are hermetically sealed in a feedback-controlled heatable container. Suppressing any solvent evaporation, limitations in experimental durations are eliminated and extended waiting times to reduce thermal drift are affordable. Nonetheless, optimizations in terms of neat thermal exchange across the entire STM aim to improve thermal equilibration and the fast reduction of thermal drift. With the development of the I-STM, the origin of solvent-induced polymorphism in TMA monolayers and the possible existence of kinetic limitations in NDA self-assembly can be evaluated with the aid of variable-temperature I-STM experiments. Complementary evaluation of thermodynamic quantities, by variable-temperature UV-vis spectroscopy, vacuum effusion experiments as well as computational density-functional theory and molecular mechanics calculations will provide further inside in the underlying thermodynamic forces and proposed kinetic effects.

This thesis continues with an introduction to the theoretical background and basic principles of scanning tunneling microscopy. In chapter 3, UV-vis spectroscopy and vacuum effusion are presented and discussed as experimental methods to derive enthalpy changes during dissolution and sublimation processes, respectively. A brief overview of the used molecules and surfaces in the experimental parts is given in chapter 4. Chapter 5 provides an introduction to monolayer self-assembly at the liquid-solid interface, including thermodynamics, kinetics and all relevant parameters. The main part of the thesis starts with a comprehensive description of the conception and design of the I-STM as well as with an evaluation of its performance (chapter 6). With the aid of the I-STM, the phenomenon of solvent-induced polymorphism of TMA monolayers is studied and presented in chapter 7. In a second study (chapter 8), desorption kinetics of NDA monolayers is evaluated and quantified by variable-temperature STM experiments. All results and findings of this thesis are summarized and concluded in the final chapter 9 including an outlook.

Chapter 2

Scanning Tunneling Microscopy

STM is a surface sensitive, real space imaging method to visualize surface topographies at the atomic scale.[10,11,13] In the context of molecular monolayers on surfaces, a STM is a very powerful tool to analyse molecular structures. Owing to its high resolution capability and sensitivity to the electronic configuration of the adsorbate-surface system, STM can be used to measure bond-length, the lattice parameter of the monolayer or the degree of surface coverage. Various environments are feasible for STM such as ambient,[16,17] vacuum,[10,30] high pressure[18,31] and even in liquids[19–22]. Furthermore, STM can operate at temperatures ranging from mK[32] to high temperatures of $>1000\ K$.[33,34]

2.1 Principle and Theoretical Background

As STM belongs to the family of scanning probe microscopy (SPM), a probe, i.e. a sharp metal tip, is used to analyse the surface of a sample (Fig. 2.1).

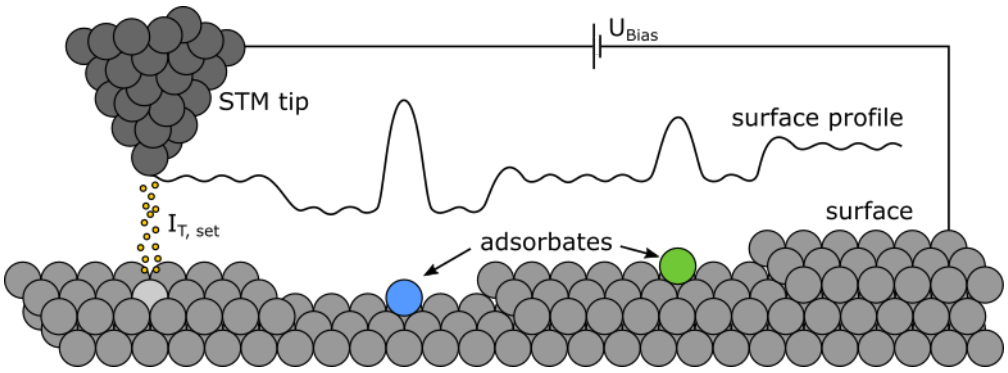

Figure 2.1: Basic principle of an STM scanning in constant current mode. Depending on the density of states of the adsorbate-surface system the topographic surface profile (contrast) can differ between different adsorbates.

While moving the tip along a straight line, the vertical deflection of the topology is recorded. This is done line by line until the specified area is completely mapped. To obtain the surface information, a tunneling current is established between the

tip and the surface. This results in a limitation on STMs, as they can only analyse conductive surfaces with a conductive tip. Since no mechanical contact is established between the tip and the surface, electrons have to tunnel through a barrier from the tip to the surface or vice versa.

In the view of classical physics, it is impossible for an electron with the energy E to penetrate a potential barrier V_0 if $E < V_0$. Considering the wave-particle dualism in quantum mechanics, electrons can be treated as waves with corresponding wave functions Ψ. The wave function of an electron ($E < V_0$) is not reflected like a particle in classical physics, but rather decays exponentially inside the potential barrier (Fig. 2.2a) as expressed with Eq. 2.1.[35]

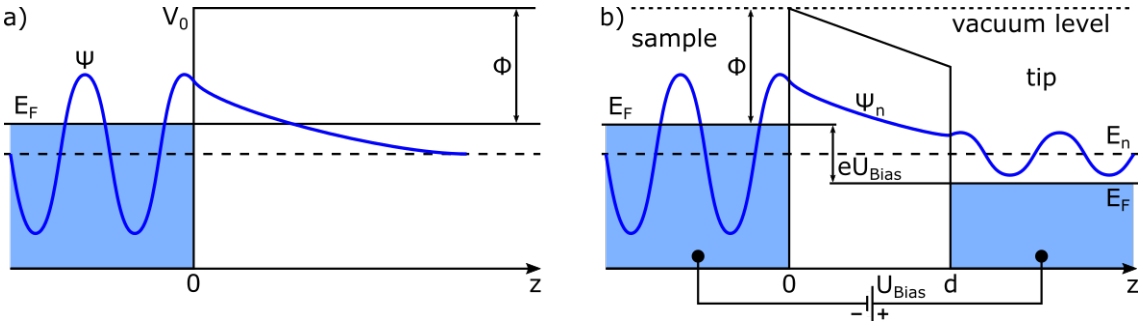

Figure 2.2: (a) Wave function Ψ of an electron before and inside a finite potential step. (b) Wave function Ψ of an electron tunneling through a finite vacuum barrier (thickness = d) between two metal electrodes (sample and tip) with applied bias U_{Bias}. Adapted and reproduced from Chen[35] *Introduction to Scanning Tunneling Microscopy: Second Edition* Copyright (2007), with permission of Oxford Publishing Limited through PLSclear.

$$\Psi(z) = \Psi(0)e^{-\kappa z} \tag{2.1}$$

Here, $\kappa = \sqrt{2m(V_0 - E)}/\hbar$ is the reciprocal exponential decay length of the wave function inside the barrier. m is the electron mass, $\hbar$ the reduced Planck constant and z the spatial coordinate. Considering two electrodes in close proximity, i.e. the gap d is small enough to render $e^{-\kappa d} > 0$, a non-zero probability exists for an electron to tunnel through the finite potential barrier between the two electrodes.[35]

In a STM, the two electrodes are the sample and the tip. For simplicity, sample and tip are considered to be metals with equal work functions Φ. Furthermore, thermal excitation will be neglected in this simplified approach making the Fermi level to the upper limit for occupied states in a metal. Now, defining the vacuum level as the reference level for energy, the energy of the Fermi level is equal to the work function ($E_F = -\Phi$). With sample and tip at the same potential, electrons will spontaneously tunnel in both directions, establishing an equilibrium. Applying a bias U_{Bias} between sample and tip, both Fermi levels shift with respect to each other and defining an energy window $[E_F - eU_{Bias}, E_F]$ (Fig. 2.2b). Now, electrons at the sample state Ψ_n with the energy E_n located in the interval $[E_F - eU_{Bias}, E_F]$ can tunnel from the sample (negative electrode) to the tip (positive electrode),

establishing a net tunneling current I_T. Considering a very small interval, i.e. for a bias much smaller than the work function ($eU_{Bias} \ll \Phi$), the energy levels E_n of all relevant sample states are close to the Fermi level energy E_F. The probability to observe an electron initially located in the sample with the energy E_n at the tip is proportional to,

$$|\Psi_n(d)|^2 = |\Psi_n(0)|^2 e^{-2\sqrt{2m\Phi}d/\hbar} \tag{2.2}$$

with $e^{-2\sqrt{2m\Phi}d/\hbar}$ being the transmission coefficient.[35] Hence, the net tunneling current I_T is proportional to the sum of all sample states n located in the energy interval $[E_F - eU_{Bias}, E_F]$, it can be stated with their respective tunneling probabilities:

$$I_T \propto \sum_{E_n=E_F-eU_{Bias}}^{E_F} |\Psi_n(0)|^2 e^{-2\sqrt{2m\Phi}d/\hbar} \tag{2.3}$$

For small eU_{Bias} the variation of the density of states (DOS) within the energy interval [E_F - eU_{Bias}, E_F] is negligible. Applying the local density of states (LDOS) of the sample ρ_s the tunneling current I_T is given by:

$$I_T \propto U_{Bias}\ \rho_s(0, E_F) e^{-2\sqrt{2m\Phi}d/\hbar} \tag{2.4}$$

More sophisticated models to determine I_T are stated by Bardeen, Tersoff, Hamann and Chen.[35–37] Nonetheless, the simplified model of Eq. 2.4 elucidates two key features of STM imaging. At first, it shows that the contrast strongly depends on the LDOS of the sample, i.e. high LDOS results in higher current which in turn leads to a higher brightness in the STM images and vice versa. Second, Eq. 2.4 explains the high vertical resolution of STMs. Owing to the exponential dependency of the tunneling current on the tip-sample distance d, STM is very sensitive to any variation of d, e.g. I_T changes about a magnitude with $\Delta d = 1$ Å.[38]

STM can operate in two modes: Constant high and constant current mode. In the constant high mode the tip height remains constant. The surface information is collected through the variation of I_T as d changes along the sample topology. Consequently, this mode bears the threat of a tip crash as d is not adjusted at all. More common is the constant current mode illustrated in Fig. 2.1. Here, a set point tunneling current $I_{T,set}$ is maintained. The tip-sample distance d is constantly adjusted by a feedback loop to eliminate the variation of $I_{T,set}$. The Z-position of the tip is recorded and used to extract a height profile to gain a topographic surface image. Yet, small variations of I_T cannot be excluded completely but used to extract an additional tunneling current image. For both, the images are generated by the assignment of respective height or current values to a colour code. The controlled manipulation of the tip with respect to the surface in X, Y and Z is discussed in the following section 2.2.

2.2 Piezoelectric Actuators

The relative movement between probe and sample must be controlled in a very precise way. Usually, the tip is the moving part and the sample is fix. Apart from the scan movement, the tip must be positioned and stabilized in close proximity to the surface to enable electron tunneling. This is commonly achieved with the aid of a fully automated coarse approach (cf. section 2.4) including a nanopositioner (cf. section 2.3). For both, scanning and distance stabilization, the ability of piezo actuators to deform in a very precise and controllable manner is used. The most common piezoelectric materials are lead zirconate titanate composites (PZT). Depending on composition, the individual PZT types differ in their piezo electrical properties.[39,40] In the following two sections the two most commonly, and also in this work, used piezo actuator types are introduced: The tube piezo actuator and the multilayer piezo actuator.

2.2.1 Tube Piezo Actuator

Tube piezo actuators are used in STM to perform the movement of the tip in the X, Y and Z directions. These tube piezo actuators consist of a monolithic PZT tube with a Z-electrode fully covering the inside and four equally segmented outer electrodes ($X+$, $X-$, $Y+$ and $Y-$). Tube piezo actuators are polarized radially, either towards the inside or outside of the tube (Fig. 2.3).

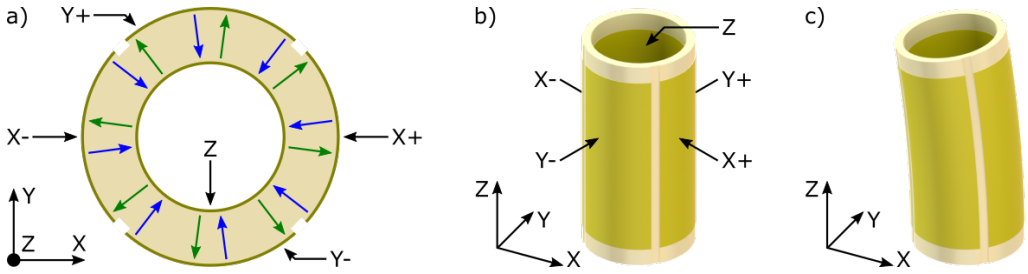

Figure 2.3: (a) Cross section scheme of a tube piezo actuator. The two possible polarizations are indicated by green and blue arrows, respectively, while the arrows point in the positive polarization direction. (b) Tube piezo actuator in its initial state and (c) bended towards $Y-$.

Polarized PZT features a tetragonal crystal unit cell ($A = B \neq C$) with its polarization axis along C. Upon applying an electrical field, the tetragonal crystal is expanded or contracted along its polarization axis if the polarization of the electrical field is orientated equally or unequally to the polarization axis, respectively. At the same time, the dimension of the unit cell perpendicular to the polarisation axis changes: An expansion along the polarization axis results in perpendicular contraction of the unit cell and a contraction along the polarization axis leads to a perpendicular expansion. The relation between the applied electrical field and the deformation along the polarisation axis is given by the piezoelectric coefficient d_{33} (m/V) and for the perpendicular deformation d_{31} (m/V). For a tube piezo actuator

only the deformation perpendicular to the polarization axis is used to generate the X, Y and Z movement. For the deformation along the Z-axis, a voltage U is applied between the inner and all outer electrodes. The travel ΔZ_P can be estimated with:

$$\Delta Z_P \approx d_{31} \cdot Z_P \cdot \frac{U}{d_T} \tag{2.5}$$

Here, Z_P is the initial length of the electric contacted tube and d_T is the wall thickness of the tube.[39]

For the lateral bending of the tube in the X-Y plane the electrodes are addressed individually. For instance, by applying a voltage U between the Z and the $Y-$ electrodes, the piezo will either bend towards $Y-$ or $Y+$ depending on the polarization of the material and the polarity of the voltage U. The bending results from the perpendicular expansion or contraction of the PZT crystals between the electrodes. Figure 2.3c shows the bending towards $Y-$ through a contraction. The elongation along $Y-$ can be doubled by additionally applying the inverted U signal (bipolar mode) to the opposing electrode, e.g. expansion at $Y+$. The lateral bending of a tube piezo actuator ΔS in the X-Y plane can be estimated with Eq. 2.6.

$$\Delta S \approx \frac{n\sqrt{2} \cdot d_{31} \cdot Z_T^2 \cdot U}{\pi \cdot D_I \cdot d_T} \tag{2.6}$$

Here, Z_T is the initial length of the tube, D_I is the inner diameter of the tube and the factor n considers to the operation mode ($n = 1 \rightarrow$ unipolar mode, $n = 2 \rightarrow$ bipolar mode).[39] During scanning the tip sample distance d is constantly adjusted, hence, the voltage signal for the Z deformation is superimposed to the signals for scanning of the tube.

2.2.2 Multilayer Piezo Actuator

Multilayer piezo actuators consist of several parallel-connected layers of PZT separated by metal electrodes as indicated in Fig. 2.4.

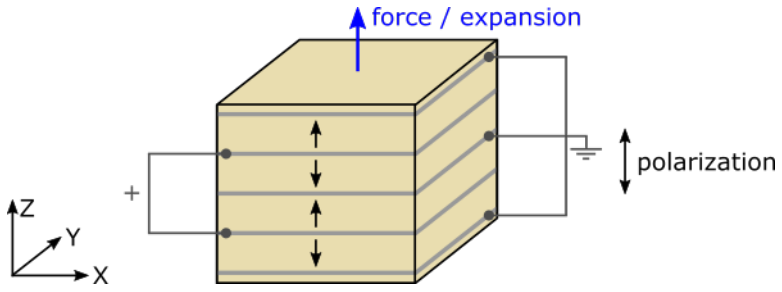

Figure 2.4: Scheme of a unipolar multilayer piezo actuator.

The electrodes contact the PZT material between them similar to the tube piezo actuator. The generated force/deformation is parallel to the polarization axis (Z-direction). Hence, the used piezoelectric charge constant is d_{33} (m/V) and the total expansion ΔZ_P can be calculated with:

$$\Delta Z_P = d_{33} \cdot n \cdot U \tag{2.7}$$

Here, U is the applied voltage and n is the number of PZT layers.[39] Multilayer piezo actuators work unidirectional in expansion mode and cannot compress any further from their initial geometry. These types of piezo actuators are highly appropriate for the integration into stick-slip nanopositioners that are widely used for the automated coarse approach in SPM.

2.3 Stick-Slip Nanopositioner

For electrons to tunnel, probe and sample must be in close proximity to each other with $d < 1nm$. To meet this condition, a very precise mechanical positioning system is needed. One component of this system is the nanopositioner. Several types of nanopositioners exists[41] as simple leverage systems[19] or stick-slip based systems like the beetle[42] or pan type.[43] Here, for the I-STM, a stick-slip nanopositioner is used (cf. chapter 6). Its basic setup is shown in Fig. 2.5.

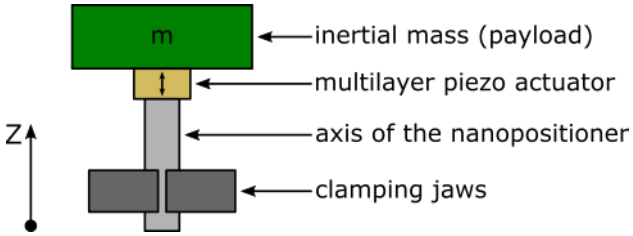

Figure 2.5: Scheme of the of stick-slip nanopositioner applied in the I-STM.

The actuator of this nanopositioner is a multilayer piezo glued between a mass (the payload) and an axis that is clamped between two spring loaded clamping jaws. In order to move the axis relative to the jaws, a force F_P greater than the clamping force F_C must be applied. For making a step, the actuator expands along Z and lifts the mass up while the position of the axis relative to the jaws is preserved ($F_P < F_C$). In the next setep, the multilayer piezo returns to its initial geometry. This is done fast enough to overcome the clamping force F_C of the jaws ($F_P > F_C$), hence, the nanopositioner makes a step. Depending on the expansion and compression dynamics of the piezo the nanopositioner moves forward or backward. A slow expansion and fast compression results in a forward step. In turn, a step back is taken for a fast expansion of the piezo followed by a slow compression. The corresponding saw-tooth drive signals are illustrated in Fig. 2.6.

The step size is proportional to the amplitude of the drive signal. Step sizes for the automated coarse approach (cf. section 2.4) are typically chosen between 40 nm – 50 nm, while for a fast manual tip-sample manipulation the step sizes can be increased to 100 nm – 150 nm. The saw-tooth frequency corresponds to the speed of motion and is typically set to 1000 Hz during manual manipulation.

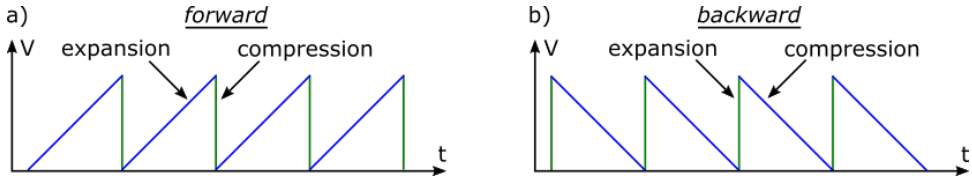

Figure 2.6: Saw-tooth drive signal for a stick-slip nanopositioner for (a) forward and (b) backward movement.

2.4 Automated Coarse Approach

The approach of the tip within a distance of less than 1 nm to the sample surface cannot be achieved with the discrete step size of a stick-slip nanopositioner alone ($\sim$40 nm). However, the required precision can be achieved through the combination of the nanopositioner and the STM scan unit, i.e. the tube piezo actuator. The tube piezo actuator expands continuously and bridges the distance between the discrete steps of the nanopositioner in a repeated approach cycle. Figure 2.7 shows the position of the tip with respect the surface during the automated coarse approach.

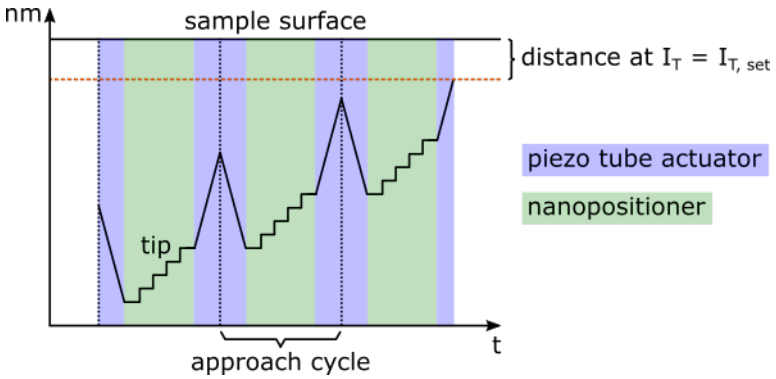

Figure 2.7: Position of the tip with respect to the sample surface during the automated coarse approach.

The starting point of the approach cycle is the fully expanded tube piezo actuator with the attached tip as illustrated in Fig. 2.7. For the I-STM, a tube piezo actuator with a total theoretical Z-range of $\sim$470 nm from maximum compression at -130 V to maximum expansion at +130 V is used (cf. section 6.5.1).[44] In the first step of the approach cycle, the tube piezo actuator compresses completely. In the next step, the nanopositioner moves a defined number of steps toward the sample surface. It is important that the total travel of the nanopositioner is set to less than the maximum Z-range of the tube piezo actuator. Otherwise, there is a risk of a tip-surface crash. After the movement of the nanopositioner, the tube piezo actuator expanse to its maximum. During the expansion, the STM controller applies a constant tunneling bias U_{Bias} between the tip and the sample. The feedback compares the measured tunneling current I_T with the setpoint current $I_{T,set}$. If the tube piezo actuator is fully expanded and $I_T < I_{T,set}$, the approach cycle ends without establishing tunneling current, i.e. the tip is still too far away from the

sample. For the automated coarse approach the approach cycle is repeated until $I_T = I_{T,set}$.

As this process is rather time consuming, it is recommended to place the tip via manual control in close proximity to the sample surface before the automated coarse approach is started. For instance, during the automated coarse approach the tip moves about $\sim$600 nm per second. With the aid of a digital camera, it is possible to manually placed the tip in a distance of $\sim$0.2 mm to the sample. In this case, the automated coarse approach takes already $\sim$55 min.

Chapter 3

Thermodynamic Methods

In the following section the theoretical background for the experimentally determination of the dissolution (ΔH_{diss}) and sublimation (ΔH_{sub}) enthalpy will be described. Furthermore, the used experimental setup and the experimental procedure to acquire the data are explaned.

3.1 Variable-Temperature UV-vis Spectroscopy

The enthalpy of dissolution (ΔH_{diss}) is the enthalpy change during the transition of a substance from its bulk crystal structure into a solution. Apart from the physical and chemical properties of a substance and solvent, pressure and temperature strongly affect with the solubility. At constant pressure, ΔH_{diss} can be determined through temperature dependent concentration measurements of a saturated solution via variable-temperature UV-vis spectroscopy.

3.1.1 Theoretical Background

A well-suited technique to measure the solubility of a solution is UV-Vis spectroscopy (UV = ultra violet, Vis = visible). UV-Vis spectroscopy is an electron absorption spectroscopy. While the Einstein-Bore equation grants access to the type of substance by its unique broad bands, the Beer-Lambert-Bouguer law (Eq. 3.1) is the physical foundation for the absorption intensity – the absorbance A.[45]

$$log(\frac{I_0}{I}) \equiv A = \epsilon \cdot c \cdot d \tag{3.1}$$

The intensity of the light transmitted through the pure solvent is I_0 and through the solution is I. d is the optical path length, c the concentration, and the adsorption of the transmitting light is taken into account with the extinction coefficient ϵ.

The absorbance A is related to the solute concentration. With a standard bulk concentration of 1 $mmol\ L^{-1}$, A is proportional to the equilibrium constant K_c (Eq. 3.2).

$$K_c = \frac{c_{diss}}{c_{bulk}} = c_{diss}\ with\ c_{bulk} = 1\ (mmol L^{-1}) \tag{3.2}$$

The van't Hoff equation can be applied to derive the standard dissolution enthalpy and the standard dissolution entropy from the temperature dependency at the solubility (Eq. 3.3).

$$ln(A) = Ln(K_c) = -\frac{\Delta G^\circ}{RT} = -\frac{\Delta H^\circ}{RT} + \frac{\Delta S^\circ}{R} \tag{3.3}$$

Here, ΔG° is the Gibbs free energy at standard conditions, ΔH° the standard enthalpy and ΔS° the standard entropy of dissolution. To derive the enthalpy of dissolution, the absorbance A of a saturated solution must be determined for a set of different temperatures $(T_1, T_2, \ldots, T_n)$. Plotting the logarithm of the measured absorbances $ln(A)$ over the reciprocal temperature T^{-1} yields the standard enthalpy H° that directly corresponds to the dissolution enthalpy ΔH_{diss} ($\Delta H^\circ = \Delta H_{diss}$). The slope of a linear fit directly corresponds to ΔH_{diss}. Furthermore, the interception with the Y-axis corresponds to the standard entropy change of dissolution ΔS°_{diss}.

3.1.2 Experimental Setup

Variable Temperature UV-vis Spectrometer

To quantify the temperature dependent solubility via UV-vis spectroscopy, a conventional fibre optic UV-vis spectrometer has been extended with a feedback controlled cuvette heater. A sketch of the setup is depicted in Fig. 3.1.

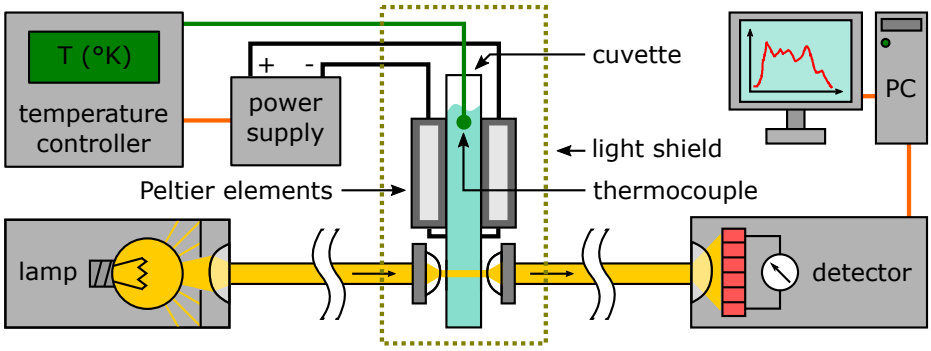

Figure 3.1: Scheme of the UV-vis spectrometer setup with cuvette heater.

A *DH-mini UV-Vis-NIR* light source from *Ocean Optics* with two light bulbs (tungsten and deuterium) is covering a wavelength range of 200 nm to 2500 nm.[46]

In turn, the *Ocean Optics USB4000* spectrometer only detects wavelength from 200 nm to 1100 nm, setting the detection limit of the setup.[47]. A macro cuvette (*110-QX* from *Hellma Analytics*) with a transmission range between 200 and 3500 nm and an optical path length of 1 mm is used. The source-to-cuvette and cuvette-to-detector light guidance is implemented via glass fibre cables and a simple lens system.

Heating of the cuvette is realized with two standard Peltier elements (*QC-17-1.4-8.5M* from *Quick-Ohm Küpper*) at both sides.[48] The solution temperature is measured via a *5SRTC* K-type thermocouple from *OMEGA Engineering* reaching into the cuvette.[49] The *EA-PS 3032-05-B* DC power supply from *Elektro Automatik* is proving the heating power in combination with a *2416* temperature controller (*Eurotherm*).[50] A detachable *PTFE* frame is used to fix and orientate the cuvette in the light path. To avoid noise from ambient light, the cuvette and its heater unit are completely covered. UV-Vis spectra are recorded with the *Ocean Optics* software *Spectra Suit v6.1*.

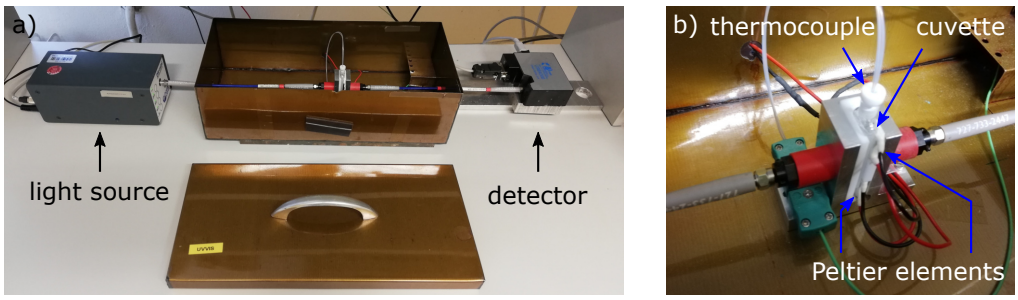

Figure 3.2: (a) Setup of the temperature-controlled UV-vis spectrometer. (b) Cuvette mounted in the heater unit with immersed thermocouple.

Stock Solution Thermostat

To determine the dissolution enthalpy, a saturated solution must be prepared and conditioned at the exact same temperature at which the absorbance measurement takes place. Saturated solutions can be simple prepared by adding a sufficient amount of solute to a solvent. A stable solute sediment at the beakers bottom guarantees the saturation and serves as a solute reservoir during temperature changes. Unfortunately, this approach bears the risk to pick up some of the sediment during pipetting. To avoid this, a relatively large solvent volume in a high beaker establishes enough space between the settled sediment and the solution surface and provides enough volume for the measurement series. This is considered in a home-built heatable and hermetically sealed container – the stock solution thermostat.

So far, two versions of the thermostat are developed. The first version featured an inner container out of *PTFE* in which the solvent and the solute crystals are filled in (Fig. 3.3a). Unfortunately, metal abrasions were implemented in the *PTFE*, leading to a contamination of the solution. Therefore, a revision of the thermostat was unavoidable.

Figure 3.3: Disassembled stock solution thermostat (a) version 1 and (b) version 2. (c-d) Assembled version 2 stock solution thermostat on top of the magnetic stirrer. For additional thermal isolation a glass beaker with plastic hood is covering the device.

In the second version, the inner container is a high glass beaker (filling level = ∼18 mL) covered by a thin glass plate. Both parts are sealed inside a stainless steel container via a lid made out of the same material and an O-ring gasket. Eight stainless steel screws are providing the needed sealing pressure. The heating is implemented via a heating wire (∼45 Ω) wrapped around the outer container. A K-type thermocouple is measuring the temperature in a bore at the containers bottom. The temperature is kept constant by a *Eurotherm 2416* temperature controller setting the output of a *EA-PS 3032-05-B* DC power supply from *Elektro Automatik*. To promote a homogeneous solute distribution in the solution, a magnetic stirrer is used driven by the *MR Hei-End* magnetic stirrer from *Heidolph* (heating function was not used).[51]

3.1.3 Experimental Procedures

The procedures starts with the preparation of a saturated solution with the stock solution thermostat. Therefore, the inner glass container is filled with ∼18 mL of pure solvent and a sufficient amount of the bulk solute to ascertain saturation at all temperatures (establishment of sediment). Depending on the solubility at higher temperatures, a preliminary test to determine the required amount of substance can be appropriate. After the immersion of the magnetic stirrer, the glass container is covered by a microscopy slide and sealed inside the heatable container. Finally, the container can be heated to the first measurement temperature while the solution is slowly stirred at ∼100 rpm. The protocol consists of 2 h of steering after the container reached its target temperature followed by at least 18 h of halt. Within this equilibration period the undissolved bulk crystals can settle to the bottom of the inner container. Thereafter, the saturated solution is ready for the UV-vis absorbance measurement.

The preparation of the UV-vis spectrometer consists of the preheating of the lamps to their operation temperature. Otherwise, intensity variations can distorted the data. *Ocean Optics* states a warm-up time of 6 min + safety for the *DH.mini*

UV-Vis-NIR light source.[46] In parallel, the cuvette can be pre-heated to the desired measurement temperature, the same as the preparation temperature of the solution. The first measurement is the determination of the reference spectrum of the pure solvent (I_0). Therefore, ∼140 μL of pure solvent are pipetted into the pre-heated cuvette. At this filling level the thermocouple is immersed into the pure solvent for a reliable temperature measurement. It is recommended to wait for additional 10 min to assure a homogeneous temperature distribution of the solvent before the reference spectrum is taken as an average of 1000 single spectra. The integration time is always set to the maximum to fully exploit the dynamic range of the detector unit (60 ms for the used fatty acid solutions). It is important that the integration time of the reference and solution spectra are always identical.

Thereafter, the cuvette is emptied with a lint free paper tissue. For that, the cuvette can be removed from the heater together with its *PTFE* frame. The fitting of the frame assures the similar orientation of the cuvette to the light path before and after removal. For the measurement of the solution spectrum (I) the cuvette is again pre-heated. Now, the preparation device is carefully opened and ∼140 μL of solution are pipetted and placed into the pre-heated cuvette. This should be done relatively fast to avoid substantial cooling, i.e. concentration changes, of the stock solution and the taken sample. In the cuvette, the solution should be heated to the measurement temperature for at least ∼10 min before the spectrum is taken. In parallel, the preparation device is sealed again and heated or cooled down to the next temperature following the same procedure as mentioned before. It is recommended to select the measurement temperatures in a non-monotonic order to identify kinetic influence on the dissolution process.

Figure 3.4 illustrates the data processing of a temperature dependent absorbance measurement at the example of a saturated NDA-9A solution. In order to minimize the influence noise in the absorbance, it is recommended to integrate an absorbance range instead of taking a single peak value. Note that large fluctuations at the lower detection limit (200 nm) can drastically alter the absorbance. Hence, the selected absorbance range should be in a spectral range, where the absorbance is stable. For instance, in Fig. 3.4c, the region around the smaller peak at ∼295nm is more appropriate as the region around the strong peak at ∼245nm, which may be influenced by the lower detection limit.

The cleaning protocol for the cuvette consists of the extraction of the solution with a twisted lint free paper tissue first, followed by flushing of the cuvette with isopropanol. After the isopropanol is extracted (paper tissue), the cuvette is flushed with clean water. Now, a 1 % solution of a cuvette cleaning agent (*Hellmanex III* from *Hellma*) with distilled water is prepared to flush the cuvette with the aid of a disposable syringe. Until the next measurement, the cuvette is placed in the prepared cleaning solution for at least 2 h. Before the next measurement is conducted, the cleaning agent is removed by flushing the cuvette with pure distilled water. To accelerate the drying process, the cuvette can be placed in an oven at ∼70 $^{\circ}C$.

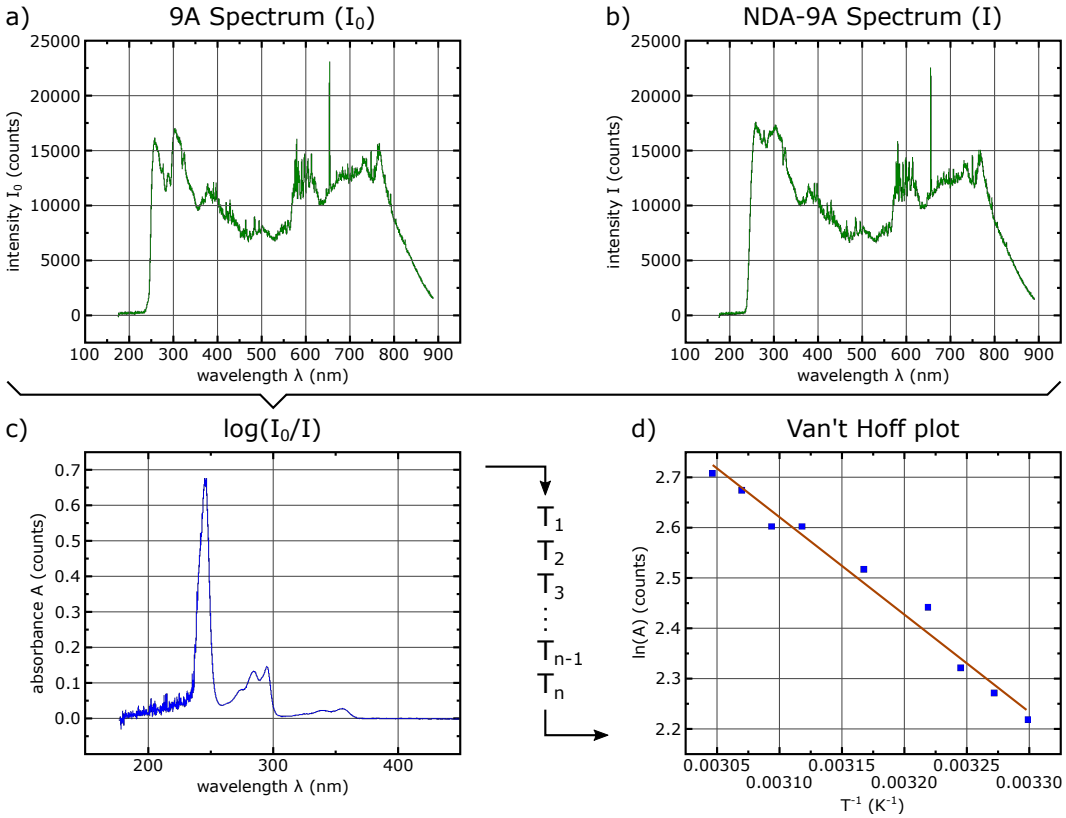

Figure 3.4: UV-vis spectrum of (a) pure 9A solvent and (b) NDA-9A solution. (c) The absorbance corresponds to the NDA concentration in the NDA-9A solution. (d) Van't Hoff plot. Blue squares correspond to single temperature dependent absorbance measurements. The slope of the linear fit corresponds to the standard dissolution enthalpy ΔH° and the Y-axis intercept to the standard dissolution entropy change ΔS°

3.2 Vacuum Effusion

The required enthalpy for the phase transition of a substance from its solid state to its gas phase without an intermediate liquid phase is the enthalpy of sublimation ΔH_{sub}. The sublimation enthalpy can be extracted from the temperature dependant vapour pressure of a substance, which is approximately proportional to the effusion rate. A well-established method to derive the enthalpy of sublimation is the deployment of a Knudsen effusion cell in combination with a quartz crystal microbalance (QCMB) to count the effused mater.

3.2.1 Theoretical Background

A Knudsen cell is a heatable container with a small orifice that can create a molecular beam in vacuum. Inside the Knudsen cell an equilibrium is maintained between the solid (or liquid) phase and the vapour of the test material, while a portion of the vapour escapes from the container through the orifice (molecular beam).[52,53]

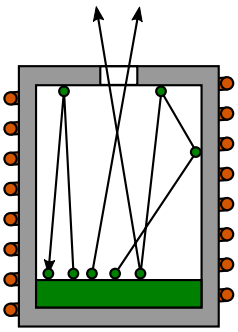

Figure 3.5: Scheme of a Knudsen effusion cell (substance = green).

This statement remains valid if the actual device meets some requirements. First, the device must be able to provide a high degree of temperature stability (isothermal environment).[52] The effusion of mater should not disturb the equilibrium between the vapour and the solid material. Hence, the orifice must be small and a sufficient amount of solid mater always available.[52] The wall thickness of the orifice must be small compared to its diameter. Otherwise, i.e. with a tube like orifice geometry, molecules might be reflected.[53] Furthermore, the diameter of the orifice must be comparable small to the mean free path of the molecules within the cell[52,53]. Under vacuum conditions the loss of material through the orifice can be calculated with Eq. 3.4:

$$\frac{\Delta m}{\Delta t} = \frac{1}{4}\frac{p(T)}{RT}\langle v\rangle A_O \quad with \quad \langle v\rangle = (8k_BT/\pi M)^{1/2} \tag{3.4}$$

Here, Δm is the effused mass in the time period Δt, $p(T)$ is the vapour pressure within the cell, R is the gas constant, T is the temperature, A_O is the area of the orifice, and $\langle v\rangle$ the average gas velocity with the Boltzmann constant k_B and the molecular mass M. The mass effusion per unit time $\Delta m/\Delta t$ corresponds with the vapor pressure inside of the Knudsen cell $p(T)$ multiplied with $T^{-1/2}$.[54] The influence of $T^{-1/2}$ on the effusion rate can be neglected within a sufficiently small temperature range. Accordingly, $\Delta m/\Delta t$ can be expressed as:

$$\frac{\Delta m}{\Delta t} \propto p(T) \tag{3.5}$$

Hence, the effusion rate $\Delta m/\Delta t$ serves as an approximation for the vapour pressure. The effusion rate can be measured with a QCMB. A standard QCMB consists of a thin quartz plate with electrodes on both sides (Fig. 3.6a). Quartz is piezoelectric and can be deformed by an electrical field. An applied oscillating electrical field induces an acoustic sheer oscillation (Fig. 3.6b). Hence, a transversal wave propagates perpendicular to the surface of the plate and meets its minimum impedance when the thickness of the plate is a multiple of a half wavelength (standing shear wave).[55,56]

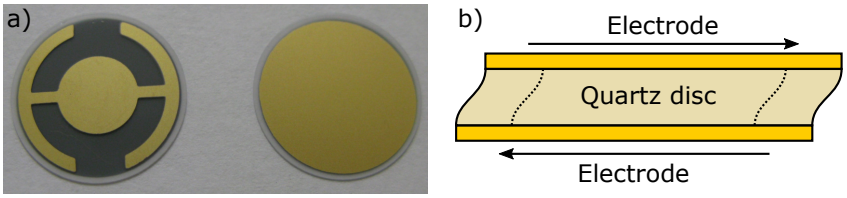

Figure 3.6: (a) Front side (left) and back side (right) of a *6MHz CNT06IG* QCM from *Colnatec*. (b) Scheme of a QCMB operating in shear mode. Adapted with permission from Deakin and Buttry[55]. Copyright (1989) American Chemical Society.

Adding an adsorbed layer to a QCMB results in a reduction of the discs fundamental frequency through the increased oscillating mass. As the fundamental frequency of a quartz oscillator can be measured with high precision, a plate quartz crystal oscillator can be used as a very sensitive instrument to weigh thin layers.[57] The change of the fundamental frequency can be measured to calculated the mass of the adsorbed layer with the Sauerbrey equation (Eq. 3.6).

$$\Delta f = -\frac{2f_0^2}{A_Q \upsilon_{tr} \rho_Q} \Delta m \quad with \quad \upsilon_{tr} = 2N_Q \tag{3.6}$$

Here, Δf is the change of the fundamental frequency, f_0 is the fundamental frequency of the pristine QCMB, Δm is the deposited mass, A_Q is the active area of the QCMB, and ρ_Q is the density of quartz (2.648 $g\ cm^{-3}$). The propagation velocity of the transversal wave is υ_{tr}, defined as the doubled frequency constant of the quartz crystal cuts N_Q (N_Q for AT-cuts = 1670 $kHz\ mm$ and for BT-cuts N_Q = 2500 $kHz\ mm$).[55,57]

Furthermore, the frequency change Δf over a time period Δt correlates to the mass deposition Δm over the same period. Hence, the effusion rate of a Knudsen cell ($\Delta m/\Delta t$) is proportional to the rate of frequency change of a QCMB ($\Delta f/\Delta t$):

$$\frac{\Delta f}{\Delta t} = \frac{\Delta m}{\Delta t} \propto p(T) \tag{3.7}$$

With the temperature dependency of the vapour pressure, the enthalpy of sublimation ΔH_{sub} can be obtained from the Clausius-Clapeyron equation (Eq. 3.8).[54]

$$\frac{dp}{dT} = \frac{\Delta H_{sub}}{\Delta V_m T} \tag{3.8}$$

With the assumption that the molar volume of the gas $V_{m,gas}$ is much bigger as the molar volume of the bulk crystal $V_{m,bulk}$, the change of the molar volume ΔV_m can be approximated with the molar volume of an ideal gas $V_{m,gas} = RT/p$, leading to:

$$\frac{dp}{dT} = \frac{p\Delta H_{sub}}{RT^2} \tag{3.9}$$

The intergration of equation 3.9 results in a logarithmic relation of the vapour pressure p to the sublimation enthalpy ΔH_{sub} (Eq. 3.10).

$$ln(p) = \frac{\Delta H_{sub}}{RT} \tag{3.10}$$

With equation 3.10 and the relation of the QCMBs rate of frequency change to the vapour pressure of a Knudsen cell (Eq. 3.7), the enthalpy of sublimation ΔH_{sub} can be obtained by measuring the frequency decline rate $\Delta f/\Delta t$ vs. Knudsen cell temperature T (Eq. 3.11).

$$ln(\frac{\Delta f}{\Delta t}) \propto \frac{\Delta H_{sub}}{RT} \tag{3.11}$$

To derive ΔH_{sub} from a set of $\Delta f/\Delta t$ vs. T data points facilitates a Van't Hoff plot ($ln(\Delta f/\Delta t)$ vs. $1/T$). The data points can be fitted with a linear function, where the slope corresponds to the sublimation enthalpy ΔH_{sub}. A high quality of the fit indicates a negligible temperature dependency of ΔH_{sub} in the respective temperature range and also a negligible influence of $T^{-1/2}$ (Eq. 3.5).

3.2.2 Experimental Setup

Effusion Chamber

The effusion rate is measured at vacuum conditions with a pressure of at least $10^{-7} mbar$. The effusion chamber is a six way CF63 crosspiece (Fig. 3.7a). Two opposing flanges are reduced to CF40 flanges to host the Knudsen cell and QCMB. Both, the Knudsen cell and QCMB are centered at the flange axis in a distance of about 6cm to each other (Fig. 3.7b).

The chamber is evacuated by a turbo molecular pump *TMU 260* and a dual stage rotary vane vacuum pre-pump *DUO 004 B*, both from *Pfeiffer Balzers*. The pressure is measured via the *VSI19PN* vacuum gauge from *Thyracont*.

Knudsen Cell

The design of the used Knudsen cell (Fig. 3.7d-e) is further development from the setup proposed by Gutzler et al.[58] In this setup, the Knudsen cell consists of a crucible (purple) closed by a detachable orifice cap (light blue). The crucible volume ($\sim$93 mm^3) to orifice diameter ($\varnothing 1\ mm$) ratio is reasonable and meets the requirements stated by Knudsen and Freedman (Eq. 3.4).[52,53] Isothermal conditioning of the crucible and orifice is promoted by an Al_2O_3 tube, heating the crucible via a

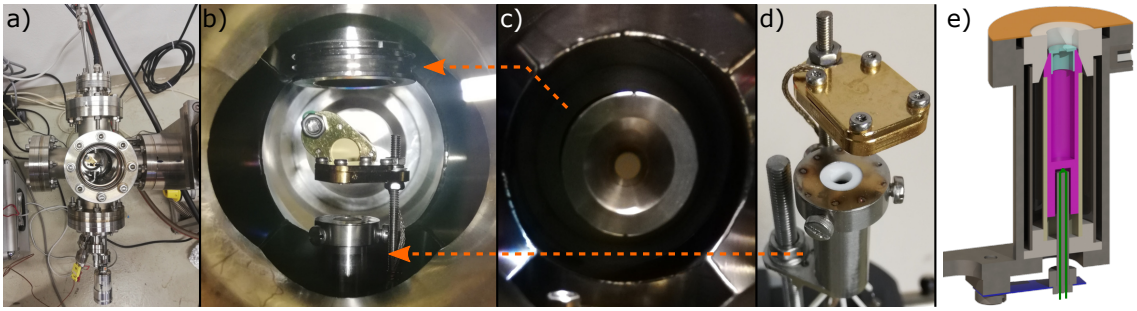

Figure 3.7: (a) Effusion vacuum chamber with attached Knudsen cell and a water cooled QCMB. (b) View through the view port onto the QCMB holder and Knudsen cell in their axial arrangement. Note that the additional QCMB perpendicular to the effusion axis has no function in this setup (c) Top view on the mounted QCMB. (d) Knudsen effusion cell based on the design from Gutzler et al.[58] (e) 3D CAD sectional view of the Knudsen cell assembly (purple = Knudsen cell, light blue = orifice cap, green = thermocouple, orange = annular spring, dark blue = leaf spring).

closely wrapped around tungsten heating wire. Thermal isolation is implemented via two *Macor* isolators and an inner radiation-shield. The temperature measurement (green) takes place in close proximity to the crucible bottom using a thermocouple. For a reliable temperature determination, the thermocouple is pushed against the crucible bottom via a leaf spring (dark blue). The crucible in turn is pressed against the upper rim of the Al_2O_3 by the spring loaded upper *Macor* isolator (orange = annular spring). For filling, the crucible can be detached from Al_2O_3 heating tube. Therefore, the upper isolator and its spring loaded downholder ring can be removed. Note that the crucible in this version is electrically insulated from its metal support structure.

The Knudsen cell is concentrically attached to a CF40 flange via a threaded rod. The distance between flange and Knudsen cell can be adjusted. The setup additionally features a shutter with integrated QCMB (Fig. 3.7b, d), but for the determination of sublimation enthalpy a different QCMB was used. The heating current is provided by a *EA-PS 3032-05-B* from *Elektro Automatik*, a *2408* controller from *Eurotherm* is used to stabilize the target temperature.

Quartz Crystal Microbalance (QCMB)

The close proximity of the internal QCMB in the shutter of the Knudsen cell to the hot crucible can lead to fluctuations in the frequency measurement. Therefore, an external water-cooled QCMB was used. (Fig. 3.7b-c). In this setup, the QCMB is fixated via a bayonet lock in its support structure. The used type is a *6MHz CNT06IG* QCMB from *Colnatec* with a disc diameter of 14 mm. Temperature stabilization is archived by water cooling. The *D8-G* cooling device from *Haake* provides a constant coolant flow and promotes temperature conditioning between room temperature and $-15\ °C$. The QCMB frequency is excited and measured by

a Q-pod quartz crystal monitor and recorded by the Q-pod Transducer Software, both from *Inficon*.[59]

3.2.3 Experimental Procedure

In the first step, the carefully cleaned and outgassed Knudsen cell crucible must be filled with the compound of interest. After reassembling the crucible, it is important to check the electrical contact between the crucible and the thermocouple to ensure reliability of the temperature measurement. Next, the QCMB is placed in its support structure and flanged to the chamber. After the chamber is evacuated to a pressure of at least $10^{-7} mbar$ and the QCMB stabilized to 20 $°C$, the measurement can be started.

To measure the effusion rate the Knudsen cell is heated up until initial effusion is detected through a decline of QCMB frequency. After the temperature is stable for at least 15 min and the effusion rate is constant, the frequency decline rate $\Delta f/\Delta t$ can be recorded. To acquire reliable data, the frequency decline rate should be recorded over at least 10 min (∼1000 data points) after the QCMB has stabilized. Thereafter, the temperature can be raised to the next temperature to record the next frequency decline rate, and so on. After acquisition of all frequency decline rates the enthalpy of sublimation can be determined as described in section 3.2.1. Figure 3.8 depicts this process at the example of NDA.

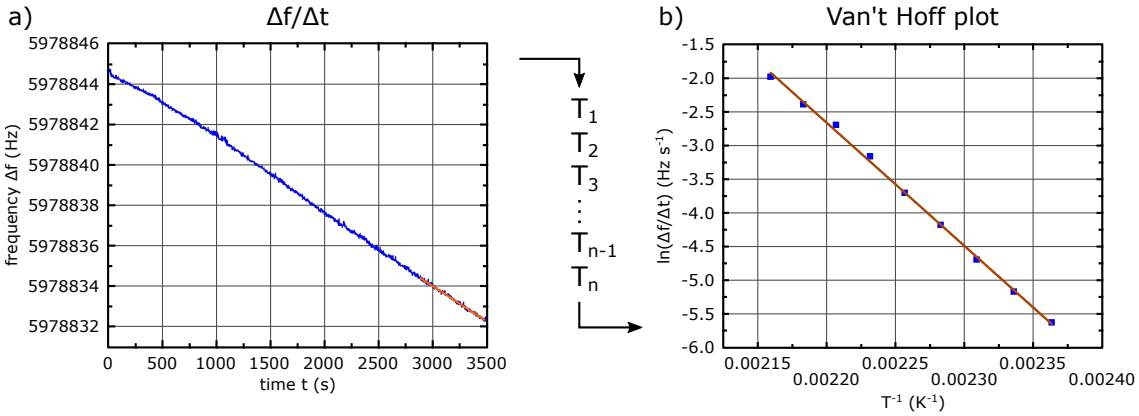

Figure 3.8: (a) Frequency decline vs. time trace at a single temperature during the sublimation of NDA. Only the last 10 min are used (orange line) to determine the slope as the not yet stabilized setup at the beginning would affect the results. The different rate at the beginning indicates that the crucible temperature has not yet stabilized. (b) Van't Hoff plot and linear fit of the measured frequency decline rates $\Delta f/\Delta t$.

Chapter 4

Molecules and Substrate

4.1 Molecules

Two carboxylic acid building blocks were studied in the course of this thesis: 2,6-naphthalene-dicarboxylic acid (NDA) and benzene-1,3,5-tricarboxylic acid or trimesic acid (TMA), illustrated in Fig. 4.1.

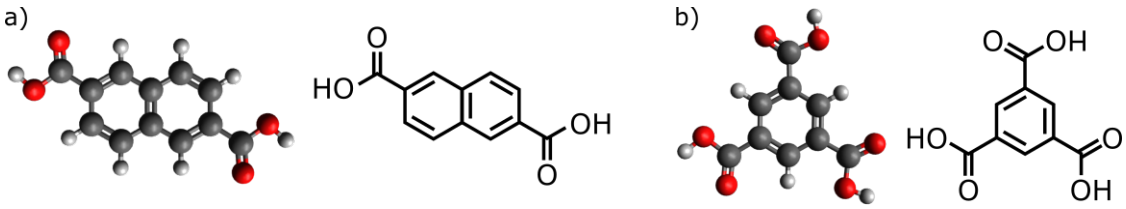

Figure 4.1: Chemical structures of (a) 2,6-naphthalenedicarboxylic acid ($C_{10}H_6(CO_2H)_2$) - NDA, (b) Benzene-1,3,5-tricarboxylic acid or trimesic acid ($C_6H_3(CO_2H)_3$) – TMA.

Both molecules feature an aromatic backbone functionalized with carboxylic acid groups to form hydrogen bonds with themselves or with an appropriate binding partner like the homologous series of fatty acids (cf. section 4.2). NDA and TMA were both purchased from Sigma-Aldrich with a purity of 99 %. For STM and UV-Vis experiments the molecules were used as received, while for the sublimation experiments the molecules were outgassed in vacuum.

4.2 Solvents

For the preparation of solutions hexanoic acid (6A), heptanoic acid (7A) and nonanoic acid (9A) from the homological series of fatty acids were used as solvents as well as two branched hexanoic acid derivates 2-methylhexanoic acid (methyl-6A) and 2-ethlyhexanoic acid (ethyl-6A) (Fig. 4.2).

These solvents are highly appropriate for monolayer formation at the liquid-solid interface, due to their carboxylic acid groups (protic solvents). The protic solvents are able to form hydrogen bonds with the used carboxylic acid solutes TMA and

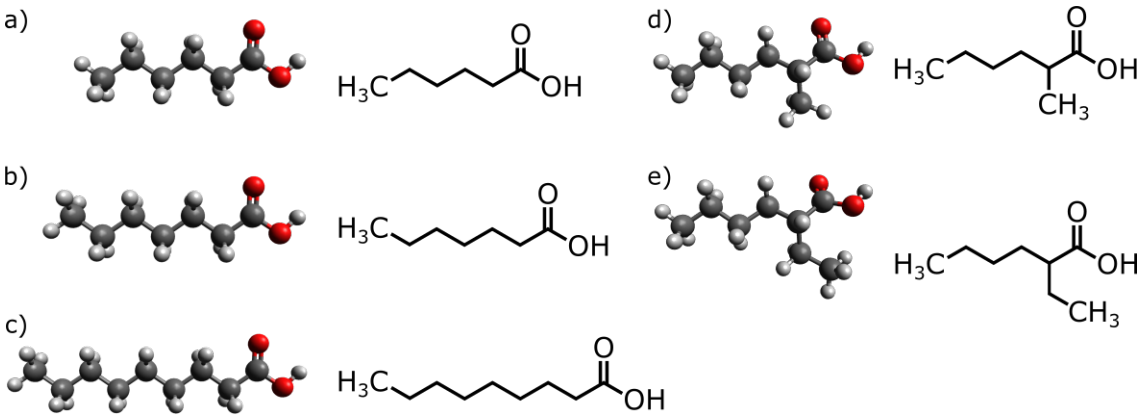

Figure 4.2: Chemical structure of fatty acid solvents and hexanoic acid derivates: (a) hexanoic acid ($C_6H_{12}O_2$) - 6A, (b) heptanoic acid ($C_7H_{14}O_2$) - 7A, (c) nonanoic acid ($C_9H_{16}O_2$) - 9A, (d) 2-methylhexanoic acid ($C_7H_{14}O_2$) - methyl-6A, (e) 2-ethlyhexanoic acid ($C_8H_{16}O_2$) - ethyl-6A.

NDA. The five solvents feature a low dielectric constant ϵ in the range from $\sim$2.5 - 3.2 due to extended aliphatic chains, giving them a non-polar character.[60] All solvents are used as received and were purchased from *TCI* (*Tokyo Chemical Industry*) with purities of >98 %.

4.3 Substrate

In this study, exclusively highly oriented pyrolytic graphite (HOPG) in the (0001) orientation was used as substrate for self-assembly and as a calibration standard for the STM.

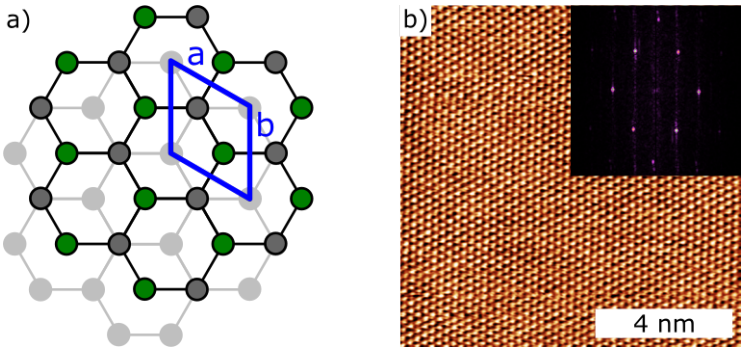

Figure 4.3: (a) Scheme of two graphite (0001) layers with indicated rhombus unit cell. The C-atoms that are visible in STM are highlighted in green, (b) atomically resolved STM image of HOPG with corresponding FFT insert (STM sample voltages and current setpoint: 4.4 mV, 59 pA). Adapted and reprinted with permission from Ochs et al.[61]. Copyright (2020) Review of Scientific Instruments.

HOPG was purchased from *Optigraph* in the ZYB grade (mosaic spread = 0.8° ± 0.2°). HOPG features an in plane C-C distance of 1.422 ± 0.001 Å and a lattice

parameter of a = b = 2.464 ± 0.002 Å, $\gamma = 120°$.[62] The *ABAB* stacked layers are separated by a distance of 3.35 Å.[63] In STM images, only every second atom of the top layer is visible. According to the stacking, every second C-atom of the top layer is located above an atom of the layer below. These atoms are not visible in an STM image as their local electron densities is reduced by neighbouring C-atoms below.[64,65] The visible C-atoms are highlighted in green in Fig 4.3a with an apparent atom spacing corresponding to the lattice parameter. A clean substrate surface was always prepared by cleaving the top layers with an adhesive tape shortly before solution was applied.

Chapter 5

Molecular Self-Assembly on Surfaces

Molecular self-assembly is a thermodynamically driven process. It encompasses the spontaneous organization of initially unordered molecules into structurally well-defined arrangements stabilized by non-covalent interactions.[1,3,66,67] At surfaces, molecular self-assembly is defined as the confinement of single adsorbed molecules to a 1D or 2D assemblies under the reduction of their degrees of freedom. For the formation of such structures, diffusion and reorientation are key. Yet, these processes require thermal activation to overcome activation barriers. Temperature must be high enough to induce molecular mobility but low enough that monolayers / structures remain thermodynamic stable.

Monolayer self-assembly can take place at the vacuum-solid or the liquid-solid interface at UHV or ambient conditions, respectively. Under UHV vacuum conditions, these process are controlled by molecule-molecule and molecule-substrate interactions, while at liquid-solid interfaces additionally contributions to self-assembly arise from molecule-solvent and solvent-substrate interactions (Fig. 5.1).[68] Since the focus of the present work is self-assembly at liquid-solid interfaces, self-assembly under UHV conditions will not be further addressed.

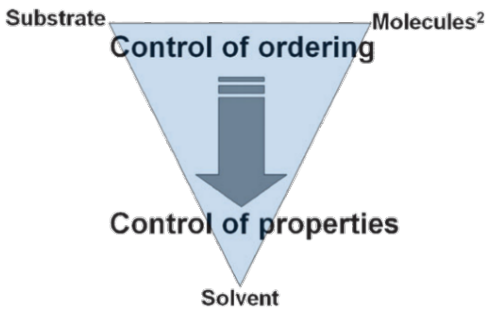

Figure 5.1: Influencing parameters for self-assembly at the liquid-solid interface. Reproduced from Kudernac et al.[68] with permission from The Royal Society of Chemistry (2009).

Molecular self-assembly exclusively uses non-covalent interactions. Characteristic for non-covalent interactions is their rather weak bond strength.[66] Van der Waals interactions, Halogen- and Hydrogen-bonds π-π interactions are prominent

examples for non-covalent interactions. The common assumption for self-assembly is its stabilization by a dynamic equilibrium.[68–70] The equilibrium is determined by the adsorption / association and dissociation / desorption of molecules between the solution and the interface. The weak nature of non-covalent interactions is a requirement to achieve high degree of structure quality as it permits rearrangements and error corrections.[68,71,72].

5.1 Thermodynamics

The self-assembly of molecular structure is always associated to a gain in Gibbs free energy $\Delta G < 0$ towards its minimum, i.e. the equilibrium state of the system. Gibbs free energy is an extensive thermodynamic potential. It combines the enthalpy and entropy to describe the thermodynamic state of a system at a given temperature. For isobaric and isothermal conditions the change of Gibbs free energy can be expressed by:

$$\Delta G = \Delta H - T \cdot \Delta S \tag{5.1}$$

ΔH is the enthalpy change, ΔS is the entropy change, and T is the temperature of the respective system. During the formation of a monolayer the single molecules change from a disorganized state with many degrees of freedom to a highly constrained and ordered structure. This will normally lead to a reduction of the systems overall entropy ($\Delta S < 0$). Following the second law of thermodynamics, any spontaneous process in a closed system is associated with an increase of total entropy. Yet, self-assembly in the most cases implies the reduction of entropy. However, to yield a negative ΔG, the enthalpy gain $\Delta H < 0$ from bond formation must exceed the entropy cost ΔS.

Apart from being the driving force for monolayer formation, ΔG can be used to identify the thermodynamic most stable monolayer polymorph. In this context, it is important to consider the area an adsorbed molecule occupies on a surface. According to the study from Conti and Cecchini, the thermodynamically most stable polymorph is the one that results in the highest free energy gain per unit area A.[73]

$$\Delta g = \frac{\Delta G}{A} = \Delta h - T \cdot \Delta s \tag{5.2}$$

Here, Δg, Δh Δs are the free energy, enthalpy and entropy change per unit area A, respectively. The determination of the enthalpy and entropy changes with full account of the solvent influence is challenging. Considering the enthalpic contribution, the enthalpy change ΔH during self-assembly cannot be assessed directly. Yet, to obtain accurate values for the enthalpy change associated with the formation of a monolayer from solution $\Delta H_{sol \rightarrow monolayer}$, an adapted Born-Haber cycle can be deployed (Fig. 5.2).

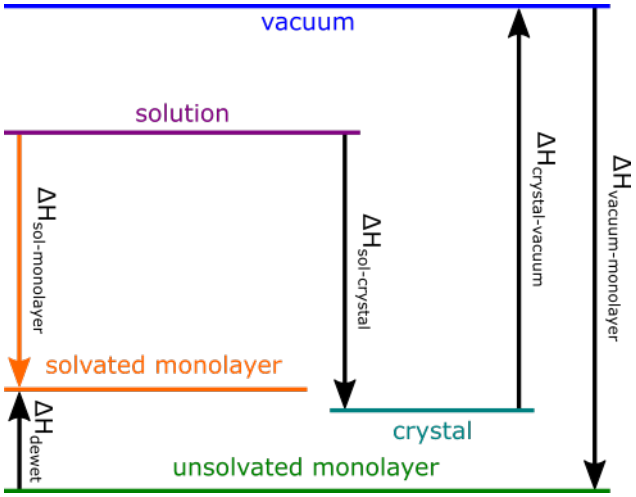

Figure 5.2: Adapted Born-Haber cycle. $\Delta H_{sol \rightarrow monolayer}$ (orange arrow) is not directly accessible, but a detour via crystal, vacuum, unsolvated monolayer and solvated monolayer (blue arrows) facilitates quantification of the overall enthalpy difference.[74] Adapted with permission from Song et al.[74]. Copyright (2013) American Chemical Society.

In a Born-Haber cycle, one unknown enthalpy in a cyclic process, i.e. where the final state is similar to the initial state, can be determined with the knowledge of all other enthalpies. The adapted Born-Haber cycle connects accessible reference states of a molecule with the reaction enthalpies to transfer the molecule from one state to another. These states are: The molecules dissolved in solution, the molecule's bulk crystal, the isolated single molecule in vacuum, the unsolvated monolayer, and the solvated monolayer.[74] Note, that there is a difference in enthalpy between the monolayer at the vacuum-solid (unsolvated monolayer) and at the liquid-solid interface (solvated monolayer) due to the contribution of the solvent molecules covering the adsorbed monolayer. The enthalpic difference in the interfacial energies of the solvent-substrate and solvent-monolayer interactions is taken into account with the solvent dewetting enthalpy ΔH_{dewet}. In the moment the substrate is covered by a solution, the substrate is initially precovered by a solvent layer that has to desorb first before the solutes can adsorb and from the monolayer. Hence, ΔH_{dewet} includes the enthalpy cost for the dissolution of the solvent molecules and the enthalpic gain due to the solvation of the adsorbed solute monolayer.[74]

With the knowledge of $\Delta H_{sol \rightarrow crystal}$, $\Delta H_{crystal \rightarrow vacuum}$, $\Delta H_{vacuum \rightarrow monolayer}$ and ΔH_{dewet}, one can determine the missing $\Delta H_{sol \rightarrow monolayer}$. Taking the direction of response into account as illustrated in Fig. 5.2, $\Delta H_{sol \rightarrow monolayer}$ can be calculated with:

$$\Delta H_{sol \rightarrow monolayer} = \Delta H_{sol \rightarrow crystal} + \Delta H_{crystal \rightarrow vacuum} + \Delta H_{vacuum \rightarrow monolayer} + \Delta H_{dewet} \tag{5.3}$$

Note that the arrows in the Born-Haber cycle indicate the direction of the process. For instance, $\Delta H_{sol \rightarrow crystal}$ corresponds to the dissolution enthalpy. Hence, $\Delta H_{sol \rightarrow crystal} = -\Delta H_{diss}$ and can be determined by variable-temperature UV-vis spectroscopy (cf. section 3.1). The enthalpy $\Delta H_{crystal \rightarrow vacuum}$ corresponds to the sublimation enthalpy and can be accessed via effusion experiments (cf. section 3.2). $\Delta H_{monolayer \rightarrow vacuum}$ is corresponds to the binding and adsorption energies of an unsolvated monolayer in vacuum and can be quantified by Temperature Programmed Desorption experiments (TPD). Both enthalpies can also be obtained theoretically. Typical methods for the calculation of crystal and monolayer binding energies are Density Functional Theory (DFT) and Molecular Mechanics (MM). The dewetting enthalpy ΔH_{dewet} is theoretical accessible with MM simulations providing the adsorption energies of both a solvent monolayer on substrate and on a solute monolayer. A detailed description of the used experimental methods can be found in chapter 3, while the theoretical backgrounds of DFT calculations and MM simulations are not further detailed in this thesis.

The entropy contribution to monolayer formation $\Delta S_{sol \rightarrow monolayer}$ to the free energy change ΔG is experimentally intricate to access. However, theoretical approaches can provide estimates of $\Delta S_{sol \rightarrow monolayer}$ like the model proposed by Whitesides et al.[75] Here, the total entropy change $\Delta S_{sol \rightarrow monolayer}$ can be expressed as the sum of the individual entropy changes including translational, rotational, vibrational and conformational contributions (Eq. 5.4).

$$\Delta S_{sol \rightarrow monolayer} = \Delta S_{trans} + \Delta S_{rot} + \Delta S_{vib} + \Delta S_{conf} \tag{5.4}$$

The entropy contribution through conformation ΔS_{conf} is only significant for larger flexible molecules with relevant degrees of freedom in their conformation or in strong chemisorbed molecule-surface interactions.[70,75] The conformational change for small and relatively rigid physisorbed molecules is minimal and can be neglected.[75]

Björk et al.[76] proposed a slightly different model considering the electronic contribution ΔS_{elec}. In physisorbed systems ΔS_{elec} can be typically ignored as differences in the chemical states are insignificant. But if the molecule-surface interactions is strongly affecting the chemical state of the molecules, ΔS_{elec} cannot be neglected, i.e. in the case of strong chemisorption.[76]

The entropy change through restricting the translational degrees of freedom ΔS_{trans} can be determined with:

$$\Delta S_{trans} = Rln[\frac{V_{free}}{n}(\frac{2\pi m k_B T e^{5/3}}{h^2})^{3/2}] = Rln[\frac{1}{c}(\frac{2\pi m k_B T e^{5/3}}{h^2})^{3/2}] \tag{5.5}$$

R is the gas constant and c is the solute molar concentration ($c = n/V$).[75 24] To avoid an overestimation of the translational entropy, the free volume V_{free} of the solvent can be taken into account as proposed by Mammen et al..[75] The free volume

V_{free} of the solvent can be calculated via the hard cube approximation as described in the original publication from Mammen et al.[75]

The rotational contribution to the total entropy change can be calculated with Eq. 5.6.

$$\Delta S_{rot} = Rln[\frac{1}{\gamma}\pi^{1/2}(\frac{8\pi^2 k_B T e}{h^2})^{3/2}(I_1 I_2 I_3)^{1/2}] \tag{5.6}$$

Here, γ considers the symmetry of the molecule and I_1, I_2 and I_3 corresponds to the principle moments of inertia. Adapting equation 5.6 for liquids, the result only differs by 2 % from the gas phase values.[75] This is probably related to the fact that γ is independent of solution concentration and the structure of the solvent molecules.[75,77] Finally, the vibrational entropy ΔS_{vib} is taking the inter and intramolecular vibrations into account (Eq. 5.7).[76,78]

$$\Delta S_{vib} = k_B \sum_{\beta=1}^{\alpha}[\frac{h\nu_\beta}{k_B T}\frac{1}{e^{(h\nu_\beta/k_B T)}-1} - ln(1-e^{(-h\nu_\beta/k_B T)})] \tag{5.7}$$

Here, h is Plank's constant, k_B is the Boltzmann constant, e is Euler's number, T is the absolute temperature of the system, α is the index of the normal modes and ν_β is the vibrational frequency of the β-th normal mode. The magnitude of $T\Delta S_{vib}$ is for almost all vibrational modes of a molecule very small and typically less than 2 $kJ\ mol^{-1}$ at 25 °C.[75] Compared to the magnitude of ΔS_{trans} and ΔS_{rot} the contribution of ΔS_{vib} to the total change of entropy during monolayer formation $\Delta S_{sol\rightarrow monolayer}$ can be neglected. Hence, for a physisorbed monolayer $\Delta S_{sol\rightarrow monolayer}$ renders to:

$$\Delta S_{sol\rightarrow monolayer} \approx \Delta S_{trans} + \Delta S_{rot} \tag{5.8}$$

5.2 Kinetics

A thermodynamically controlled system will always evolve towards its dynamic equilibrium that is characterized and maintained by an equality of forward and backward reactions. Any hindrance effecting the forward or backward reactions inevitably result in kinetic trapping and can lead the system to a different state. These kinetically trapped states correspond to a higher free energy state compared to the thermodynamic minimum. The evolution of a system either towards the thermodynamic or kinetically trapped equilibrium depends on the available activation energy (thermal activation) and existing barriers, i.e. the free activation energy $\Delta G^{\ddagger}$ (Fig. 5.3).

Considering a system in its initial state at (A), an activation energy that is sufficient to overcome $\Delta G^{\ddagger}_{TS,Therm}$ will transfer the system to its thermodynamic optimum at (C). If the activation energy is too small to overcome $\Delta G^{\ddagger}_{TS,Therm}$ but is still high enough to overcome $\Delta G^{\ddagger}_{TS,Kin}$, the system will still evolve but towards a

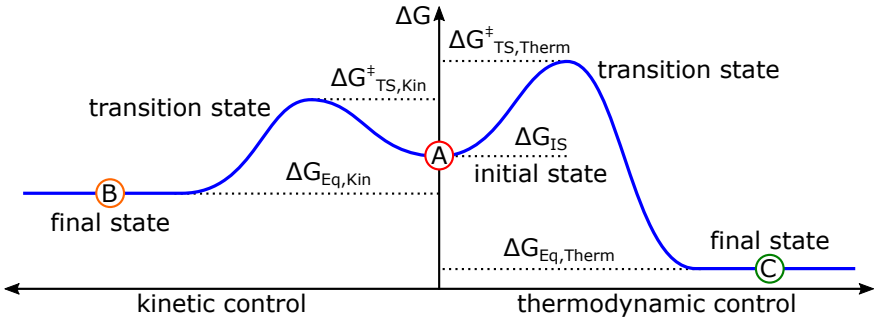

Figure 5.3: Comparison of a thermodynamic and kinetically controlled reaction. A system in its initial state (A) evolves under thermodynamic control to (C) while kinetics steer the system to (B). Adapted with permission from Björk[76]. Copyright (2018) Springer International Publishing AG part of Springer Nature.

kinetically trapped state (B). For instance, (B) can be a kinetically trapped polymorph and (C) the thermodynamic most favoured one. But with sufficient thermal activation the molecules will remain in solution (A). Hence, thermal activation can be used to steer the evolution of a molecular system as it influences adsorption, desorption and diffusion processes (cf. section 5.3.6).

Any transition from one state to another will proceed at a certain reaction rate k. A simple model that describes the temperature dependency of the reaction rate k is the Arrhenius equation (Eq. 5.9).[79]

$$k = k_0 \, e^{(-E_{barrier}/RT)} \tag{5.9}$$

$E_{barrier}$ is the activation barrier and k_0 the pre-exponential factor taking the frequency of the collisions of molecules and their orientation into account. An extended model to determine k is the transition state theory proposed by Eyring.[80] Every change of state of a system is connected by a transition state with a corresponding activation barrier, hence, a state with high potential energy. Considering the dissolution of a bulk crystal, the transition state is the instant where bulk molecule-to-molecule interactions are already broken, but a molecule-to-solvent interaction has not yet formed, i.e. the molecule experiences hardly any favourable interaction. According to the Eyring equation the reaction rate k is given by:[79,80]

$$k = \kappa \frac{k_B T}{h} K^{\ddagger} \tag{5.10}$$

Here, k_B is the Boltzmann constant, h is the Planck constant, T is the temperature, κ is the transmission coefficient, and $K^{\ddagger}$ is the equilibrium constant at the transition state. $K^{\ddagger}$ can be expressed via the ratio of concentrations between the activated complex and the initial and final components. For the example of a dissolution process ($[bulk]+[solvent] \rightleftharpoons [solution]$) $K^{\ddagger} = [transition\ state]/[bulk][solvent]$.

Generally, the equilibrium constant K can be expressed through the standard Gibbs free enthalpy ΔG° (Eq. 5.11).[79]

$$K = e^{(-\Delta G^\circ/RT)} \tag{5.11}$$

With Eq. 5.11 the Eyring equation 5.10 can be written as:

$$k = \kappa \frac{k_B T}{h} e^{(-\Delta G^\ddagger/RT)} = \kappa \frac{k_B T}{h} e^{(-\Delta H^\ddagger/RT)} e^{(\Delta S^\ddagger/R)} \tag{5.12}$$

$\Delta H^\ddagger$ is the enthalpy of activation of the transition state, $\Delta S^\ddagger$ the entropy of activation of the transition state, and R is the gas constant.[79,80]

5.3 Influences on Molecular Self-Assembly

The prediction and controlled synthesis of molecular self-assemblies is challenging as there formation under dynamic equilibrium conditions depends on several tuning parameters.[69] At the liquid-solid interface the properties of the molecular building blocks[81,82], the type of adsorption[70], the type of solvent[83,84], the solution concentration[85,86] and the temperature[24,25] and can influence the final monolayer structure. In the following sections these parameters will be discussed further.

5.3.1 Molecular Interactions

Any supramolecular arrangement is based on the interaction between the constituting molecules. A general classification of intermolecular interactions is possible through their range. Short range interactions are based on the transfer of electrons (ionic bonds) or the sharing of electrons though the overlap of orbitals to form a covalent bond. Hence, short range interactions influence the chemical configuration of the binding partners. Long range interactions are non-covalent like hydrogen bonds, halogen bonds, $\pi - \pi$ interactions and Van der Waals forces. A characteristic of long range interactions is the proportionality of their strength to the distance r^{-m} (m = positive integer).[66] In molecular self-assembly, long range non-covalent interactions contribute primarily to the formation of a supramolecular structure without affecting the chemical state of the contributing components. In the following two sections, Van der Waals interactions and hydrogen bonds will be addressed as other interactions are not in the focus of the present work.

Van der Waals Forces

Van der Waals interactions are of electrostatic nature and describe the non-covalent interactions of atomic and/or molecular dipoles. Dipoles in atoms and molecules arise from the polarisation of their electron clouds.[87] Van der Waals interactions

can be distinguished by the type of the participating dipoles. Generally, three types of dipole interactions exist: permanent-permanent dipole (Keesom forces), permanent-induced dipole (Debye forces) and the induced-induced dipole interaction (London dissipation forces),[88] while the term Van der Waals interaction is often related only to the latter. In molecular self-assembly, the London dissipation force is of great interest as it contributes to the adsorption of molecules. London dissipation forces originate from non-homogeneous electron density distributions in the electron clouds. These fluctuations establish a transient dipole in the atom or molecule. A transient dipole in one atom/molecule can induce another transient dipole in a neighbouring atom/molecule, resulting in an attractive force.[66,87] For atoms the attraction strength vary with the distance proportional to r^{-6}, while for molecule-molecule and molecule-surface interactions r^{-m} can differ. Typically, these interactions are weak with binding energies less than 5 $kJ\ mol^{-1}$.[89] But since they are additive, their summation can be significant in terms of molecule-molecule and molecule-surface interaction.[66,87]

Hydrogen Bonds

Hydrogen bonds or hydrogen bridges describes the intermolecular attraction between a hydrogen atom H covalent bound to an atom X with an atom Y ($X-H\cdots Y$).[66] Both, atom X and Y, feature a strong electronegativity. By virtue of its strong electronegativity, X is pulling the electron of the hydrogen atom closer to itself, resulting in a polar covalent bond. As a result, H becomes positively charged, rendering $X-H$ a H-bond donor group. The strong electronegativity of Y in its own intramolecular configuration is in most cases leading to a negative potential at Y, whereby it becomes a H-bond acceptor. Consequently, the electrostatic attraction of the negative charge of Y and the positive charge of H leads to an attractive interaction. In this configuration the hydrogen is bridging between X and Y.[66,90] Typical H-bond donors are $N-H$, $O-H$, $S-H$, $P-H$, $F-H$, $Cl-H$, $Br-H$ and $I-H$, while H-bond acceptors include N, O, P, S, F, Cl, Br and I.[66]

The wide energy range of hydrogen bonds has its origin in the various contributions of different interaction types to the overall H-bond strength. Depending on the strength, hydrogen bonds can have a van der Waals, electrostatic and even a pronounced covalent character.[90,91] Therefore, hydrogen bonds gradually increase their electrostatic and decrease their dispersive character with rising bond strength.[90] The strength of a hydrogen bond strongly correlates with electronegativity of X and Y. In weak hydrogen bonds (2 - 20 $kJ\ mol^{-1}$) the electronegativity of at least X or Y is moderate to low.[91,92] For instance, $P-H\cdots O$, $C-H\cdots O$ and $C-H\cdots N$ feature a weak donor to strong acceptor binding, while $O-H\cdots S$ or $N-H\cdots\pi$ are strong donor to weak acceptor bonds. Strong hydrogen bonds (20 - 40 $kJ\ mol^{-1}$) feature a strong donor to strong acceptor binding like $O-H\cdots O$ or $N-H\cdots O$.[90,92]

With increasing energy the bond distance $d(H\cdots Y)$ decreases. For weak H-bonds d is in the range of 0.3 to 0.15 nm, while for strong bonds the distance becomes reduced to 0.15 to 0.12 reaching covalent distances.[92,93] This is also reflected in the

bond geometry. Strong hydrogen bonds like $O-H\cdots O$ can arrange in a nearly linear manner with a bond angle of ∼180 °, while weaker associations like $C-H\cdots O$ tend to smaller angles (160 ° ± 20 °).[92]

The directionality and strength in combination with their non-covalent character explains the great role of hydrogen bonds in molecular self-assembly. In monolayer self-assemblies, molecules with functional carboxylic acid groups (COOH) are often used as they reliably form cyclic hydrogen bonds between molecules (Fig. 5.4a).

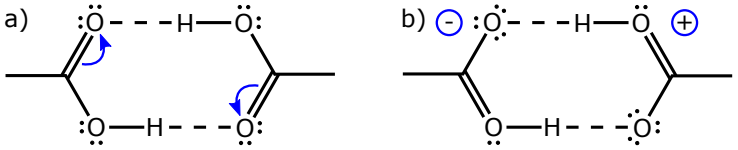

Figure 5.4: (a) Cyclic hydrogen bond dimer of two carboxylic acid groups(COOH). (b) Resonance assistance through π polarization in the cyclic hydrogen bond dimer from (a). Adapted with permission from Grosch et al.[94] https://pubs.acs.org/doi/10.1021/acs.jpca.7b12635. Copyright (2018) American Chemical Society. (Further permissions related to the material excerpted should be directed to ACS)

These cyclic configurations feature an increased bond strength of ∼60 $kJ\ mol^{-1}$ through resonance effects (Resonance Assisted Hydrogen Bond, RAHB).[89,95] RAHBs can occur intra- and intermolecular. Generally, RAHBs consist of a chain of π conjugated double bonds connecting the H-bond donor and acceptor group. The increased bond strength originates from a circular electron density transfer in the π system (Fig. 5.4b). By transferring the electrons to the H-bond acceptor side, it increases its electronegativity. Consequently, the electron density is transferred away from the donor group rendering them more positive. This cooperative effect increases the electrostatic interaction between the donor and acceptor and shortens the bound distance $d(H\cdots Y)$ (covalent character).[94,96,97]

Apart from the cyclic dimer configurations also cyclic trimers benefit from resonance effects. Figure 5.5 shows binding motifs for carboxylic acid groups.

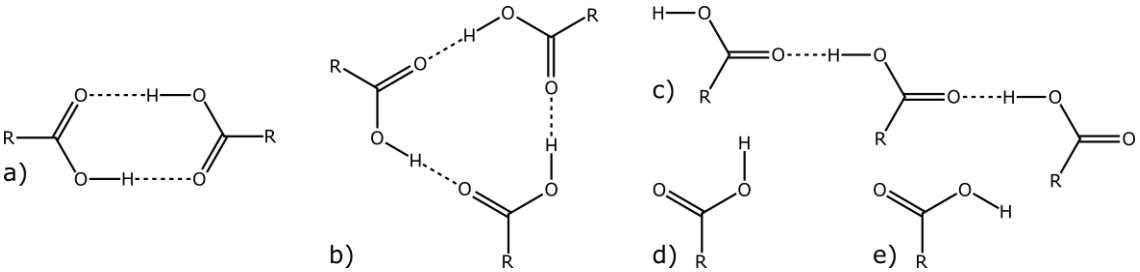

Figure 5.5: Binding motifs of hydrogen bonds between carboxylic acid groups: (a) cyclic dimer, (b) cyclic trimer, and (c) catemeric motifs. The carboxylic groups of the catemeric motifs can be either in the (d) syn-planar or (e) anti-planar configuration. Adapted and reprinted with permission from Lackinger and Heckl[81]. Copyright (2009) American Chemical Society.

5.3.2 Adsorption

The adsorption of molecules is controlled by the same forces that also apply for molecular interactions. Yet, it must be considered that one binding partner, the surface, has an quasi infinite amount of electrons.[98,99] Therefore, the molecules interact with a continuum of unsaturated states. Hence, despite many similarities to chemical bounding among molecules, adsorption requires a separate treatment.[99] Generally, two types of absorption exists: chemisorption and physisorption. The former, chemisorption, forms strong molecule-surface interactions that resembles the formation of ionic or covalent bonds. Thereby, the charge transfers (ionic) or orbital overlapping (covalent) are leading to the formation of new hybrid orbitals.[99] Even the formation of new species can be observed through dissociative chemisorption like in the adsorption of thiols on gold surfaces leading to a strong chemisorption of the sulfur to the gold surface and the release of H_2.[99–101] Surfaces with high reactivity like the transition metals Cu, Ag and Au promote the chemisorption of reactive molecular partners, in particular those that feature heteroatoms with lone electron pairs, e.g. oxygen, nitrogen or sulfur.[70]

A prominent example for a less reactive surface is HOPG (cf. section 4.3). Adsorption on HOPG is mostly controlled by weak interactions through physisorption processes. In contrast to chemisorption, the electronic structure of the molecule is mostly unaffected during physisorption.[99] The underlying binding forces are dissipative Van der Waals interactions (cf. section 5.3.1) and for coadsorption of aromatic solvents $\pi - \pi$ interactions (cf. section 5.3.4). Instead of inducing a transient dipole with a transient dipole in another molecule, here, a transient dipole of a molecule or atom induces an image charge within the surface. This changes the distance dependence of the physisorption potential to z^{-3} as compared to the atom-atom interactions r^{-6}.[98,99] Here, z is the distance between surface and the nucleus of the adsorbing atom, while r is the distance between two nuclei of interacting atoms.

Upon adsorption the molecules optimize their adsorption geometry, i.e. also their orientation with respect to the surface. Covalently bonded chemisorbed molecules tend to optimize the overlap of their orbitals with the surface. Physisorbed molecules generally tend to optimize their average distance to the surface. Consequently, molecules with bulky peripheral substituents show a tendency to adsorb with their bulky groups in hollow sites instead of top sites. Hence, the atomic structure of the surface can be exploit to steer the final outcome of the monolayer self-assembly.[70] However, the impact of this tendency on the final monolayer structure depends on the adsorption strength in relation to the additionally contributing molecular interactions. For instance, MM simulations conducted from Martsinovich for our recent kinetic study (cf. chapter 8) revealed, that the adsorption energy of single physisorbed NDA molecules on HOPG only differ by 0.95 $kJ\ mol^{-1}$ between the best and worst adsorption sides. Repeating the same calculations for an island of 5×5 molecules the value is even less (0.04 $kJ\ mol^{-1}$). Hence, in this case, the influence of the adsorption geometry even decreases with monolayer formation.

5.3.3 Molecular Structure

The sophisticated choice of molecular building blocks can steer the final monolayer structure in the desired direction. Structural parameters are the molecules backbone geometry as well as the number and positions of functional groups. Carboxylic acid (COOH) functionalized molecules with 2- and 3-fold symmetric backbone geometries are particular interesting as they create lamellar or/and hexagonal patters.[24,29,102] Prominent examples of 2-fold molecules that exclusively form row structures are shown in Fig. 5.6a-d, while the molecules in Fig. 5.6e-f self-assemble into honeycomb networks like the chickenwire or flower structures and in the case of BTB additionally in a row[24] or an oblique[103] structure.

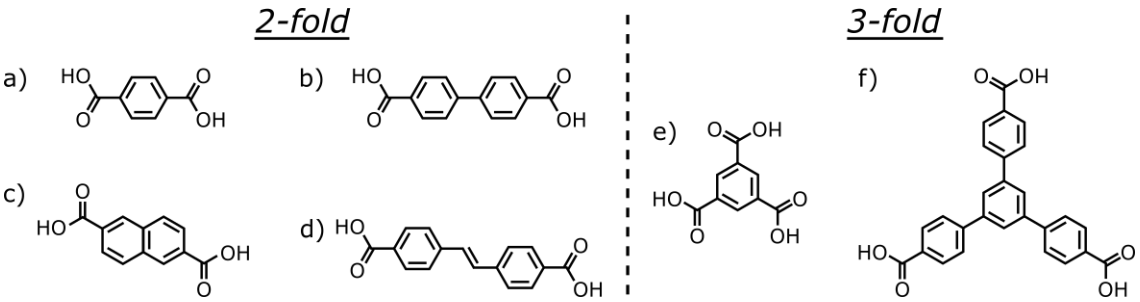

Figure 5.6: Molecular structure of 2- and 3-fold carboxylic acids: (a) Benzene-1,4-dicarboxylic acid or terephthalic acid (TPA), (b) 4,4′-biphenyldicarboxylic acid (BPDA), (c) 2,6-naphthalenedicarboxylic acid (NDA), (d) 4,4′-stilbenedicarboxylic acid (SDA), (e) Benzene-1,3,5-tricarboxylic acid or trimesic acid (TMA), and (f) 1,3,5-benzenetribenzoic acid (BTB). Adapted and reprinted with permission from Lackinger and Heckl[81]. Copyright (2009) American Chemical Society.

Except for the BTB row structure[24], all of those molecules adsorb planar on the surface promoted by their aromatic backbone featuring at least on phenyl ring. 3-fold carboxylic acids are highly appropriate to self-assemble into planar porous monolayers. By adding phenyl rings to the three lobes of the molecular backbone, the cavity size of the evolving network can be controlled. In terms of host-guest chemistry this is an essential parameter to select potential guest species.

As illustrated in Fig. 5.5, carboxylic acid groups can form cyclic dimer, cyclic trimer and the catemeric H-bond motifs. This motifs gives raise to the expression of different polymorphs, e.g. for BTB the oblique and chickenwire structure[103] and for TMA the chickenwire and flower structure (cf. Fig. 7.1 of section 7.2).[81,104]

5.3.4 Solvent Effects

Solvents can be classified in polar and non-polar solvents reflecting their ability to dissolve certain solutes: Polar solvents dissolve polar solutes and non-polar solvents dissolve non-polar solutes. The polarity of a solvent can be quantified by the dielectric constant ϵ (higher ϵ = higher polarity). Further characteristics are the existence of aromatic groups ($\pi - \pi$ interactions) or the ability to form hydrogen bonds with

solutes or not, i.e. protic vs. aprotic solvents, respectively. Solvent-solute interactions contribute to the enthalpic stabilization of the molecules in solution ΔH_{diss}. Generally, this contribution is less than the enthalpy gain of the molecule-molecule interactions in a bulk crystal or trough monolayer formation on surface. The thermodynamic driving force behind dissolution is the gain in entropy ΔS_{diss}, rendering ΔG_{diss} negative. The magnitude of ΔG_{diss} defines the solubility, i.e. the chemical potential of a solute in solution. A high or low solubility corresponds with a lower or higher chemical potential of the solutes in solution, respectively. Self-assembly can occur if the chemical potential of the solutes is lower on the surface as in solution, i.e. $\Delta G_{sol \rightarrow monolayer} < \Delta G_{diss}$.

The stronger the gain of free energy through dissolution, the less a solvent promotes self-assembly. Hence, comparing the ΔG_{diss} of different solvents can reveal the solvent that yields the strongest thermodynamic driving force for self-assembly. Furthermore, by comparing the free energy per unit area Δg_{diss} of different solvents the thermodynamic most stable polymorph can be identified as proposed by Conti and Cecchini (cf. section 5.1) - primary solvent effect.[73] Hence, the choice of solvent can be used to steer the monolayer structure, known as solvent-induced polymorphism.[103,105–107]

At the liquid-solid interface, an adsorbed monolayer is always solvated by solvent molecules. This interaction must always be taken into account when it comes to analyse $\Delta G_{sol \rightarrow monolayer}$ as solvation can drastically reduce the desorption energies, i.e. monolayer stability.[74,102] Compared to UHV, where higher desorption energies ($> 150\ kJ\ mol^{-1}$) prohibit desorption at room temperature, solvation renders this value lower and desorption at room temperature becomes possible.[61,74] In a Born-Haber cycle, this is considered with the reference state of a solvated monolayer and ΔH_{dewet} (cf. Fig. 5.2). The magnitude of ΔH_{dewet} depends on the type of solvent, i.e. the type of interaction contributing to the enthalpic gain of solvation. For instance, fatty acids are able to interact with solute monolayer via H-bonds and Van der Waals forces, while $\pi - \pi$ interactions are feasible for aromatic solvents.

An additional solvent effect is solvent coadsorption.[83,108] Like solute molecules, solvent molecules can adsorb on surfaces and assemble into ordered structures. Apart from pure solvent monolayers, solvents can coadsorb with the solute on the surface. Coadsorption is always associated with a gain of free energy, i.e. the coadsorbed monolayer is more stable as the pure solute monolayer. Solvents can replace solute molecules of a pure solute monolayer or adsorb in the cavities of porous solute monolayer (e.g. honeycomb networks) as a guest species without affecting the initial solute network. For the latter, solvent coadsorption can stabilize a solute polymorph even if another polymorph would be favoured by a primary solvent effect.

Solvents containing H-bond donors or acceptors, alkyl chains or aromatic rings are able to coadsorb at the liquid-solid interface.[23] Surface adsorption and intermolecular interactions like H-bonds, van der Waals forces and $\pi - \pi$-interactions promote the coadsorption of these solvent types. For fatty acids, only H-bonds and van der Waals forces apply through the lack of aromatic rings. Here, the increase of the overall H-bond density of the monolayer might be a factor for the additional

gain of $\Delta G < 0$. An early study from Tao et al. gives a hint in this direction.[109] In this study, the coadsorption of 6A, 8A and 10A fatty acid solvents to a monolayer comprised of long chain di-acids $HOOC-(CH_2)_n-COOH$ (n = 10, 12, 14, 16, 18, 20) showed a correlation between the amount of solvent coadsorption and overall H-bond density.

5.3.5 Concentration

For the most cases, the packing density of a self-assembled monolayer can be tuned with the concentration of the solution – a phenomenon known as concentration-induced polymorphism. As a general rule, high solution concentrations promote high packing densities in the monolayer. This can be explained with an enhanced chemical potential of the solute at higher concentrations. The higher chemical potential reduces the entropy cost for the self-assembly, whereby more densely packed structures become thermodynamically stable. For instance, BTB molecules assembles in a densely packed row structure for saturated BTB heptanoic acid solutions on HOPG.[24] At 50 % saturation a coexistence of the BTB row and chickenwire polymorphs can be observed indicating fairly similar free energy of both polymorphs. Below 10 % saturation only the porous chickenwire structure emerges.[24] Another example is the concentration induced polymorphism of alkoxylated dehydrobenzo[12]annulenes (DBAs) dissolved in 1,2,4-trichlorobenzene. On HOPG, the densely packed linear structure assembles from high solution concentration (1.1×10^{-4} $mol\ L^{-1}$), while the porous honeycomb structure is formed at low concentration (5.7×10^{-6} $mol\ L^{-1}$).[86]

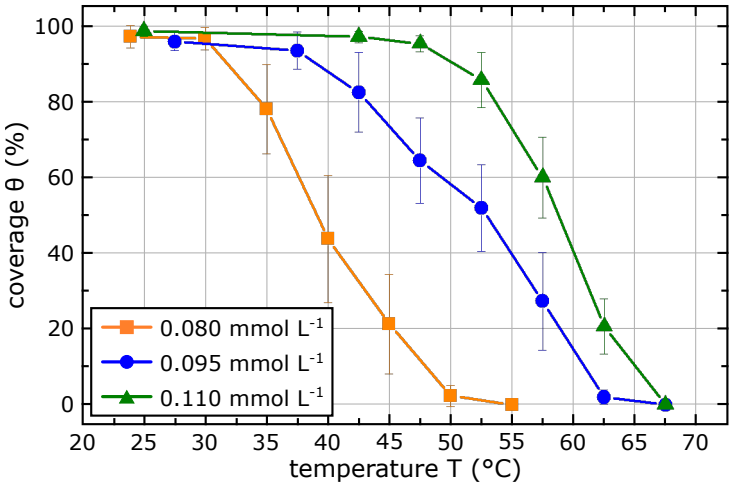

Figure 5.7: NDA monolayer coverage on HOPG assembled from a NDA-9A solutions of different concentrations versus temperature. Vertical error bars correspond to the standard deviation.

Apart from polymorphism, concentration can be used to control the monolayer coverage. High solution concentrations promote high, i.e. typically full, coverage and low concentrations partial monolayer coverage with an adjustable range between full

and zero. A preliminary study to the work from chapter 8 revealed the concentration dependent monolayer stability of an initially adsorbed full NDA monolayer at the 9A-HOPG interface. The coverage was traced for three different solution concentrations while the temperature was raised by increments of 5 °C with at least 18 h between every temperature step (Fig. 5.7). Each coverage value was evaluated from a set of 25 images ($350 \times 350\ nm$, total area $\sim 3.5\ \mu m^2$). Unfortunately, ultraslow kinetics occurs in this molecular system. Depending on the temperature, the desorption processes need $\sim$4 to $\sim$7 days for a solution concentration of 0.11 $mmol\ L^{-1}$ to settle at an equilibrium coverage. Even if the equilibrium coverage is not reached after 18 h, Fig. 5.7 shows a clear concentration effect with an enhanced monolayer stability with increasing concentration.

5.3.6 Temperature

Thermodynamics

According to thermodynamics, the equilibrium between solution and the monolayer on the surface exists, independent from the way it is reached. This equilibrium can be quantified by Gibbs equation for the change of the free energy of self-assembly (cf. Eq. 5.1). Here, temperature directly effects the magnitude of the term for the entropy cost: $-T\ \Delta S_{sol \rightarrow monolayer}$. Increasing T, increases $-T\ \Delta S_{sol \rightarrow monolayer}$, and hence, destabilizes the monolayer till complete desorption occurs ($\Delta H \leq T \Delta S$). Apart from monolayer stability, this relation can influence the structure of the monolayer as other polymorphs can become thermodynamically more stable, i.e. temperature-induced polymorphism.[24,25] Let us consider two different polymorphs: One featuring a lower packing density (LPD) and the other a higher packing density (HPD). For the HPD-polymorph, more molecules adsorb on the surface per unit area and an enhanced binding energy per unit area exist compared to the less densely packed polymorph. In this example we consider $\Delta h_{HPD} > \Delta h_{LPD}$. Furthermore, the entropy costs are higher for the HPD-polymorph as more molecules are adsorbed on surface ($\Delta s_{HPD} > \Delta s_{LPD}$). Hence, even if the HPD-polymorph features a higher binding energy as the LPD-polymorph, the higher slope Δs of the HPD-polymorph enforces a faster increase of Δg_{HPD} per temperature. Provided that the monolayers are sufficiently stable, a phase change can occur with increasing temperature as illustrated in Fig. 5.8.

At T_{eq}, the free energies per unit area of both polymorphs are equal and a coexistence of the HPD- and LPD-polymorph can occur. Figure 5.8 shows a generally higher temperature stability of less densely packed polymorphs if other contributions are neglected. For instance, coadsorption of solvent molecules can additionally stabilize, in particular, a less densely packed polymorph and may alter the final outcome. Such more subtle effects were neglegted in this general example.

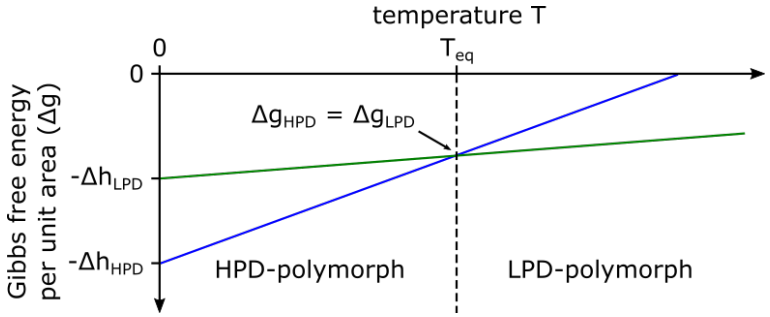

Figure 5.8: Gibbs free energy per unit area vs. temperature for two polymorphs. One with a higher packing density (HPD) and one with a lower packing density (LPD) in blue and green, respectively. At T_{eq}, Δg is equal for both polymorphs ($\Delta g_{HPD} = \Delta g_{LPD}$). With increasing temperature a phase transition occurs from the HPD- to the LPD-polymorph.

Kinetics

From a kinetic viewpoint, the equilibrium between solution and monolayer can be defined as a dynamic equilibrium between adsorption and desorption with similar rates (k_{adsorb} and k_{desorb}). As stated in section 5.2, a reaction rate k can be quantified with the Arrhenius equation (cf. Eq. 5.9) or the transition state theory by Eyring (cf. Eq. 5.12). Accordingly, all reaction rates depend on temperature. With increasing temperature, more reactants can overcome the activation barrier resulting in an acceleration of the reaction rates. Furthermore, higher adsorption and desorption rates lead to an enhanced error correction with increasing temperature.[68,71]

A kinetic limitation at the liquid solid interface exists if the adsorption or/and desorption rate is diminished by a limiting factor. With a limitation in the adsorption rate the monolayer growth will be slowed down but the energetically most favoured polymorph may still evolve. On the other hand, a reduced desorption rate will often give rise to metastable structures as excess molecules cannot desorb fast enough from the surface. Hence, a kinetically trapped polymorph with a non-optimal free energy might be stabilized. Temperature can be a ways to transfer the system to the thermodynamically favoured polymorph if the desorption barrier is sufficiently high enough (cf. Fig. 5.3).[110]

At the liquid-solid interface, kinetic limitations in the adsorption or/and desorption rates can have their origin in the supernatant solution as it provides the solute transport to and from the sample surface, i.e. the solute diffusion rate. A low diffusion rate reduces the solute flux towards the surface and less building blocks are available for adsorption, hence, the monolayer growth is slowed down. Furthermore, a low solute diffusion rate can also limit desorption as less solutes can be transported away from the interface. Diffusion through a solution is driven by a concentration gradient, while temperature can contribute to the diffusion rate through the temperature dependency of the solute properties. The solute diffusion rate $k_{sol,diff}$ can be stated with Fick's law:[111,112]

$$k_{sol,diff} = D(T)\frac{dc}{dz} \; with \; D(T) = \frac{k_B T}{6\pi\eta R_0} \tag{5.13}$$

Here, c is the concentration of the solute and z is the perpendicular distance from the surface. The term $\frac{dc}{dz}$ is the concentration gradient perpendicular to the surface, which will reach zero if the dynamic equilibrium is reached. $D(T)$ is the temperature dependent diffusion coefficient, while k_B is the Boltzmann constant, R_0 is the hydrodynamic radius of the diffusing molecules, and η the dynamic viscosity, which in turn is also a function of the temperature T (decreasing with raising temperature for the most liquids).

In summary, temperature can be used to steer self-assembly by manipulating the thermodynamic equilibrium or to overcome kinetic limitations. Yet, monitoring and controlling the temperature of self-assembly from solution over an extended time scale via STM is challenging, but possible as Jahanbekam et al. demonstrated.[27] In chapter (6), the development and design of a designated STM suitable to perform long-term experiments at liquid-solid interfaces at elevated temperatures are discussed.[113]

Chapter 6

Immersion-Scanning-Tunneling-Microscope

This chapter describes the development process and characterisation of the I-STM. Parts of this chapter are reproduced and adapted from O. Ochs, W. M. Heckl, and M. Lackinger. Immersion-scanning-tunneling-microscope for long-term variable-temperature experiments at liquid-solid interfaces. *Rev. Sci. Instrum.* 2018, 89, 053707, with the permission of AIP Publishing.

Fundamental insights into the kinetics and thermodynamics of supramolecular self-assembly on surfaces are uniquely gained by variable-temperature high-resolution STM. Conventionally, these experiments are performed with standard ambient microscopes extended with heatable sample stages for local heating. However, unavoidable solvent evaporation sets a technical limit on the duration of these experiments, hence prohibiting long-term experiments. These, however, would be highly desirable to provide enough time for temperature stabilization and settling of drift but also to study processes with inherently slow kinetics. To overcome this dilemma, we propose a STM that can operate fully immersed in solution. The instrument is mounted onto the lid of a hermetically sealed heatable container that is filled with the respective solution. By closing the container, both the sample and microscope are immersed in solution. Thereby solvent evaporation is eliminated and an environment for long-term experiments with utmost stable and controllable temperatures between room-temperature and 100 °C is provided. A recent study on the solvent-induced polymorphism of self-assembled TMA-monolayers at the solution-graphite interface even proved the short-term stability (∼3 h) of the I-STM at 110 °C (highest temperature reached so far with the I-STM, cf. chapter 7). Important experimental requirements for the I-STM and resulting design criteria are discussed, the strategy for protection against corrosive media is described, the temperature stability and drift behavior are thoroughly characterized, and first long-term high resolution experiments at liquid-solid interfaces are presented.

I performed the development, fabrication, assembly and commissioning of the I-STM as well as all experiments and corresponding data analysis / interpretation under the supervision of PD Dr. M. Lackinger.

6.1 Requirements

For experiments on self-assembled monolayers at liquid-solid interfaces operating temperatures up to 100 $°C$ are envisaged, resulting in basic requirements: First of all, parts and glued joints must be resistant against the utilized solvents. For many self-assembly studies at liquid-solid interfaces fatty acids are the solvents of choice.[81] However, fatty acids are incompatible with the typically used epoxy glues and would dissolve the glued joints of the STM over the course of time, even progressively faster at elevated temperatures. For optimized thermal drift properties, the container temperature, and consequently the temperatures of solution and STM should be maintained as stable as possible (at least within 0.1 K) over the entire temperature range. Thermal equilibration times and heating of the surroundings should be minimized. The container has to be hermetically sealed to avoid any solvent evaporation. Cold spots inside the container, where solvent would condensate must be avoided. The STM should feature a reliable and efficient fully automatic coarse approach to be able to also retract and re-approach the tip when the STM is lowered into the container, i.e. without optical access. Tips and samples should be easily exchangeable. As for any other SPM, the design must be rigid and compact to minimize its vibration susceptibility. In addition, the STM should be integrated into an external vibration isolation and well shielded against acoustic and electromagnetic noise.

6.2 Conception

A liquid-solid STM with the ability to measure at elevated temperature would be a door opener to new types of experiments with regards to thermodynamic and kinetic influences on monolayer formation / disintegration. Two main issues are identified as keys to the development of such an instrument; high drift and elevated evaporation rates through the heating process / higher temperatures. A high drift level will ultimately lead to a distortion of the images lowering the relevance of the acquired images. Furthermore, solvent evaporation will always change the solvent-to-molecule (i.e. concentration) ratio resulting in a variation of the solution properties, e.g. shift of the dynamic equilibrium in a self-assembly process. This effect will even increase for measurements at higher temperatures. To avoid these problems the following concept has been deployed, as illustrated in Fig. 6.1.

A simple but effective way to prevent a liquid from evaporation is to seal it hermetically without any void space to transfer into the gas phase. To implement this in the design of the I-STM, the entire STM is completely immersed into solution and hermetically sealed in a heatable chamber to prevent any solvent from

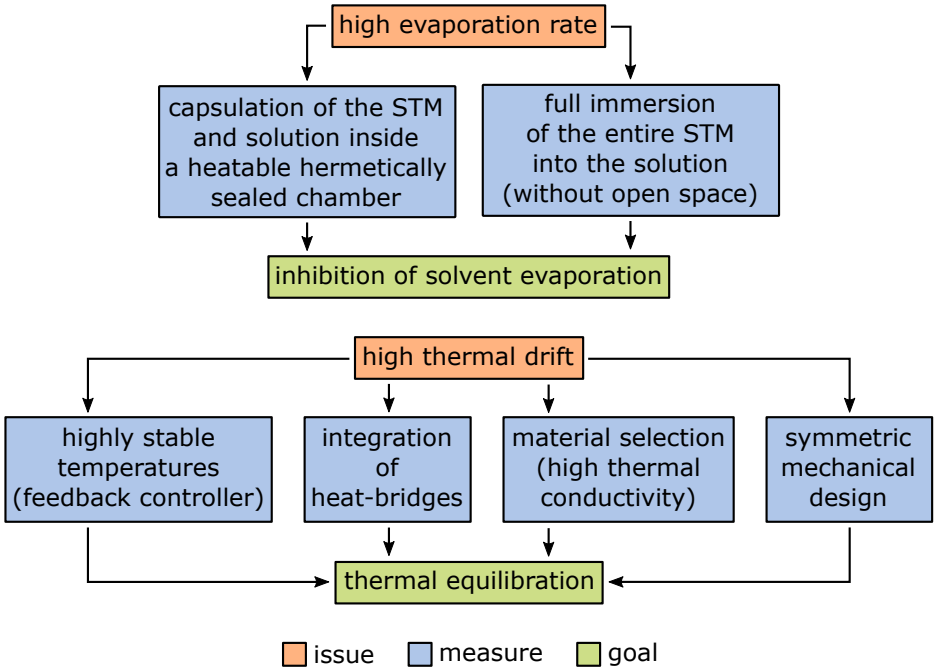

Figure 6.1: Concept to minimize high thermal drift and an enhanced evaporation rate at elevated temperatures.

evaporation and to control the operating temperature. As a direct consequence of the heating process high drift will emerge due to temperature gradients across the microscope. To reduce these temperature gradients the first step is the integration of a well-designed temperature feedback controller to precisely stabilize both STM and solution at the target temperature. Upon reaching the target temperature the drift or rather the temperature gradients have to be reduced as fast as possible. Integration of heat bridges in the STM design and the selection of materials with good thermal conductivities promotes a faster reduction of temperature gradients, and hence thermal drift. In order to minimize the drift-level from the start, a rotationally symmetric design is deployed to promote a more homogeneous temperature distribution, since the heating is radially applied from the sealing chamber (cylindrical shape). Another effect of a highly symmetric design is the partial drift self-compensation through a symmetric thermal deformation of the structure.

6.3 Corrosion Protection

The design of the I-STM includes a combination of different materials, i.e., metals, ceramics and plastics for the mechanical and electrical construction as well as glues to fuse parts together. A highly important material property is the chemical resistance against the used corrosive fatty acids. Tests to identify this property, and to find sufficient coating materials for vulnerable materials, were conducted. Their procedures and results are all described in the following sections.

6.3.1 Chemical Resistance of the Applied Materials

The chemical resistance of a material, especially against the highly appropriate fatty acids, has emerged to be key for the long-term stability of the I-STM and the purity of the solution. Some less noble metals and glues have proven to be not sufficiently inert against the corrosive behaviour of these acids. Therefore, every material with direct contact to the hot fatty acid solution during the operation of the I-STM had to pass a test procedure to validate its chemical inertness. Materials like aluminium alloys, which were only used for applications without any direct contact to the fatty acid solvents, e.g. frameworks or support structures, were spared out of this test procedure. A material was ranked as inert if it withstood the corrosive behaviour of 100 $°C$ hot nonanoic acid over a time period of 2 weeks without any indication of degradation of the material or contamination of the solution. The test setup consists of simple glass beaker filled with nonanoic acid (*TCI*, 98 % purity) placed on a heating plate with steering function. A PTFE coated magnetically stirrer inside the glass beaker is constantly sirring the 100 $°C$ hot nonanoic acid around a completely immersed material sample. As a result of this test procedure six metals / alloys could be identified that failed the criteria to be ranked as inert: OFHC-copper, Brass, Samarium-cobalt, Silver (pure or as alloy component in solders), Lead (in leaded solders) and Super Invar 32-5 (Table 6.1).

All six materials resulted in a contamination of the nonanoic acid and a degradation of the material itself. In terms of OFHC-copper (oxygen-free high conductivity, purity ($\geq$99.99 %), 0.017 $\Omega\ mm^2\ m^{-1}$ at 20 $°C$), the immersed sample looked perfectly clean without the typical indications of corrosion, but the nonanoic acid experienced a dramatic colour change from its clear transparent state to an intense turquoise colouring (Fig. 6.2a).[119] However, after the removal from the nonanoic acid also the OFHC-copper sample started to evolve a raw turquoise patina on its surface which both could be a hint for the formation of a copper(II)-compound (not further investigated). As expected, the same behaviour was observed for brass since it possesses a high share of copper. The only application in the I-STM for brass are IC-pins (gold coated brass) used as plugs and connectors for separable electrical connection. Before the IC-pins where tested the gold layer was removed. Unfortunately, the datasheet of the used IC-sockets does not tell the exact composition of the used copper/zinc alloy but in terms of its original application in microelectronics an alloy with a good electrical conductivity (low share of zinc) would be highly appropriate, e.g. CnZn5 (5% zinc).[134] After the exposure to nonanoic acid, Samarium-cobalt (*Sm2Co17*) was completely corroded accompanied by a dark-brownish colour shift of the acid and residuals at the bottom of the test beaker. In the design of the I-STM, silver is used for the electrodes of the nanopositioner piezo. For the determination of its inertness, a complete piezo was immersed in the nonanoic acid. The result was a complete removal of the silver electrodes without any residuals at the bottom of the beaker or a visual colour shift of the nonanoic acid. For testing the solders, all three (*Sn60Pb40*, *Sn96.5Ag3.5* and *Au80Sn20*) were applied to a tube piezo actuator, but only the gold/tin-solder passed the test procedure (Fig. 6.2c -

Table 6.1: List of all metals, ceramics and plastics tested in terms of their chemical resistance after exposure to nonanoic acid over a time period of 2 weeks at 100 °C.

Material	**Result**	**Typ of degradation**
Au80Sn20 Gold/tin-solder[114]	inert	—
Brass[115]	not inert	corrosion of the sample; turquoise discolouration of the acid
FKM (*Viton*)[116]	inert	—
Gold[117]	inert	—
Kapton[118]	inert	—
OFHC-copper[119]	not inert	corrosion of the sample; turquoise discolouration of the acid
PEEK[120]	inert	—
Platinum-Iridum *Pt90Ir10*[121]	inert	—
PTFE[122]	inert	—
PZT[39]	inert	—
Samarium-cobalt *Sm2Co17*[123]	not inert	corrosion of the sample; dark brownish discolouration of the acid
Shapal Hi-M soft[124]	inert	—
Silver (piezo electrodes)[125]	not inert	corrosion of the sample
Sn60Pb40 leaded solder[126]	not inert	corrosion of the solder points; dark grey residuals in the acid
Sn96.5Ag3.5 silver solder[127]	not inert	corrosion of the solder points; dark grey residuals in the acid
Stainless steel - type 1.4057[128]	inert	—
Stainless steel - type 1.4301[129]	inert	—
Stainless steel - type 1.4401[130]	inert	—
Stainless steel - type 1.4571[131]	inert	—
Super Invar 32-5[132]	not inert	dark corrosion of the sample; brownish residuals in the acid
Zirconium dioxide[133]	inert	—

blue circle). The leaded *Sn60Pb40* and the silver substituted lead free *Sn96.5Ag3.5* solders failed the inertness test, resulting in a dark grey discolouration accompanied by a complete loss of their stability – both crumbled of the test piezo. The failure of both solders can most likely be traced back to their silver and lead share as all other compounds have been proven inert against the nonanoic acid. Super Invar 32-5 showed a comparable behaviour as samarium-cobalt with a dark corroded surface, brownish residuals at the glass beaker bottom and a brownish colour shift of the acid (Fig. 6.2b). All these materials where at least used once in the develop-

ment processes of the I-STM as they feature desirable properties, but their limited corrosion resistance requires protection. The applied corrosion protection concept will be discussed in the mechanical and electrical design sections 6.4 and 6.5, since it evolved and changed closely connected to design changes from version to version.

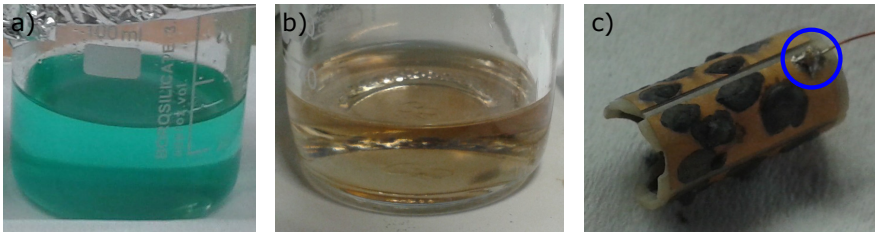

Figure 6.2: Nonanoic acids after 2 week in contact with test samples of (a) OFHC-copper and (b) Super Inver 32-5 both at 100 $°C$. (a) The OFHC-copper was most likely oxidized to $Cu2+$ as indicated by the turquoise discolouration of the acid. (b) The nonanoic acid from the Super Inver 32-5 test showed a brownish colour shift with residuals from the material corrosion. (c) Tube piezo actuator (mechanically damaged test piece) with several crumbled test soldering points of the leaded *Sn60Pb40* and the lead free silver substituted *Sn96.5Ag3.5*. Only the AuSn-solder point is still intact, without any sign of degradation (blue circle).

For the metals, ceramic and plastics this test procedure is sufficient, since the mechanical stress on these materials during their application is negligible. In terms of the applied glues a much higher mechanical stress level occurs, especially at the nanopositioner piezo. During the probe-sample approach the nanopositioner piezo expands and contracts at a frequency of 1 kHz, and the resulting accelerations apply an alternating tearing and pushing load at the joints. The highest acceleration occurs at the steep flank of the saw-tooth signal. To rank a glue as inert it is fundamentally important to additionally test its mechanical behaviour under operating conditions. Hence, for testing of the glues an additional setup was necessary (Fig. 6.3). The highest mechanical stress appears at the nanopositioner piezo. Consequently, a nanopositioner was fabricated for each glue for tests under real conditions. Since the effort to fabricate a nanopositioner is rather high, the glues were first tested under static conditions, i.e. with the same protocol as applied for the metals, ceramics and plastics. All together 16 glues based on different chemistries were tested and the results are summarized in table 6.2.

Only three glues withstand the 2 weeks exposure to 100 $°C$ hot nonanoic acid: *KL06-B*, *KGL 130 EP* and *PJ1390-1*. The *KL06-B* and the *KGL 130 EP* from *Klebe- und Gießharztechnik Dr. Ludeck GmbH* are both based on the same epoxy / anhydride chemistry, and show the same level of inertness.[141] The only difference in their properties is a better processibility of the *KGL 130 EP*. The PJ1390-1 is a single component, solvent containing, low viscosity polyimide-based glue with properties comparable to *Kapton*.[145] With all three glues an adapted test-nanopositioner was fabricated and immersed in a glass beaker filled with constantly steered 100 $°C$ hot nonanoic acid. To test the stability of each glue under a dynamic load the

Table 6.2: List of the glues tested in terms of their chemical resistance after exposure to nonanoic acid over a period of 2 weeks at 100 $°C$.

Glue	**Result**	**Typ of degradation**
353ND[135]	not inert	disintegration/dissolution
Araldite 2015[136]	not inert	disintegration/dissolution
Duralco 4460[137]	not inert	disintegration/dissolution
EP-P 653[138]	not inert	disintegration/dissolution
EP-P 655T[139]	not inert	disintegration/dissolution
EP-P 695	not inert	disintegration/dissolution
H74[140]	not inert	disintegration/dissolution
KGL 130 EP[141]	inert	—
KL06-B[142]	inert	—
Master Bond EP42-2LV[143]	not inert	disintegration/dissolution
OD2002[144]	not inert	disintegration/dissolution
PJ1390-1[145]	inert	—
UHU Plus Endfest[146]	not inert	disintegration/dissolution
UHU Plus Schnellfest[147]	not inert	disintegration/dissolution
UHU Plus Sofortfest[148]	not inert	disintegration/dissolution
X60[149]	not inert	disintegration/dissolution

respective test-nanopositioner was alternating driven up and down over a period of 2 weeks. The movement of the test-nanopositioner was controlled by a home-built controller unit based on an *Arduino Uno* microcontroller board connected to a *E-870.11* piezo driver unit from *PI.*[150] Via two end switches the *Arduino Uno* is able to read the upper and lower position of the nanopositioner, and to trigger a direction change. Both end switches are implemented by simple metal contacts and a U-shaped aluminium counterpart screwed on top of the test-nanopositioner. The whole setup was sealed in a glass beaker with plastic cap.

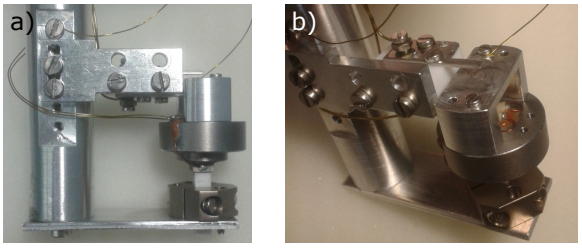

Figure 6.3: (a, b) Test setup of the adapted nanopositioner to determine the chemical resistance and mechanical stability of the glues under operation conditions. An aluminium rod attached to the glass beaker's lid works as a stand for the upper and lower metal contact (end switches) and as a base plate, onto which the nanopositioner's fixed clamping jaws are attached to. During the stress test the setup is immersed in 100 $°C$ hot nonanoic acid, and the nanopositioner is driven alternating up and down by a home-built controller unit, based on a *Arduino Uno* microcontroller board.

Unfortunately, all three glues did not withstand the mechanical stress level of an expanding and contracting nanopositioner piezo. Especially, the *PJ1390-1* performed very badly as it fell off immediately after the start of the nanopositioner. This is most likely attributed to a low adhesion level. In the case of the *KL06-B* and *KGL 130 EP* both glues endured the stress test a slightly longer (∼2 h), but finally it came to the destruction of the piezo itself. Concluding from the fracture pattern the problem is not the adhesion of both glues, but rather the inability to compensate the alternating deformation of the piezo during the movement of the nanopositioner (low elasticity).

To overcome this problem a two layer approach was proposed consisting of a mechanically stable glue, shielded by a covering layer for the protection against the harmful influence of the fatty acids. A glue that provides the necessary mechanical properties, and has been proven ideal for the fabrication of nanopositioners at ambient and vacuum conditions is the *H74* from *Epoxy Technology*. So far, the *H74* is the best choice for the fabrication of a nanopositioner and was deployed in every version of the I-STM. Different protection concepts for the *H74* were applied, and adapted during development of the I-STM. This concepts will be described in detail in the next section. For the joining of all other mechanical parts the chemically inert *KGL 130 EP* was used as this glue provides the required mechanical stability for the respective applications in combination with an improved processability as compared to the *KL06-B*.

6.3.2 Corrosion Protection Principles

Preliminary corrosion tests of all materials revealed a high vulnerability of less noble metals and epoxy glues to fatty acids that, in turn, are highly appropriate and relevant solvents for self-assembly studies. Specifically, copper, brass, Super Invar, samarium-cobalt, silver and lead were ranked as not inert in the corrosion tests. For the glues, two candidates (*KL06-B* and *KGL 130 EP*) were proven inert against the corrosive fatty acids but unfortunately, they can only be used in applications with static loads due to their lack in elasticity. Especially for the dynamic loads of the nanopositioner, the well established, but not inert *H74* is highly appropriate through its combination of elasticity and adhesion. So far, the *H74* is the only option to manufacture a reliable stick-slip nanopositioner. In order to use the less noble metals and the *H74* glue for the I-STM, these materials have to be protected. Since the requirements to a coating material differ between the materials and their specific application, different coating materials are needed. Until now, four coating materials could be identified: Parylene type C, gold, gold solder (Au80Sn20) and the fluoroelastomer *LET-VITSEAL* (Fig. 6.4).

Parylene

Parylene is an electrical insulating, hydrophobic, optical transparent polymeric coating material with a high chemical resistance against organic and in-organic substances, e.g. acids, solutions, gases and water. It is widely used as a corrosion

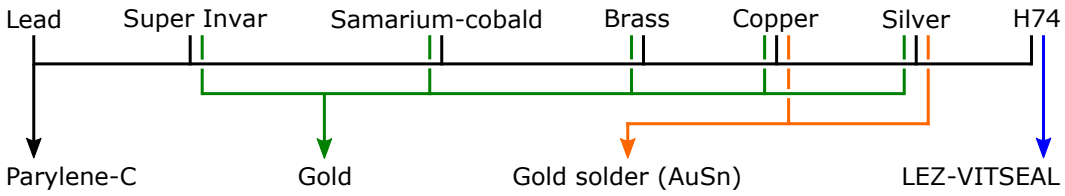

Figure 6.4: Assignment of the seven not corrosive resistant materials to four appropriate coating materials.

protection layer to shield materials from harmful substances, even in medical applications due to its inherent bio-compatibility and bio-stability.[151,152] The application of Parylene takes place through a CVD-process (Chemical Vapour Deposition) at room temperature, particularly important for temperature sensitive materials. This coating method creates pinhole-free layers with thicknesses varying from 0.1 μm to 20 μm, coating even smallest cavities as compared to liquid solution-based coating processes.[153]

The starting material for a non-halogenated parylene coating is the di-p-xylylene dimer sublimated at 150 $°C$ (1) (figure: 6.5).[154–156]

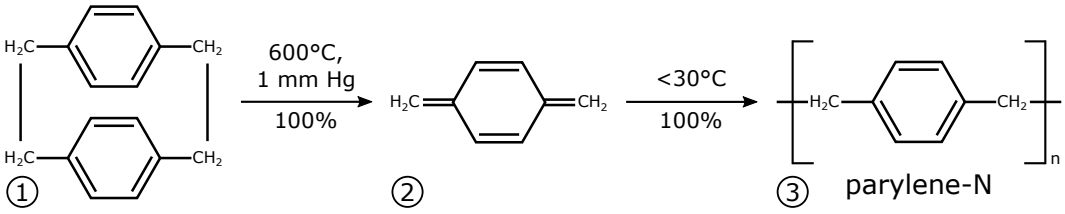

Figure 6.5: Di-p-xylylene dimer to poly(p-xylylene) (parylene-N) reaction. Adapted with permission from Gorham[154]. Copyright (2003) John Wiley and Sons.

The di-p-xylylene dimer can be dissociated by vacuum vapour-phase pyrolysis at 600 $°C$ to form two molecules of the reactive intermediate, p-xylylene radical (2). After the dissociation, the p-xylylene intermediate spontaneously polymerizes on surfaces maintained below 30 $°C$ to form linear poly-p-xylylene (3), also called parylene-N.[154] Besides the non-halogenated p-xylylene there are also a wide range of halogenated dimers to create different types of parylene coatings. The most common parylene-types are: parylene-C-, parylene-D- and parylene-F (also called parylene-HT) (figure: 6.6).[152,157]

These parylene-types differ in their electrical and physical properties. Their synthesis procedure is similar to the N-type's, but with different temperatures for sublimation, pyrolysis and deposition. One very interesting parylene type for the coating of the I-STM is the C-type as it offers the best combination of chemical resistance with a low moisture/gas permeability, elasticity and good adhesion.[152] If needed, the adhesion can be further enhanced through the preliminary application of a SiO_2 primer. Beside the deposition at room temperature, parylene-C can also be applied at higher temperatures (deposition at 90 $°C$), but then develops slightly different material properties.[158] For the thermal endurance of parylene-C over 100000

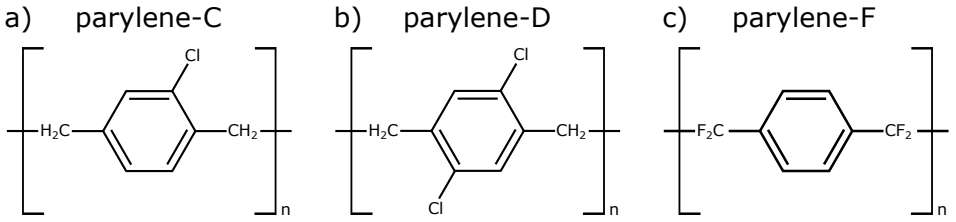

Figure 6.6: Halogenated parylene types: (a) parylene-C, (b) parylene-D and (c) parylene-F (parylene-HT)

h in air a temperature of 106 $°C$ has been stated, determined by *Advanced Coating* through an Arrhenius extrapolation based on an induction-time to initial weight-loss method.[159] Since exposure to fatty acids imposes a much higher chemical load, a SiO_2 reinforced parylene-C layer was applied to a test-nanopositioner assembled with the *H74* glue. The test-nanopositioner endured ∼4 weeks in 100 $°C$ hot nonanoic acid while running alternatingly up and down (∼2 mm travel; ∼15000 cycles) without any degradation and contamination of the acid. This test qualifies parylene-C as a suitable coating material for the protection of the I-STM in fatty acid solvents.

Gold

Gold (Au) is a very effective coating material to protect metal components from corrosive media via the application of a pinhole-free layer. Depending on the coating quality a pinhole-free gold layer can be galvanically achieved with a layer-thickness from ∼2 to 4 μm.[160,161] Compared to parylene, gold coated metal parts do not loss their electrical conductivity which is particularly important for the design of inert electrical feedthroughs or other electrically conductive setups, e.g. the tip/sample exchange systems. With an exception for lead, gold can be applied to all less noble metals of the I-STM design (Fig. 6.4).

The most appropriate way of applying a pinhole-free gold layer to a metal part is electro-galvanic coating using an electrolyte. Most modern gold electrolytes are based on a cyan-complex, e.g. potassium dicyanoaurate(I) ($K[Au(CN)_2]$) with a pH-value of ∼4.[162] To apply a pin-hole free gold layer on metals like super invar or stainless steel an intermediate adhesion layer like copper and nickel has to be applied preliminary.

An alternative to an intermediate metal layer is the usage of more acidic gold electrolytes based on potassium tetracyanoaurate(III) with a pH-value of ∼2.[163] However, the deposition rate of this electrolytes is rather low as compared to the potassium dicyanoaurate(I) based electrolytes. To accelerate the growth, the potassium tetracyanoaurate(III) based electrolyte can be used as primer followed by a potassium dicyanoaurate(I) based electrolyte with a significantly higher deposition rate. A well-established electrolyte combination for such a task is the potassium tetracyanoaurate(III) based electrolyte *Flash* with a deposition rate of 1.5 μm h^{-1} at 0.7 A/dm^2 and the potassium dicyanoaurate(I) based electrolyte *Midas* with a

higher deposition rate of 5.5 μm h^{-1} at 0.5 A/dm^2), both from *Tifoo*.[162,163] To guarantee a pinhole-free gold layer a layer thickness of 6 μm was applied to all parts (1 μm with *Flash*, 5 μm with *Midas*). Growing gold-layers >20 μm is not possible as the layers will start to detach with further growth.

The corrosion resistance of a 6 μm thick gold layer was tested via a Super Invar and copper sample, both immersed in 100 $°C$ hot nonanoic acid over a time period of 2 weeks without any indication of corrosion at the sample or contamination of the pure acid.

Gold Solder (AuSn)

Apart from pure gold also gold solder (AuSn), an alloy of gold and tin, has been proven as a reliable and inert coating material for copper and silver. Thinly applied via a soldering iron at ~380 $°C$, a copper sample withstood the corrosion in 100 $°C$ hot nonanoic acid for 2 weeks without any alteration of the sample or solution. Many standard tin solders used in electrically bonding are alloyed with copper, lead or silver. As a consequence, all electrically bonding points of the I-STM were realized with the *Au80Sn20* solder from *IPT Albrecht* to create reliable electrical contacts in a corrosive environments.[114]

Fluoroelastomers

Fluoroelastomers are in general fluorocarbon based elastic rubbers with a high level of chemical resistance. A popular type of fluoroelastomers is *FKM* (fluorcaoutchouc), widely used for the fabrication of gaskets and sealing pastes due to its high chemical resistance and thermal stability. Compared to *FKM*, *FFKM* (perfluoro-elastomer) contains an even higher amount of fluorine, providing this material with a higher chemical and thermal stability.[164] Certainly, *FKM* were proven as sufficiently inert for the application in the I-STM as gaskets (O-rings) and as a sealing compound (2 weeks exposure to 100 $°C$ hot nonanoic acid). For instance, the sealing compound *LEZ-VITSEAL* from *AET Lézaurd GmbH* was proven inert and suitable to withstand the mechanical load of an operating stick-slip nanopositioner, hence represents a reliable alternative to parylene-C. *LEZ-VITSEAL* is a *FKM* based sealing compound with a ketone-alike solvent, rapidly creating a passivation layer at air. This material can be used in a temperature range from -40 to +250 $°C$,[165] but especially for the use with fatty acids, further corrosion tests are necessary before temperatures well above 100 $°C$ can be targeted. Furthermore, *LEZ-VITSEAL* is easy to apply and does not require specialized equipment or knowledge as compared with the deposition of parylene-C through a service provider.

6.4 Mechanical Design Principle

The following subsections are dedicated to the description of the mechanical design principle of the I-STM, which can be separated into three major parts: The actual STM (Section 6.4.1), the hermetically sealed and heatable container (Section 6.4.2), and the external vibration isolation with the μ-metal enclosure for electro-acoustic shielding (Section 6.4.3), constituting the I-STM setup (Fig. 6.7).

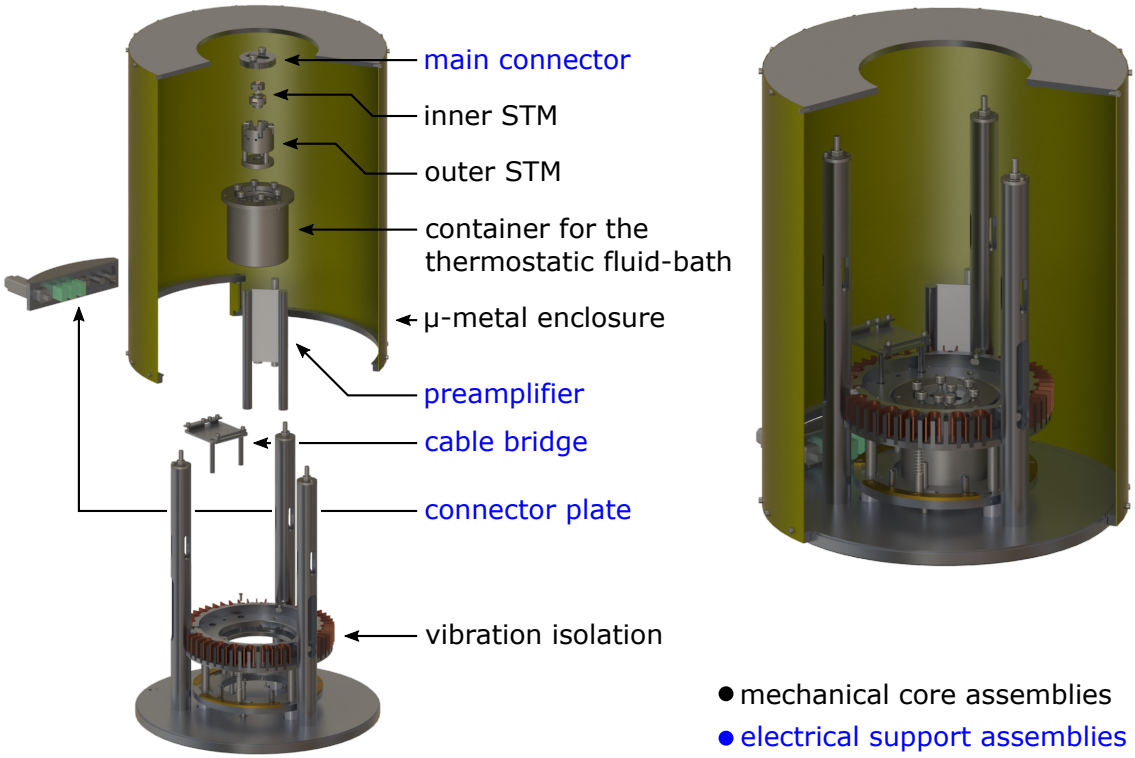

Figure 6.7: Explosion view of the main assemblies of the I-STM (μ-metal enclosure in sectional view) categorized in mechanical core and electrical support assemblies. The mechanical core assemblies are all described in this section while the electrical support assemblies and the wiring are all explained in section 6.5

In the proposed design, the STM body is mounted on the inside of the containers lid, and thus becomes immersed in solution within the container just by closing the lid. The heatable inner container itself is integrated into an outer container and both are forming the assembly of the container for the thermostatic liquid-bath (CTLB). This assembly again is integrated in the base plate of the external vibration isolation. To minimize the length of the tunnelling current signal wire, the preamplifier is located close to the lid. A main connector plugged into the containers lid connects all electrical signals going into or coming from the STM, and distributes them via single wires to an external connector plate and the preamplifier, safely guided by a cable bridge. A more detailed description of the electrical support assemblies and the wiring can be found in section 6.5.

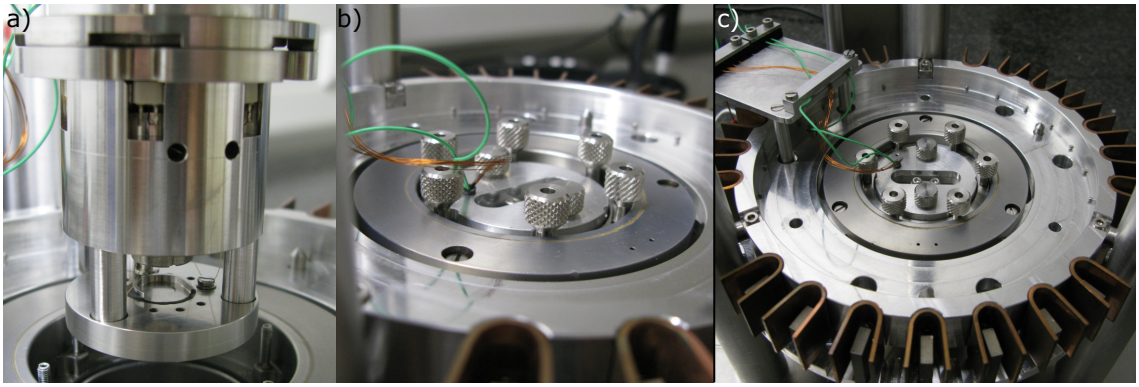

Figure 6.8: (a) STM (version 3 inner STM; version 2 outer STM) mounted in the manipulator and placed above the CTLB. (b - c) STM immersed and sealed inside CTLB with attached main connector (wires are guided by a cable bridge). The CTLB is mounted inside the massive vibration isolation (spring suspended and eddy current damped).

6.4.1 Scanning Tunneling Microscope

Apart from mechanical stability, the main design focus was to realize a system with low susceptibility to thermal drift, in particular after temperature changes. The impact of temperature gradients is minimized by the implementation of favourable design principles. In this respect, the use of either highly heat conductive materials and the introduction of heat bridges, reduces temperature gradients and facilitates fast thermal equilibration times. For didactic reasons the detailed description of the STM is divided into two subassemblies: The *inner STM* and the *outer STM*.

- **Inner STM**

  The inner STM represents the STM's core unit. It includes the scan unit - performing the actual scan movement while maintaining a defined distance to the sample surface - and an integrated stick-slip nanopositioner for a manually controlled and fully automated tip-sample coarse approach. A tip exchange system glued onto the scan unit and a corresponding tip holder, allows the quick change of scanning tips.

- **Outer STM**

  The outer STM assembly consists of a two-part metal framework that houses the inner STM, and the integrated sample exchange system with its associated sample holder.

Inner STM

The design of the inner STM fuses a scan unit with tip exchange system together with a stick-slip nanopositioner to a compact and rotational symmetric unit. Altogether, provides the inner STM all necessary movement capacities for the operation of a STM immersed in solution. Apart from some intermediate stages, so far, three working versions of the inner STM were fabricated and tested. The latest version is illustrated and marked as version no. 3 (Fig. 6.9), and represents the only version that was applied for scientific use.

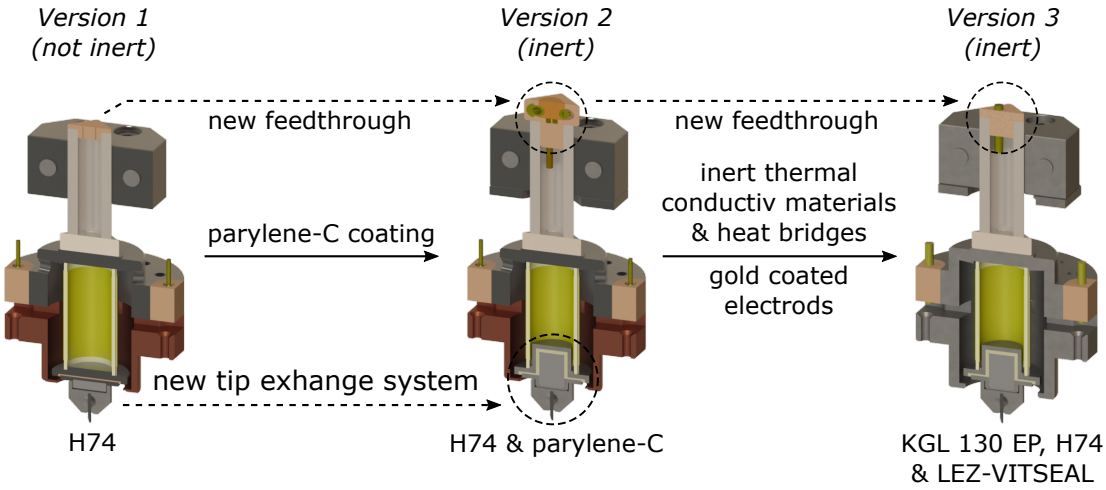

Figure 6.9: Version 1 to 3 of the inner STM with indications of major changes and key features of each version.

From version to version weaknesses in terms of endurance and chemical inertness were identified and eliminated. Between every version some improvements were key in the development of the inner STM, and will be mentioned during the presentation of the latest design of the inner STM (version 3). All single parts of the inner STM version 3 can be looked up in the explosion view of Fig. 6.11 with their corresponding designation.

The scan-unit (Fig. 6.10b) consists of a lead zirconate titanate (PZT) tube piezo actuator (*EPL# 2 / PZT-5A*, 6.5 mm outer diameter, 12.7 mm length and a wall thickness of 0.675 mm from *EBL Products, Inc.*) with one single inner and four 90 ◦ segmented outer gold over copper electrodes.[44]

Electrical insulation of the piezo electrodes against each other in solution is not required as fatty acids are completely insulating without any leakage current detectable even at higher temperatures. In terms of corrosion protection, the copper adhesion layer of the electrodes is not sufficiently shielded by the gold layer applied from the manufacturer. Furthermore, the fabrication processes of the tube piezo leads to bare copper edges between the four outer electrodes, since the gold is applied before the closed outer electrode is segmented. To protect the intermediate copper layer an additional 6 μm thick gold layer is galvanically added to the existing Au-electrodes with the gold electrolyte *Midas*.

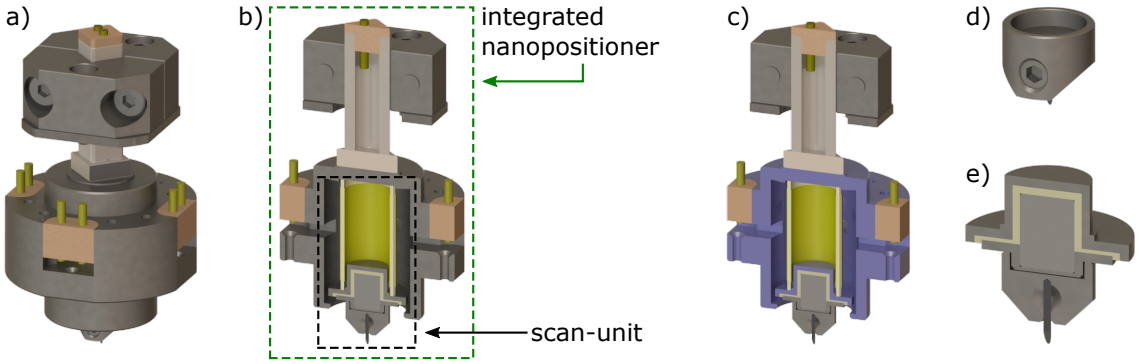

Figure 6.10: (a) Complete assembly of the inner STM, (b) Sectional view of the inner-STM with highlighted integrated nanopositioner and scan-unit, (c) Piezo shielding coloured in blue consisting of: the scanner platform, four scanner shields and shielding platform, (d) tip-holder with attached tip, (e) Sectional view of the tip holder socked and attached tip holder.

The tube piezo actuator carries the counterpart for the exchangeable tip holders - the tip holder socket (Fig. 6.10e) - both firmly glued together with the *KGL 130 EP*. The tip holder socket consists of four parts (Fig. 6.11): the electrically grounded shielding platform (1.4571 – stainless steel), an electrical insulator (*Shapal*), a magnet (*Sm2Co17*) and the counter disk to which the tunneling voltage is applied. The *Sm2Co17*-magnet is placed inside the electrical insulator, and covered and protected by the hat-shaped counter-disk. The tip holders are pulled against the counter disk by this magnet and the matching cylindrical geometries of both parts are establishing a reliable mechanical and electrical attachment. To expedite thermal equilibration of the tip exchange system, three thin interwoven 0.2 mm thick PTFE coated stainless steel wires are used for flexible thermal (and electrical) grounding of the shielding platform. This becomes necessary because the whole subassembly is thermal isolated due to the low thermal conductivity of the tube piezo actuator. The tip exchange system of version 3 was adapted from a system where the magnet was direct contact with the tip holders (Fig. 6.9 - version 1). Only a thin gold layer against the fatty acids was covering the magnet. Due to the brittle behaviour of the magnetic *Sm2Co17* material the edges of the magnet started to break off during the exchange of the tip holders. This was drastically lowering the stability and the fatigue life of the inner STM. The required curing temperature of the *KGL 130 EP* (220 $°C$) is sufficiently lower as the *Sm2Co17*-magnet's Curie temperature of 350 $°C$.[141 123] Hence, the magnets are able to preserve their magnetic properties throughout the curing.

The tip holders are fabricated out of the magnetic stainless steel 1.4057. Their geometry features a ⌀0.5mm thick hole into which the STM tips (⌀0.25 mm platinum-iridium wire) are placed, and fixed by a M2 screw.

As illustrated in Fig. 6.10b, the scan unit is concentrically glued (*KGL 130 EP*) to the scanner platform (1.4571 – stainless steel) – the base plate of the inner STM. To avoid crosstalk between the sensitive tunneling signals (tunnelling voltage U_{TV} in mV-range, tunnelling current I_{TC} in pA-range) and the high piezo driving

voltages (±130 V), the tube piezo actuator is surrounded by a closed metal shielding. This shielding consists of the scanner platform, four stainless steel (1.4571) scanner shields and the shielding platform, all parts are blue coloured in Fig. 6.10c. In the first two versions, the four scanner shields were fabricated out of OFHC-copper, protected by a closed gold layer (version 1), and an additional layer of parylene-C in version 2. Unfortunately, both protection layers failed at the contact area with the screws, since the screw-heads start to remove the protecting layers. To prevent this, the piezo shields were fabricated out of stainless steel 1.4571 for version 3 (Fig. 6.9).

The shape of the scanner platform features four equally spaced out grooves for electrical feedthroughs (*PEEK*) at its lateral surface. One of these feedthrough is only used as a strain relieve for the tunnelling voltage wire, while the other three double feedthroughs (*PEEK* isolator with gold coated stainless steel pins (type 1.4301)) additionally conduct the driving voltages of the scanner.

All parts together – the scanner platform with its four feedthroughs, the scan unit and the four scanner shields – are constitute the inertial mass, i.e., the payload of the integrated stick-slip nanopositioner (∼20 g, design inspired and adapted from the *ANPz51* series from *attocube systems*). The nanopositioner is driven by a unipolar piezo-stack actuator (*PL055.30* from *PI*) with a z-travel of 2.2 μm at 100 V. citepPL0xx2020 Both silver electrodes are protected against the harmful fatty acids through a closed layer of gold solder which simultaneously connects each electrode to a PTFE coated stainless steel wire (pre-coated with gold to facilitate soldering). In this design the piezo is glued between the scanner platform and a hollow zirconiumoxid axis with a quadratic cross-section – the nanopositioner axis – with the *H74* glue from *Epoxy Technology*. The nanopositioner axis is clamped between two jaws (1.4571 – stainless steel) loaded by two springs pushing the jaws against the axis. Both springs are adjusted by screws to a force of friction F_C of ∼5 N, which has been proven ideal for the operation of these nanopositioners. The springs are placed inside the loose jaw, while the fixed jaw is firmly attached to the STM body of the outer STM.

To prevent the ingress of liquids and to establish an electrical connection of the nanopositioner piezo, the hollow nanopositioner axis is sealed by a *PEEK*-feedthrough at its upper end (*KGL 130 EP*). The connection wires of the nanopositioner piezo are passed through the hollow nanopositioner axis to the internal soldering points of the *PEEK*-feedthrough – gold coated stainless steel pins at both sides. Two versions of *PEEK*-feedthroughs were developed before. The first version (Fig. 6.9) was a simple *PEEK*-plug with two holes to guide the nanopositioner's connection wires (sealed with the *H74* glue) out of the hollow axis. However, in the case of a torn wire the whole nanopositioner had to be replaced. This problem was solved in version 2 by the implementation of a *PEEK*-feedthrough featuring a plug-connector system consisting of two gold coated brass IC-Pins. Unfortunately, repeated plugging and unplugging destroyed the gold protection layer. This was eventually solved by using the gold coated stainless steel pin based soldering connection of version 3.

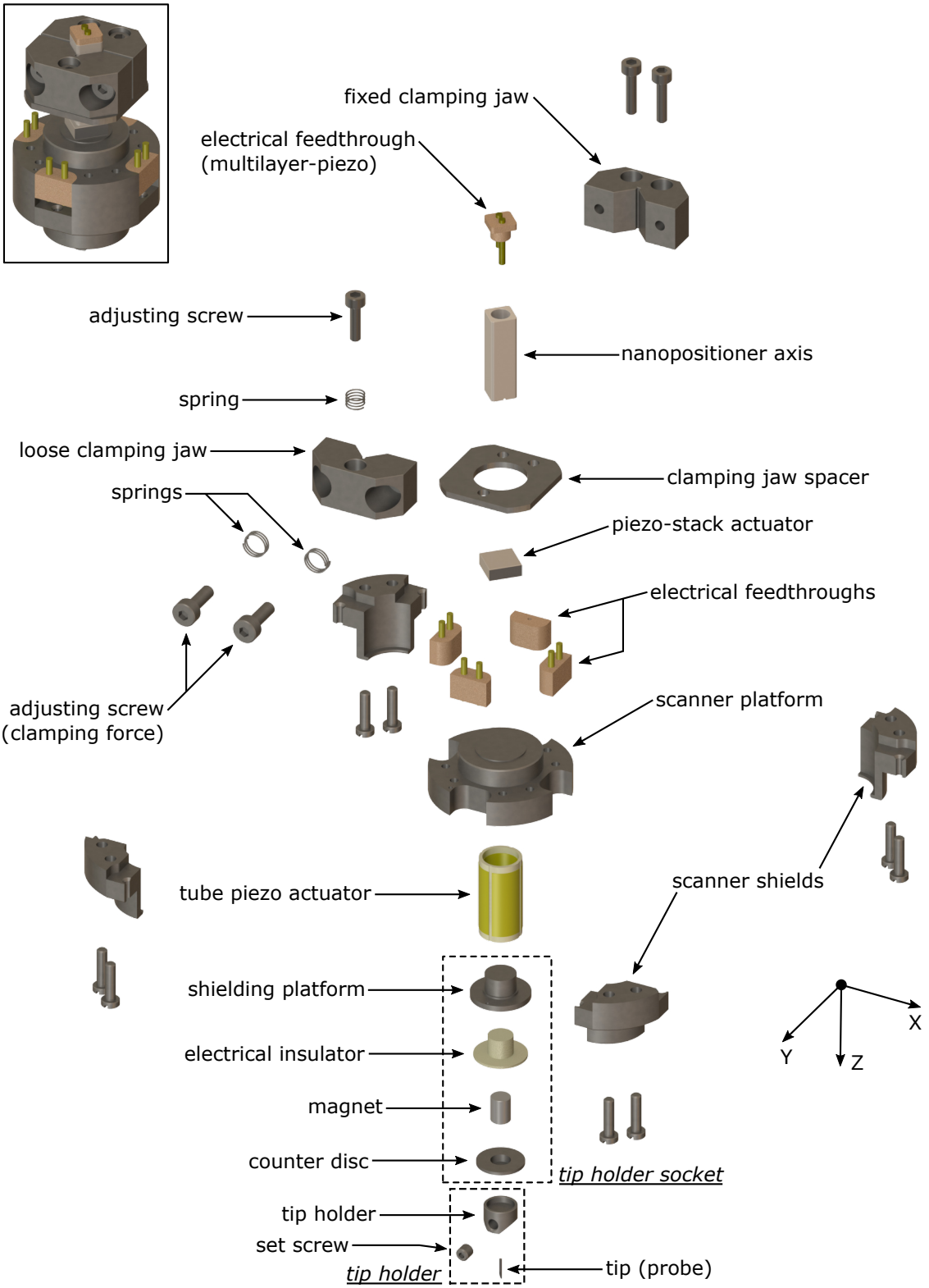

Figure 6.11: Assembly of the inner STM (version 3) in explosion view.

In a first attempt to protect the not inert *H74* glue used for the nanopositioner, both gluing points and nanopositioner piezo were coated with parylene-C (version 2). Since parylene-C is applied via a CVD-process the deposition cannot be re-

stricted to a specific area, hence the entire inner STM is coated with parylene-C. Nevertheless, to guarantee the functionality of the nanopositioner the surface of its axis had to be spared out, as well as the surface of the tip exchange systems contact disc to provide electrical contact to tip holders. This was archived by masking of the respective areas with tape before the deposition. The chemical and mechanical stability of parylene-C was proven through preliminary test. Yet, after ∼1 year of operation in contact with the corrosive fatty acids a delamination between the nanopositioner piezo and the parylene-C layer occurred, despite the use of a SiO_2-primer. According to the damage pattern the delamination started at the edge of the spared out nanopositioner axis, which has always been the weakest spot of the protection layer. As a consequence, parylene-C was no longer used as a protection layer for the inner STM. Starting with version 3 the *H74* glue, and additionally the nanopositioner piezo were both protected by a ∼0.5 mm layer of the *LEZ-VITSEAL* fluoroelastomer sealing paste. With the application of *LEZ-VITSEAL* temperatures above 100 $°C$ are theoretically possible (cf. section 6.3.2). In a recent study on the solvent-induced polymorphism of TMA-monolayers self-assembled at the solution-graphite interface, measurements at 110 $°C$ over a period of ∼3 h were achieved. For extended long-term studies at even higher temperatures, further corrosion tests at the targeted temperatures are required.

Outer STM

The development of the I-STM also results in three versions of the outer STM. All were fabricated and tested, but only version 2 of the outer STM was deployed for the scientific studies of this work.

Parallel to the scientific application of version 2, further development took place and a 3rd version of the outer STM was created and fabricated. Both, versions 2 and 3, feature a version 3 inner STM and can be used independently. Between version 1 and 2 a new design approach was implemented (6.12). With respect to the usage of materials with low thermal expansion coefficients and the implementation of a drift compensation, a concept that keeps thermal drift at a minimum was realized in version 1. In turn, the latest versions 2 and 3 feature a principle that expedites thermal equilibration (fast reduction of thermal drift) through enhanced thermal conductivity in combination with the introduction of heat bridges. In this section only version 2 and 3 of the outer STM will be described in detail, since versions 1 was not applicable for scientific use. An overview of both versions is shown in the explosion view of Fig. 6.17.

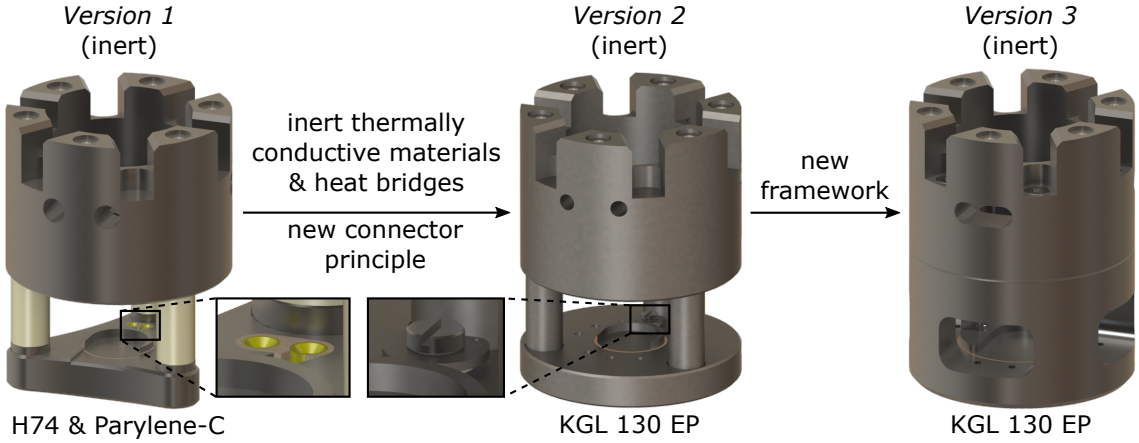

Figure 6.12: Version 1 to 3 of the outer STM illustrating its development history. Version 1 of the outer STM is optimized in terms of low thermal expansion during a temperature change through the implementation of PZT columns as a drift compensation and the usage of Super Invar 32-5 for all metal parts. Version 2 of the outer STM is optimized for fast thermal equilibration instead of low thermal expansion through the implementation of heat bridges, e.g. stainless steel for the columns. Version 3 represents a further development of the outer STM in terms of fast thermal equilibration and accessibility.

The version 2 outer STM consists of a massive STM body (1.4571 – stainless steel), i.e. a monolithic cylindrical framework with three pillars onto which the sample holder stage (accommodating the sample holder exchange system) is firmly screwed on. Together with the inner STM, the outer STM constitutes the complete assembly of the STM, while the STM body represents the scaffold for the sample holder stage and the inner STM. The inner STM is attached to the mounting stage of the STM body via two screws inside the fixed clamping jaw of the inner STM (Fig. 6.13).

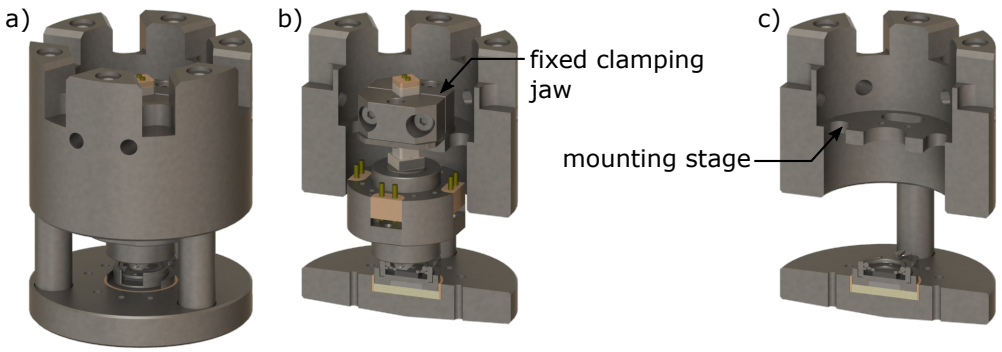

Figure 6.13: (a – b) complete assembly of the STM consisting of a version 3 inner- and version 2 outer STM with attached tip- and sample holders, (b) in sectional view. (c) Sectional view of the outer STM version 2 with attached sample holder.

The STM is primarily heated through heat conductance from the container via the lid, onto which the STM is attached to (chapter. 6.4.2). Hence, swift thermal equilibration is promoted by an efficient coupling between the STM and container lid as well as efficient heat transport across the STM. In this respect, the contact area between the STM body and the container lid was maximized. For a better heat transport from the container lid to the sample holder stage, the three pillars are now integral parts of the stainless steel STM body. In version 1, with focus on low thermal expansion, this pillars were made out of PZT, creating a drift compensation for the thermal expansion of the scan- and nanopositioner-piezo (same thermal expansion). But, by the same token, this introduces a heat barrier in the system (thermal conductivity of *PZT-5A* = 1.5 $Wm^{-1}K-1$).[44] When the container is filled, thermal equilibration is additionally mediated by the solution that perfectly connects the heatable container and the STM. However, the thermal conductivities of typically employed solvents (nonanoic acid = 0.150 $W\ m^{-1}\ K^{-1}$ at 290.3 K, heptanoic acid = 0.144 $W\ m^{-1}\ K^{-1}$ at 290.3 K)[166] are modest, rendering this contribution relatively low. Hence, it cannot replace the efficiency of heat transport through the stainless steel pillars or an external heat bridge. Especially the heat transport between the outer and inner STM is rather problematic as the heat flow is hampered by the zirconium nanopositioner axis (2 $W\ m^{-1}\ K^{-1}$ at 293.15 K).[133] This is compensated by four flexible 0.2 mm thick pure gold wires (297 $W\ m^{-1}\ K^{-1}$ at 290.3 K)[167] connecting the sample holder platform (outer STM) and the scanner platform (inner STM), hence, bypass the insulating zirconium axis of the nanopositioner. Each wire is clamped between one piezo shields and the scanner platform (inner STM). At the opposite end they are firmly attached to the sample holder platform of the outer STM via two screws (1.4301 stainless steel, two wires one screw).

The sample exchange is provided by magnetic attachment of cylindrical sample holders in a matching geometry – the sample holder stage (Fig. 6.14 and 6.17). This setup consists of seven parts: The contact disc (1.4571 – stainless steel), a Sm2Co17 magnet, an insulating *Shapal* disc, the grounded sample holder platform, a *PEEK*-insulator, a TC-connector nut (1.4571 – stainless steel, TC = tunneling current) with its matching TC-connector disc (1.4571 – stainless steel) for the connection of the tunnelling current signal wire. Analogous to the tip holder exchange system of the inner STM, a *Sm2Co17* magnet is placed underneath the contact disc, pulling the sample holder against its cylindrical geometry to arrange and fixate the sample concentrically to the tip holder. A short *Kapton* isolated copper wire connects the contact disc and TC-connector nut. Both stainless steel parts were preliminary gold coated at the soldering points. For electrical insulation a Shapal disc is placed underneath the contact disc, and a PEEK isolator surrounds the TC-connector nut. All parts are fused together and sealed with the *KGL 130 EP* glue forming a closed unit that is firmly attached to the STM body via three M3 screws (1.4301 stainless steel). A 0.2 mm thin PTFE coated stainless steel wire type 1.4401 is soldered to the TC-connector disc. In turn, the TC-connector disc is attached to its matching TC-connector nut via a M2 screw (1.4301 stainless steel) to establish a removable electrical connection to the contact disc.

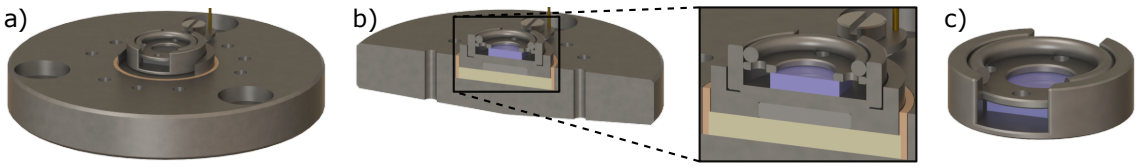

Figure 6.14: (a) Sample holder exchange system of version 2 outer STM with magnetically attached sample holder, and (b) sectional view with blue highlighted sample. (c) Sample holder with blue highlighted sample

This principle for a removable connection to the contact disc is inherited from a previous concept implemented in version 1 of the outer STM (Fig. 6.12a). In the first version a *PEEK*-connector with two IC-pins was embedded into the triangular sample holder platform with a matching *PEEK* plug. The core material of these pins is brass protected by a thin layer of galvanically applied gold. Brass was proven to be not inert against the corrosive fatty acids (cf. section 6.3.1). Over time, the gold layer got compromised, leading to a contamination of the fatty acid solution. This results in the need of a new and inert conception that was finally implemented starting with version 2 of the outer STM. The triangulare shape of the first sample holder platform minimized the solution volume needed for a complete filling (see section 6.4.2).

Samples are placed in cylindrical sample holders for a convenient sample exchange and firm fixation without the usage of a glue (Fig. 6.14). A stainless steel washer (1.4571 type), pushed down by a snap ring (1.4301 – stainless steel) clamps sample. During tunneling contact the tip holder is in close proximity to the sample holder. Depending on the tip length the spacing between the tip holder and the sample holder snap ring can be very narrow ($\sim$1 mm), hence, the accessibility of the solution in the sample holder can be inhibited to a certain level, ultimately leading to inhomogeneities in the solution composition, particular after heating. To avoid this, two notches are carved into the sample-holder socket and four 1.5 mm holes are drilled into the washer.

With version 2, the concept of expediated thermal equilibration was proven to be very effective. To further improve this, major changes were implemented in the design of the version 3 outer STM (Fig. 6.15). The main idea was to enhance the thermal conductivity through whole structure. For that, the STM body and the sample holder stage are forming now a massive cylindrical and monolithic framework with a larger contact area between them. Apart from that, the structure features a higher mechanical stability in combination with a better accessibility during maintenance.

The outer STM can now be split into two parts: The STM body (stainless steel 1.4571) - connecting the STM to the container lid while accommodating the inner STM - and the new sample holder stage providing the sample exchange. Both parts are firmly attached to each other via six screws (Fig. 6.17). The screw holes are sealed with thin PTFE gaskets underneath the screw heads. To avoid any leakage of solution into the interspace of both parts, two O-rings are sealing the assembly.

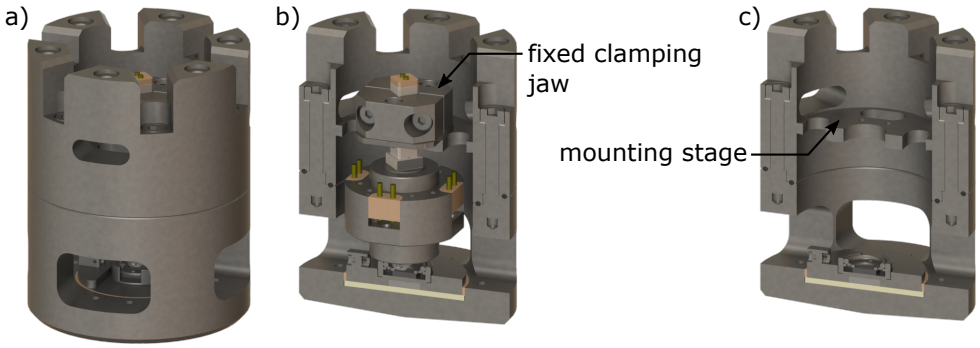

Figure 6.15: (a) Complete assembly of the STM consisting of a version 3 inner- and version 3 outer STM with attached tip- and sample holders, (b) sectional view. (c) Sectional view of the outer STM version 3 with attached sample holder.

Access to the sample holder is now provided through four windows, radially milled into the sample holder platform (stainless steel 1.4571).

The sample exchange system of version 3 (Fig. 6.16) follows the same principle as implemented in version 2 of the outer STM. A $Sm2Co17$ magnet is placed underneath the contact disc (1.4571 – stainless steel), pulling a sample holder against it. A Shapal disc is providing the efficient electrical insulation of the contact disc to the grounded sample holder platform. The tunneling current signal wire is directly attached to the contact disc, making additional components, like the contact nut and cable connector of version 2, redundant and the assembly less complex and prone to defects. A 0.5 mm thick gold coated metal pin (1.4301 – stainless steel) is soldered to the end of the tunneling current signal wire, a 0.2 mm thick PTFE coated stainless steel wire (type 1.4401). The pin is clamped by a M2 set screw (1.4301 – stainless steel) inside the connector box, which is an integral part of the contact disc (Fig. 6.16b). All parts of the sample holder stage are fused and sealed with the inert *KGL 130 EP* glue.

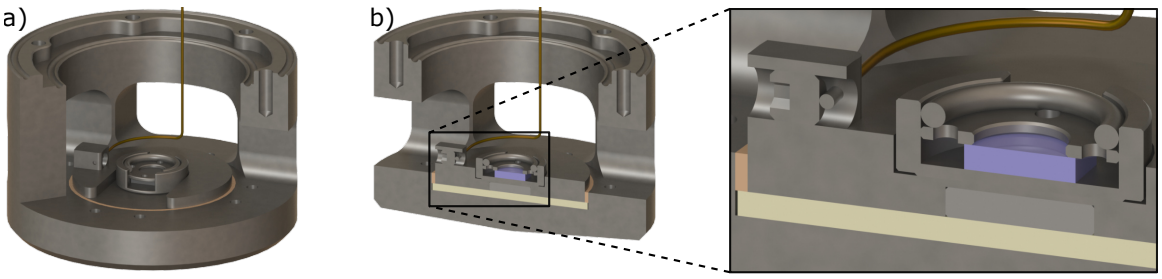

Figure 6.16: (a) Sample holder exchange system of version 3 outer STM with magnetically attached sample holder, and (b) sectional view with close up of the sample holder and the integrated connector box.

To facilitate fast thermal equilibration of the inner STM, four flexible 0.2 mm solid gold wires are connecting the scanner platform of the inner STM with the sample holder platform of the outer STM. Similar to version 2, two gold wires are

screwed together onto the sample holder platform with a M2 screw (stainless steel 1.4301).

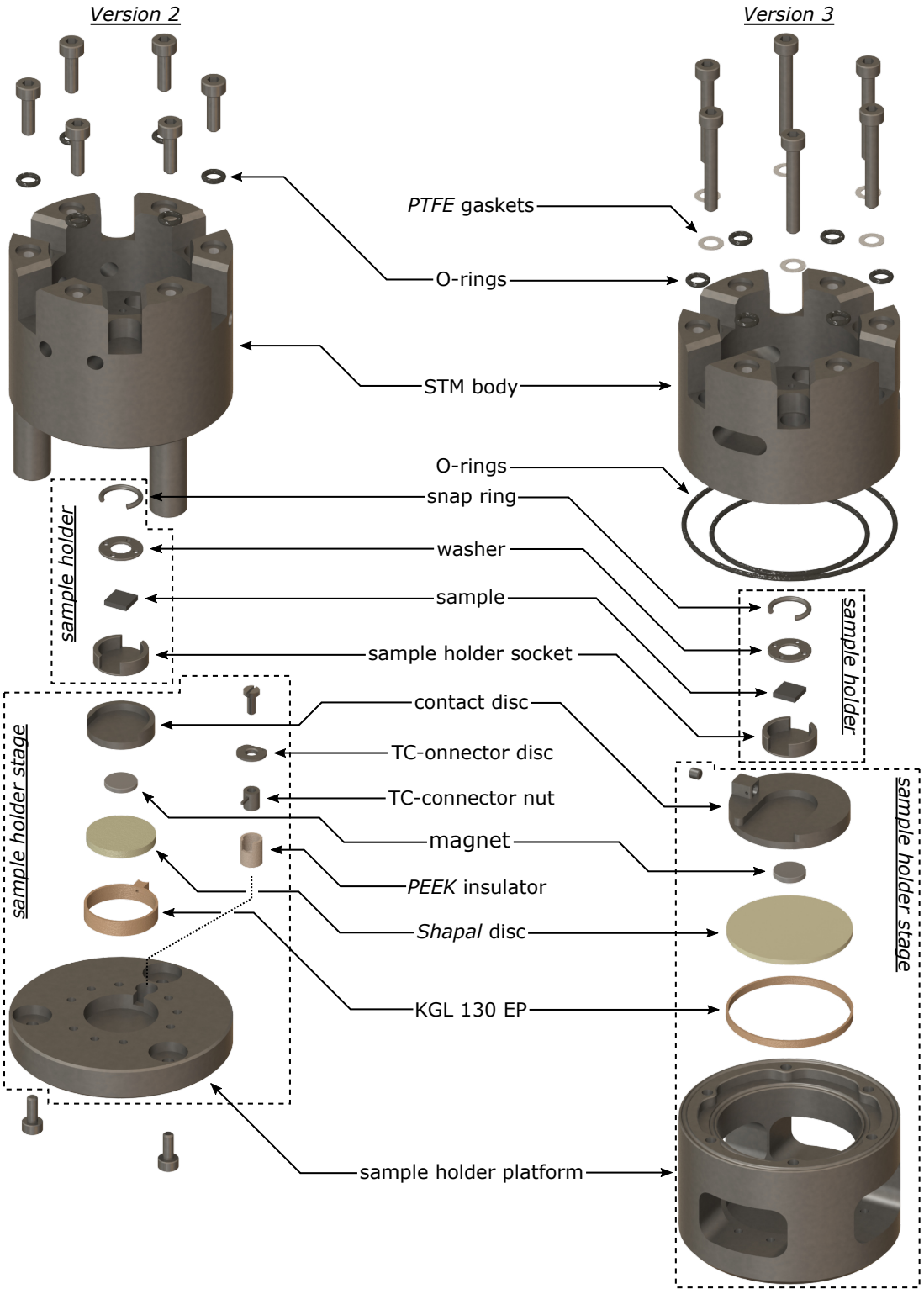

Figure 6.17: Exploded views of version 2 and 3 of the outer STM with sample holder assemblies.

6.4.2 Container for the Thermostatic Liquid-Bath

Immersion of the STM in a completely or partially filled heatable and hermetically closed container is the core idea behind the development of the I-STM. Beside the ability to keep the temperature of the STM stable by means of a closed-loop temperature control, the hermetical sealing of the STM prevents any evaporation of solution over an extended time period, even at higher temperatures. This functionality is implemented in the CTLB. In this section, the latest version 2 of the CTLB is presented as it is the only version that is applied to scientific use.

The heart of this assembly is the inner container, a heatable stainless steel (type 1.4571) basin for the solution with a total filling volume of ~72.0 mL (Fig. 6.18a and b). The size of the container was determined through a compromise between keeping its volume reasonably low to reduce the amount of required solution and having enough space for safely lowering the STM into the inner container. With the STM immersed, the container has a free volume (filling capacity) of $\sim$ 36.9 mL for the version 2 outer STM, and $\sim$ 34.8 mL for version 3. It is notable that complete filling of the container is not always necessary. In principle, a $\sim$ 40% filling level is sufficient to submerge the sample without any notable influence on the performance as compared to a completely filled container. Alternatively, just a μL droplet of solution could be applied on the sample-substrate as in conventional experiments with an additional amount of solution at the container bottom for generating a saturated vapour atmosphere, as proposed in the design by Hipps *et al.*.[27]

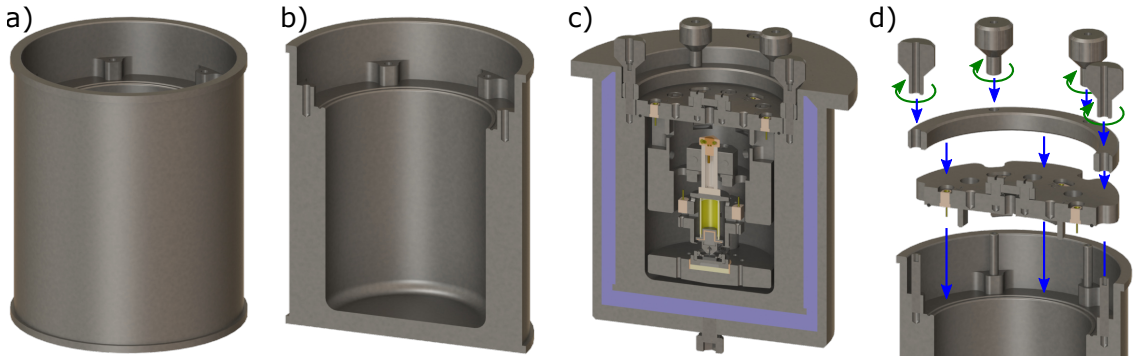

Figure 6.18: (a) Version 2 of the inner container, (b) sectional view. (c) Sectional view of the complete CTLB assembly with immeresed STM (version 3 inner and outer STM). (d) Closing of the inner container realized through a hold-down ring pressed down by six nuts.

The CTLB is heated through a tightly wrapped heating wire (Isotan CuNi44, diameter 0.40 mm, 25 windings, 45 Ω total resistance, polyurethane based wire enamel – *E6146*) around the inner container, fixated via *Teflon*-tape (PTFE). For the heating wire, a comparatively small diameter was chosen to increase its resistance in order to supply a given heating power with relatively high voltages and small currents. This allows usage of smaller lead wires, thereby minimizing mechanical coupling (see section 6.4.3 and 6.5.2). In terms of achieving a homogeneous heat distribution across the container, a highly heat conductive material is desir-

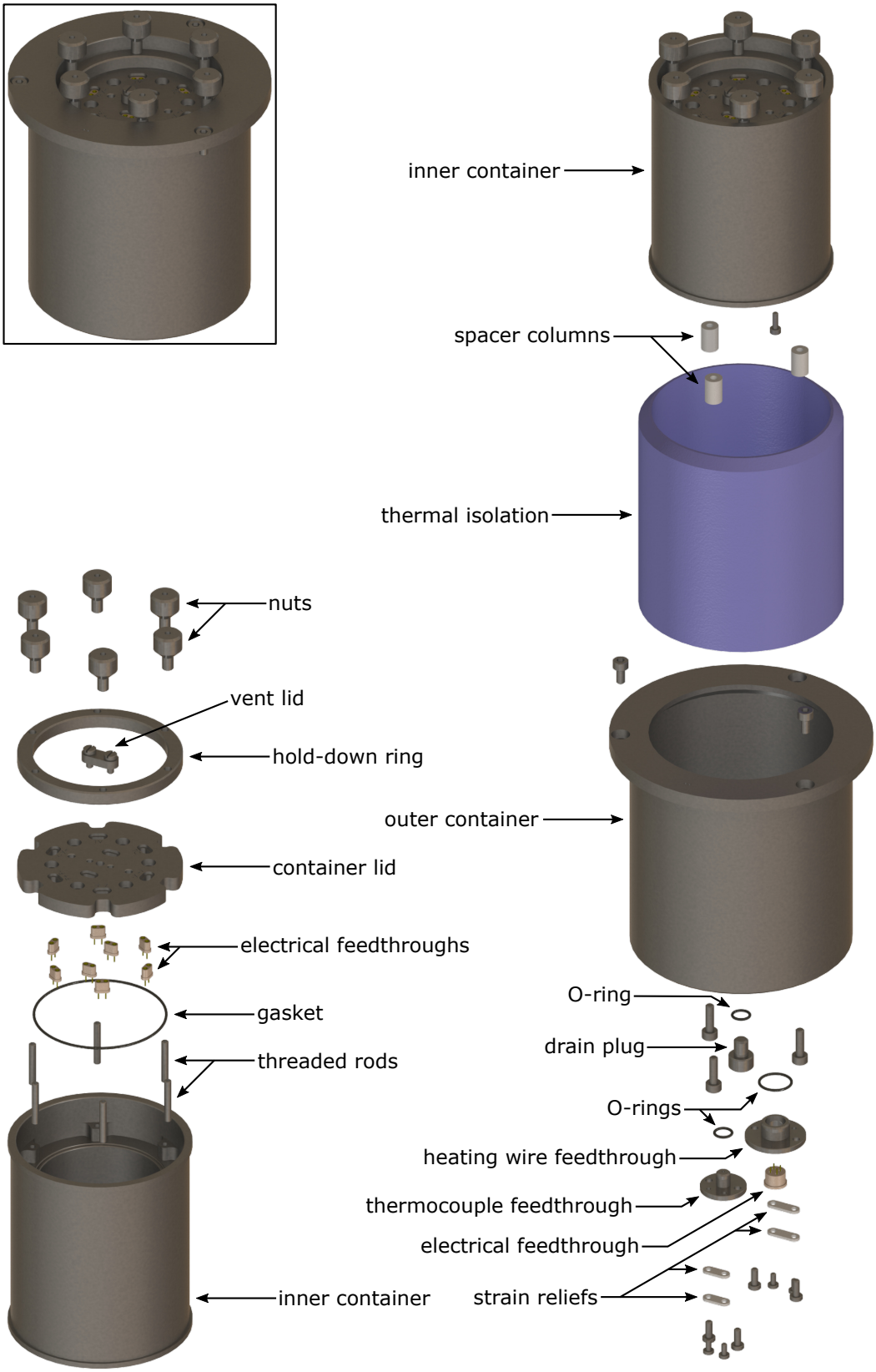

Figure 6.19: Exploded view of the CTLB version 2.

able for the inner container. However, an initial attempt (version 1 of the CTLB) with a galvanically gold plated OFHC-copper inner container proved to be insufficiently protected against corrosion. A leakage in the gold protection layer lead to a strong turquoise discolouration of the nonanoic acid (6.20a, cf. chapter 6.3.1). The defect occurred at the sharp edge of a triangular groove at the bottom of the inner container. Together with the matching triangular shape of the outer STM's first version (Fig. 6.12), this geometry was implemented in order to minimize the solution volume.

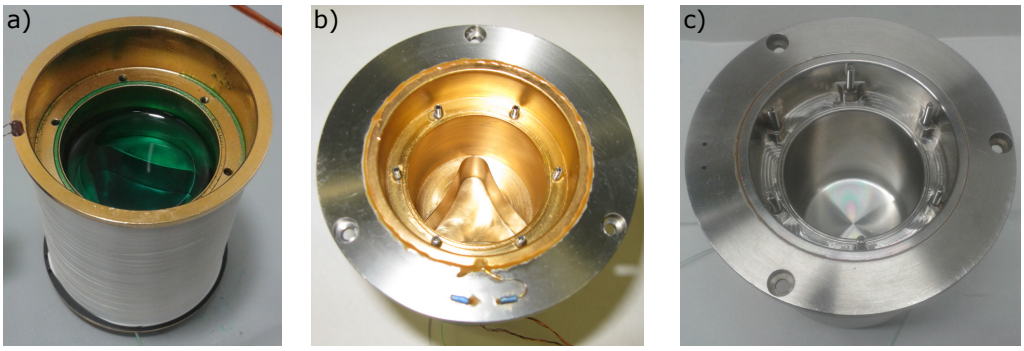

Figure 6.20: (a) Inner container of the CTLB version 1 after a repeated inertness test. A leakage in the gold layer, presumably at the edges of the triangular groove resulted in a strong contamination of the nonanoic acid. (b) Version 1 of the CTLB. (c) Version 2 of the CTLB with rounded edges at the inner containers bottom (stainless steel 1.4571).

Since gold plated copper showed a great vulnerability, stainless steel 1.4571 was chosen for the final version, as a compromise between inherent inertness and heat conductivity (Fig. 6.20c). As a further precaution, the design was changed in order to avoid any sharp edges. Hence, the triangular groove at the bottom was removed for a big rounding (⌀6 mm). This was also easier to manufacture, but resulted in an additional solution volume of ∼10 mL for the version 2 outer STM, and ∼8 mL for version 3.

To reduce the required heating power and warming of the surroundings, the inner container is integrated in a larger stainless steel 1.4571 outer container. For further thermal isolation, the interspace between inner and outer container is filled with aerogel granulate (0.012 $Wm^{-1}K^{-1}$ at ambient conditions),[168] and the contact area between both parts is minimized. The temperature is measured by a type K thermocouple (*5SRTC* from *Omega*) inside a bore at the bottom of the inner container.[49]

The container lid features a groove for a Viton O-ring gasket and is pushed against the inner container by six nuts via a metal ring (hold-down ring, 1.4571 – stainless steel), to evenly distribute the pressure and accomplish hermetical sealing of the STM (Fig. 6.18d). Temperature gradients are reduced by setting the lid back inside the inner container, in order to avoid cooling of exposed parts. At the same time, the container lid serves as the base plate for the STM, which is firmly attached at the inside of by six O-ring sealed stainless steel screws (type 1.4301). Furthermore,

the lid also accommodates all electrical feedthroughs for the drive voltages and signal wires. These feedthroughs consist of glued in gold plated IC-pins (*brass*) isolated by PEEK-bodies. All electrical connections (including signal wires) are simultaneously established by a single custom designed multipole connector at the outside of the lid (Fig.6.21). For a detailed described of the pin-assessment see section 6.5.2.

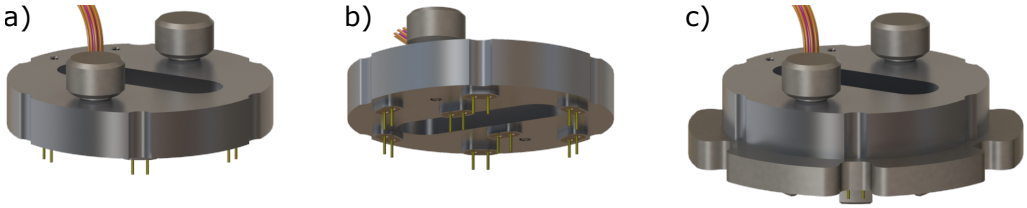

Figure 6.21: (a) Top and (b) bottom view of the multipole main connector. (c) Top view of the main connector plugged into the container lid.

6.4.3 Vibration Isolation and Electro-Acoustic Shielding

The image quality of an operating STM is strongly related to its susceptibility to external noises, hence, its mechanical stability, electro-acoustic shielding and vibration isolation. The shielding from electro-acoustic noises can be achieved via a grounded housing, covering the whole STM. For the protection against floor vibration a two-step damping stage is highly appropriate. Every damping stage and the STM itself have their own frequency transfer functions, describing the frequency-dependent response of the system to an external excitation. Since the damping stages and the STM are serially coupled, the total frequency-dependent response of the entire system $G_{sys}(\omega)$ can be calculated by the product of the individual frequency transfer functions ($G_1(\omega)$ = first damping stage; $G_2(\omega)$ = second damping stage; $G_{STM}(\omega)$ = STM; Eq. 6.1).[38]

$$G_{sys}(\omega) = G_1(\omega) \cdot G_2(\omega) \cdot G_{STM}(\omega) \tag{6.1}$$

The resonance frequency of tube scanners is typically in the range between 0.5 kHz and 10 kHz, which in turn will always be the limiting factor for the scanning speed of a STM.[38] Hence, for an efficient shielding of the STM, it is important that both damping stages should be strongly damped with the characteristics of low pass filters and resonance frequencies well below the expected acoustic and floor vibrations.

In the specific case of the I-STM an air-suspended optical table is used as the first stage ($G_1(\omega)$) followed by a spring suspended eddy current damping ($G_2(\omega)$) - the vibration isolation of the I-STM. Unfortunately, no data or even the manufacturer or type of the used optical table (1 x 2 m; 3 cm thick granite plate over a 3 cm thick steel plate; four air-suspended absorbers integrated in a massive steel frame) are available but resonance frequencies of comparable devices range between 1 - 2 Hz.[169,170] Hence, optimizing the vibration isolation is the most effective measure.

To design a damping system based on a spring suspended harmonic oscillator with a low eigenfrequency, a high inertial mass m in combination with a low spring constant k is needed (Eq 6.2).

$$f_0 = \frac{\omega_0}{2 \cdot \pi} = \frac{1}{2 \cdot \pi} \cdot \sqrt{\frac{k}{m}} \tag{6.2}$$

The implementation for the I-STM consists of a ring shaped base plate that accommodates the CTLB, and, in turn, is suspended by three parallel stainless steel spring (each $k = 0.07\ Nmm^{-1}$) supported on three outer pillars (Fig. 6.25 and 6.26, design inspired by the four point suspended vibration isolation of the *UHV VT-SPM* from *Scienta Omicron*). For eddy current damping, 21 U-shaped sheet metals made of copper (copper fins) are radially mounted on the ring, each embracing a fixed *Sm2Co17* permanent magnet. At the top of each pillar an adjustment screw allows the levelling and centring of the ring. Both, the softness of the springs ($k_{total} = 0.21\ Nmm^{-1}$) and the relatively high inertial mass of the moveable assembly (∼2.6 kg) yield a desirably low resonance frequency of ∼1.4 Hz. This should facilitate efficient damping at higher frequencies through its low pass characteristics.

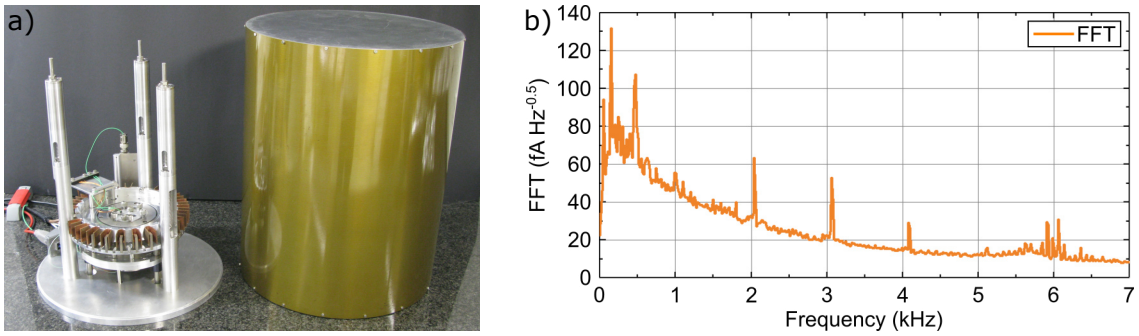

Figure 6.22: (a) Complete assembly of the I-STM with its outer μ-metal enclosure aside. (b) Square root of the tunneling current power spectral density. During the acquisition, the tunneling current feedback was active but slowed down. The setpoint current was 0.5 nA and an average of 24 spectra is presented.

All these measures effectively shield the STM from external noise, reflected in a very low noise level of the tunneling current as shown by the spectrum in Fig. 6.22b. The overall level with a peak of ∼130 $fAHz^{-0.5}$ is quite low, but the spectrum shows mechanical resonances of the STM setup and their overtones at ∼1.02 kHz and around ∼6 kHz that, however, have proven negligible in terms image quality. Furthermore, the STM is fairly insensitive to external acoustic noise even without the μ-metal enclosure. For instance, in the retracted state (STM mounted in the manipulator (section 6.6.1) and placed above the CTLB, Fig 6.8a) with arrested vibration isolation, the lab-background noise resulted in a peak of 650 $fAHz^{-0.5}$ at a frequency of 0.5 kHz. The additionally exposure to a sound level of 87 dB raised that spectrum to a peak-value of ∼5 $pAHz^{-0.5}$ at 0.8 kHz (Fig. 6.23).

In the immersed state (STM sealed inside the CTLB) with unlocked vibration

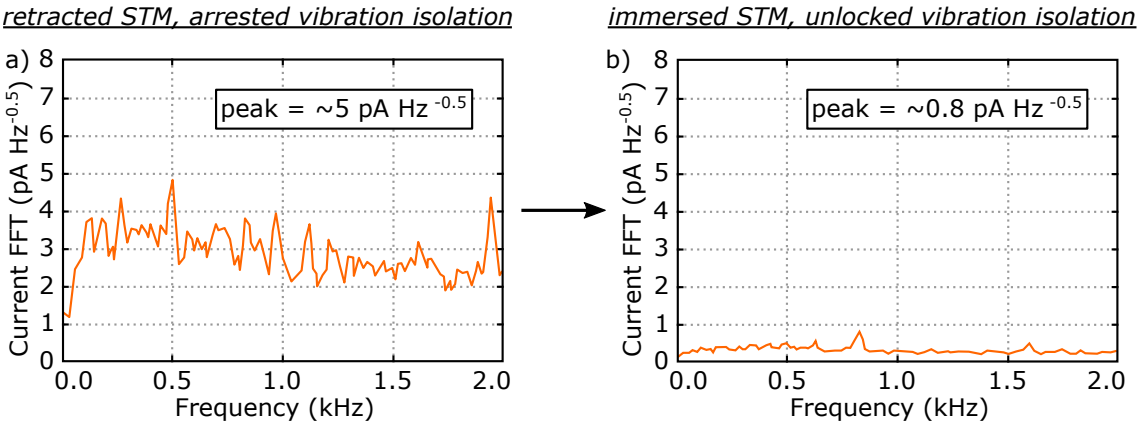

Figure 6.23: Square root of the tunneling current spectral power density with exposure to an acoustic noise of 87 dB (a) STM in the retracted state with arrested vibration isolation, and (b) in the immersed stated with unlocked vibration isolation.

isolation the tunneling current only results in a peak of 800 $fAHz^{-0.5}$ at a frequency of 0.8 kHz. Additional isolation from acoustic noise can be achieved with the μ-metal enclosure reducing the impact of the external noise on the tunneling current to nearly zero. The excellent signal-to-noise ratio of the tunneling current spectra from Fig. 6.22 also reflects the superb electrical screening concept implemented in the I-STM.

For handling purposes, e.g. for retracting the STM from the container in order to exchange tips or samples, the vibration isolation can be arrested by means of a locking device (Fig. 6.25), whose principle is illustrated in Fig. 6.24.

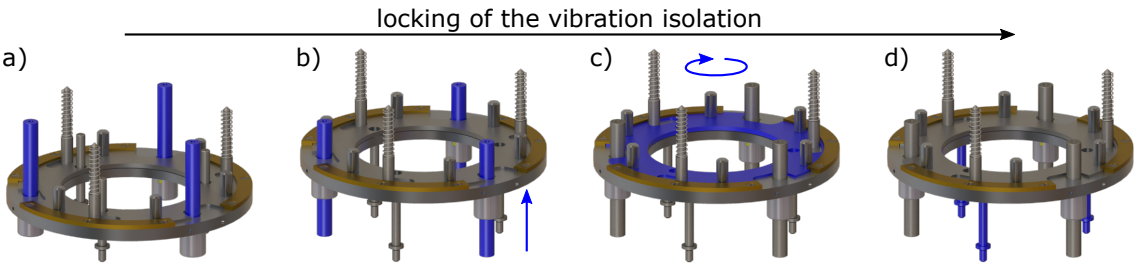

Figure 6.24: Mechanism of the locking device. (a) In open state (blue highlighted stator support works as linear guidance). (b) Pushed up against the oscillator base plate. (c) Rotating of the locking disc (clockwise = closing, counter clockwise = opening. (d) In closed state.

The locking device consist of a ring shaped base plate, guided by three bushes sliding on the stator supports of the magnet holder (blue highlighted in Fig. 6.24a and b). By pushing the locking device base plate up (Fig. 6.24b) three spring loaded clamping bolds are engaging in matching holes of the oscillator base plate. This pushes the oscillator base plate against three fixed stops (lower spring holders pushed against the notch of the spring columns, cf. Fig. 6.26). To arrest the device in the upper locked position a rotatable locking disc with three holes (blue highlighted in Fig. 6.24c) is integrated into the ring shaped base plate. By rotating

the closing disc clockwise the holes are sliding to the side and the whole locking device is fixated (Fig. 6.24d). Unlocking is archived in reverse order (Fig. 6.24d to a).

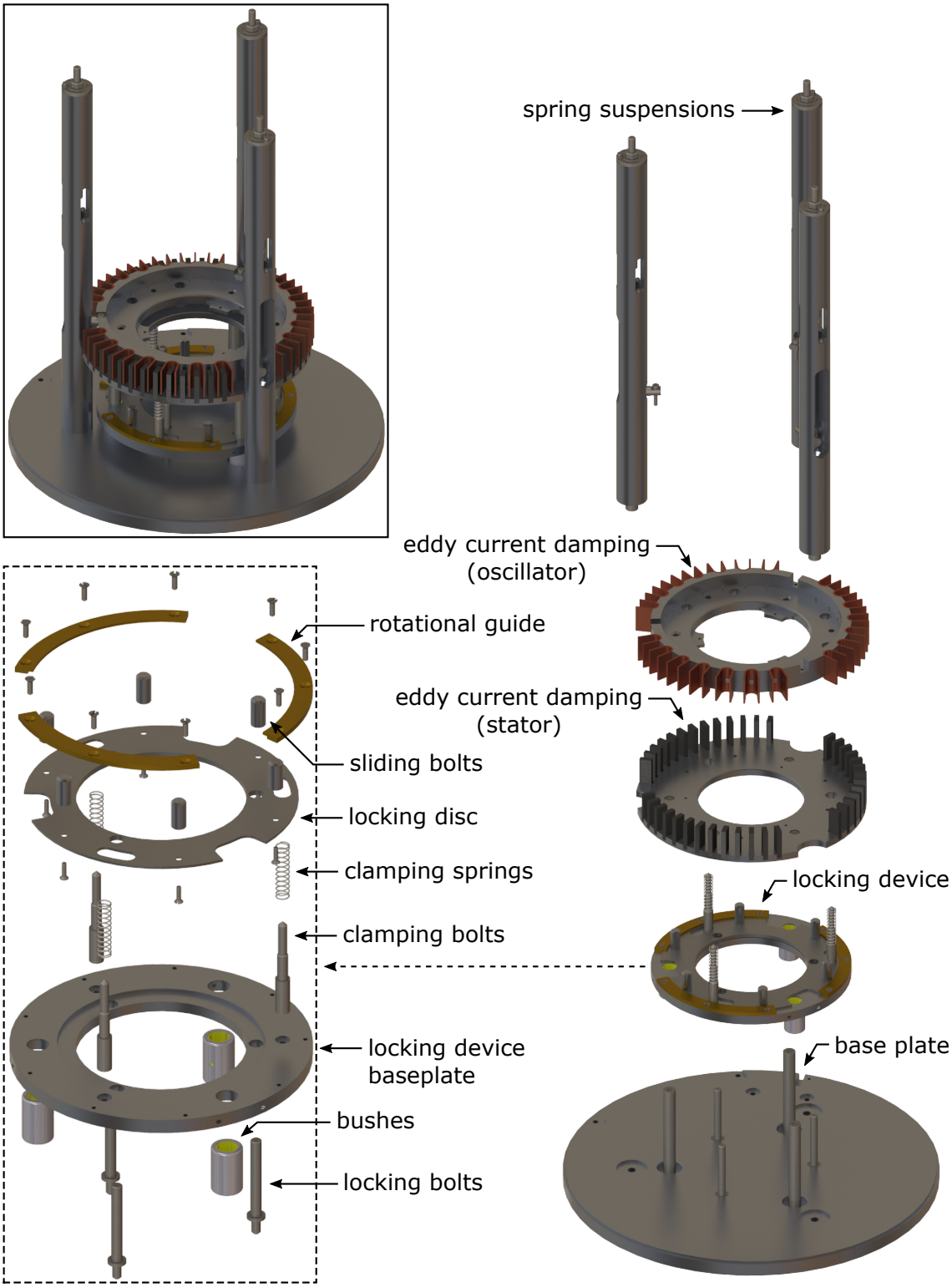

Figure 6.25: Exploded view of the vibration isolation and the locking device in detail. For a detailed exploded view of the vibration isolations subassemblies see the following Fig. 6.26.

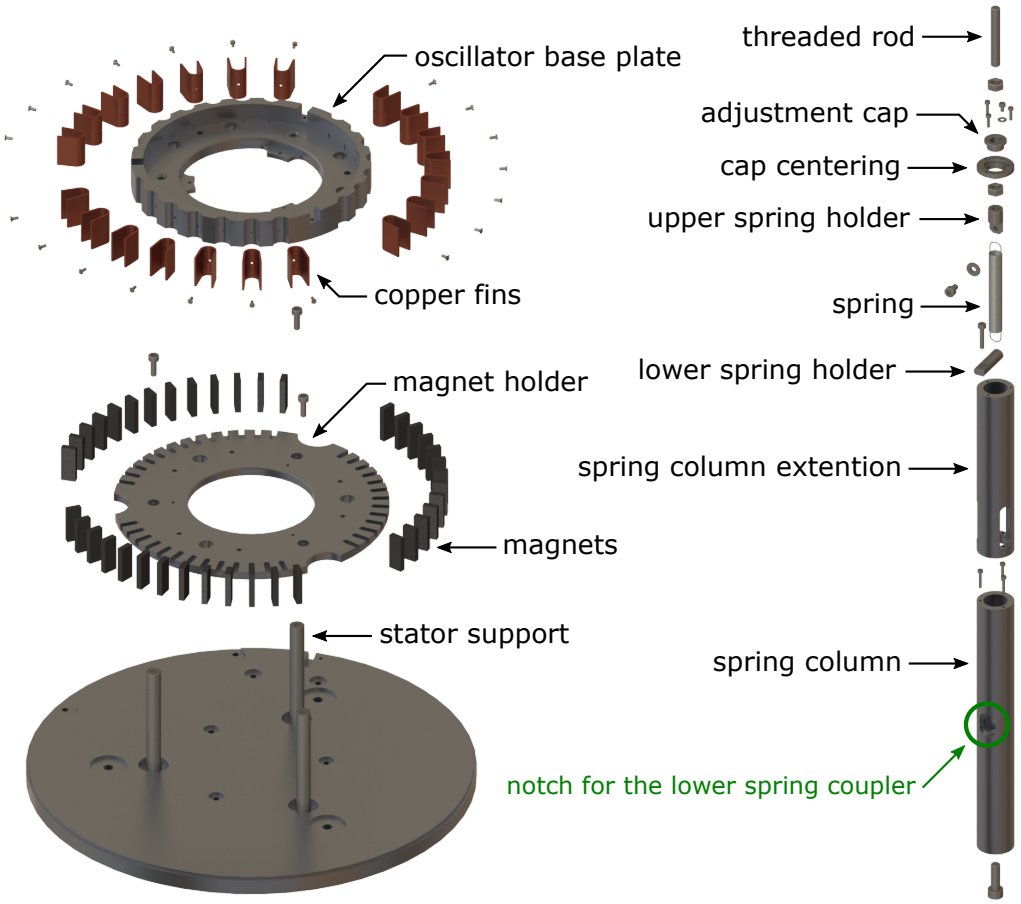

Figure 6.26: Detailed exploded view of the vibration isolation's subassamblies.

6.5 Electrical Design Principle

The operation of the I-STM requires different electronical devices, e.g. a STM-controller, a preamplifier, a power supply etc. All signals and drive voltages provided by these electronics are connected to the internal components of the I-STM following a wiring concept. The electronics and their wiring are constituting the electrical design of the I-STM, divided in an external and internal (everything inside the μ-metal enclosure) part.

6.5.1 External Driver Devices

Scan Control Devices

During scanning of the STM tip, the tunneling current I_{TC} is maintained to a defined value. Accordingly, the tip-sample distance needs to be adjusted continually through a feedback controlled manipulation of the piezo driving signals ($X+$, $X-$ $Y+$ $Y-$ and Z). For the I-STM, the analog *SPM 100* controller with the analog-to-digital converter *V-Scan* is used, constituting the *SPM 1000* control electronics system from *RHK Technology* (Fig. 6.27a).

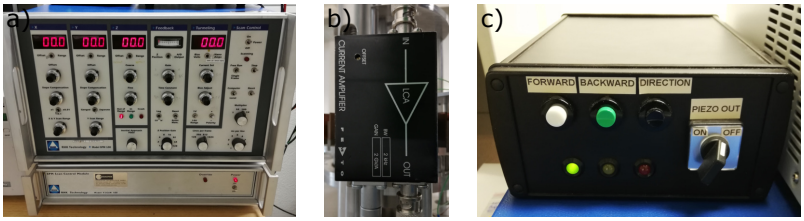

Figure 6.27: (a) *RHK SPM 100* STM control electronics and *RHK V-Scan* analog-to-digital converter (*RHK SPM 1000*). (b) *Femto LCA-2K-2G* transimpedance amplifier. (c) Housing of the *Physik Instrumente E-870.11* drive electronic with its manual control interface.

The *SPM 100* electronics can generate tunneling voltages (U_{TV}) between 0.01 V to 10 V.[171]. Since the *SPM 100* can only process voltage signals, the tunneling current I_{TC} is preliminary transformed and amplified to an equivalent voltage signal (U_{TC}). To simplify further explanations, U_{TC} and I_{TC} will be both termed with tunneling current. The current to voltage transformation is done by the *LCA-2K-2G* transimpedance preamplifier from *Femto* (Fig. 6.27b). The amplifier provides a 2 GV/A gain limited by a maximum output voltage of ±10 V at a bandwidth of 2 kHz.[172]. To maintain the probe-sample distance and for scanning, the *SPM 100* provides piezo drive signals from -130 V to +130 V.[171] The interconnection of the *SPM 100* and the *LCA-2K-2G* is depicted in Fig. 6.28.

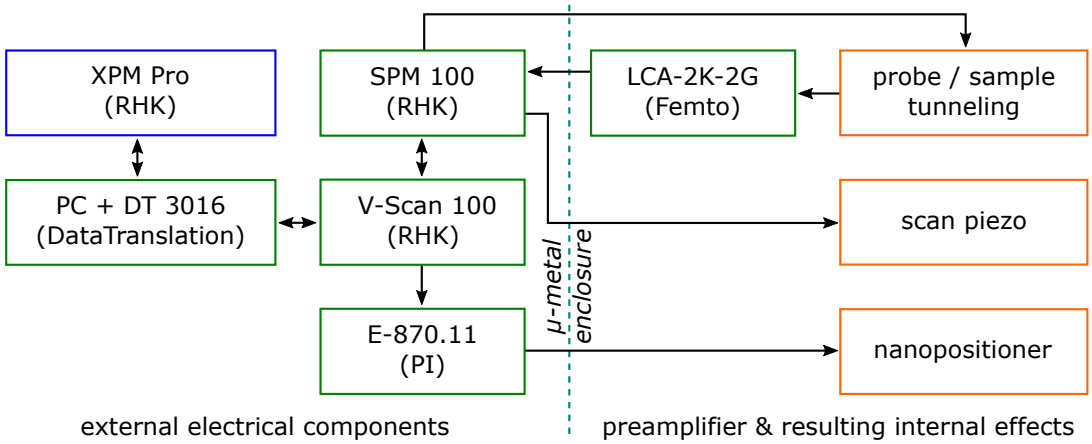

Figure 6.28: Connection scheme of all external electrical devices.

The communication between the analog-to-digital converter *V-Scan* and the *PC* is done by the multifunction data acquisition board *DT3016* from *Data Translation.*[173] Process control and visualization of the acquired data is realized with the *XPM Pro* Software from *RHK Technology.*

For the movement of the integrated nanopositioner a *E-870.11* drive electronic from *Physik Instrumente* generates a saw-tooth voltage signal (continuous or single pulses) with amplitudes between 0 V to 100 V with a maximum repeat frequency of 1 kHz.[150] A manual pre-approach or movement of the nanopositioner is granted via an interface (simple buttons) integrated in the housing of the *E-870.11* (Fig. 6.27c).

The automated tip/sample coarse approach requires the synchronized interaction of the nanopositioner and the tube piezo actuator. During this process, the *E-870.11* is controlled via TTL-pulses (transistor-transistor-logic) generated by the *V-Scan 100*. The pulses result in a defined number of single nanopositioner steps, followed by an extension of the tube piezo actuator through the *SPM 100*.

Temperature Control Devices

The temperature conditioning of the STM is provided by the CTLB. For that task, a 160 W DC-power supply (0 - 65 V; 0 - 2.5 A) introduces the required electrical power to the heating wires of the CTLB (*EA-PS 3065-03 B* from *Elektro Automatik*, Fig. 6.29a).[50]

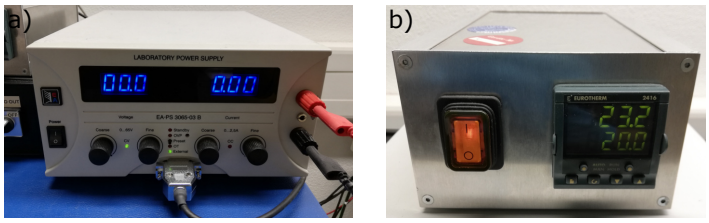

Figure 6.29: (a) *EA-PS 3065-03 B* DC-power supply from *Elektro Automatik*. (b) *2416* process controller from *Eurotherm*.

A *5SRTC* K-type thermocouple from *Omega* integrated in the bottom of the inner container of the CTLB is measuring the temperature. The temperature read out is done by a programmable *2416* process controller from *Eurotherm* (Fig. 6.29b).[174 49] Together with the *EA-PS 3065-03 B* DC-power supply a PID feedback control loop is closed to maintain the temperature of the CTLB or to run predicted temperature programs. These programmes can be edited with the *Eurotherm*'s *itool* software (Fig. 6.30).

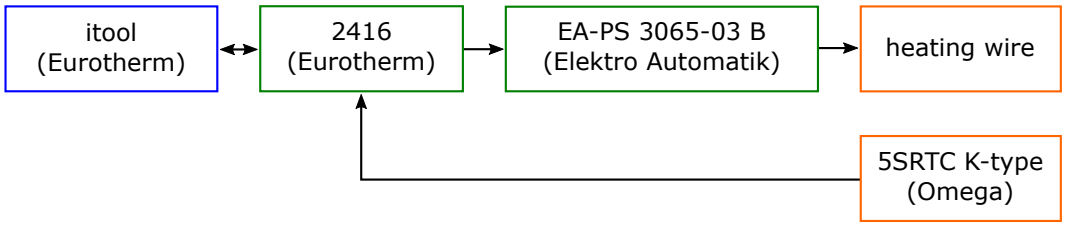

Figure 6.30: Connection scheme of the temperature feedback control.

External Wiring

All wires are connected at an integrated connector panel perfectly matching the μ-metal enclosure (Fig.6.31). Only the power supply for the preamplifier (1) is guided underneath the μ-metal enclosure through a groove.

The tunneling signals U_{TV} and U_{TC} are both routed via low noise coaxial cables with BNC-connectors from the *SPM 100* to the connector panel ((2) = U_{TC}, (3) =

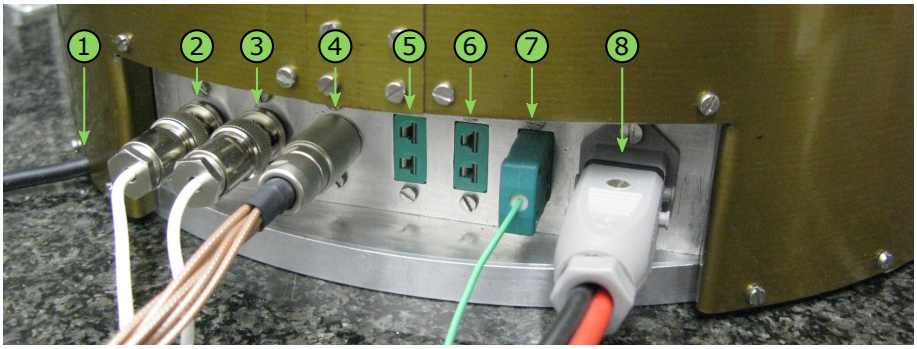

Figure 6.31: *LCA-2K-2G* preamplifier power supply cable (1) and the connector panel accommodating all signal feedthroughs. (2) = tunneling current U_{TC} (BNC), (3) tunneling voltage U_{TV} (BNC), (4) Scan and nanopositioner control voltages (multi-pin connector), (5) and (6) spare thermocouple feedthroughs (K-type), (7) K-type thermocouple connector for the temperature measurement of the CTLB, (8) heating current of the CTLB (2-pole connector).

U_{TV}). Shielded BNC-connectors are used for the connection of the drive voltages $X+$, $X-$, $Y+$, $Y-$ and Z of the tube piezo actuator to the *SPM 100*, as well as for the connection of nanopositioner signals $P+$ and $P-$ to the *E-870.11*. Each of the five drive voltages ($X+$, $X-$, $Y+$, $Y-$ and Z) is individually connected, hence via shielded low noise coaxial cables. For the nanopositioner, the inner wire is used for $P+$ and the coaxial shielding for the ground electrode $P-$. At the connector panel, all seven drive voltages ($X+$, $X-$, $Y+$, $Y-$, Z, $P+$ and $P-$) are jointly connected in one multi-pin connector (4). With an exception for $P+$ and $P-$, all signal wires are routed via a coaxial cable that are shielded by the *SPM 100*'s shielding ground $\perp_S$. For the control of the *E-870.11* an additional BNC cable is connecting the controller to the *SPM 100*.

The thermocouple can be accessed at the connector panel (7). Therefore, a (Ni/Cr) thermocouple cable with K-type connectors at both ends is connecting the signal to the *2416* temperature controller. Two thick copper wires are used for the transportation of the heating current. At the power supply, two banana jacks are used, while at the connector panel a universal 2-pin connector is used (8). The *2416* is controlling the *EA-PS 3065-03 B* via a voltage signal (0 – 10 V), connected with a home-built BNC to D-sub (15-pin) cable.

External Grounding

The grounding of all external components is shown in Fig. 6.32. Since the power supply from the local power grid my result in noise pick up, an uninterruptable power supply (UPS) is used as a filter. The used device is the *Pinnacle Plus 700* from *Alpha Technologies* providing a clean 230 V sine signal at 50 Hz (±0.5 Hz).[175] The *SPM 100*, the *V-Scan 100*, the *PC*, the *2416*-temperature controller and the *EA-PS 3065-03 B* power supply are directly connected to the UPS ground potential.

Both, the connector panel and the *E-870.11* piezo driver are connected to the *SPM 100* ground potential – the shielding ground $\perp_S$. Hence, the I-STM is connected to the *SPM 100*'s shielding ground $\perp_S$ (cf. section 6.5.2).

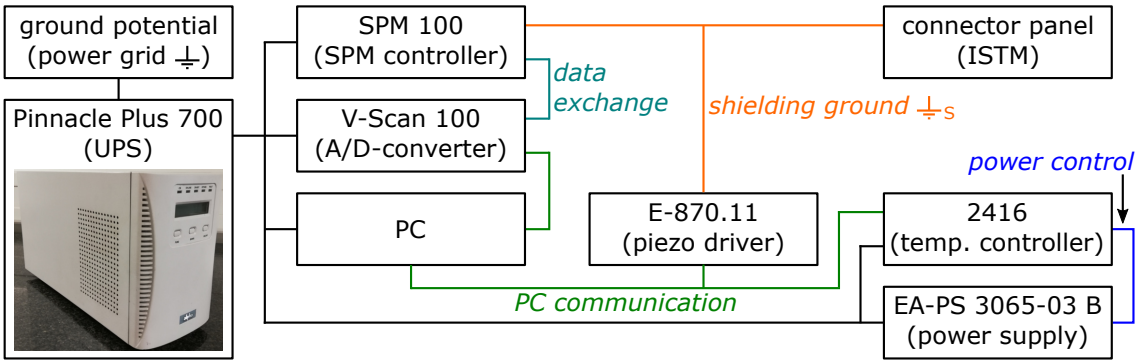

Figure 6.32: Grounding of all external electronics and the I-STM: Black = ground potential of the power grid and the *Pinnacle Plus 700*; green = ground potential connected over the PC communication ports; turquoise = ground between the *SPM 100* and *V-Scan*; blue = ground connection between the *2416*-temperature controller and *EA-PS 3065-03 B* power supply; orange = shielding ground of the *SPM 100*.

Unfortunately, the additional interconnections between the electrical components can create ground loops (coloured connections in Fig. 6.32). But since the connector panel, i.e. the I-STM, is only connected to the shielding ground potential $\perp_S$, the I-STM is unaffected. This is archived through a rigorous separation of all signals and supply voltages from the shielding ground potential $\perp_S$ (insulated connector panel feedthroughs).

6.5.2 Internal Wiring and Shielding

In this section the complete internal wiring of the I-STM inside the μ-metal enclosure is described and illustrated in detail. The wiring is always described from the signals application site (STM or CTLB) to the connector panel, regardless of their direction of action. An overview of the complete internal wiring is provided by Fig. 6.33. Fig. 6.34 illustrates the pin assignment of the main connector (I-STM) and the container lid (CTLB).

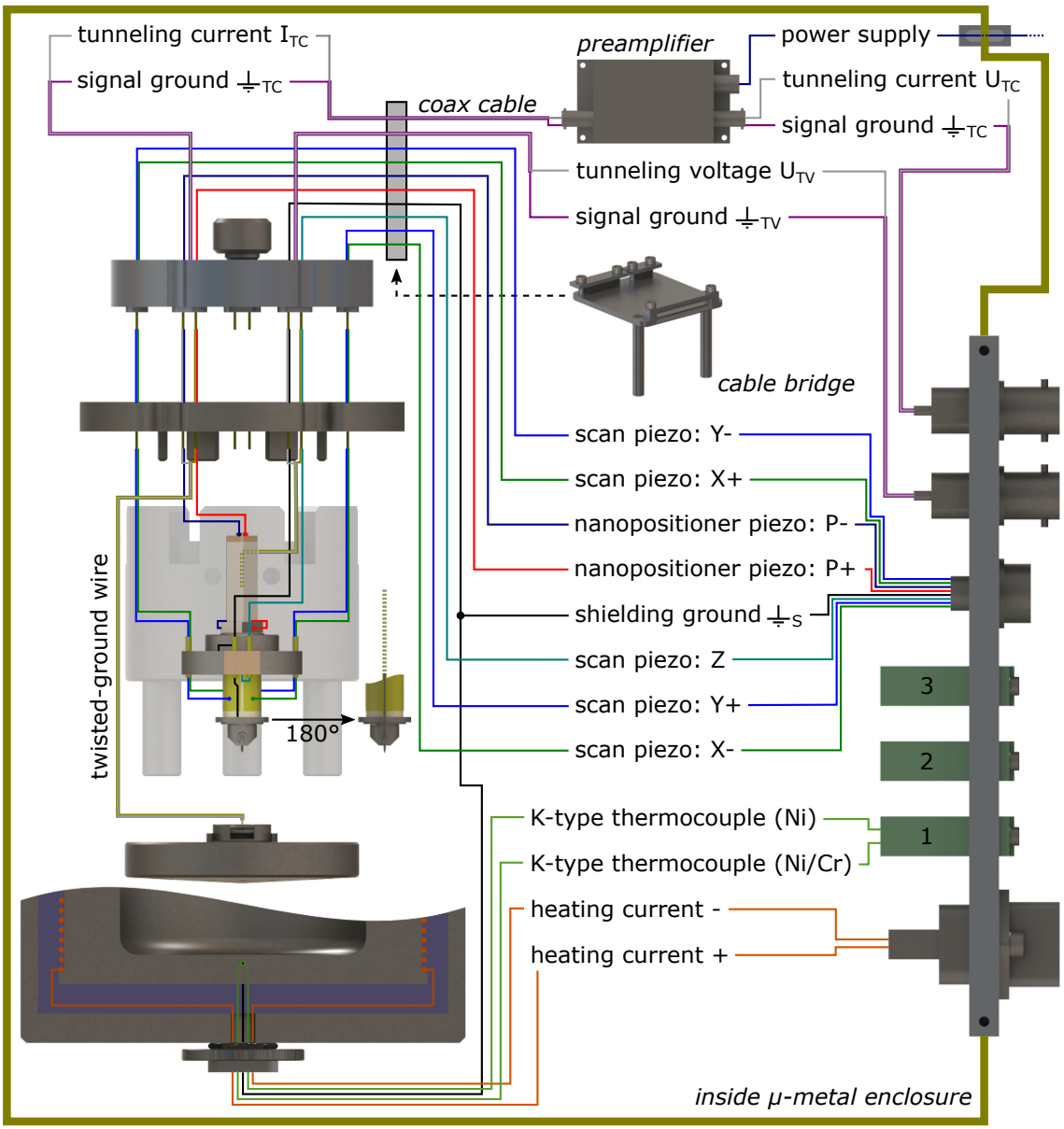

Figure 6.33: Internal wiring of the STM and CTLB.

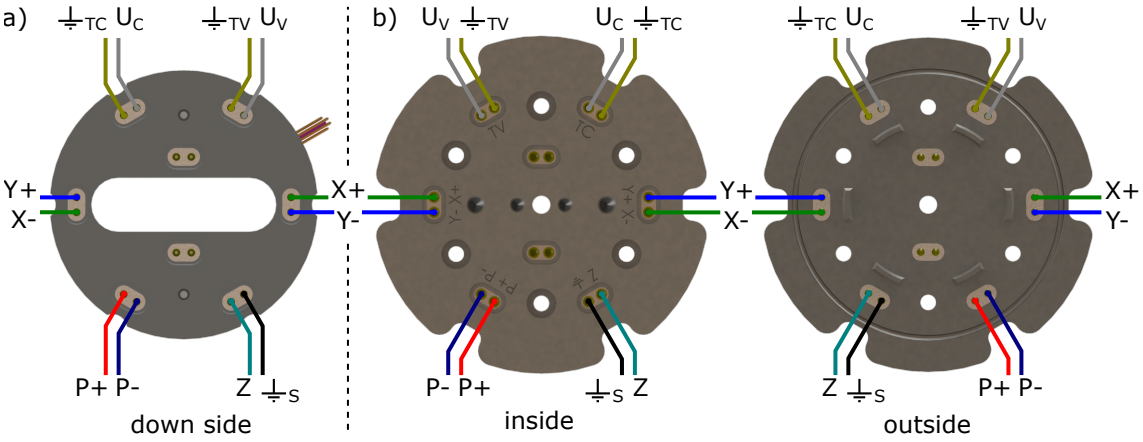

Figure 6.34: Pin assignment (a) of the I-STM main connector and (b) of the CTLB lid viewed from both sides.

Tunneling Voltage

The tunneling voltage U_{TV} is applied to the tip via the electrical contact between the tip holder and its matching counter disc. A solder tail at the counter disc promotes the soldering to a thin 0.2 mm thick PTFE coated stainless steel wire (type 1.4401). For that, both parts are preliminary gold coated. The PTFE coated stainless steel wire is shielded by a tightly wrapped 0.2 mm thick solid gold wire connected to the signal ground $\perp_{TV}$). To avoid ground loops, the wire is connected at one end only.

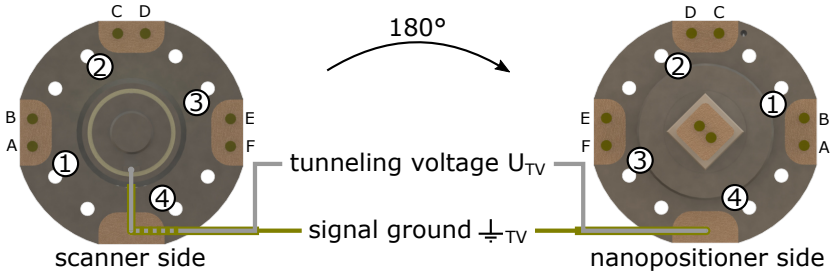

Figure 6.35: Wiring of the tunneling voltage and its shilding from the tip holder socket to the feedthroughs of the scanner platform: tunneling voltage with signal ground wire = feedthrough 4.

Starting from the solder tail, the tunneling voltage cable is running outside of the piezo shielding through a hole in feedthrough no. 4 of the scanner platform. A strain relief is provided by gluing (*KGL 130 EP*) the cable into the feedthrough. At the other side of the tunneling voltage cable, U_{TV} and the signal ground $\perp_{TV}$ are separated, and soldered onto two IC-pins of a *PEEK*-feedthrough from the container lid (Fig. 6.34b). Each gold over brass IC-pin from the container lid was additionally covered with gold solder to establish a solid protection against the corrosive fatty acids.

Both, U_{TV} and $\perp_{TV}$ are picked up by a 2-pole *PEEK*-plug glued into the main connector (Fig. 6.34a). Right after the *PEEK*-plug, both signals are joined into a thin low noise coaxial cable (purple wire in Fig. 6.33). Before, both signals are

always shielded by the grounded container lid and main connector. Outside of the main connector, the coaxial cable is guided safely over the vibration isolation by a cable bridge to its BNC-feedthrough at the connector panel.

Tunneling Current

The tunneling current I_{TC} is connected to the substrate and the preamplifier. The principle to connect the tunneling current cable to the contact disc is different for version 2 and 3 (Fig. 6.14 and 6.16).

In both versions a 0.2 mm thick *PTFE* coated stainless steel wire is used for I_{TC}. Similar to the tunneling voltage, the tunneling current wire is shielded by a tightly wrapped 0.2 mm thick solid gold wire (signal ground $\perp_{TC}$). The stainless steel wire from version 2 (Fig. 6.36) is soldered to the TC-connector nut, while the twisted gold wire stops closely (∼2 mm) before the soldering spot. In version 3 the TC-connector is replaced by a 0.5 mm thick gold coated stainless steel pin to which the tunneling current wire is wired.

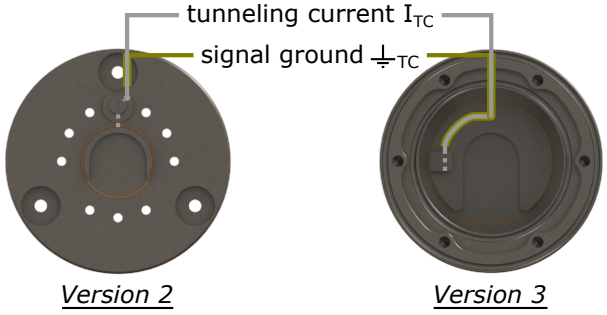

Figure 6.36: Version 2 and 3 sample holder stages with schematically added tunneling current wires.

For both versions, any further wire routing is the same. Analogous to the tunneling voltage, I_{TC} and $\perp_{TC}$ are separately soldered to two feedthrough pins (Fig. 6.34b) after running through the STM body. After the main connector, a thin low noise coaxial cable (purple wire in Fig. 6.33) is transporting the tunneling current to the preamplifier. In order to protect the unamplified tunneling current signal, the wire is kept as short as possible, hence, the preamplifier is located closely to the container lid. For the amplified and transformed tunneling current signal U_{TC} a thin low noise coaxial cable is used to connect the BNC-socket of the preamplifier to the BNC-feedthrough of the connector panel.

Drive Signals of the Scan Piezo

The movement of the tube piezo actuator is controlled by five voltage signals, each applied to the PZT piezo ceramic over a separated gold over cooper electrode: $X+$ and $X-$ for the X-axis, $Y+$ and $Y-$ for the Y-axis and Z for the Z-axis. Each electrode is contacted via a thin 0.2 mm *PTFE* coated stainless steel wire to their corresponding feedthrough pin (Fig. 6.37).

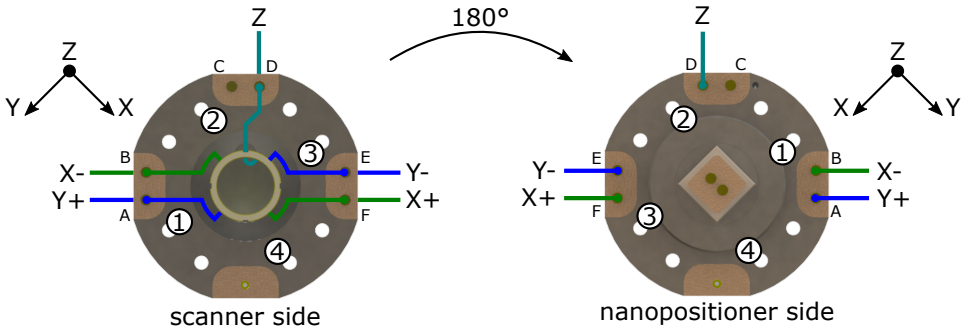

Figure 6.37: Wiring of the tube piezo actuator from its five electrodes to the feedthroughs of the scanner platform: $X+$ = pin F of feedthrough 3, $X-$ = pin B of feedthrough 1, $Y+$ = pin A of feedthrough 1, $Y-$ = pin E of feedthrough 3, Z = pin D of feedthrough 2.

The signals $X+$ and $Y-$ run through feedthrough 3, $X-$ and $Y+$ over feedthrough 1 and Z is sharing feedthrough 2 with the shielding ground $\perp_S$ (Fig. 6.39). For the outer electrodes ($X+$, $Y-$, $X-$ and $Y+$) the stainless steel wires can directly access the electrodes, while the wire for the Z-electrode is routed underneath the tube piezo actuator. Therefore, a small groove is milled into the scanner platform. To prevent any ingress of liquids, this groove is sealed. For all further cable routing the signal pairing from the scanner platform is maintained. After running through the STM body every control signal is soldered to an IC-pin of the container lid. Outgoing from the main connector, all five signal wires are directly guided to the connector panel by means of a cable bridge. In order to reduce the susceptibility to external vibrations by mechanical coupling through the wires, flexible *Kapton*-isolated copper wires (⌀0.2 mm) are used between the main connector and the connector panel.

Drive Signals for the Nanopositioner

Two signals ($P+$ and $P-$) are required for driving the piezo of the nanopositioner. Inside the inner container these signals are connected by a 0.2 mm thick *PTFE*-isolated stainless steel wire. Starting from the two silver electrodes of the piezo, each wire is guided through the hollow axis of the nanopositioner (Fig. 6.38).

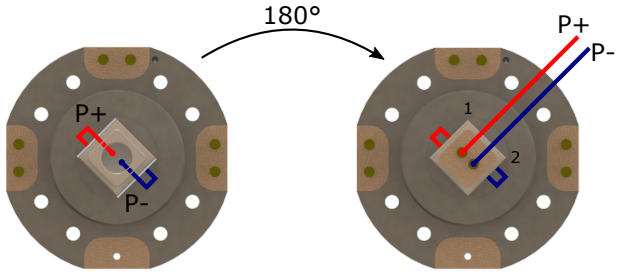

Figure 6.38: Wire routing of the drive signals $P+$ and $P-$ through the hollow axis of the nanopositioner to the electrical feedthrough.

The grooves where the wires enter the axis are already sealed with *H74*, by

joining the piezo and the axis. Inside the axis, the two wires are connecting the electrodes to the *PEEK*-feedthrough (two gold coated 1.4301 stainless steel pins) that terminates the axis at the opposite end. At the outside, two 0.2 mm stainless steel wires are soldered to the pins of the *PEEK*-feedthrough. The wires are guided through the STM body to their feedthroughs at the container lid. From there, on the wiring is similar to the five tube piezo drive signals.

Shielding Ground

To avoid cross talk between the drive signals of the tube piezo actuator with the tunneling signals U_{TV} and I_{TC}, the enclosure of the tube piezo actuator (piezo shielding, cf. Fig. 6.10c) is separating the signals from each other. One part of this shielding is the scanner platform, which consequently has to be connected to ground potential - the shielding ground $\perp_S$. This is realized by a short 0.5mm thick gold coated stainless steel wire, soldered into a small bore next to the bottom side of feedthrough 2 (Fig. 6.39).

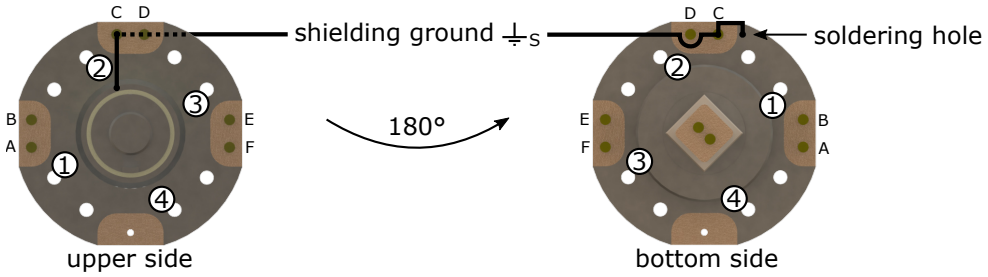

Figure 6.39: (a) Scheme to connect the shielding platform of the tip exchange system and the scanner platform with ground potential: shielding ground = pin C of feedthrough 2.

The wire is soldered to the scanner platform (partial gold coating around the soldering bore) and pin C of feedthrough 2. The four piezo shields surrounding the tube piezo actuator are screwed to the scanner platform, hence, these four parts are directly connected to $\perp_S$. The shielding platform of the tip exchange system is already connected to the ground potential of the scanner platform via its thermal grounding (three twisted 0.2 mm thick PTFE coated stainless steel wires). However, the wires are not directly connected to the scanner platform, but through the upper side of pin C. All further wiring is identical with wiring of the piezo drive signals.

Heating Current and Thermocouple Wiring

The heating power is applied via a heating wire tightly wrapped around the inner container. From there, both ends of the heating wire are guided through the aerogel heat isolation that is filling the interspace between the inner- and outer container. The heating current is connected to the outside through to a 4-pin *PEEK*-feedthrough at the bottom of the outer container (Fig.6.40).

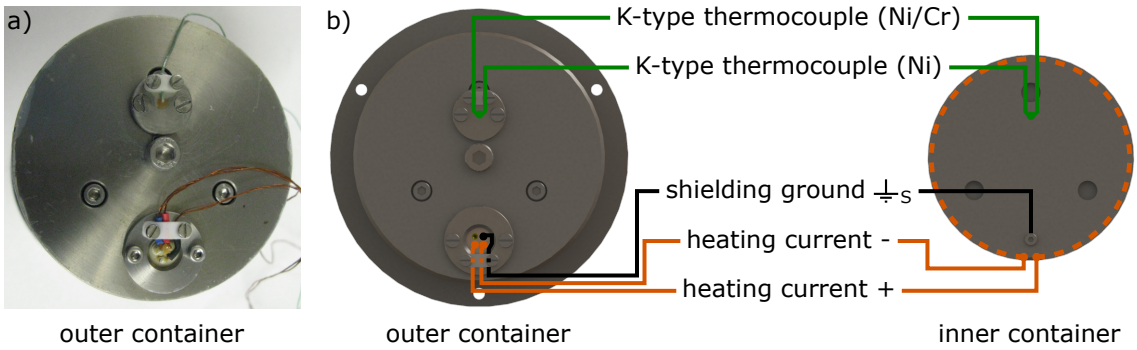

Figure 6.40: (a) Bottom side of the CTLB with its separable electrical *PEEK*-feedthroughs. (b) Wiring scheme.

To prevent mechanical coupling, a flexible meshwork of 0.2 mm thick *Kapton*-isolated copper wires is used. This meshwork is connecting the heating current of the CTLB to the connector panel. For efficient shielding, the outer container is connected to the shielding ground $\perp\!\!\!\!\!\!=_S$. A bare 0.5 mm thick copper wire is clamped between the inner container and a screw. The other end of the wire is soldered to an IC-pin of the 4-pin *PEEK*-feedthrough. Similar, to the heating current, a flexible meshwork of 0.2 mm thick *Kapton*-isolated copper wires is used to establish the connection between the shielding ground ($\perp\!\!\!\!\!\!=_S$) and the connector panel.

The temperature of the inner container is measured with the *5SRTC* K-type thermocouple from *Omega*, placed inside a ⌀1 mm bore at the bottom of the container. For electrical insulation between the heating wire and inner container an insulating paint is used (the *74117* heat-resisting spray paint from *NIGRIN*). To guarantee a proper contact between the thermocouple and the bottom of the hole, the thermocouple cable is glued into a *PEEK*-feedthrough, with the cable length longer than the bore. Hence, by screwing the feedthrough into the outer container the thermocouple is pushed against the inner container. To minimize mechanical coupling the used thermocouple wire is only 0.5 mm thick (AWG 24).

Internal Grounding

For the efficient shielding of the tunneling signals U_{TV}, U_{TC} respectively I_{TC}, a five layered shielding concept is implemented in the design of the I-STM, as illustrated in Fig. 6.41.

The ground potential $\perp\!\!\!\!\!\!=_S$ of the *SPM 100* is directly connected to the connector panel. From there, the ground potential is further distributed to the μ-metal enclosure and the entire vibration isolation assembly. Beside its screening against acoustic noises, the μ-metal enclosure also represents the first shielding layer against external electromagnetic noise. The outer container is connected to the ground potential through its firm attachment to the vibration isolation and is the second shielding layer. The inner container and the inner STM have a direct connection to the shielding ground $\perp\!\!\!\!\!\!=_S$ (cf. Fig. 6.33). The sealed inner container (with its lid) represent the third shielding layer by enclosing the entire STM. The outer STM as well as the

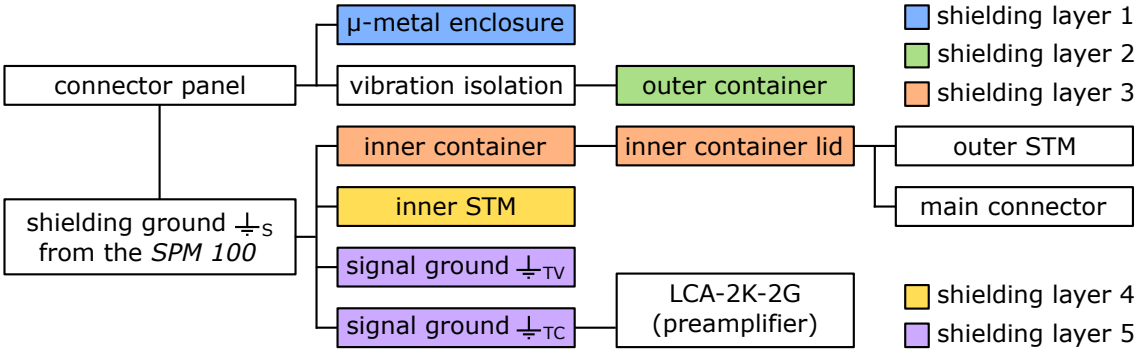

Figure 6.41: Connection of all assemblies to the ground potential of the *SPM 100*-controller, i.e. shielding ground. Assemblies who represents the shielding layers 1 to 5 are highlighted by colour.

main connector have direct contact to the lid, hence, are connected to the ground potential. The final shielding layer 5 are the signal grounds $\frac{1}{\pm}_{TV}$ and $\frac{1}{\pm}_{TV}$ protecting the tunneling signal wires. To avoid ground loops, the BNC-feedthroughs of the tunneling signal wires are insulated from the connector panel.

6.6 Support Devices

The mechanical core and electrical support assemblies constitute the complete setup of the I-STM (Fig. 6.7). Apart from those, several additional support devices are crucial to provide the operability of the I-STM, regarding the experimental pre- and post-preparation, maintenance as well as the assembly / disassembly of the STM.

6.6.1 Manipulator

Critical steps in the preparation and termination of experiments is the immersion and retraction of the STM. The space between the STM and the inner container is very narrow (∼1 mm) bearing the risk of a crash. To avoid damages, the STM is guided by means of a manipulator for vertical movements to guarantee the save immersion and retraction (Fig. 6.42).

The manipulator is a tripod with a vertical linear guidance system at its centre. Each tripod leg has a machined out bolt at its lower end, fitting into one of three bores that were drilled into the base plate of the vibration isolation. By placing the manipulator legs into the bores, the STM is centered to the inner container. To connect the STM with the manipulator a customized mechanical connector is attached to the carriage of the linear guidance system (Fig. 6.42c). Two knurled-head screws (brass) inside the mechanical connector are pushing the lid against the base body of the connector, while the STM is firmly screwed to the lid. In this configuration, the lid with attached STM can be moved vertically. There is an end stop for insertion and the base plate of the manipulator limiting the maximum travel. The vertical manipulation is manually operated. Therefore, an aluminium rod with

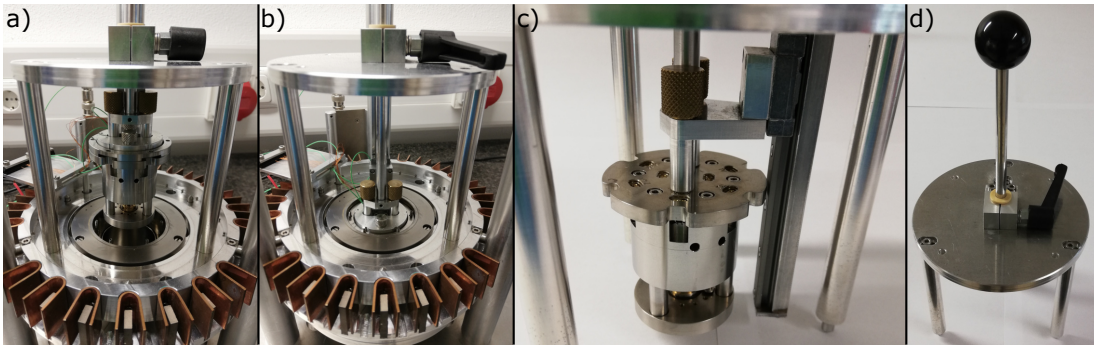

Figure 6.42: Vertical manipulator with mounted STM standing on the vibration isolation, centred above the CTLB (a) in the retracted state and (b) in the inserted state. (c) Side view of the linear guidance system with mounted STM. (d) Top view of the manipulator.

a ball handle at its upper end (Fig. 6.42d) is attached to the connector. A clamping lever on top provides the arrestment of the vertical manipulator. The precise linear guidance system is protecting the STM from any mechanical damage during insertion or retraction. Furthermore, the manipulator provides the save transportation of the STM during cleaning or maintenance.

6.6.2 Camera System

Since the I-STM operates in a sealed container without any optical accesses, a fully automated coarse approach is mandatory. Depending on the initial tip-sample distance, the approach process can be rather time consuming. In order to save time, it is highly recommended to place the probe in close proximity to the sample surface before the approach is started. This in turn bears the risk of a tip crash. To minimize this threat and to provide better control, the manual pre-approach can be monitored by a magnifying camera system (Fig. 6.43).

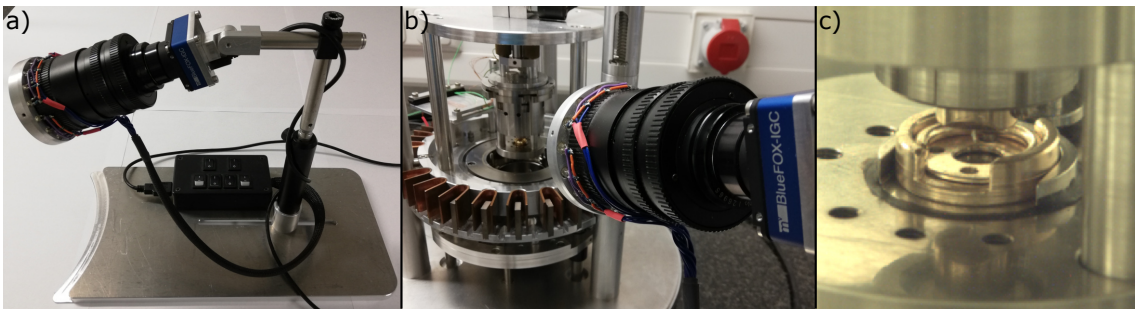

Figure 6.43: (a) Digital *mvBlueFox-IGC 200w* industrial camera with magnifying lens system mounted on its support stative. A LED ring is attached to the lens system with its control box aside. (b) Camera system focused on the sample. (c) Image acquired with the *mvBlueFox-IGC 200w*.

The used camera is the digital industrial camera *mvBlueFox-IGC 200wc* from *Matrix Vision* with a resolution of 752 x 480 pixels.[176] The camera is equipped

with a magnifying lens system (manufacturer unknown; focal length 8.5 – 51 mm; 6x zoom). A stative allows the adjustment of the camera to optimize the view on the sample (∼30°). This is done while the STM is mounted in the manipulator at the highest vertical position. Since the camera assembly easy picks up vibrations it should never be in contact with the I-STM during a measurement. However, to keep the focus settings of the camera, the distance between the camera and sample surface must always be the same. Therefore, a base plate was designed for the camera stative that matches with the circular base plate of the vibration isolation (Fig. 6.43a). After the manual pre-approach the camera system can be removed in order to protect the I-STM from vibrations. Furthermore, due to the centering of the sample to the vibration isolation base plate, the camera system can be used from all sides (360°) without changing the focus. This can be very helpful to find the optimal viewing spot.

For a proper illumination of the sample, an aluminium ring with 16 LEDs is mounted onto the front-end of the lens system. The 16 LEDs are separated into 90°-segments (4 LEDs). Each segment can be individually controlled to find the optimal lighting of the sample. The brightness can be adjusted by activating either all or every second LED.

6.6.3 Cleaning Device

Immersing the STM into solution inevitably results in solvent residues on the entire instrument. Yet, complete removal of all solution residues is crucial before starting new experiments with altered conditions such as concentration, solvent, or solutes. Cleaning the complex geometry of the STM by wiping is virtually impossible. Therefore, development of a dedicated cleaning device and protocol (cf. section 6.8) was necessary.

An effective way of removing remaining residues is flushing of the whole STM with a cleaning agent. In this case 100% ethanol, as isopropanol caused MΩ short circuits at the sample holder stage. Straightforward immersion of the STM into a beaker filled with 100% ethanol is already removing the majority of the residues, but it has shown that still some residues remain. This is particularly true for the unavoidable cavity between the piezo shielding and the scanner. A significant improved cleaning result can be achieved through the continuous flow of a cleaning agent throughout the STM assembly and its cavities by the aid of a cleaning device (Fig. 6.44).

In the proposed design, a peristaltic pump - the *CP83* in the 24 V configuration from *Gemke Technik* - is creating a flow of cleaning agent between ∼60 mL/min (at 30 rpm) and ∼310 mL/min (at 145 rpm) with adjustable flow rate.[177] The cleaning agent is stored in a 250 mL glass bottle reservoir and flows in a closed loop through flexible and chemical inert *Santoprene*-tubes.[178] Starting from the reservoir, the cleaning agent is pumped into a 3-ways splitter. Each of the two tube is again connected to a 4 way splitter to finally distribute the cleaning agent onto six *Santoprene*-tubes. The six tubes are individually connected to one of the six inlets

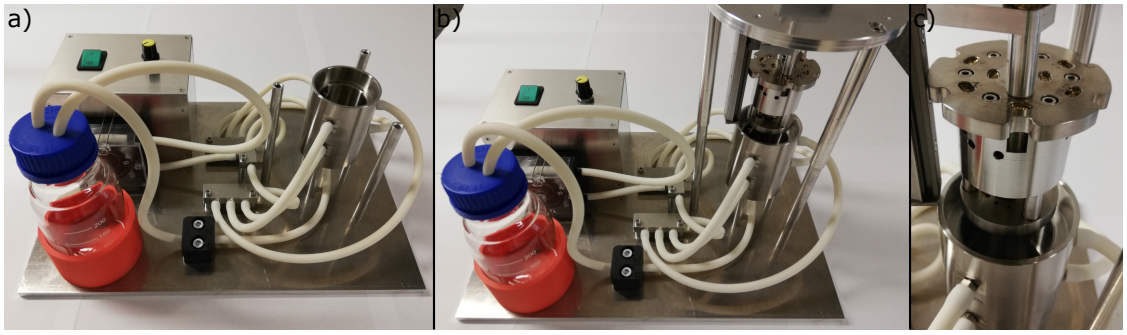

Figure 6.44: (a) Complete assembly of the cleaning device with its cleaning agent reservoir, peristaltic pump and the cleaning basin, all connected through flexible *Santoprene* tubes. (b) Cleaning device with attached tripod manipulator holding the STM over the cleaning basin. (c) Close up.

integrated in stainless steel cleaning basin. The basin features a similar geometry as the inner container of the CTLB and can be sealed during cleaning. Efficient flushing of the STM from all sides is realized through the arrangement of the inlets. A drain at the bottom of the basin leads the cleaning agent over a *Santoprene*-tube back into the reservoir.

For save immersion of the STM into the cleaning basin, three columns with centric drilled bores at their upper ends are arranged around the basin for the docking of the vertical STM manipulator (Fig. 6.44b and c).

6.6.4 Docking Station

The docking station is a very useful tool during the assembly process of the STM and for maintenance by simplifying the access to all electrical in- and outputs. The setup consists of two parts: The docking port and the patch field (Fig. 6.45).

Figure 6.45: (a) Docking station consisting of the docking port and the patch field. (b) STM connected to the docking port.

The docking port represents a counterpart for the container lid with the same pin arrangement as in the main connector. By plugging the STM onto the docking port, all in- and output signals can be accessed over a connected patch field. Especially in the assembly process, when it comes to the adjustment of the retention force (∼5 N) of the nanopositioner, the docking station is a very helpful device.

6.6.5 Assembly Rail

The final step in the STM assembly is the joining of the container lid, the outer and the inner STM. This includes the electrical wiring of all parts. Since all wires have to fit into the limited space of the STM body, the wires are kept reasonable short, not at the least to avoid cluttering or jamming. Hence, the interspace is very narrow, and soldering is only possible if all parts are well arranged with respect to each other, as provided by the assembly rail illustrated in Fig. 6.46.

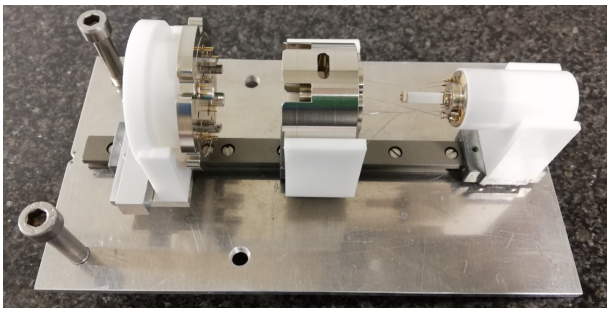

Figure 6.46: Assembly rail with the fixated and mutually centered container lid, STM body (version 3) and inner STM.

The assembly rail provides customized supports for the container lid, the STM body and the inner STM that also facilitate their rotation around the main axis. Every support is placed on a carriage running on a linear guidance rail. The ability to adjust the distance and the angle of every part / subassembly simplifies the assembly process and reduces the risk of damages, which a likely to occur during the fusion of the STM body with the inner STM.

6.7 Experimental Procedures

The procedures to perform a new experiment starts with the preparation and verification (e.g. UV-Vis spectroscopy) of the solution, followed by the filling of the inner container up to the intended level. For that, the STM is connected to the vertical manipulator and placed above the container. Note that the main connector must be plugged into the lid preliminary. In order to establish hermetical sealing of the STM, an O-ring gasket is placed in the groove on top of the inner container. With the aid of a tweezer, first the tip holder and then the sample holder are introduced into the STM. For the preparation of the tip, a platinum-iridium wire is clamped into a tip holder via a M2 set screw (Fig. 6.11). By grapping the wire with a blunt wire cutter right next to the tip holder (in a very steep angle), followed by a combination of cutting and tearing, a sharp tip can be created. The preparation of the substrate depends on its kind, e.g. for HOPG, cleaving via an adhesive tape is the most common method. After the substrate is prepared, it is locked inside the circular sample holder socked (Fig. 6.17). After introducing the tip and sample holder into the STM, a pre-approach is performed still outside of the inner container

with the aid of a camera (cf. section 6.6.2) until the tip is in close proximity to the sample surface. Now the STM can be immersed into the filled inner container by means of the vertical manipulator. Finally the STM can be sealed, i.e. the container is closed by a hold-down ring and six nuts. Even when the STM is still in the manipulator outside of the container, the noise level is sufficient for checking the imaging quality of the tip and stability of the STM. After the vibration isolation is de-arrested and the μ-metal enclosure installed, the desired operation temperature is selected at the *2416* temperature control unit. During heating, it is advisable to hold the tip, i.e. the scan unit, retracted until the setpoint temperature is stabilized. With the reach of the setpoint temperature the automatic coarse approach is used to establish tunneling contact and scanning can be started.

6.8 Cleaning Protocol

After finishing an experiment the STM is completely covered with residuals of the used solution. Before the STM can be retracted from the inner container it is important that the nanopositioner is retracted completely. Next, the main connector can be detached and the six nuts removed with their downholder ring. Finally, the STM can be retracted from the inner container and the sample and tip holder removed with the aid of a tweezer.

For an efficient removal of all solution residuals, the cleaning protocol of the STM comprises a preliminary cleaning through a quick wiping of its accessible exterior parts with a low-lint paper tissue. This is followed up by its immersion into a glass beaker filled with 100 % ethanol, and sonication for $\sim$15 min. After this treatment the STM is continuously flushed for $\sim$30 min under the aid of the cleaning device (section 6.6.3). Finally, to remove possible remaining residues and to dry the STM, it is placed into a preheated oven at 100 $^{\circ}C$ for at least $\sim$1 h. For all cleaning steps the STM is mounted in the vertical manipulator for controlled immersion and save transportation through the lab.

Apart from the STM, also the inner container of the CTLB is completely covered with solution and a large residue at its bottom. The simple geometry of the inner container makes cleaning easier. At first, the solution is pumped out of the inner container with a disposable syringe and wiped out with an ethanol soaked low-lint paper tissue. In the next step the complete assembly is removed from the vibration isolation. The inner container is filled with 100% ethanol and sonicated for $\sim$15 min. After further wiping with ethanol soaked paper tissues the whole assembly is heated at 100 $^{\circ}C$ for at least $\sim$1 h. The disassembled tip and sample holder are cleaned in the same way. After all components have been cleaned and dried, the CTLB will be mounted back to the vibration isolation. Before the main connector can be attached, the STM must be inserted into the inner container. Now the manipulator can be detached and the downholder ring placed onto the container lid. Finally, the main connector can be attached to re-establish the electrical connections and the I-STM is ready for a new experiment.

6.9 Characterization of the I-STM

6.9.1 Temperature Control

In order to evaluate the temperature stability of the CTLB, the thermocouple reading was recorded over time for different setpoint temperatures between room-temperature and 100 $°C$. The corresponding standard deviations for different operation temperatures range from ± 0.011 $°C$ to ± 0.025 $°C$. As shown in Fig. 6.47, a pronounced maximum occurs around ~ 75 $°C$.

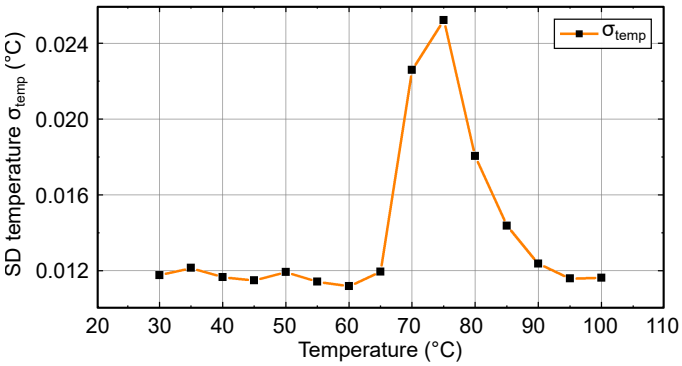

Figure 6.47: Standard deviation of the inner container temperature vs. setpoint temperature. For each measurement, the temperature was recorded for 1 h with a sampling time of 1 s. Measurements were started 2 h after the respective setpoint temperature was reached.

This peculiar behaviour is related to the characteristics of the digital power supply, as it switches between output transformation circuits when the power exceeds ~ 14.3 W (rising output) or falls below ~ 11.6 W (falling output). For the heatable inner container, this happens between 65 $°C$ and 90 $°C$. If necessary this less stable temperature range could be shifted by a series resistor or a single circuit power supply that covers the complete power range. Applying the highest tolerable electrical power of ~ 30 W (0.81 A, 36.1 V) in terms of heating wire rating results in a heating rate of ~ 1.4 $°C\ min^{-1}$, allowing to reach a temperature of 100 $°C$ within ~ 54 min. Maintaining a temperature of 100 $°C$ requires ~ 14 W heating power (0.55 A, 25.5 V), while the outer container reaches a surface temperature of ~ 53 $°C$.

6.9.2 Drift and Long-Term STM Experiments

An important figure of merit for ambient STMs is not only absolute value of the steady state drift velocity of lateral drift, but also how fast it can be reached. Therefore, the temporal evolution of drift velocity was quantified in long-term STM experiments for ~ 6 h after a specific setpoint temperature had been reached. These measurements were carried out for different operation temperatures ranging from room-temperature up to 100 $°C$, and the results are summarized in Fig. 6.48.

Therefore, the positions of unique features were determined in subsequently acquired 150 x 150 nm^2 STM images (with similar slow scan directions) by means of

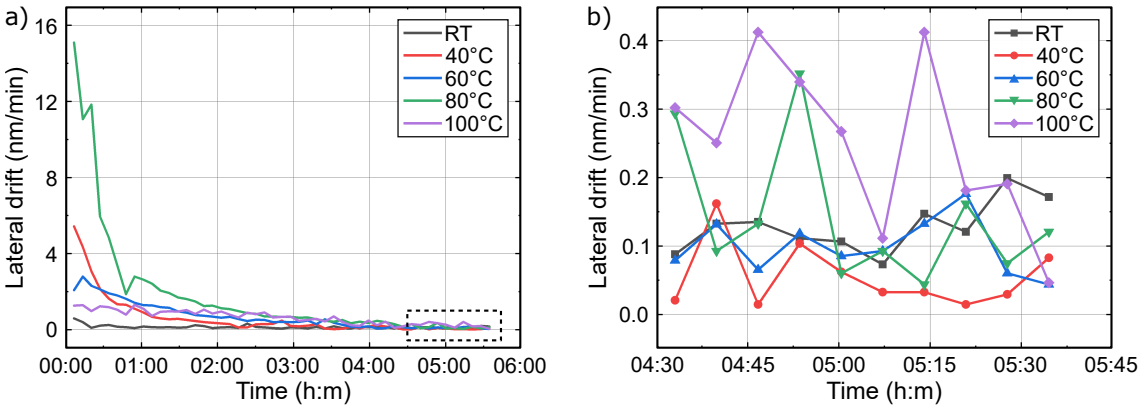

Figure 6.48: (a) Time evolution of lateral drift velocity for different operation temperatures (see the text for details), (b) Enlarged view of the last ∼hour as marked in (a), i.e., when drift reached its steady state value.

a cross-correlation. The average drift velocity was obtained simple by dividing the offset by the elapsed time. STM measurements were started ∼10 min after the setpoint temperature was reached (except for the room-temperature measurements), and data were taken every ∼7 min. Consequently, initial drift velocity values may also include piezo creep. For all operation temperatures, the lateral drift substantially decayed in the first 1-2 h, and settles after about ∼4 h to values between 0.06 nm min^{-1} and 0.25 nm min^{-1}. As evident from Table 6.3, average drift velocities increase with operational temperatures.

Table 6.3: Lateral drift velocities at different temperatures; uncertainties were determined as standard deviations of all values obtaines after 04:30 h.

Temperature (°C)	**Lateral drift (nm/min)**
Room temperature (no feedback)	(0.13 ± 0.04)
40	(0.06 ± 0.05)
60	(0.10 ± 0.04)
80	(0.14 ± 0.10)
100	(0.25 ± 0.12)

The notably larger decay time observed for a setpoint temperature of 80 $°C$ (cf. green curve in Fig. 6.48) is possibly related to the aforementioned switching behaviour of the output of the used digital power supply. However, it seems not to have any influences on the steady state value. The oscillating behaviour observed after ∼4 h gives rise to the high uncertainties in Table 6.3, but its origin remains unclear at the moment.

6.9.3 Calibration and Scan Range

The piezoelectric coefficient – the proportionality factor between applied electrical field and piezo deformation – increases with increasing temperature.[179] Therefore,

both the scan range and the STM calibration are temperature-dependent, with notable effects in the temperature range between room-temperature and 100 $°C$.[27] Accordingly, for a precise determination of lattice parameters and distances from the images, a temperature dependent calibration of the STM is required. Therefore, atomically resolved images of graphite ($10 \times 10\ nm^2$) were acquired for a range of operation temperatures after an equilibration time of ∼6 h, i.e. when drift was settled. Short image acquisition times of ∼25 s aid in reducing the influence of the remaining lateral drift below ∼1 % (at 100 $°C$) of the image size. The results are summarized in Fig. 6.49, indicating a ∼14 % increase of the proportional factor between room-temperature and 100 $°C$ with a mostly linear behaviour between 40 $°C$ and 80 $°C$. Note, that remarkably differences in the piezo coefficients for the X- and Y-direction were deduced, yet with similar temperature dependence. The origin of this asymmetry presumably is a non-uniform polarization of the piezo tube. In any case, the low drift during calibration provides us with confidence to apply these different calibration factors for the X- and Y-direction.

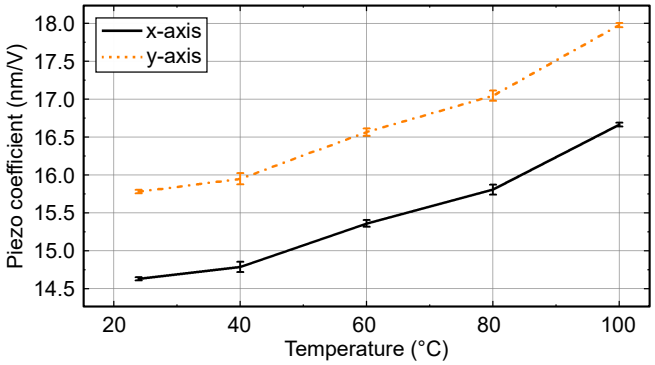

Figure 6.49: Piezo coefficients for the X- and Y-direction vs. operation temperature.

6.9.4 Imaging Properties

The imaging capabilities of the I-STM are demonstrated at operation temperatures between room-temperature and 100 $°C$ by means of self-assembled monolayers of 2,6-napthalendicarboxylic acid (NDA) at the nonanoic acid-graphite interface and pristine graphite, respectively. Selections of acquired images are presented in Fig. 6.50.

Both the clearly resolved submolecular features in NDA and the atomic resolution of graphite demonstrate the high resolution capabilities of the I-STM at elevated temperatures. Moreover, the evolution of supramolecular assemblies can now be monitored over arbitrary long periods of time, opening up possibilities to reveal processes with ultraslow kinetics. For instance, the image of NDA domains in Fig. 6.50b was acquired at 60 $°C$. The suitability of the I-STM for long-term experiments is exemplified by Fig. 6.50(d) showing an image of a NDA monolayer acquired ∼18 h after the solution was heated to 70 $°C$. The sample was already dwelling in

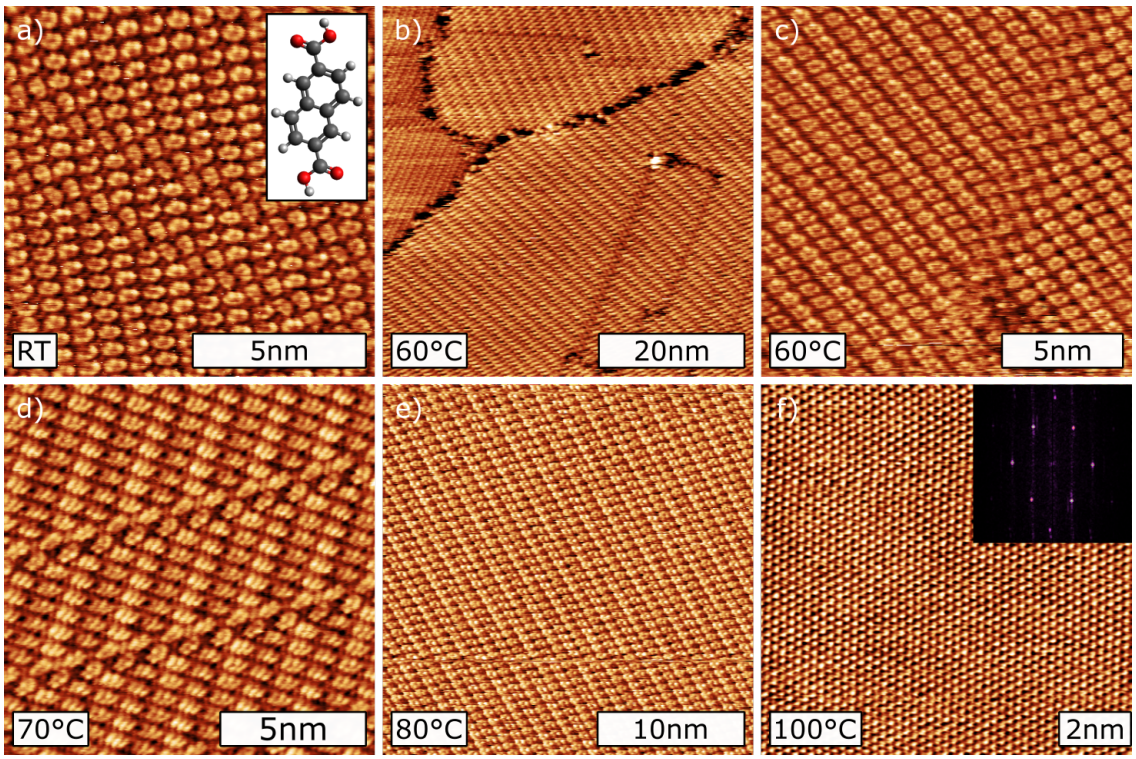

Figure 6.50: STM images of (a)–(e) 2,6-naphthalene dicarboxylic acid (NDA) monolayers at the nonanoic acid-graphite interface (saturated solution) and (f) atomically resolved image of graphite (inset: corresponding 2D FFT) recorded in a dry state, i.e., without solution in the container; all images were acquired after settling of the thermal drift at the temperatures indicated in the lower left corner. Tunneling parameters: (a) 0.23 V, 59.9 pA, (b) 0.52 V, 50.2 pA, (c) 0.27 V, 58.2 pA, (d) 0.27 V, 49.6 pA, (e) 0.16 V, 50.2 pA, and (f) 4.39 mV, 59.4 pA.

solution at temperatures between 30 $°C$ and 70 $°C$ for ∼10 days (stepwise ramping of temperature) in the sealed container. In addition, the low drift facilitate precise measurements of lattice parameters. For instance, by applying the temperature-dependent calibration factors, the atomically resolved graphite image (acquired at 100 $°C$) shown in Fig. 6.50(f) results in lattice parameters of a = (0.241 ± 0.004) nm, b = (0.241 ± 0.004) nm, and $\gamma = 120°$ (cf. chapter 4). Even through precise geometric measurements in the images require thermal equilibrium and settling of the thermal drift, the proposed I-STM even allows image acquisition during heating with low rates. In this respect, the same sample area could be tracked over 1:15 h while heating with a rate of 4 $°C\ h^{-1}$. However, larger lateral drifts are unavoidable, but can be actively compensated using tracking features of the control software.

6.10 Summary and Conclusion

In summary, we have demonstrated a new instrumental approach to long-term STM experiments at liquid-solid interfaces with variable temperatures between room-temperature and 100 $°C$. Solvent evaporation - the main reason for limitations of the experimental duration - is completely eliminated by working in a hermetically sealed heatable container. Thereby extended waiting times for complete thermal equilibration and settling of thermal drift can be afforded, resulting in the possibility to obtain low-drift high-resolution images at elevated temperatures. Further ingredients to fast settling times and low steady state values of lateral drift are temperature constancy as achieved with a temperature controller and optimized heat transport across the instrument as implemented by design and choice of materials. All solvent exposed parts are inherently inert (stainless steel) or protected by a fluoroelastomer-based sealing paste, facilitating experiments even in more corrosive solutions, such as the in self-assembly of ubiquitous fatty acids. The main field of application of the I-STM lies in supramolecular self-assembly, where temperature is a crucially important parameter that affects both kinetics and thermodynamics. Even though irreversible temperature-induced changes could already be studied with conventional instrumentation by heating and subsequently characterizing the sample after cooling down again to room-temperature, the proposed I-STM allows the direct and effective determination of transition temperatures with high precision. Moreover, the dynamics and hysteresis of reversible changes in self-assembled monolayers can now be studied in unprecedented detail as arbitrary long experiments enable quasi-static temperature changes. The proposed setup is not limited to liquid environments and might similarly be used for temperature-dependent studies in defined gas atmospheres or for experiments that require the absence of oxygen. Therefore, the container lid features additional inlets that could be used for vacuum pumping or as a gas inlet. Finally, the I-STM could also act as a platform for further SPM developments. In this respect, integration of a tuning-fork sensor could introduce non-contact AFM capabilities. Therefore, the extraordinary low lateral drift achieved upon thermal equilibration is beneficial in terms of the longer acquisition times for non-contact AFM images. Alternatively, the proposed setup could similarly be extended to operate as a temperature-controlled electrochemical STM by further developing the sample holder stage into an electrochemical cell.

Chapter 7

Solvent-Induced Polymorphism

This chapter is reprinted and partially adapted with permission from O. Ochs, M. Hocke, S. Spitzer, W. M. Heckl, N. Martsinovich, and M. Lackinger. Origin of Solvent-Induced Polymorphism in Self-Assembly of Trimesic Acid Monolayers at Solid–Liquid Interfaces. *Chem. Mater.* 2020, 32, 12, 5057-5065. Copyright (2020) American Chemical Society.

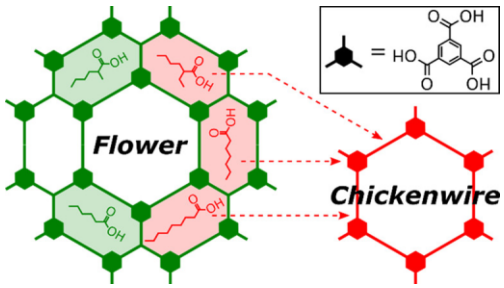

Encoding information in the chemical structure of tectons is the pivotal strategy in self-assembly for the realization of targeted supramolecular structures. However, frequently observed polymorphism in supramolecular monolayers provides experimental evidence for a decisive additional influence of environmental parameters, such as solute concentration or type of solvent, on structure selection. While concentration-induced polymorphism is comparatively well understood, the thermodynamic and molecular origins of solvent-induced polymorphism remain elusive. To shed light on this fundamental aspect of selfassembly, we explore the solvent-induced polymorphism of TMA monolayers on graphite as a prototypical example. Using the homologous series of fatty acids as solvents, TMA self-assembles into the anticipated chickenwire polymorph for longer chain fatty acids, whereas the more densely packed, but still porous flower polymorph emerges in shorter chain fatty acids. According to our initial working hypothesis, the origin of this solvent-induced polymorphism lies in the solvent dependence of the free energy gain. Utilizing an adapted Born Haber cycle constructed from measured TMA sublimation and dissolution enthalpies as well as DFT-calculated monolayer binding energies, we quantitatively assessed the selfassembly thermodynamics of both polymorphs in 6A, 7A, and 9A.

Yet, in contrast to the experimental findings, these results suggest superior thermodynamic stability of the chickenwire polymorph in all solvents. On the other hand, additional experiments comprising variable-temperature STM corroborate that the flower polymorph is thermodynamically most stable in 6A. To resolve this apparent contradiction, we propose a thermodynamic stabilization of the flower polymorph in 6A through the stereochemically specific coadsorption of shape-matched solvent molecules in its unique smaller elongated pores. This alternative explanation gains further support from experiments with side-substituted 6A solvents. Combination of a quantitative thermodynamic analysis and studies with systematic variations of the solvent's molecular structure holds great promise to enhance the understanding of thus far underexplored solvent effects.

I performed the variable-temperature STM experiments (TMA-6A solution), the sequential room-temperature STM experiments (TMA-6A to TMA-7A solution), the concentration dependent room-temperature STM experiments (TMA-6A and TMA-7A solutions) and variable-temperature UV-vis experiments (TMA-7A and TMA-9A solutions) as well as the corresponding data analysis / interpretation and preparation of the manuscript under the supervision of PD Dr. M. Lackinger. TMA sublimation experiments were done by PD Dr. M. Lackinger. Variable-temperature UV-vis experiments (TMA-6A solution) were provided by S. Spitzer under the supervision of PD Dr. M. Lackinger. Room-temperature STM experiments with TMA-fatty acid solutions, using 9A and side substituted 6A as solvents, were performed by M. Hocke under the supervision of PD Dr. M. Lackinger. MM and MD calculations were provided by Dr. N. Martsinovich from the University of Sheffield.

7.1 Introduction

The power of molecular self-assembly lies in its potential to realize targeted supramolecular structures by encoding their blueprints in the chemical structure of the tectons through the stereochemical arrangement of functional groups for intermolecular binding. The reliable expression of specific intermolecular binding motifs either facilitates structure prediction or provides the basis for tailoring tectons for targeted structures. Carboxylic acid moieties are a prominent example thereof as they predominantly form, according to graph-set notation,[180] R_2^2 (8) cyclic double hydrogen bonds (H-bonds). Exclusive and full expression of this intermolecular binding motif, for instance, in C_{3v} symmetric tricarboxylic acids, necessarily results in honeycomb networks.[81] Supramolecular monolayers at liquid-solid interfaces constitute an ideal study object for fundamental research, not at least because structures are readily resolved by STM.[22] Moreover, due to their vast variability in structure, composition, and chemistry, as well as the straightforward preparation, interfacial supramolecular monolayers bear great potential for applications in surface patterning and functionalization.

Frequently observed polymorphism in supramolecular monolayers, however, clearly indicates that structures are not always predetermined by the tecton's chemical

structure but rather reveals an additional, occasionally decisive influence of environmental parameters such as type of solvent, solute concentration, surface, and temperature.[24,25,84–86,103,105,107,108,181–187] It is by no means obvious whether the observed polymorphism originates from kinetic effects or is governed by equilibrium thermodynamics.[188,189] For the concentration-induced polymorphism, the observation of more densely packed polymorphs for higher solute concentrations seems to hold universally and is consistently explained by a generic thermodynamic origin: higher solute concentrations are associated with enhanced chemical potential; thereby, more densely packed structures gain thermodynamic stability, essentially due to the reduced entropy cost of self-assembly. This readily explains why even polymorphs with energetically inferior binding motifs can become thermodynamically selected.[190] While the physicochemical effect of solute concentration on polymorph selection is arguably best understood, the role of further environmental parameters remains elusive. Among those, the type of solvent is crucially important, because solvents can have a pronounced effect, but are chosen on a largely empirical basis. Often, various solvents are tediously tested until self-assembly of stable monolayers is eventually accomplished. For a more insightful approach, it is desirable to gain fundamental knowledge either on thermodynamic grounds or even more profoundly at the molecular level on why and how specific solvents stabilize distinct polymorphs. As a widely studied model system, we explore the solvent-induced polymorphism of TMA monolayers. This small, highly symmetric, and conformationally rigid tecton gives rise to an astonishingly large number of distinct structures and intriguing observations.[28,191–208] Here, we concentrate on the solvent-induced polymorphism observed for the homologous series of fatty acid solvents on graphite[28] as the first reported case of a phenomenon that turned out to be common.[25,84,86,103,105,107,108,181–186] Although our original publication dates back to the year 2005, no detailed account on the origin of this paradigmatic finding has been yet provided.

7.2 Results and Discussion

Using the homologous series of unbranched fatty acids as solvents, two hexagonal TMA monolayer polymorphs termed flower and chickenwire are observed at the interface of graphite, whereby the former polymorph self-assembles in shorter chain fatty acids up to 6A and the latter polymorph in longer chain fatty acids from 7A onward.[28] STM images alongside with corresponding DFT-optimized structures of both polymorphs on graphite are presented in 7.1.

The chickenwire polymorph exclusively features R_2^2 (8) cyclic double H-bonds between all carboxylic acid groups, resulting in a hexagonal structure with two TMA per unit cell and a = b = (1.65 ± 0.05) nm. In the flower polymorph, one out of the three carboxylic acid groups of each TMA is involved in R_3^3 (12) cyclic H-bonds, resulting likewise in a hexagonal structure, yet with six molecules per unit cell and a = b = (2.60 ± 0.05) nm. Both polymorphs feature H-bonded supramolecular rings composed of six TMA as secondary buildingblocks that delimit circular pores with a diameter of ∼1.0 nm (green circles in Fig. 7.1). In the chickenwire polymorph,

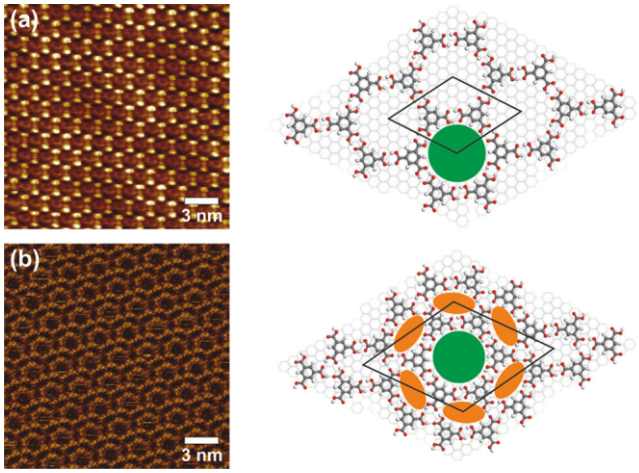

Figure 7.1: STM images of TMA (a) chickenwire and (b) flower polymorphs on graphite(0001) acquired in saturated 9A and 6A solutions, respectively. On the right hand side, the corresponding DFT-optimized structures are shown (for clarity, only the topmost graphite layer is depicted, while the calculations were carried out on two-layer slabs). The hexagonal unit cells are outlined by black lines. Green circles highlight the ∼1 nm large circular pores that are common to both polymorphs, while orange ovals highlight the smaller elongated pores that are unique for the flower polymorph. (Sample voltages and current setpoints: (a) 510 mV, 41 pA; (b) 1.01 V, 84 pA).

these hexameric rings are interwoven, that is, each TMA simultaneously belongs to three adjacent rings, whereas in the flower polymorph, these rings are hexagonally close packed and each TMA uniquely belongs to one ring. This packing results in smaller elongated pores between the edges of the hexameric rings that are unique for the flower polymorph (orange ovals in Fig. 7.1). In both polymorphs, all TMA are equivalent with respect to their intermolecular binding. Remarkably, other TMA polymorphs are not known at liquid-solid interfaces, with the exception of heavily sonicated solutions.[200] However, in this case, structure formation is not well understood, and its reasons may as well lie beyond equilibrium thermodynamics. A possible explanation is provided under the premise that at least one carboxylic acid group of each TMA must form R_2^2 (8) H-bonds. If alternatively only R_3^3 (12) H-bonds are allowed, the only remaining fully H-bonded polymorphs are chickenwire and flower.

7.2.1 Quantitative Thermodynamics

According to the fundamental theoretical study by Conti and Cecchini, the polymorph that results in the lowest (most negative) free energy per unit area

$$\Delta g = \frac{\Delta G}{A} = \Delta h - T \cdot \Delta s \tag{7.1}$$

is thermodynamically most stable at liquid-solid interfaces.[73] This work forms the foundation for our initial working hypothesis: the origin of the TMA solvent-induced polymorphism lies in a distinct solvent and polymorph dependence of Δg (primary solvent effect). Consequently, Δg would be lower (more negative) for the flower than for the chickenwire polymorph in 6A, whereas Δg would be lower for the chickenwire than for the flower polymorph in 7A and longer chain fatty acids. Thereby, solvent influences on either the enthalpy gain or the entropy cost for self-assembling TMA from solution are similarly conceivable and could both give rise to higher thermodynamic stability of the flower polymorph in 6A. An accurate quantification of solvent effects on the enthalpy gain is of primary importance, while any assessment solely based on monolayer binding energies with respect to vacuum is insufficient. Yet, obtaining accurate values for the monolayer enthalpy with respect to solution is challenging for both experiment and theory. As a first step toward quantifying the solvent influence, we proposed a Born-Haber cycle for selfassembly from solution,[74] as illustrated in Fig. 7.2.

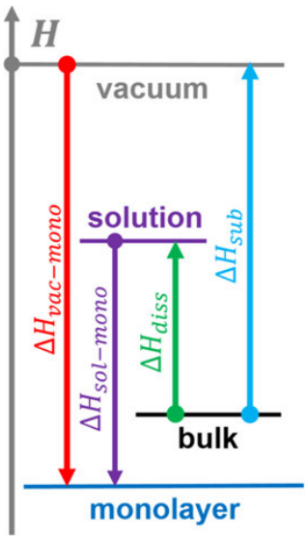

Figure 7.2: Born-Haber cycle for the indirect determination of the enthalpic driving force $\Delta H_{sol-mono}$ of monolayer self-assembly on solid surfaces from solution

The enthalpy difference between solution and monolayer ($\Delta H_{sol-mono}$) is indirectly determined from the sublimation enthalpy (ΔH_{sub}), the monolayer binding enthalpy with respect to vacuum ($\Delta H_{vac-mono}$), and the dissolution enthalpy (ΔH_{diss}):

$$\Delta H_{sol-mono} = -\Delta H_{diss} + \Delta H_{sub} + \Delta H_{vac-mono} \tag{7.2}$$

Within this approach, the solvent dependence is contained in ΔH_{diss}; hence, measurements for different solvents are the key for unveiling the solvent dependence of $\Delta H_{sol-mono}$ as a possible thermodynamic origin of solvent-induced polymorphism. For a complete assessment, a non-negligible dewetting enthalpy ΔH_{dewet} has to

be included that accounts for differences in interfacial energy, when the graphite-solution is replaced by the monolayer-solution interface.[74] For the moment, we ignore ΔH_{dewet}, but we will discuss its influence later.

Effusion experiments in high vacuum yield $\Delta H_{sub} = 154\ kJ\ mol^{-1}$ for TMA (Fig. 7.3) in perfect agreement with literature values.[209]

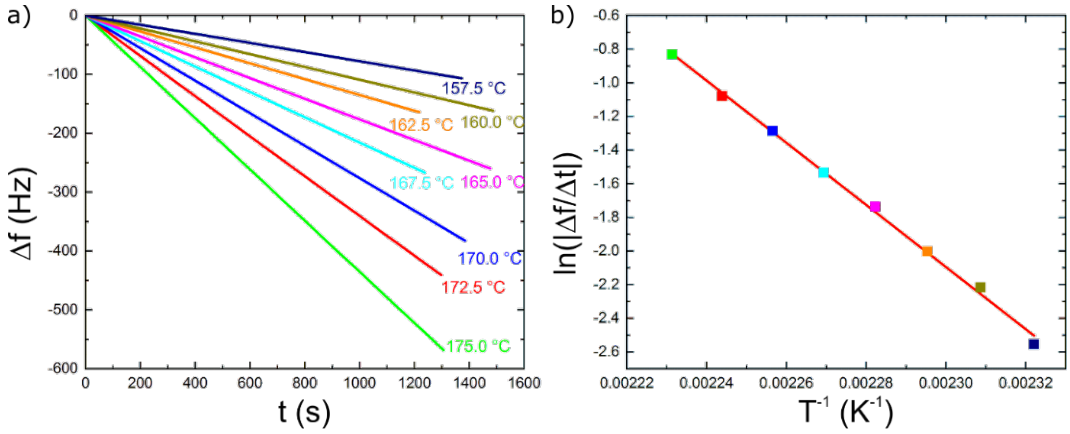

Figure 7.3: The TMA sublimation enthalpy ΔH_{sub} was determined from indirect measurements of the TMA saturated vapor pressure as a function of temperature in effusion experiments using a home-built Knudsen cell and a water-cooled Quartz Crystal Microbalance (QCMB).[58] (a) Change of the QCMB resonant frequency Δf versus time t traces for the indicated crucible temperatures of the Knudsen cell. Slopes of individual traces (corresponding to deposition rates) were obtained from linear fits. (b) Corresponding Van't Hoff plot of deposition rates and crucible temperatures. The red line represents a linear fit to the individual data points and from its slope a TMA sublimation enthalpy of $\Delta H_{sub} = 154\ kJ\ mol^{-1}$ is deduced. The perfectly linear behavior indicates a negligible temperature dependence of ΔH_{sub} in this temperature range.

$\Delta H_{vac-mono}$ was obtained from DFT calculations. Detailed analysis of the Moiré pattern inherent in the chickenwire polymorph revealed its incommensurability with respect to graphite.[206] To nevertheless facilitate periodic boundary conditions, we used a quadrupled unit cell based on a commensurate $\begin{pmatrix} 14 & 1 \\ -1 & 13 \end{pmatrix}$ superstructure containing eight TMA. Thereby, the tensile strain in comparison to a freestanding monolayer could be kept below 1%, and the resulting angle between TMA and graphite lattice of 3.9° lies well within the experimental range. For the flower polymorph, we used a commensurate $\begin{pmatrix} 11 & 1 \\ -1 & 10 \end{pmatrix}$ superstructure for a single unit cell containing six TMA, in accord with experimental lattice parameters (cf. appendix A, Fig. A.1). DFT calculations result in $\Delta H_{sol-mono}$ per TMA of -180.3 $kJ\ mol^{-1}$ for the chickenwire and -173.0 $kJ\ mol^{-1}$ for the flower polymorph in agreement with reported values.[73,204,210] The corresponding intermolecular binding energies, that is, without TMA-graphite interactions, amount to -91.9 $kJ\ mol^{-1}$ and -80.6 $kJ\ mol^{-1}$

per TMA for chickenwire and flower polymorphs, respectively. An enthalpic preference for the chickenwire polymorph was expected and originated in the diminished strength of R_3^3 (12) as compared to R_2^2 (8) H-bonds.[211] Interestingly, the chickenwire polymorph features a slightly weaker adsorption energy per TMA (unit cell averaged) of -88.4 $kJ\ mol^{-1}$ as compared to -92.4 $kJ\ mol^{-1}$ for the flower polymorph, suggesting more favorable TMA adsorption sites in the flower polymorph, as plausibly expected for a commensurate superstructure.

ΔH_{diss} were experimentally determined in 6A, 7A, and 9A through measuring the temperature dependence of TMA solubility by UV-vis absorption spectroscopy (cf. appendix A, Figs. A.3 to A.5). Van't Hoff plots for all three solvents are summarized in Fig. 7.4.

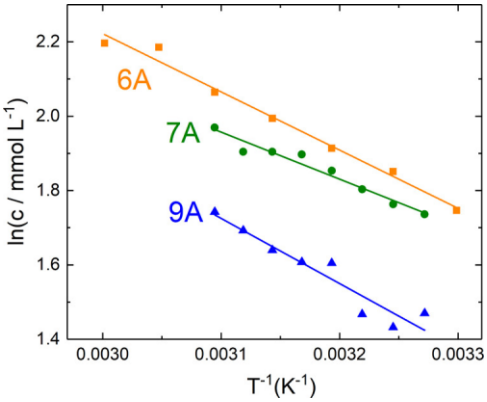

Figure 7.4: Van't Hoff plots of the temperature dependence of TMA solubility in 6A (orange squares), 7A (green circles), and 9A (blue triangles), as determined from UV-vis absorption spectroscopy. Symbols represent individual measurements, whereas the lines represent linear fits. The negative slope corresponds to the dissolution enthalpy ΔH_{diss} in the respective solvent, whereas the intercepts correspond to the standard dissolution entropies ΔS^0_{diss} (both in units of the universal gas constant R).

The (negative) slopes correspond to ΔH_{diss}, while the intercepts correspond to the standard dissolution entropy ΔS^0_{diss}. Fitting the data with straight lines results in $\Delta H_{diss}(6A) = +13.0\ kJ\ mol^{-1}$, $\Delta H_{diss}(7A) = +10.5\ kJ\ mol^{-1}$, and $\Delta H_{diss}(9A) = +14.6\ kJ\ mol^{-1}$. These values are rather similar and do not show a clear trend but appear surprisingly small. Dissolving TMA could be expected to be highly endothermic because of the strong H-bonded networks in the bulk crystal, as reflected by the large ΔH_{sub}. Yet, the small ΔH_{diss} can readily be explained by a superb stabilization of TMA solutes in solution through solvation by H-bonding with fatty acid solvent molecules. Thereby, the broken H-bonds from the bulk crystal are retained and their contribution to ΔH_{diss} becomes effectively neutralized.[74,102] As evident from Fig. 7.2, for a given molecule, hence a fixed ΔH_{sub}, a larger (more endothermic) ΔH_{diss} leads to a higher $\Delta H_{sol-mono}$, that is, a larger enthalpic driving force for adsorption from solution. For a meaningful comparison of competing polymorphs, however, molecular packing densities have to be taken

into account. Therefore, we evaluated the enthalpy gain per unit area

$$\Delta h = \frac{\Delta H_{sol-mono}}{A_{molecule}} \tag{7.3}$$

Thereby, $A_{molecule}$ is the average area per TMA in the monolayers and was derived from the experimental lattice parameters. Results for both TMA polymorphs in all three solvents are summarized in 7.1 and indicate an enthalpic preference for the chickenwire polymorph in all three solvents. Yet, the differences in Δh are comparatively small and possibly lie below the experimental error.

Table 7.1: Experimental lattice parameters a = b of both hexagonal structures, resulting area per molecule molecule, and enthalpy gain per unit area Δh for both polymorphs in all three solvent as estimated from the Born-Haber cycle.

parameter	**chickenwire**	**flower**
a (nm)	1.65	2.60
$A_{molecule}$ (nm^2)	1.18	0.976
$\Delta h(6A)$ $(\frac{kJ}{nm^2 \cdot mol})$	-33.4	-32.8
$\Delta h(7A)$ $(\frac{kJ}{nm^2 \cdot mol})$	-31.2	-30.3
$\Delta h(9A)$ $(\frac{kJ}{nm^2 \cdot mol})$	-34.7	-34.4

On the other hand, self-assembly of more densely packed polymorphs is also associated with higher entropy cost. Hence, it is not sufficient to solely consider the enthalpy gain, but the entropy cost similarly has to be taken into account. Yet, its accurate quantification is even more challenging and currently remains beyond reach. Hence, we propose using the absolute values of ΔS^0_{diss}, that reflects the entropy difference between TMA in solution and in the bulk crystal, as the relative measure for the solvent dependence of the entropy cost. This approach implies comparable entropies of TMA in the monolayer and in the bulk crystal, as justified by the essentially similar H-bonding environment. Even though minor differences could arise from vibrational entropy, it is important to state that the solvent dependence is captured. Standard dissolution entropies ΔS^0_{diss} correspond to the intercepts of the van't Hoff plots in Fig. 7.4, resulting in $\Delta S^0_{diss}(6A) = 57.5\ J\ mol^{-1}\ K^{-1}$, $\Delta S^0_{diss}(7A) = 48.9\ J\ mol^{-1}\ K^{-1}$, and $\Delta S^0_{diss}(9A) = 59.5\ J\ mol^{-1}\ K^{-1}$. The higher value for 6A than for 7A not only explains the higher TMA solubility but also indicates a larger entropy cost per molecule for TMA self-assembly from 6A solutions. However, again, it is the entropy cost per unit area

$$\Delta s = \frac{\Delta S}{A_{molecule}} \tag{7.4}$$

that is relevant for monolayer self-assembly. A molecule for the chickenwire poly-

morph is about 20% larger than for the more densely packed flower polymorph (cf. Table 7.1). Consequently, for equal entropy cost per molecule ΔS, the entropy cost per unit area Δs is about 20% larger for the flower than for the chickenwire polymorph. Although the differences in Δh are relatively small between both polymorphs, the significantly larger Δs of the flower polymorph results in a pronounced thermodynamic preference of the chickenwire polymorph in all solvents. In particular, 6A, which features an almost 20% larger ΔS than 7A, while the Δh values are comparable, would be a less likely solvent to thermodynamically stabilize the flower polymorph through a primary solvent effect.

Lastly, we qualitatively discuss the influence of the experimentally hardly accessible dewetting enthalpy ΔH_{dewet} on TMA polymorph selection. Our previous molecular mechanics calculations suggested that the solution-monolayer interface is energetically less favorable than the solvent-graphite interface,[74] in particular for alkanoic solvents that adsorb relatively strongly on graphite. Consequently, the enthalpy contribution from dewetting should be endothermic. Moreover, the chickenwire polymorph exposes a larger area fraction of the underlying graphite to solution due to its smaller packing density, i.e., higher porosity (cf. 7.1). Based on these considerations, we propose that the endothermic ΔH_{dewet} should be larger for the flower polymorph, further contributing to its inferior thermodynamic stability.

7.2.2 Thermodynamics Versus Kinetics

In all experiments with 6A as the solvent, exclusively, the flower polymorph was observed despite its putative thermodynamic instability against the chickenwire polymorph. This raises the question of a possible kinetic stabilization. Several studies unambiguously demonstrate kinetic trapping of supramolecular monolayers at liquid-solid interfaces,[83,110,212–214] implying that the perception of an effective dynamic equilibrium does not necessarily hold true. The most common way of experimentally addressing this crucial point are additional thermal treatments to promote attainment of the thermodynamic equilibrium.[83,110,213] Commonly, samples are ex situ heated and subsequently characterized by STM at room temperature. Yet, in situ experiments with STM imaging at elevated temperatures provide unique and detailed molecular level insights by directly assessing the sample state at the respective temperature.[24,25,215] To conduct these experiments with the comparatively volatile 6A solvent, we employed our recently developed I-STM.[113] This instrument was designed for long-term experiments at liquid-solid interfaces at elevated temperatures with unprecedentedly low drift and high resolution, while solvent evaporation is fully eliminated by a hermetic enclosure.

We first studied the stability of the flower polymorph in 6A for increasing temperatures. A representative STM image acquired after heating from room temperature up to 80 $°C$ is presented in Fig. 7.5a.

Full coverage of the flower polymorph is maintained at this relatively high temperature, indicating a remarkable overall stability. Even after further increasing the temperature to 110 $°C$, TMA monolayers still remained stable. Yet, as shown

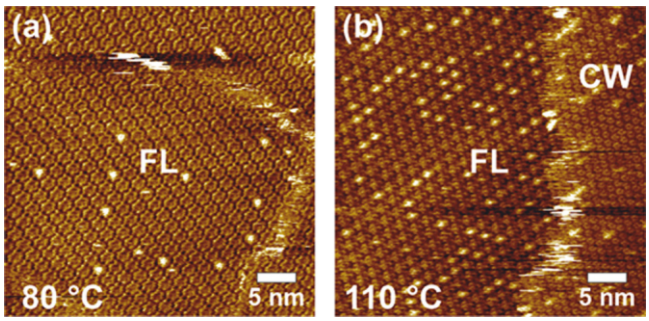

Figure 7.5: STM images of TMA monolayers on graphite(0001) acquired in saturated 6A solution after consecutive heating from room temperature to (a) 80 $°C$ and (b) 110 $°C$. At a sample temperature of 80 $°C$, we exclusively observed the flower polymorph (FL), whereas domains of the chickenwire (CW) polymorph emerged at 110 $°C$ (see the right hand side of (b)). Even though the contrast in these STM images can be uncommon, both polymorphs can be easily and unambiguously distinguished by the vast difference in lattice parameters. (Sample voltages (a) +0.53 V; (b) +0.51 V; setpoint currents were in the order of 30-50 pA, but precise values cannot be stated here due to the superposition with a temperature-dependent offset current).

in Fig. 7.5b, we observed the coexistence of chickenwire and flower domains. In a subsequent STM experiment after cooling down to room temperature again, we exclusively observed the flower polymorph, indicating the back conversion of the chickenwire domains. This finding is in qualitative agreement with the theoretically predicted TMA phase diagram,[73] where the chickenwire polymorph constitutes the high-temperature phase, due to the reduced entropy cost associated with its lower molecular packing density. Hence, this reversible phase transition at around 100 $°C$ provides evidence for superior thermodynamic stability of the flower polymorph in 6A at lower temperatures.

In variable temperature experiments with 6A solution, we always observed few pores of the TMA polymorphs with bright appearance, as also evident in Fig. 7.5. This STM contrast indicates filling with an unknown, but fairly defined guest species. Moreover, we also noticed the development of an offset to the tunneling current that further increased with increasing temperatures and persisted after cooling down again to room temperature. We tentatively attribute both observations to heating induced chemical changes of the TMA solution. A conceivable reaction would be anhydride formation between solute and solvent molecules, where either one or more carboxylic groups of TMA become functionalised by alkanoic acid groups or 6A-6A anhydride dimers are formed. According to this hypothesis, the filled pores result from stable adsorption of the anhydride species, and the offset current is related to the water released by the condensation reaction. DFT structure optimization followed by molecular dynamics simulations of various anhydride species indicate their stable adsorption in the larger TMA pores with reasonably strong binding energies to account for the unknown species in STM images (cf. appendix A, Fig.

A.6).

In a second series of experiments, we addressed the question whether the less stable chickenwire can be converted into the flower polymorph in 6A. To prepare samples with a metastable chickenwire polymorph at the 6A-graphite interface, we first applied a small droplet of saturated TMA in 7A solution onto graphite in order to cover the entire surface with the chickenwire polymorph (Fig. 7.6a, b).

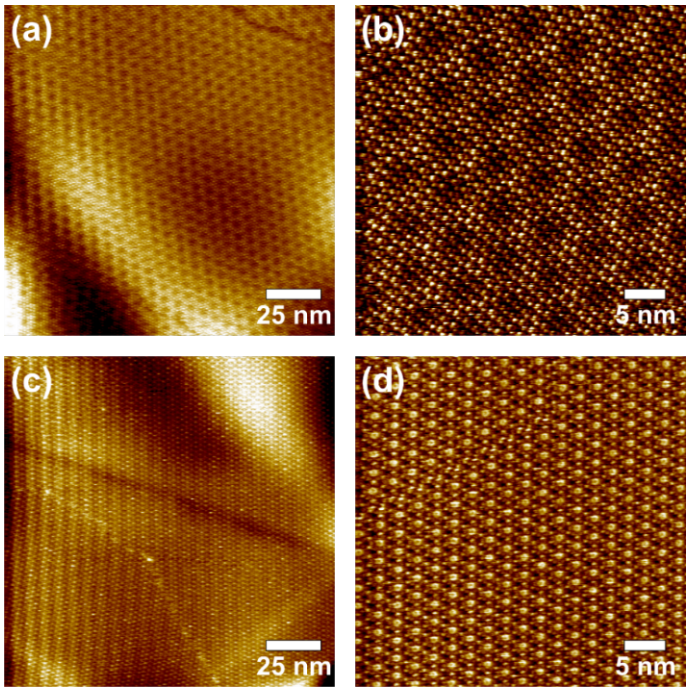

Figure 7.6: STM images of TMA monolayers acquired (a) / (b) after initially applying saturated TMA in 7A solution onto graphite(0001) and (c) / (d) after additionally applying an excess of saturated TMA in 6A solution (sample voltages and current setpoints: (a) / (b) +690 mV, 50.9 pA; (c) / (d) +590 mV, 56.3 pA).

In large scale images the chickenwire polymorph can be immediately identified by its characteristic Moiré pattern.[206] Next, an excess of saturated TMA in 6A solution was applied to this sample. Subsequent STM imaging at room temperature exclusively showed the flower polymorph (Fig. 7.6c, d). The immediate spontaneous conversion of the preassembled chickenwire to the flower polymorph in 6A not only corroborates superior thermodynamic stability of the latter but also demonstrates the absence of kinetic trapping at room temperature, even in these strongly H-bonded monolayers.

In addition, we explored the concentration dependence of TMA self-assembly for 6A and 7A solutions. Yet, we could not find any indications for a concentration-induced polymorphism. As anticipated, self-assembly of stable TMA monolayers was not observable anymore by STM below critical concentrations that were determined as $(0.42 \pm 0.06)\ mmol\ L^{-1}$ for 6A and $(0.40 \pm 0.02)\ mmol\ L^{-1}$ for 7A. These findings neither confirm nor contradict thermodynamic control.

7.2.3 Solvent Coadsorption

On the one hand, we found unambiguous experimental evidence for superior thermodynamic stability of the flower polymorph in 6A. On the other hand, according to our assessment of Δh and Δs, this cannot be explained by a primary solvent effect. To resolve this apparent contradiction, we propose solvent coadsorption as a recognized important additional stabilizing or even structuredetermining contribution for monolayer self-assembly at liquid-solid interfaces.[23,24,199,216] Intriguingly, both TMA polymorphs are porous, while the chickenwire is "more porous" than the flower polymorph on account of the molecular packing densities. Even though both polymorphs feature one large circular 1.0 nm-wide pore in each unit cell, the chickenwire polymorph exhibits an approximately 2.5 times higher area density of these pores than the flower polymorph owing to its smaller unit cell area (2.35 nm^2 for chickenwire vs 5.85 nm^2 for flower). Consequently, any thermodynamically favorable contribution from solvent coadsorption in the larger pores would stabilize the chickenwire rather than the flower polymorph. Hence, stabilization of the flower polymorph by solvent coadsorption must be related to its unique smaller and more elongated pores (orange ovals in Fig. 7.1). Based on the seemingly good geometric match of extended (all trans) 6A solvent molecules with the smaller pores of the flower polymorph, we propose that stereochemically specific solvent coadsorption in these pores tilts the thermodynamic balance. According to this hypothesis, the additional thermodynamic stabilization is no longer feasible for 7A or longer chain fatty acids, simply because their dimensions exceed the pore size.

To corroborate our hypothesis, we conducted experiments with side-substituted 6A solvents. The underlying idea is to evaluate polymorph selection for cases where the proposed solvent coadsorption becomes sterically hindered, while the overall solvent characteristics are preserved. To avoid interferences with the monolayer H-bonding, the side groups should not form strong H-bonds. For these reasons, we further explored 2-methylhexanoic acid (methyl-6A) and 2-ethylhexanoic acid (ethyl-6A) as solvents (cf. Fig. 7.7).

We reckon that a significant contribution to the stabilization of 6A coadsorption arises from H-bonds involving the solvent's carboxylic acid groups. Hence, we anticipate steric hindrance to be most effective when the side groups are in close proximity to the head group. Experimental results obtained for TMA saturated solutions are presented in Fig. 7.7. Using methyl-6A as solvent still results in the flower polymorph, confirming a behavior analogous to unsubstituted 6A. It is worth to note that the intuitive contrast of the flower polymorph with bright-appearing TMA molecules (see Fig. 7.7a) was an exception, whereas an inverted contrast where both types of pores appeared brighter (see Fig. 7.7b) was commonly observed. This holds also true for unsubstituted 6A (cf. appendix A, Fig. A.2) and may hint toward solvent coadsorption in both type of pores of the flower polymorph. In contrast, further experiments using ethyl-6A as solvent indeed resulted in self-assembly of the chickenwire polymorph (cf. Fig. 7.7c) in accord with our working hypothesis. The characteristic Moiré pattern indicates equivalency of the chicken-

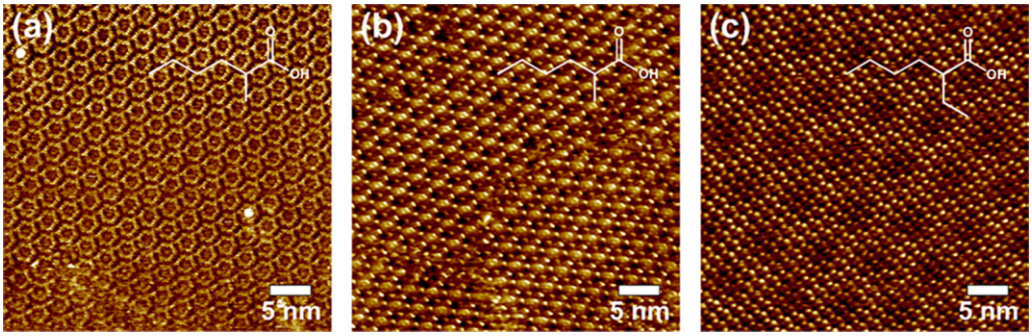

Figure 7.7: STM images of TMA monolayers on graphite(0001) acquired in saturated solutions using (a)/(b) methyl-6A and (c) ethyl-6A as solvent. Overlays show chemical structures of respective solvents. While methyl-6A still results in the flower polymorph, the chickenwire polymorph is observed in ethyl-6A. (Sample voltages and current setpoints: (a) -582 mV, 61 pA; (b) -582 mV, 54 pA; (c) -571 mV, 54 pA).

wire polymorph in ethyl-6A and the typical 7A or 9A solvents. We conclude that steric hindrance imposed by the ethyl side-group inhibits solvent coadsorption in the smaller pores of the flower polymorph. As a consequence, the flower polymorph is thermodynamically less stable in ethyl-6A, resulting in self-assembly of the then thermodynamically favored chickenwire polymorph. These results support our hypothesis that the flower polymorph is eventually stabilized against the chickenwire polymorph by coadsorption of solvent molecules in its smaller pores.

7.3 Summary and Conclusions

We present a comprehensive study of solvent-induced polymorphism in TMA monolayer self-assembly at fatty acid-graphite interfaces. This phenomenon is inherently more complex than concentration-induced polymorphism because exchanging the solvent can have profound effects on the enthalpy gain, while varying solute concentrations primarily, if not exclusively, affects the entropy cost in a predictable manner. To provide a thermodynamic explanation, we evaluated Δg. The enthalpy gain per unit area Δh was quantified for both polymorphs in all three solvents with the aid of a Born-Haber cycle constructed from the measured TMA sublimation and dissolution enthalpies as well as DFT-calculated monolayer binding energies. The results indicate a slight enthalpic preference of the chickenwire polymorph in all solvents, but the differences in Δh are too small to be conclusive. Yet, the entropy cost per unit area Δs is significantly larger for the flower than for the chickenwire polymorph owing to the 20% higher molecular packing density of the former. From this, we conclude on the superior thermodynamic stability of the chickenwire polymorph in all solvents. Complementary variable-temperature experiments in 6A solution unveiled a reversible phase transition from flower to chickenwire polymorph for increasing temperatures. With further support from the observed spontaneous conversion of the metastable chickenwire into the thermodynamically more stable

flower polymorph in 6A already at room temperature, a kinetic stabilization of the flower polymorph in 6A can be ruled out. To explain the solvent-induced polymorphism of TMA on thermodynamic grounds, we propose a stabilizing contribution from the stereochemically specific solvent coadsorption in the unique smaller elongated pores of the flower polymorph. This was corroborated by experiments with side-substituted 6A solvents, where sufficiently large steric hindrance resulted in self-assembly of the chickenwire polymorph.

The present study exemplifies a case of thermodynamic stabilization of a distinct monolayer polymorph by solvent coadsorption, which is extremely sensitive to the solvent's molecular structure with a sharp threshold: Addition of just one methylene unit either in the main chain (7A instead of 6A) or in the side chain (ethyl-6A instead of methyl-6A) sterically hinders solvent coadsorption in the smaller pores of the flower polymorph. These results demonstrate that polymorph-specific solvent coadsorption is particularly relevant when the molecular structure of the solvent becomes comparable to pore sizes and shapes. Extending these studies to further literature-reported systems whose polymorphs exhibit differently sized and shaped pores would be desirable for concluding on the generality of this stabilizing mechanism.

Overwhelming and unambiguous results indicate a far more important and active role of solvents rather than just being a supply medium and background continuum. Solvent-induced polymorphism in interfacial monolayers constitutes an ideal study object and versatile model system to promote the thermodynamic and molecular level understanding of solvent effects: STM facilitates a straightforward structural characterization, including the possibility to even directly image immobilized solvent molecules. Moreover, the temperature evolution of supramolecular systems can be directly studied by variable-temperature STM experiments, where in situ imaging at elevated temperatures allows capturing of reversible phase transitions. These remain unnoticed in ex situ heating experiments but serve as strong indicators for thermodynamic control. Lastly, solvent effects are anticipated to be particularly pronounced in monolayers as they are fully solvent-exposed. In addition to STM imaging, monolayer self-assembly can be further explored by quantifying its thermodynamics or by the systematic variation of solvents. The thermodynamic analysis applied here based on the Born-Haber cycle and dissolution entropies is widely applicable and appropriate to unveil primary solvent effects. To explore further possible origins of solvent-induced polymorphism, it would be rewarding to also extend these studies to different classes of solvents, for instance, nonprotic solvents and solvents that exhibit inferior interaction with graphite such as 1,2,4-trichlorobenzene or phenyloctane. To complement the thermodynamic analysis, structural variations of solvents that do not affect the main modes of interaction, for instance, side substitution of widely used alkanoic solvents, are invaluable for identifying and understanding solvent effects at the molecular level. The combined application of these two complementary approaches to prevalent cases of solvent-induced polymorphism, for instance, of halogen or van der Waals-bonded monolayers, holds great promise to enhance and deepen the understanding of ubiquitous solvent effects. Eventually, this can bring

us one step closer to the holy grail of a priori structure prediction.

7.4 Materials and Methods

7.4.1 Experimental Details

Room-temperature and variable-temperature STM experiments were carried out with homebuilt instruments. Details of the variable-temperature instrument are described elsewhere (chapter 6).[113] Highly oriented pyrolytic graphite (grade ZYB, *Optigraph GmbH*) samples were cleaved with adhesive tape prior to each experiment, and mechanically cut PtIr (90/10) tips were used for imaging. TMA and fatty acid solvents were acquired from commercial sources (*TCI* and *Sigma-Aldrich*) and used as received. The TMA sublimation enthalpy and the TMA dissolution enthalpies in 6A, 7A, and 9A were determined, as described in chapter 3 and in our previous work.[74] Absorbance spectra were calibrated by comparison with solutions of known concentration for each respective solvent.

7.4.2 Computational Details

Calculations of TMA adsorption on graphite were carried out using DFT, as implemented in the CP2K software.[217] The van der Waals density functional (vdW-DF) by Dion et al. was used,[218] with Goedecker-Teter-Hutter pseudopotentials[219] and double-zeta valence polarized basis sets.[220] The Brillouin zone was sampled only at the Γ point. The graphite surface was modeled using periodic cells, with dimensions chosen such as to be commensurate with the experimentally measured size of the TMA chickenwire and flower polymorphs: a $\begin{pmatrix} 14 & 1 \\ -1 & 13 \end{pmatrix}$ graphene supercell, which is commensurate with (2×2) cells of the TMA chickenwire polymorph (eight TMA molecules) and a $\begin{pmatrix} 11 & 1 \\ -1 & 10 \end{pmatrix}$ graphene supercell, which is commensurate with one unit cell of the TMA flower polymorph (six TMA molecules). Two layers of graphene were used to represent the graphite surface. The bottom layer was fixed and the top layer was allowed to optimize. The vertical cell dimension was 20 Å, which results in ∼13 Åof vacuum between cells in the vertical dimension. To calculate intermolecular binding energies, isolated (not adsorbed) TMA monolayers were similarly modeled as two-dimensional periodic systems, with a cell height of 20 Åin the vertical dimension. Ab initio MD calculations of guest species in pores of the TMA network on single-layer graphene used the same DFT method and were performed with the NVT ensemble, time step 1 fs, and run time of 1 ps.

Chapter 8

Ultraslow Desorption Kinetics

This chapter is reprinted and partially adapted with permission from O. Ochs, N. Martsinovich, W. M. Heckl and M. Lackinger. Quantifying the Ultraslow Desorption Kinetics of 2,6-Naphthalenedicar- boxylic Acid Monolayers at Liquid–Solid Interfaces. *J. Phys. Chem. Lett.* 2020, 11, 17, 7320-7326. Copyright (2020) American Chemical Society.

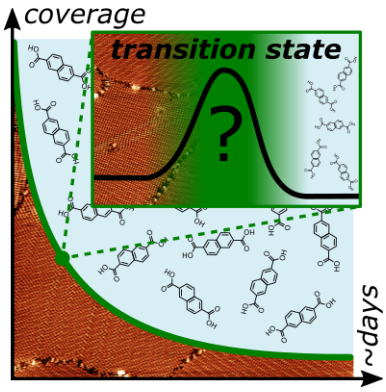

Kinetic effects in monolayer self-assembly at liquid-solid interfaces are not well explored, but can provide unique insights. We use variable-temperature STM for quantifying the desorption kinetics of NDA monolayers at 9A-graphite interfaces. Quantitative tracking of the decline of molecular coverages by STM between 57.5 $°C$ and 65.0 $°C$ unveiled single exponential decays over the course of days. An Arrhenius plot of rate constants derived from fits results in a surprisingly high energy barrier of $+208\ kJ\ mol^{-1}$ that strongly contrasts with the desorption energy of $+16.4\ kJ\ mol^{-1}$ with respect to solution as determined from a Born-Haber cycle. This vast discrepancy indicates a high energy transition state. Expanding these studies to further systems is the key to pinpoint the molecular origin of the remarkably large NDA desorption barrier.

I performed all experiments, the corresponding data analysis / interpretation and the preparation of the manuscript under the supervision of PD Dr. M. Lackinger.

MM and DFT calculations were provided by Dr. N. Martsinovich from the University of Sheffield.

8.1 Introduction

Equilibria are characterized and maintained by the equality of forward and backward reactions. Consequently, attainment of thermodynamic equilibrium necessarily requires a dynamic equilibrium, and hindering of either forward or backward reaction inevitably results in kinetic trapping. Here, we focus on kinetic effects in monolayer self-assembly at liquid-solid interfaces. According to a common assumption, interfacial supramolecular monolayers readily attain thermodynamic equilibrium through continuous exchange of molecules with the supernatant solution. This view is corroborated by observed dynamic responses of monolayers to changes in solution composition or temperature,[25,61,199,221] indicating fulfillment of the necessary precondition for applying thermodynamical models. Desorption becomes feasible already at room temperature, because solvation can drastically reduce desorption energies.[74,102] Hence, the energetics at liquid-solid interfaces is very distinct from vacuum-solid interfaces, where desorption energies $>150\ kJ\ mol^{-1}$ that prohibit room temperature desorption are common even for smaller molecules. Yet, observations of kinetically trapped phases at liquid-solid interfaces,[83,214,222] in particular for larger molecules, cast doubt on the prevalent concept of an effective dynamic equilibrium. This view gains support from recent studies that unveiled surprisingly large desorption barriers for porphyrins at liquid-solid interfaces.[223,224]

Kinetic effects are presently not well explored in monolayer self-assembly at liquid-solid interfaces. Most current studies employ STM which facilitates straightforward assessment of structures in submolecular detail, but lacks sufficient temporal resolution. Only in a few cases, kinetic phenomena with time constants ranging from milliseconds to minutes were studied by STM.[201,225–227] To nevertheless use STM for quantitative kinetic studies, model systems with exceedingly slow kinetics are desirable. In this respect, variable-temperature experiments allow matching of time constants, because most rate-determining elementary processes are thermally activated, and their rate constants vary strongly with temperature according to the Arrhenius equation. Since the self-assembly process is still too rapid to be captured by STM, we propose to study monolayer dissolution kinetics by tracking surface coverage over time. A closely related process of dissolution kinetics from molecular crystals into (aqueous) solutions also plays an important role in pharmaceutics, because it determines drug dosage rates.[228–231]

We study the dissolution kinetics of NDA (Fig. 8.1a) monolayers at the 9A-graphite interface. This choice was motivated by previous results that indicated kinetic hindering: NDA monolayers feature uncommonly large defect densities,[29] whereas comparable dicarboxylic acids self-assemble into highly ordered monolayers.[74,232,233]

In the experiments, temperatures are increased until NDA monolayers reach the verge of thermodynamic stability, as indicated by the decline of molecular coverages

from typically full at room temperature to partial at elevated temperatures. Thereafter the temporal evolution of molecular coverage is quantitatively tracked over time at constant temperature by real space imaging. Key to these novel experiments is our recently developed I-STM, devised for long-term variable-temperature experiments at liquid-solid interfaces (cf. chapter 6).[113] In most previously reported variable-temperature studies only samples were heated,[24–26,110,234] whereby solvent evaporation is unavoidable and can become limiting. We completely removed this crucial limitation by integrating the STM body into a hermetically sealed and precisely temperature-controlled container, a concept similarly implemented by the Hipps group.[27] Thereby long-term variable-temperature STM experiments with unprecedentedly high resolution and low drift become feasible, yet without any principal limitation for the duration of experiments.

8.2 Results and Discussion

STM images of self-assembled NDA monolayers acquired at the 9A-graphite interface are presented in Fig. 8.1. In the ordered domains an oblique unit cell can be assigned with experimental lattice parameters a = (1.16 ± 0.02) nm, b = (0.74 ± 0.02) nm and γ = (56 ° ± 1.0 °). Analogous to comparable dicarboxylic acids,[29,74,102,235–238] the NDA monolayer consists of densely packed molecular chains formed by $R_2^2(8)$ H-bonds between the carboxylic acid groups. Pinpointing individual NDA molecules by their STM appearance is not obvious. Yet, Molecular Mechanics (MM) calculations yield a repeat distance of 1.15 nm along the H-bonded chains (cf. appendix B, Fig. B.1). Precisely the same distance was identified in the STM images, allowing to elucidate the orientation of the H-bonded chains, and hence, that of NDA molecules. Overlaying STM images with the MM simulated chains results in a $C - H \cdots O$ distance of ∼0.24 nm between NDA molecules in adjacent chains, indicating formation of interchain H-bonds.[29,93]

At room temperature the surface is completely covered with NDA domains extending up to ∼300 nm, but smaller domains in the size range (50...100) nm are frequently observed. More importantly, NDA monolayers exhibit an uncommonly low degree of structural perfection. Molecular vacancies are often observed zero dimensional defects (see Fig. 8.1a and 8.1b). A frequently observed line-defect is shown in Fig. 8.1b and 8.1c. As illustrated by the overlay and corresponding model, it consists of two intermingled H-bonded NDA chains with a chirality opposite to both adjacent domains. These 1D defects persist even at elevated temperatures of 70 °C and are not eliminated by self-healing.

To evaluate the desorption kinetics of NDA monolayers, we studied the temperature evolution of molecular coverages in variable-temperature STM experiments. Upon heating above ∼50 °C we observed partial coverages due to desorption of molecules, driven by the thermodynamic instability of full coverages. The pivotal question, however, is whether the observed partial coverages already represent a new stationary state, i.e. a thermodynamic equilibrium partly shifted to the dissolved state, or further decline over time. To address this crucial point, we monitored the

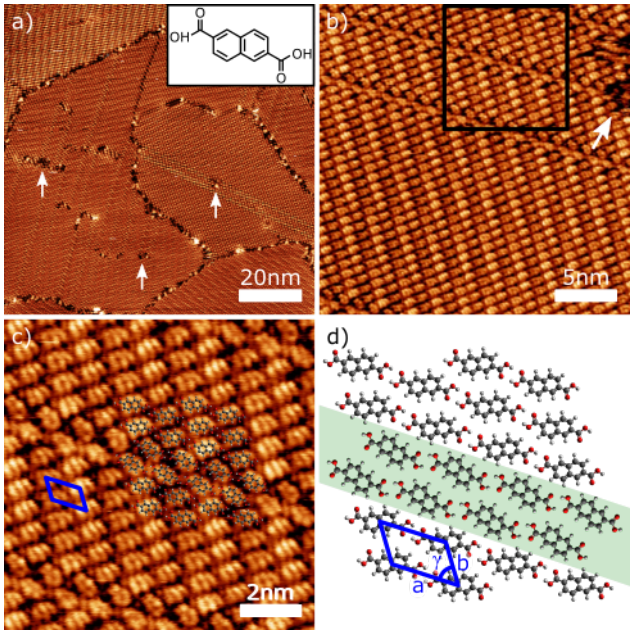

Figure 8.1: Self-assembly of NDA monolayers at the 9A-graphite interface. STM images were acquired at 70 $°C$ using room temperature saturated solution. (a) Large scale STM image showing multiple domains (insert: molecular structure of NDA). Dark appearing patches within the domains (highlighted by arrows) correspond to vacancies. (b) STM image showing a frequently observed line-defect, i.e. an anti-phase domain boundary, demarcated by two H-bonded NDA chains of opposite chirality. (c) close up of the area indicated in (b) showing the detailed molecular arrangement. (d) Molecular model as derived from (c) and indicated unit cell (image size and tunneling parameters: (a) 100 nm, 0.59 V, 60 pA; (b) 25 nm, 0.27 V, 50 pA; (c) 10 nm, 0.27 V, 50 pA;).

surface coverage at constant temperature over time. Coverages were quantified at discrete times by acquiring statistically significant STM data from a surface area of $\sim$3.5 μm^2 (cf. section 8.4.1 and appendix B, Figs. B.5 and B.6). We measured desorption traces for temperatures between 57.5 $°C$ and 65.0 $°C$, the results are summarized in Fig. 8.2a. For the lowest measured temperature of 57.5 $°C$ we find a progressively declining coverage over the course of eight days. Note that such long-term experiments were only possible, because solvent evaporation is ceased in the hermetically sealed I-STM.[113] For all traces the data points are well described by single exponential decays, indicating first order desorption kinetics, and allowing to deduce rate constants from fits. For the three lower temperatures improved fits were obtained by exponential decays to asymptotically reached finite final coverages θ_∞ rather than zero (e.g. for 57.5 $°C$ R^2 ($\theta_\infty = 0$ %) = 0.982 vs. R^2 ($\theta_\infty = 25.8$ %) = 0.996):

$$\theta(t) = \theta_{t=0} \cdot e^{-kt} + \theta_\infty \tag{8.1}$$

The fitting results are summarized in Table 8.1. θ_∞ decrease for increasing temperature, with $\theta_\infty = 0$ actually measured for the highest temperature of 65.0 $°C$. This behavior is consistent with interpreting θ_∞ as partial coverages in thermodynamical equilibrium. With increasing temperature the thermodynamic equilibrium becomes gradually shifted to lower coverages, because of the growing favorable entropy contribution to the free energy of the dissolved state.

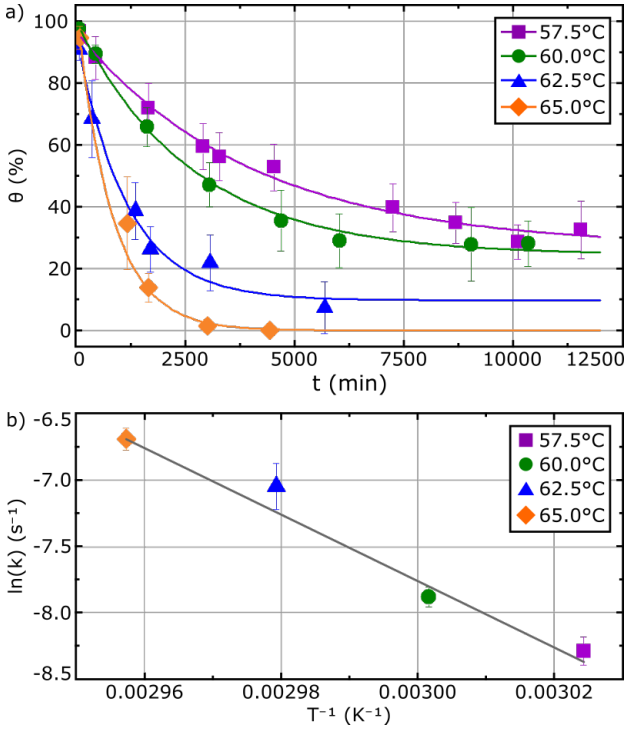

Figure 8.2: Summarized results of kinetic measurements on NDA monolayer desorption; (a) Molecular coverage θ vs. time t traces measured by STM at fixed temperatures (purple squares: 57.5 $°C$; green dots: 60.0 $°C$; blue triangles: 62.5 $°C$; orange diamonds: 65.0 $°C$); Vertical error bars correspond to standard deviations, and (invisibly small) horizontal error bars reflect the measurement duration of ∼90 min. Solid lines represent fits with single exponential decays to asymptotically reached final coverages θ_∞ (cf. Table 8.1 for fitting results). (b) Arrhenius plot of the rate constants. The solid line represents a linear fit, with a slope corresponding to an activation energy of +208 $kJ\ mol^{-1}$. Fitting uncertainties account for vertical error bars.

Activation energies of thermally driven processes can be assessed from the temperature dependence of rate constants, with several studies demonstrating the utility of STM experiments.[239–241] All four rate constants derived from fitting desorption traces lie on a straight line in the Arrhenius plot shown in Fig. 8.2b, and the slope of the linear fit corresponds to an activation energy of +208 $kJ\ mol^{-1}$. For comparison, fitting the desorption traces of Fig. 8.2a with single exponentials (i.e. without considering finite θ_∞) would result in a significantly larger desorption barrier of +289 $kJ\ mol^{-1}$ (appendix B, Fig. B.7 and Table B.1). Hence, considering base

values from thermodynamically stable partial coverages is important. Even though relatively high, a desorption barrier of $+208\ kJ\ mol^{-1}$ appears consistent with the ultraslow kinetics. Remarkably, the NDA desorption barrier is significantly larger than the barriers in the order of $(100 \ldots 150)\ kJ\ mol^{-1}$ deduced for desorption of porphyrins from monolayers into solution based on room temperature STM analysis after quenching from higher temperatures.[213,223,224]

Table 8.1: Rate constants k and asymptotically reached final coverages θ_∞ as obtained from fitting desorption traces acquired at temperatures T; fitting uncertainties are stated in parenthesis;

T $(^\circ C)$	**k** $(10^{-4}\ min^{-1})$	θ_∞ (%)
57.5	2.51 ($\pm$0.26)	25.8 ($\pm$2.74)
60.0	3.77 ($\pm$0.28)	24.4 ($\pm$2.09)
62.5	8.70 ($\pm$1.49)	9.80 ($\pm$4.52)
65.0	12.44 ($\pm$1.04)	0.0

Interpreting and explaining the experimentally derived desorption barrier is essential for a fundamental understanding. The most straightforward assumption is that desorption barriers are equal to desorption energies, i.e. the (free) energy difference between desorbed and adsorbed state of a molecule, in the end implying the absence of a transition state. However, various studies propose sizable barriers for both adsorption and desorption at liquid-solid interfaces associated with solvent rearrangement processes.[242,243] In the following, we will focus on the energetics of desorption and discuss potential entropy effects later.

We obtained theoretical estimates for NDA desorption energies from MM calculations (cf. Computational Details 8.4.2). Monolayer dissolution is expected to proceed via desorption of more weakly bound undercoordinated molecules, e.g. at domain edges. To assess their diminished desorption energies, and also the dependence on the local binding, finite islands of 5×5 molecules were calculated on graphite, results are summarized in Fig. 8.3.

In the interior of the domain, NDA desorption energies are essentially constant at $\sim$249 $kJ\ mol^{-1}$, whereas notable differences occur between the two inequivalent edges. These can be attributed to differences in H-bonding: Desorption energies are significantly lower at the edge running parallel to the $\vec{b}$ lattice vector, where NDA molecules form H-bonds with only one carboxylic acid group, while the other carboxylic acid group is dangling at the boundary. In contrast, at the edges running parallel to the $\vec{a}$ lattice vector NDA molecules form H-bonds with both of their carboxylic acid groups, and their desorption energy reaches almost that of interior molecules. The small difference of $\sim$12 $kJ\ mol^{-1}$ can be attributed to the lack of interchain bonding at one side. The desorption energy difference of $\sim$60 $kJ\ mol^{-1}$ for NDA molecules in the two non-equivalent edges largely reflects the binding energy of $R_2^2(8)$ H-bonds between two carboxylic acid groups.[95,211] Corner molecules exhibit the smallest desorption energy due to their inferior interaction with neighbors. These

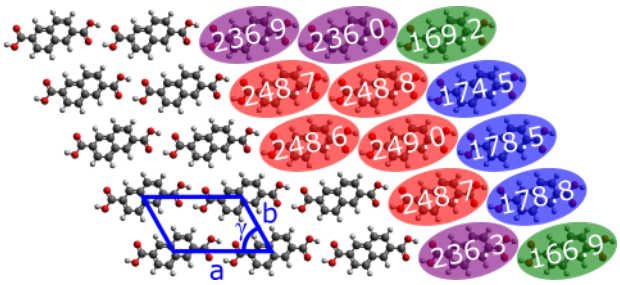

Figure 8.3: MM calculated desorption energies of NDA molecules (in $kJ\ mol^{-1}$) from a finite island of 5×5 molecules. Calculations were conducted on graphite(0001) (not shown for clarity). Depending on the position of the respective molecule in the island and the intermolecular binding to neighbour molecules, desorption energies exhibit sizable spatial variations with the highest values in the domain interior, and signficant differences between the two inequivalent edges.

results mirror our previous calculations of terephthalic acid which self-assembles into isostructural monolayers on graphite.[28] Furthermore, the outcome is virtually independent of island size. Results obtained for a 3×3 island are essentially similar (appendix B, Fig. B.4), indicating that diminished desorption energies only occur for molecules directly at the domain edge.

Dissolution and desorption are anticipated to start at and proceed from domain edges, because of the lower desorption energy of these undercoordinated molecules. Moreover, edge sites are not annihilated during the dissolution, hence available for driving it to completion. This is corroborated by STM imaging, where comparatively small NDA domains were observed throughout the monolayer dissolution that constantly provide edge molecules (appendix B, Fig. B.6). Yet, high stability of the edges parallel to the $\vec{a}$ lattice vector, and the resulting preferential desorption from edges parallel to the $\vec{b}$ lattice vector should lead to distinct shapes of NDA domains with two parallel and fairly straight edges. However, in STM images we observe rugged domains (appendix B, Fig. B.6), possibly hinting toward a two-step desorption process: First, NDA molecules detach from the islands, but still remain adsorbed on the graphite surface in a mobile 2D molecular gas phase. Only in the second step, molecules eventually desorb from the graphite surface into solution. This two-step process should be energetically more favourable, but it is not necessarily the dominating process as it could be associated with significantly lower pre-exponentials.

Based on the MM calculations we propose an average desorption energy of edge molecules in the order of $+170\ kJ\ mol^{-1}$. At first sight, the MM derived NDA desorption energy appears comparable with the activation energy extracted from the Arrhenius plot. Yet, at liquid-solid interfaces NDA molecules desorb into solution, whereas isolated molecules in vacuum were used as reference for MM. Consequently, actual desorption energies are expected to be significantly lowered by solvation and the associated enthalpic stabilization in solution.

In order to estimate enthalpy differences of molecules at liquid-solid interfaces

with respect to solution, i.e. to quantify the influence of the supernatant solution, we proposed an adapted Born-Haber cycle (Fig. 8.4).[74] It was originally devised for thermodynamic models, but is similarly applicable to kinetic models.

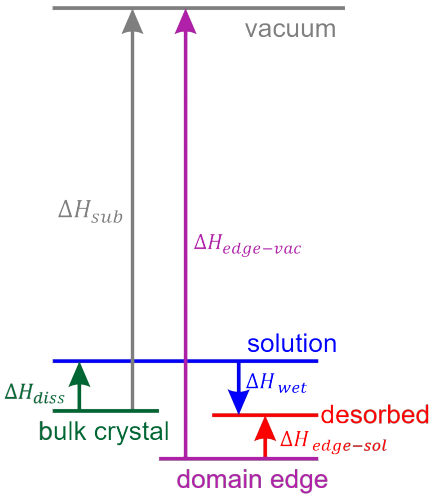

Figure 8.4: Born-Haber cycle using single NDA molecules in vacuum, molecules at domain edges, dissolved molecules in solution and the NDA bulk crystal as reference states and considering a wetting enthalpy. Respective enthalpy differences are indicated. The diagram is drawn to scale to illustrate the significant lowering of the desorption energy by the presence of solution.

Its main idea is to introduce the crystalline bulk of solute molecules as additional reference state. According to Scheme 1, the desorption energy (negative binding energy) $\Delta H_{edge-sol} = -\Delta H_{sol-edge}$ of NDA molecules at domain edges with respect to solution is given by:

$$\Delta H_{edge-sol} = \Delta H_{edge-vac} - \Delta H_{sub} + \Delta H_{diss} + \Delta H_{wet} \tag{8.2}$$

ΔH_{diss} and ΔH_{sub} correspond to NDA dissolution and sublimation enthalpies, respectively, and are both experimentally accessible (*vide infra*). $\Delta H_{edge-vac}$ represents the MM calculated desorption energy of edge molecules into vacuum. ΔH_{wet} considers solvent wetting effects, where upon NDA desorption solution-monolayer interface is exchanged for solution-substrate interface. Since the interaction of solvent molecules with the bare surface is normally stronger than with the monolayer, ΔH_{wet} is often exothermic for desorption.[74,224]

Temperature dependent measurements of NDA effusion rates in high vacuum yield $\Delta H_{sub} = 152\ kJ\ mol^{-1}$ (Fig. 8.5) in reasonable agreement with the MM calculated bulk binding energy of $= 143\ kJ\ mol^{-1}$. ΔH_{diss} was determined by measuring the temperature dependence of NDA solubility in 9A by UV-vis absorption spectroscopy (Fig. 8.6). The acquired endothermic $\Delta H_{diss} = 18.8\ kJ\ mol^{-1}$ is in the typical range for comparable solutions.[74]

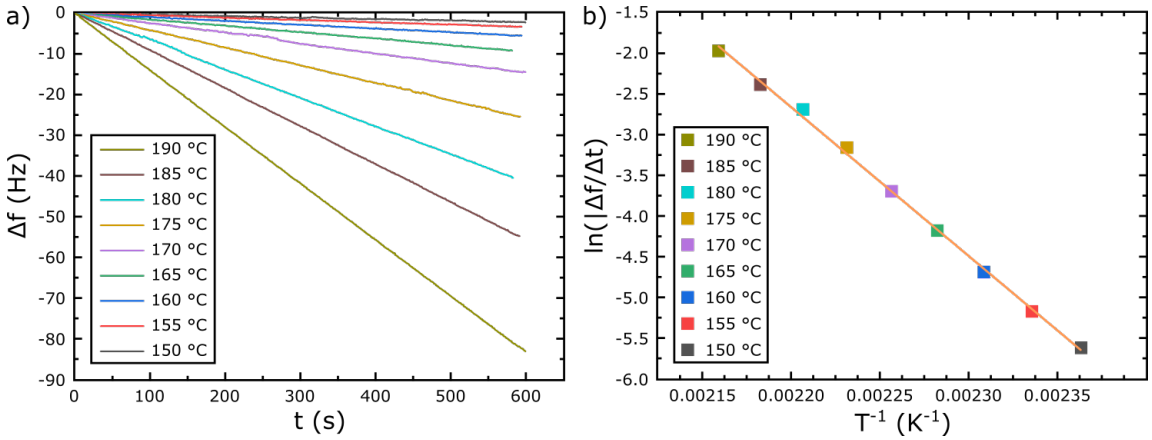

Figure 8.5: (a) Effusion rate measurements of NDA with a QCMB. The graph shows resonant frequency shifts Δf versus time t traces, acquired for crucible temperatures of a Knudsen cell as indicated. The slopes of the respective traces were determined by fitting with straight lines, and correspond to the effusion rates used for the Van't Hoff plot shown in: (b) Van't Hoff plot of the NDA effusion rates (squares) extracted from the traces shown in (a). The straight solid line represents a linear fit, and its slope corresponds to a NDA sublimation enthalpy of $\Delta H_{sub} = 152\ kJ\ mol^{-1}$. The excellent agreement between data points and fit indicates a constant, i.e. temperature independent, sublimation enthalpy and the absence of chemical changes of NDA during the sublimation.

Quantifying ΔH_{wet} is more intricate, but its effect is also often relatively small. To estimate the wetting enthalpy, we used MM to calculate adsorption energies of single 9A solvent molecules on either the NDA monolayer or bare graphite. Thereby, we assume that the intermolecular contributions to wetting are essentially similar for both cases. On graphite, 9A adsorption energies are almost constant for various adsorption sites with a modest variation between $(-69.7 ... -67.9)\ kJ\ mol^{-1}$. We use a graphene unit cell averaged value of $-68.6\ kJ\ mol^{-1}$. In contrast, 9A adsorption energies are as expected smaller on the NDA monolayer, and also exhibit larger site variations between $(-67.5 ... -42.2)\ kJ\ mol^{-1}$. We use a NDA unit cell averaged value of $-49.1\ kJ\ mol^{-1}$. This results in a wetting enthalpy $\Delta H_{wet}(9A) = -19.5\ kJ\ mol^{-1}$ for desorbing one 9A molecule from the NDA monolayer and re-adsorbing it on graphite. To derive an estimate for the wetting enthalpy $\Delta H_{wet}(NDA)$ per one NDA molecule, we renormalize $\Delta H_{wet}(9A)$:

$$\Delta H_{wet}(NDA) = \Delta H_{wet}(9A) \cdot \frac{A_{NDA}}{A_{9A}} \tag{8.3}$$

$$\Delta H_{wet}(NDA) = -19.5\ kJ\ mol^{-1} \cdot \frac{0.712 nm^2}{0.679 nm^2} = -20.4\ kJ\ mol^{-1} \tag{8.4}$$

Here, A_{NDA} and A_{9A} correspond to the surface areas occupied by a single NDA and 9A molecule, respectively. Therefore, we used the area per molecule in ordered

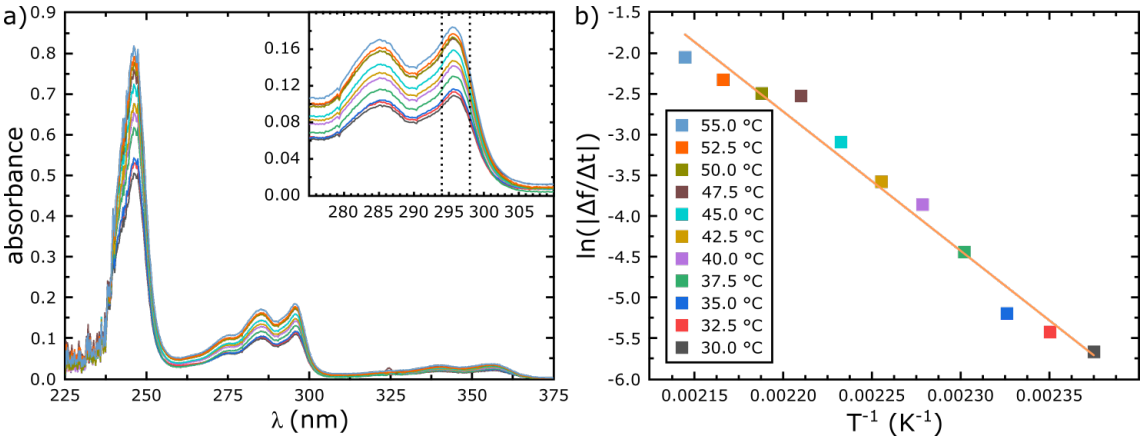

Figure 8.6: (a) UV-vis absorption spectra of saturated NDA in 9A solutions acquired for temperatures between 30.0 $°C$ (grey curve at the bottom) and 55.0 $°C$ with temperature increments of 2.5 $°C$. The increasing absorbance (i.e. concentration) for increasing temperature indicates an endothermic dissolution. Integrated absorbances (in a wavelength range of (294...298) nm, see insert) were used for the Van't Hoff plot shown in (b). In this spectral range, the absorbances were reasonably low to yield reliable values and no peak shifts occurred as illustrated in the insert. (b) Van't Hoff plot of integrated absorbances of saturated NDA in 9A solutions. The solid line represents a linear fit, and its slope corresponds to a NDA dissolution enthalpy of $\Delta H_{diss} = +18.8\ kJ\ mol^{-1}$.

monolayers as obtained from the STM derived unit cell for NDA and literature reported unit cells for 9A.[244] According to equation 8.4, adsorption of 9A on graphite is more favorable as compared to the NDA monolayer and results in an exothermic $\Delta H_{wet} = -20.4\ kJ\ mol^{-1}$. Combining all individual enthalpies in the Born-Haber cycle eventually results in a desorption energy for edge molecules into solution of $\Delta H_{edge-sol} = +16.4\ kJ\ mol^{-1}$, in vast discrepancy with the activation energy of $+208\ kJ\ mol^{-1}$ as derived from the Arrhenius plot.

The discrepancy between the two independent approaches is remarkably large. Admittedly, experimental errors in the Born-Haber cycle could also be relatively large, because each individual contribution, notably ΔH_{wet}, bears comparatively large uncertainties that add up in the error propagation. Nevertheless, the vast discrepancy is too large to be attributed to experimental errors. It rather challenges the common assumption that activation barriers and desorption energies are equal for NDA monolayers at the 9A-graphite interface. This implies a different origin of the desorption barrier, associated with the existence of a high energy transition state. The molecular origin of this transition state remains unknown, however, additional experiments hint toward an important role of solvent composition.

In repeat experiments with 9A solvent from a different batch we find substantial deviations. Remeasuring a desorption trace at 62.5 $°C$ resulted likewise in a single exponential decay, yet the rate constant was ~4.6 times lower, i.e. $1.9 \times 10^{-4}\ min^{-1}$ (repeat) as compared to $8.7 \times 10^{-4}\ min^{-1}$ (original) (Fig. 8.7a). Yet, an

additional feature in UV-vis absorption spectra of the solvent of the repeat experiment indicated its impurity (Fig. 8.7b).[245] Its chemical nature remains presently unclear, but we hypothesize that the impurity may be related to chemical changes of the solvent, rather than being a foreign species. Although the difference in rate constants appears rather drastic, it converts into a comparatively small energetic effect, where the desorption barrier is increased by only 4.3 $kJ\ mol^{-1}$ (assuming similar pre-exponentials).

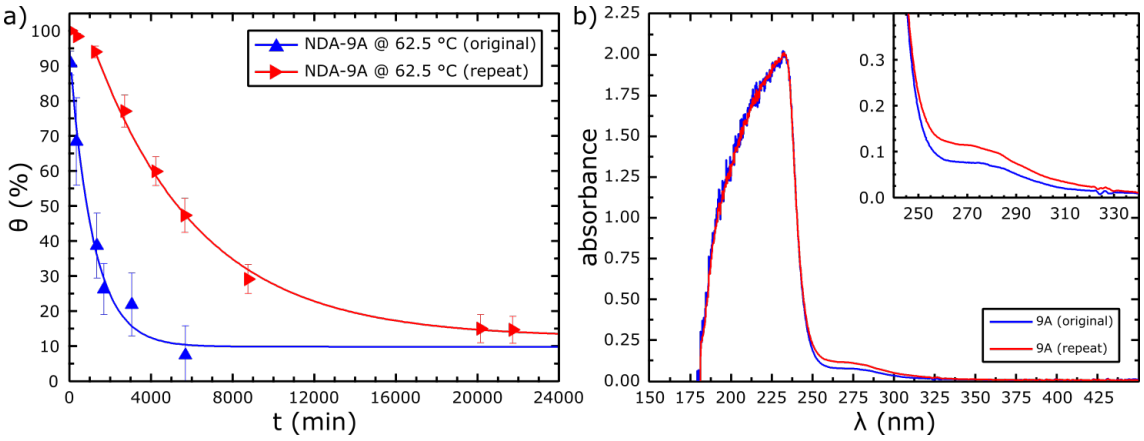

Figure 8.7: (a) Desorption traces of NDA monolayers acquired at the 9A-graphite interface for the same temperature of 62.5 $°C$. The blue curve shows the same data as in Fig. 8.2a, whereas the red curve presents data from a repeat experiment using 9A solvent from a different batch. Vertical error bars correspond to standard deviations, (invisibly small) horizontal error bars reflect the measurement duration. Solid lines represent fits with single exponential decays to an asymptotically reached final coverage resulting in $k = (8.7 \pm 1.49)\ 10^{-4}\ s^{-1}$ and $\theta_\infty = 9.8\ \%\ (\pm\ 4.52\ \%)$ for the original, and $k = (1.9 \pm 0.12)\ 10^{-4}\ s^{-1}$ and $\theta_\infty = 12.42\ \%\ (\pm\ 1.63\ \%)$ for the repeat experiment. Stated errors correspond to fitting uncertainties. (b) UV-vis absorption spectra of the pure 9A solvents used for the desorption traces shown in (a). While the strong absorbance below 250 nm arises from the carboxylic acid groups, distinct differences in the spectral range (250...330) nm indicate both notable batch-to-batch variations and a less pure state of the solvent in the repeat experiment. The chemical origin of these variations, remains presently unclear.

8.3 Summary and Conclusion

In summary, we have quantified the activation energy for NDA desorption from monolayers at 9A-graphite interfaces by quantitatively tracking the decline of molecular coverages over time at constant elevated temperatures. NDA desorption proceeds remarkably slow over the course of days. On the one hand, this facilitates quantification by relatively slow *in situ* STM measurements (∼90 min to acquire statistically significant data). On the other hand, experiments at fixed elevated

temperatures last for up to 8 days. This unprecedented experimental duration for variable-temperature STM experiments at liquid-solid interfaces could only be realized with our dedicated instrument (cf. chapter 6).[113] Over the measured temperature range from 57.5 $°C$ to 65.0 $°C$, coverages follow single exponential decays down to a base value θ_∞ that is determined by the temperature dependent position of the thermodynamic equilibrium. The extracted rate constants consistently lie on a straight line in an Arrhenius plot, indicating a constant activation energy for the rate-limiting elementary process. In addition, we quantified the desorption energy with respect to solution using a Born-Haber cycle, suggesting that the presence of solution lowers the desorption energy of $+170\ kJ\ mol^{-1}$ with respect to vacuum down to $+16.4\ kJ\ mol^{-1}$ with respect to solution. The present work focusses on the energetics of desorption, but including entropy contributions, i.e. considering free energies, would be more appropriate. Entropy is the thermodynamic driving force for desorption, and manifests itself in the decreasing equilibrium coverages for increasing temperatures. Yet, the relatively large errors in θ_∞ due to the indirect determination from fits prohibit a detailed analysis.

The key result is that the activation energy as derived from kinetic measurements differs notably from the desorption energy. From this vast discrepancy we conclude on a high energy transition state. However, also here entropic effects are vitally important, because rates are also determined by the free energy of the transition state. High transition state entropies can promote processes with large transition state energies through a large pre-exponential. Currently, we can only speculate about the origin and nature of this transition state. However, assuming a transition state where partly desorbed NDA molecules already gain entropy through leaving the surface, but are not yet energetically stabilized by solvation could explain both a high transition state energy and entropy.

Control experiments show sizeable deviations in rate constants for solvents from two different batches, where differences in the respective UV-vis absorption spectra indicate the presence of chemically distinct species in one solvent. From this, we hypothesize that the desorption kinetics, but less so the energetics, from NDA monolayers may be strongly influenced by an interfacial boundary layer between adsorbed monolayer and bulk solution. This boundary layer could be rate-determining for desorption, for instance by preventing effective solvation of the desorbing species, as the most important processes for lowering desorption energies.

Fundamental insights are expected from expanding these studies to comparable model systems, i.e. carboxylic acid tectons in fatty acid solvents, for which we recently reported an example of a dynamic structural response already at room temperature without measurable kinetic limitations (cf. chapter 7).[61] Hence, it would be rewarding to explore whether NDA is a singular example for the observed ultraslow desorption kinetics, and to unveil the underlying reasons at the molecular level. The first hint toward kinetic hindering that also originally motivated this study on NDA desorption was the low structural quality of its self-assembled monolayers, which is an exception rather than the rule. In the light of inhibited desorption, the persistence of the frequently observed line-defects (Fig. 8.1) at higher temperature

is particularly interesting as it suggests an important role of desorption-readsorption processes for self-healing, in particular for prochiral NDA molecules.

Lastly, we express our opinion that solvent purity requires more attention in the field of monolayer self-assembly at liquid-solid interfaces, in particular for quantitative studies. Solvents are almost exclusively used as received, but our study unambiguously shows that even batch-to-batch variations can have a profound effect on kinetics, potentially further extending to thermodynamics. Detailed knowledge on the chemical identity of impurities and a deeper understanding of their influence would not only be invaluable for the field, but constitutes a necessary precondition to improve both the batch-to-batch and lab-to-lab reproducibility of quantitative results.

8.4 Materials and Methods

8.4.1 Experimental Details

STM experiments

STM experiments were conducted with the I-STM operated by a commercial SPM 100 control unit (RHK) (cf. chapter 6).[113] Sample temperatures (i.e. imaging temperatures) were varied between room temperature and $\sim$70 $^{\circ}C$, and held constant with a Eurotherm 2416 temperature controller. STM images were acquired using tunneling voltages between $+0.25\ V$ and $+0.60\ V$ (at the tip) and setpoint currents around $\sim$50 pA. Mechanically cut Pt/Ir (90/10) wires used as STM tips without any further insulation, but were conditioned by short voltage pulses during the experiments. NDA (*Sigma Aldrich*, 99 % pure) and 9A (*TCI chemicals*, 98 % pure) were both used as received. For all desorption experiments NDA in 9A solutions were used with similar concentration of 0.11 $mmol\ L^{-1}$. These were obtained by diluting a saturated stock solution, and checked by UV-vis absorption spectroscopy. Freshly cleaved highly oriented pyrolytic graphite (grade ZYB, *Optigraph GmbH*) was used as substrate. For variable-temperature experiments the I-STM was filled with 10 mL of solution, resulting in complete immersion of the sample.

Coverage measurements

Molecular coverages were always evaluated the same way from a set of 25 large scale STM images ($350 \times 350\ nm^2$) covering a total surface area of $\sim$3.5 μm^2. Overlap between neighboring images was excluded by leaving a gap of at least 50 nm. Standard deviations were used as vertical error bars (see appendix B, Fig. B.6). The origin of the time axis was defined as the time when the target temperature was reached after initial heating periods of $\sim$30 min. The measurement halftime was used as time coordinate, and the (invisibly small) horizontal error bars correspond to the duration of $\sim$90 min required for each measurement.

Dissolution enthalpy measurements

To determine the dissolution enthalpy of NDA in 9A, a reservoir containing a relatively large amount of ∼18 mL solution was heated to the target temperature. Saturation was ensured by the presence of a sediment. After the targeted measurement temperature was reached, the stock solution was stirred for ∼2 h and allowed to settle and equilibrate for at least 20 h. For the actual measurement a small amount of the saturated solution was pipetted from the reservoir into the cuvette (1 mm optical path length, 110-QX macro-cuvette from *Hellma Analytics*) that was heated to the same temperature as the reservoir by Peltier elements.[74] Spectra were acquired with a USB4000 UV-vis spectrometer using a UV-vis-NIR light source (both *Ocean Optics*). Spectra of pure solvent from the same batch and heated to the same temperature served as reference. Measurements were performed for temperatures between 30.0 $°C$ and 55.5 $°C$ with increments of 2.5 $°C$. Measurement temperatures were varied non-monotonously to avoid and recognize kinetic effects (cf. chapter 3).

Sublimation enthalpy measurement

The NDA sublimation enthalpy was determined by measuring the temperature dependence of effusion rates as proxy for saturated vapour pressure.[74] These were measured using a home-built Knudsen cell[58] and a water-cooled CNT06IG quartz crystal microbalance (*Colnatex*), operated by a Q-pod quartz crystal monitor (*Inficon*) in high vacuum (cf. chapter 3).

8.4.2 Computational Details

Molecular mechanics (MM) calculations were performed using the Tinker software[246] with the MM3 force field.[247–249] Modified force-field parameters were used for the cyclic O···H-O $R_2^2(8)$ hydrogen bonds in carboxylic acid dimers as previously proposed[211] to yield a binding energy of 66.9 $kJ\ mol^{-1}$ in good agreement with experimental results[250] and both Density-Functional-Theory (DFT) and higher-level calculations.[251] For comparison, we also calculated NDA adsorption energies on graphite with DFT using previously optimized parameters.11 The excellent agreement between DFT (-94.8 $kJ\ mol^{-1}$) and MM (-93.1 $kJ\ mol^{-1}$) derived NDA adsorption energies indicates high accuracy and appropriateness of MM calculations for aromatic carboxylic acids on graphite.

Lattice parameters of the NDA monolayer were optimized by systematically scanning through a range of values for the lattice vectors a, b, and the angle γ between them to find the minimum-energy structure, similar to a previously described procedure.[74,106] Lattice parameters of NDA bulk crystals were optimized in a similar manner, by treating the 3D bulk structure as a stack of 2D layers. For these layers the previously optimized monolayer lattice parameters were used, while the lattice parameters c and the angles α and β were systematically varied to find the minimum-energy structure, similar to the procedure for the monolayers.[74]

Finite NDA islands of three sizes were considered: 3×3, 4×4 and 5×5 molecules.

Binding energies were calculated in all non-equivalent positions as energy differences upon removing a single NDA molecule. In all calculations, i.e. monolayer, islands and bulk crystal, the z coordinates of all atoms were fixed to constrain the molecules the same plane, while the in-plane coordinates x and y were optimized.

Adsorption of both a single NDA molecule and a 5×5 NDA island on graphite were also calculated using MM. The graphite surface was modelled using extended hydrogen-terminated graphene sheets, comprised of 20×20 primitive hexagonal graphene unit cells (2 carbon atoms per unit cell, i.e. in total 800 C and 80 H atoms) for adsorption of a single NDA molecule and of 24×22 non-primitive rectangular graphene unit cells (4 carbon atoms per unit cell, i.e. in total 2112 C and 140 H atoms) for adsorption of the 5×5 NDA island. The extended graphene sheets were large enough to ensure that the adsorbed molecules were at least 10 Åaway from the edges. Atomic positions within the graphene sheets were fixed, while the adsorbed NDA molecules were fully optimized. Positions and orientations of both the single adsorbed NDA molecule and the NDA island were investigated systematically by rotating the adsorbate through 120° (60° for the NDA island) in steps of 10° and translating each orientation of the adsorbate on a grid covering the whole graphene unit cell in steps of 0.1 Å, similar to a previously reported procedure.[74]

Very small variations of NDA adsorption energies were observed depending on the position and orientation of the molecules: $\leq 0.95\ kJ\ mol^{-1}$ variation for the single NDA molecule and $\leq 0.04\ kJ\ mol^{-1}$ per one NDA molecule for the 5×5 island. Note that in the island the NDA molecules occupy a range of different adsorption sites because of the incommensurability of the NDA monolayer with the underlying graphene. These results shows that the variation in adsorption sites has very little effect on the substrate contribution to NDA desorption energies.

Chapter 9

Summary and Conclusion

In this thesis, the influence of temperature and solvent on the self-assembly of molecular monolayers at the liquid-solid interface is fundamentally studied. For the characterisation of monolayers on surfaces, STM is used. In this respect, a novel approach was taken by developing a new type of STM: The Immersion Scanning Tunneling Microscope (I-STM). This new instrument is capable of performing long-term variable-temperature STM experiments at liquid-solid interfaces without any limitation in the duration of the experiments as solvent evaporation is completely suppressed. To quantify entropy and/or enthalpy changes upon dissolution and sublimation, variable-temperature UV-vis spectroscopy and vacuum effusion techniques are used, respectively. Molecular mechanics and density functional-theory calculations are applied to determine binding and adsorption energies of molecules in adsorbed monolayers and bulk crystals.

Immersion Scanning Tunneling Microscope

Liquid-solid STM experiments at elevated temperatures with locally heated samples inevitable lead to enhanced solvent evaporation rates and high thermal drift. Thermal equilibration requires time but enhanced solvent evaporation can lead to substantial concentration changes and the distortion of the final results. At the end, this type of STM experiments is less determined by scientific interests but rather by a trade-off between settling at thermal drift and minimizing solvent evaporation. This problem was solved with the development of the I-STM in the course of this thesis. The instrument is working in a hermetically sealed and heatable container, thereby solvent evaporation is completely eliminated. Hence, extended waiting times for thermal drift to settle, i.e. complete thermal equilibration, become affordable. Rapid thermal equilibration is further promoted by the choice of materials with good thermal conductivities and a design optimized in terms of heat transport across the instrument, i.e. introduction of heat bridges in a highly symmetric design. Low steady-state lateral drifts (0.06 ± 0.04 to 0.25 ± 0.12 $nm\ min^{-1}$) are achieved via a precise temperature control ($\pm$ 0.012 to $\pm$ 0.025 $°C$) between room temperature and 100 $°C$. This opens up the possibility to aquire low-drift high-resolution STM

images even at elevated temperatures. Fatty acids are highly appropriate solvents for STM experiments at the liquid-solid interface. Yet, these solvents are rather corrosive against less noble metals and epoxy based glues. To avoid corrosion of the instrumental setup and to preserve the purity of the solution, all solvent exposed parts are either made from completely inert materials or covered by a protection layer. Depending on the material, a pinhole free layer of gold or/and a layer of a fully inert fluoroelastomeric coating material is applied on the vulnerable components. Thereby, the I-STM becomes completely inert against the corrosive fatty acid solvents, while the purity of the solution is always ensured.

Being not limited to STM, the I-STM serves as a development platform for the future integration of other SPM techniques, e.g implementation of a non-contact AFM via a tuning fork probe stage. The required design implementations for AFM extensions already exists. Different environmental conditions are also feasible, e.g. experiments in defined gas atmospheres or even at vacuum conditions are possible through an additional inlet in the container lid. Use of the I-STM at even higher operating temperatures above 100 $°C$ appears also possible. While short-term measurements ($\sim$3h) at 110 $°C$ have already been performed in this thesis, further corrosion tests, especially for the coating materials, are of crucial importance before considering long-term studies at significantly higher temperatures ($\sim$150 $°C$). Furthermore, operating the I-STM as a temperature-controlled electrochemical STM is feasible by adjusting the container and sample/tip holder stages, i.e. turning the system into an electrochemical cell.

Solvent-Induced Polymorphism

In the first experimental part, the phenomenon of solvent-induced polymorphism in liquid-solid self-assembly is studied. Therefore, TMA is used as a model system. Dissolved in the homologous series of fatty acids, TMA self-assembles on graphite into two different porous polymorphs: The more densely packed flower polymorph for shorter alkyl chain length, while for longer chain length the less densely packed chickenwire structure evolves with a sharp threshold between 6A and 7A. First, the gain of Gibbs free energy per unit area Δg was quantified to provide inside in the underlying thermodynamics. To this end, Δh, the enthalpy gain per unit area, was evaluated with the aid of a Born-Haber cycle for both polymorphs in 6A and 7A and additionally in 9A. The Born-Haber cycle was constructed from density-functional theory calculated monolayer binding energies with respect to vacuum and measured sublimation and dissolution enthalpies, using vacuum effusion and variable-temperature UV-vis experiments, respectively. While the enthalpy differences between the chickenwire and flower structure are too small to gain any conclusion (slight enthalpic preference of the chickenwire structure), the entropy cost per unit area Δs is significantly larger for the flower polymorph. This is owing to the 20 % higher packing density of the flower polymorph. Hence, in contrast to the experimental observations, the chickenwire polymorph should be the thermodynamic most stable polymorph in all solvents. Variable-temperature experiments in

6A with the aid of the I-STM support this hypothesis, as with increasing temperature a reversible phase transition from the flower to the chickenwire structure occurs at 110 $°C$. With further support from additional experiments at room temperature a kinetic stabilization of the flower structure in 6A could be ruled out. Thereby, the initially assembled chickenwire polymorph in 7A spontaneously converted into the flower polymorph by applying a sufficient amount of TMA-6A solution.

In the end, stereochemically specific solvent coadsorption is proposed as the origin of the solvent-induced polymorphism of TMA. While both polymorphs feature identically hexagonal pores, the flower polymorph additional exhibits unique smaller elongated pores. Experiments with side-substituted 6A solvent derivates (methyl-6A and ethyl-6A) revealed a highly selective solvent coadsorption in the elongated pores via stereochemically selection. By just adding a single methylene unit to the main chain (6A to 7A) or to the side chain (methyl-6A to ethyl-6A), solvent coadsorption is sterically hindered in the smaller elongated pores and the chickenwire polymorph evolves. These findings indicate that solvent coadsorption can become structure determining if size and shape of the pores are comparable to the molecular structure of the used solvent.

The combination of a thermodynamic evaluation by applying an adapted Born-Haber cycle and analysing dissolution entropies together with the structural variation of solvents without affecting their main mode of interaction, e.g. side or main chain substitution of alkyl chains, holds great promise to identify and gain an enhance understanding of solvent effects. Deeper insights in these effects are expected by applying this complementary approach on other cases of solvent-induced polymorphism, e.g. in van der Waal or halogen-bonded systems. To conclude on the generality of the stabilizing effect of polymorph-specific solvent coadsorption, this study could be extended to systems whose polymorphs exhibit pores with different sizes and shapes. Furthermore, evaluating different classes of solvents, e.g. aprotic solvents like 1,2,4-trichlorobenzene or phenyloctane that exhibit inferior substrate interaction with graphite, might also provide deeper insights in the phenomenon of solvent coadsorption.

Ultraslow Desorption Kinetics

Thermodynamic equilibria in self-assembly at liquid-solid interfaces are characterized through the continuous exchange of molecules between the molecular monolayer and the supernatant solution, i.e. a dynamic equality between adsorption and desorption processes. Any hindrance in either adsorption or desorption results in kinetic trapping and might stabilize the system at a metastable state.

In novel experiments, the dissolution kinetics of NDA monolayers self-assembled at the 9A-graphite interface was studied. Using the I-STM, variable-temperature experiments were performed, where the decline of NDA monolayer coverage vs. time at constant elevated temperatures was tracked. Remarkably, the desorption of NDA monolayers proceeds very slowly over the course of days facilitating the quantification by relatively slow STM measurements. The time-dependent coverage of NDA

monolayers was tracked for four temperatures between 57.5 $°C$ and 65.0 $°C$. Coverages followed single exponential decays settling at final finite coverages. Each final coverage corresponds to the temperature-dependent position of the thermodynamic equilibrium. In an Arrhenius plot, the extracted rate constants result in a linear slope, indicating a constant activation energy of 208 $kJ\ mol^{-1}$ for the rate-limiting process. Yet, using measurement data from dissolution and effusion experiments as well as molecular mechanics calculated binding energies, an adapted Born-Haber cycle provided a desorption energy of only 16.4 $kJ\ mol^{-1}$. This value stands in vast discrepancy with the activation energy of 208 $kJ\ mol^{-1}$ extracted from the rate constants.

The discrepancy between the kinetic measurements and the data from the Born-Haber cycle hints towards the existence of a high energy transition state. However, verifying this hypothesis is virtually impossible without access to quantitative data of the transition state entropy, as the rates are determined by the free energy of the transition state. To resolve this discrepancy, a transition state is proposed in which the molecules partially leave the surface. Thereby, entropy is already gained but through the remaining interaction with the surface the molecules are not yet energetically stabilized by effective solvation. At this point, the nature and origin of this high energy transition state remain unclear. One explanation could be the existence of a boundary layer between the adsorbed monolayer and solution, determining desorption kinetics by preventing effective solvation as this is the most important mechanism to decrease desorption energy.

Further control experiments revealed a significant deviation in the rate constants for a different batch of solvents. In one solvent, UV-vis absorption spectroscopy indicated the existence of chemically distinct species resulting in a measureable decrease of the rate constant (factor $\sim$4.6). However, the influence of the impurity on the desorption energy is rather small as the barrier increases by only 4.3 $kJ\ mol^{-1}$ under the assumption of a similar pre-exponential factor.

To unveil the underlying reasons for this phenomenon of ultraslow desorption kinetics at the molecular level, further explorations are required. Expanding this study to other model systems, e.g. comparable carboxylic building blocks in fatty acid solvents, could also clarify if NDA represents a singular example for ultraslow desorption kinetics. Yet, identifying a model system featuring ultraslow kinetics can be intricate. A first hint could be an uncommonly low structure quality for self-assembly at the liquid-solid interface through the inhibition of self-healing processes, which was also the original motivation for the present study on NDA.

The study also demonstrated that the purity of solvent is crucially important and requires more attention in self-assembly research at liquid-solid interfaces. Even batch-to-batch variations can effectively alter self-assembly by affecting kinetics and potentially also the underlying thermodynamics. The chemical identification of impurities and the evaluation of their influence on self-assembly is highly desirable for a deeper understanding and to improve the lab-to-lab and batch-to-batch reproducibility of experimental results.

Final Remarks

Studying molecular self-assembly is crucially important for the further advancement of nanoscience. In this respect, temperature is a highly important parameter as it affects both, kinetics and thermodynamics. With the development of the I-STM, an instrument was realized to directly analyse the impact of temperature on monolayer self-assembly at the liquid-solid interface in real space. The instrument is highly suited for mechanistic studies. For instance, by varying the temperature, the I-STM can be used to distinguish between a kinetically or thermodynamically controlled process. Furthermore, the transition temperatures of reversible and irreversible processes at liquid-solid interfaces could now be identified in unprecedented detail via quasi-static temperature changes in long-term experiments. The I-STM also promotes the quantification of the dynamics of reversible processes in monolayer self-assembly, e.g. hysteresis in temperature-induced reversible phase transitions. Moreover, rate constants of slowly proceeding kinetic effects and final thermodynamic equilibrium states can be precisely determined and quantified as limitations in the experimental duration are efficiently eliminated.

The capability and scientific utility of the I-STM to provide high-resolution imaging data at elevated temperature from the liquid-solid interface over an arbitrary long time period was proven in two fundamental studies. With the I-STM at hand, further insights in kinetic effects and thermodynamic driving forces are expected and future extensions to other SPM techniques or environments will even enhance the applicability of this new instrument in nanoscience.

Appendix A

A.1 Lattice Parameters of the TMA Flower Polymorph

The lattice parameters of the TMA flower polymorph was derived from Fig. A.1 and other comparable images.

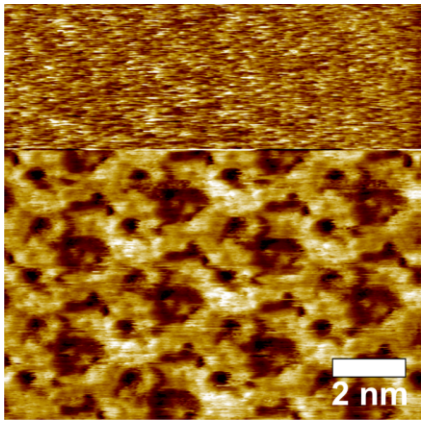

Figure A.1: STM image of the TMA flower polymorph on graphite(0001) acquired in saturated 6A solution. The lower part of this "split-image" shows the molecular structure, whereas after reducing the tunneling voltage the underlying graphite substrate was imaged in the upper part (sample voltage used for imaging TMA and current setpoint: -588 mV, 62.4 pA).

An angle of between $\alpha = 5.5° \pm 1.0°$ the lattices of the TMA flower polymorph and graphite was extracted. From STM images experimental lattice parameters of $a = b = (2.60 \pm 0.05)\ nm$ were derived for the TMA flower polymorph. These experimental data are in perfect agreement with the proposed $\begin{pmatrix} 11 & 1 \\ -1 & 10 \end{pmatrix}$ commensurate superstructure as used for the DFT simulations (*vide supra*), resulting in $\alpha_{commensurate} = 4.7°$ and $a_{commensurate} = b_{commensurate} = 2.59\ nm$.

A.2 Inverted Contrast of the TMA Flower Polymorph

In the STM contrast of Fig. A.2 both types of pores appear brighter than the TMA networks. This inverted contrast is frequently observed for the flower polymorph in 6A and provides further evidence for solvent co-adsorption in both types of pores, i.e. the smaller elongated and the larger circular pores.

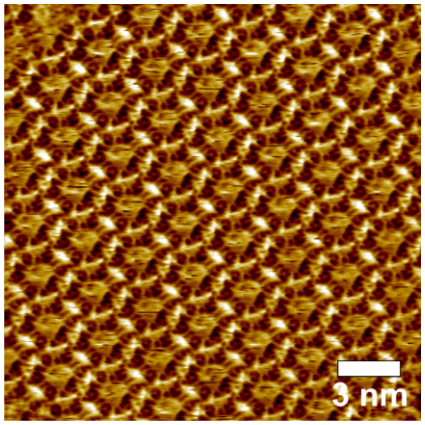

Figure A.2: STM image of the TMA flower polymorph on graphite(0001) acquired in saturated 6A solution (sample voltage and current setpoint: -600 mV, 53 pA).

A.3 UV-Vis Absorption Spectra of TMA in 6A

The increasing absorbance for increasing temperature of a saturated TMA in 6A solution (Fig A.3) indicates an endothermic dissolution. For the Van't Hoff plot (Fig. 7.4) the absorbance was integrated in the spectral range λ = (281 — 287) nm, i.e. in a region where the absorbance is reasonably low to provide reliable values.

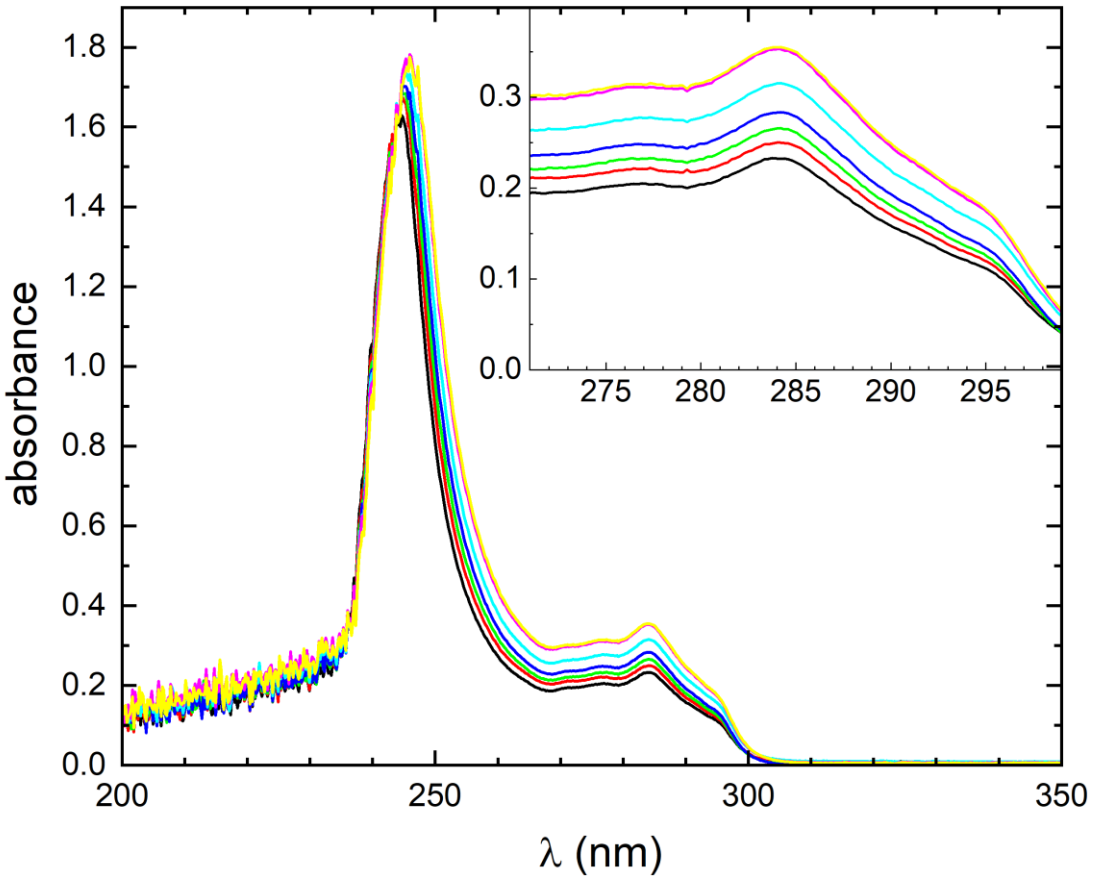

Figure A.3: UV-Vis absorption spectra of saturated TMA in 6A solutions acquired for temperatures from 30.0 °C (black curve at the bottom) to 60.0 °C with temperature increments of 5.0 °C. The increasing absorbance for increasing temperature indicates an endothermic dissolution. For the Van't Hoff plot (Fig. 7.4) the absorbance was integrated in the spectral range λ = 281 - 287 nm, i.e. in a region where the absorbance is reasonably low to provide reliable values.

A.4 UV-Vis Absorption Spectra of TMA in 7A

The increasing absorbance for increasing temperature of a saturated TMA in 7A solution (Fig A.4) indicates an endothermic dissolution. For the Van't Hoff plot (Fig. 7.4) the absorbance was integrated in the spectral range $\lambda = (281 — 287)$ nm, i.e. in a region where the absorbance is reasonably low to provide reliable values.

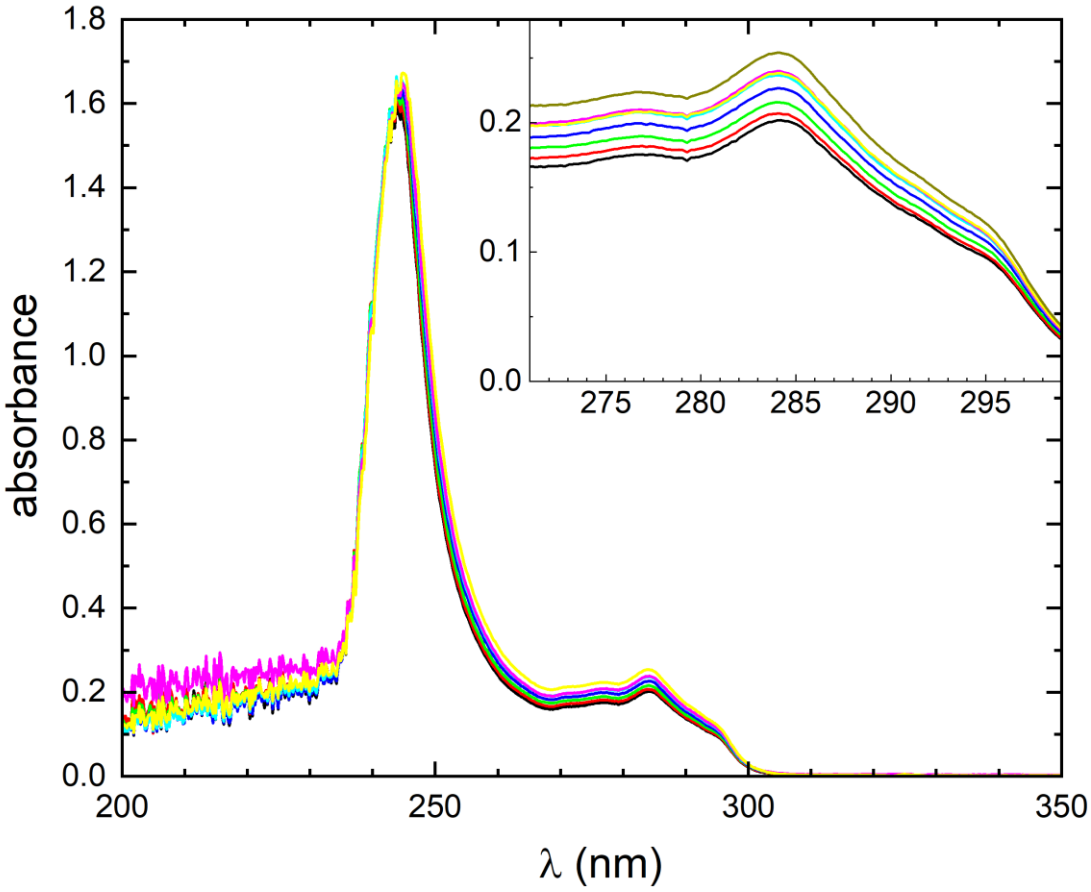

Figure A.4: UV-Vis absorption spectra of saturated TMA in 7A solutions acquired for temperatures from 32.5 °C (black curve at the bottom) to 50.0 °C with temperature increments of 2.5 °C. To exclude systematic errors due to for instance kinetic effects, temperatures were varied non monotonously. The increasing absorbance for increasing temperature indicates an endothermic dissolution. For the Van't Hoff plot (Fig. 7.4) the absorbance was integrated in the spectral range $\lambda = 281$ - 287 nm, i.e. in a region where the absorbance is reasonably low to provide reliable values.

A.5 UV-Vis Absorption Spectra of TMA in 9A

The increasing absorbance for increasing temperature of a saturated TMA in 9A solution (Fig A.5) indicates an endothermic dissolution. For the Van't Hoff plot (Fig. 7.4) the absorbance was integrated in the spectral range $\lambda = (281 — 287)$ nm, i.e. in a region where the absorbance is reasonably low to provide reliable values.

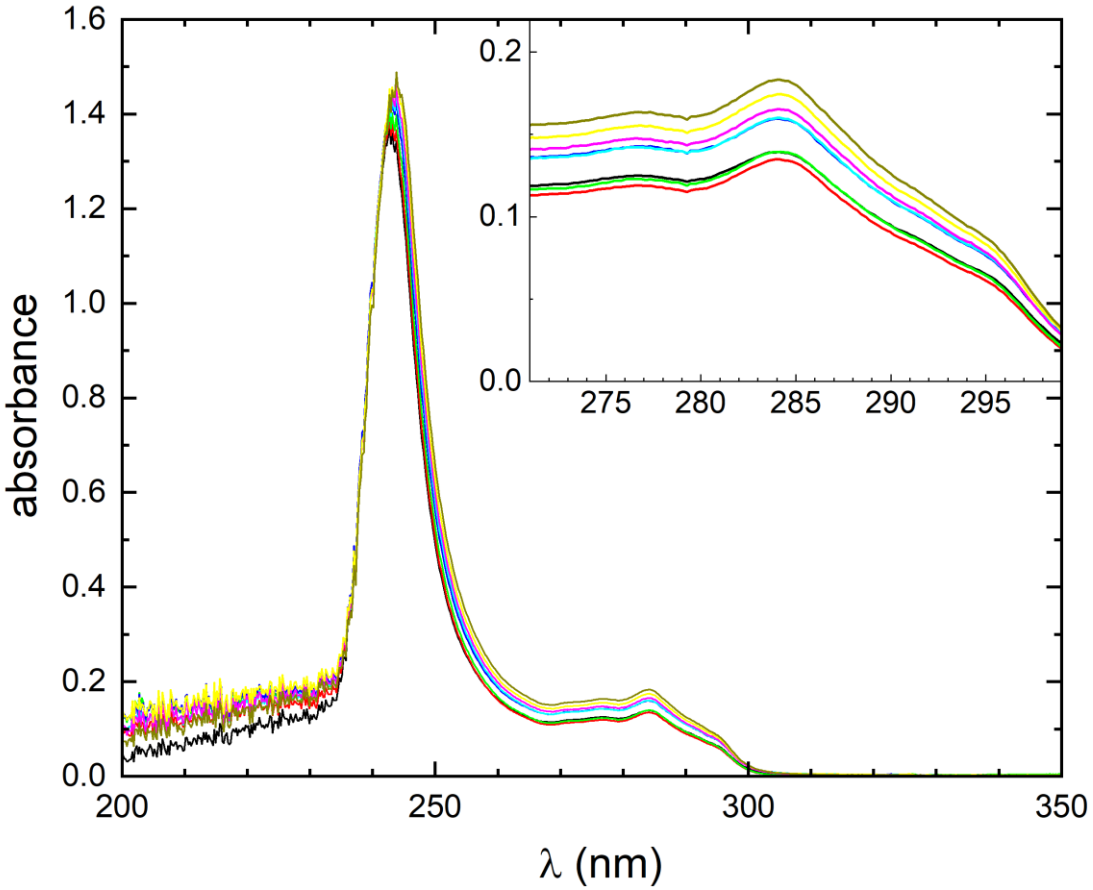

Figure A.5: UV-Vis absorption spectra of saturated TMA in 7A solutions acquired for temperatures from 32.5 °C (black curve at the bottom) to 50.0 °C with temperature increments of 2.5 °C. To exclude systematic errors due to for instance kinetic effects, temperatures were varied non monotonously. The increasing absorbance for increasing temperature indicates an endothermic dissolution. For the Van't Hoff plot (Fig. 7.4) the absorbance was integrated in the spectral range $\lambda = 281$ - 287 nm, i.e. in a region where the absorbance is reasonably low to provide reliable values.

A.6 Guest-Species in TMA Polymorphs

DFT-optimization and MD simulations of different TMA and hexanoic acid (6A) anhydrides as possible guest-species in the ∼1 nm wide circular pore that is common to both flower and chickenwire polymorph are shown in Fig. A.6. The left hand sides show the outcomes of structure optimization, whereas the structures obtained after 1 ps long MD runs are shown on the right hand sides. The influence of the supernatant solution is neglected here, the respective binding energies (stated in parenthesis) are reasonably large to conclude on stable adsorption of these species within the pores

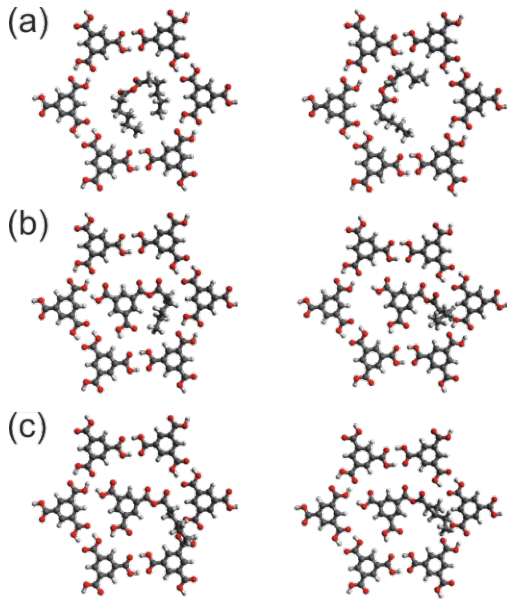

Figure A.6: DFT-calculations (left hand side) and MD-simulations (right hand side) were performed on graphene (omitted for clarity). (a) 6A anhydride (-1.25 eV); (b) TMA 6A anhydride species with initially flat adsorbed alkane tails (-1.55 eV); (c) TMA 6A anhydride species with initially upright adsorbed alkane tails (-1.43 eV).

Appendix B

B.1 NDA Monolayer Structure

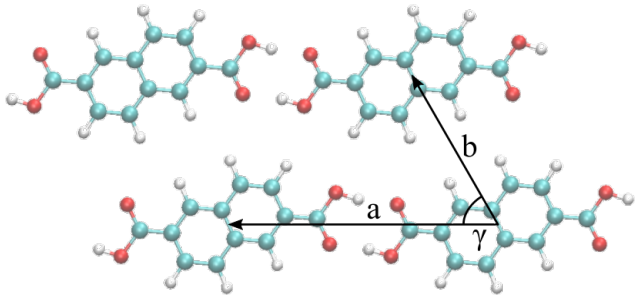

Figure B.1: NDA monolayer structure as obtained by MM calculations. The optimised lattice parameters are: a = 1.15 nm (corresponding to the repeat distance along the H-bonded chains), b = 0.74 nm, $\gamma = 60.0°$.

B.2 NDA Bulk Structure

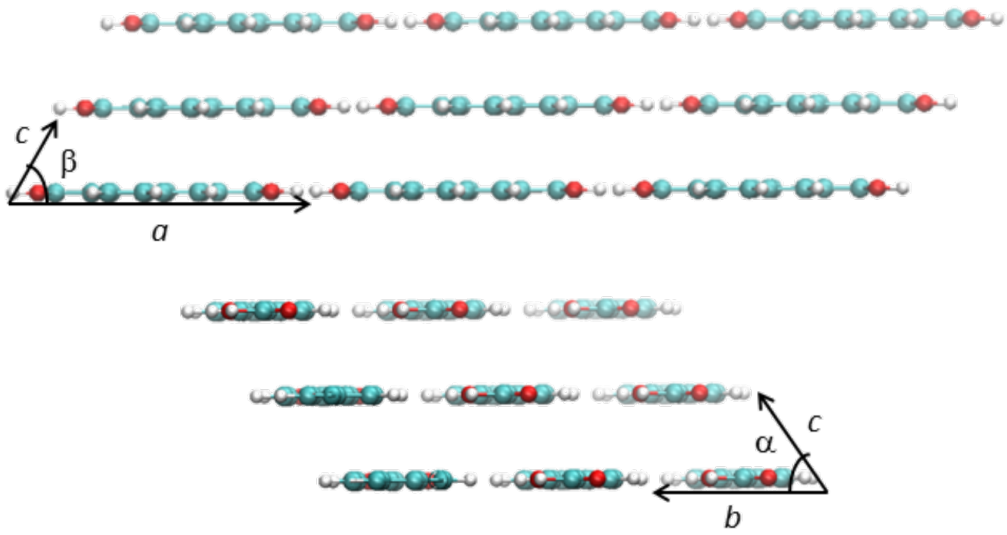

Figure B.2: NDA bulk structure as obtained by MM calculations. The optimised lattice parameters are: $a = 1.15\ nm$, $b = 0.74\ nm$, $c = 0.45\ nm$, $\alpha = 74.7°$, $\beta = 63.9°$, $\gamma = 60.0°$.

B.3 NDA 5×5 Island on Graphene

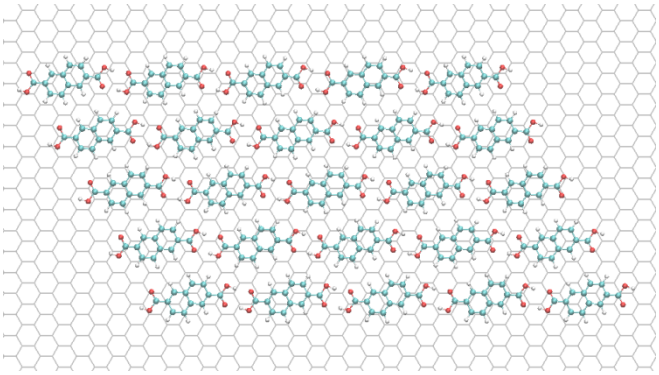

Figure B.3: MM optimized finite island comprised of 5×5 NDA molecules on graphene (not fully shown here). This structure corresponds to the energy minimum for all positions and orientations probed. Yet, the energy variations were relatively small, also because of averaging over the non-equivalent NDA adsorption sites in this incommensurate structure.

B.4 NDA Binding Energy in a 3×3 Island

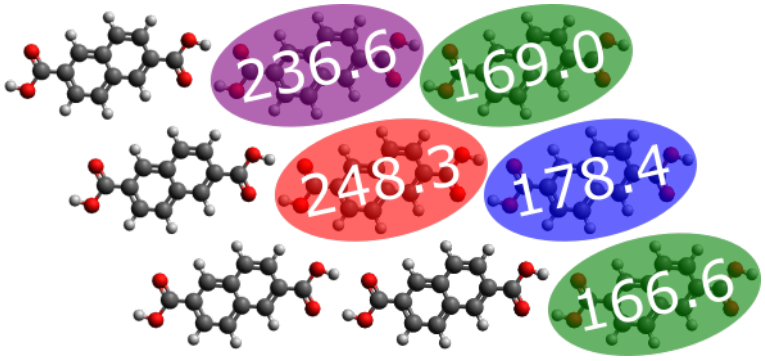

Figure B.4: MM derived desorption energies of NDA molecules (in $kJ\ mol^{-1}$) from a finite island comprised of 3×3 NDA molecules. Calculations were conducted on graphite(0001) (not shown for clarity). Desorption energies for edge molecules are similar to results obtained on a larger 5×5 island (see Fig. 8.3), indicating that desorption energies are only diminished for molecules directly at the domain edge.

B.5 Masking Method

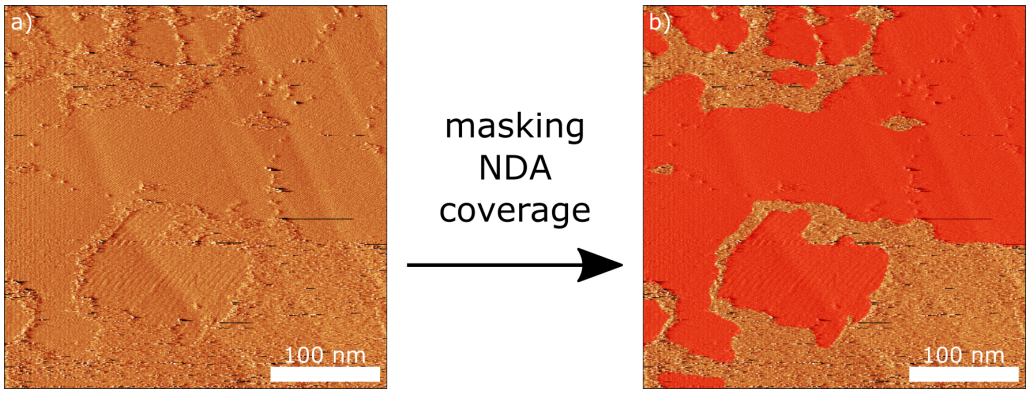

Figure B.5: Example illustrating how molecular coverages were determined from individual STM images. (a) Original large scale (350 nm) STM image (current image, tunneling parameters: 0.59 V, 49.5 pA); Even though molecular details of the NDA domains cannot be inferred anymore at this magnification, it was always possible to unambiguously distinguish NDA domains from the uncovered graphite surface. (b) Processed image with NDA domains masked in red; Therefore a feature of the image processing software Gwyddion was used.[252] The ratio of the area marked in red to the total area of the image corresponds to the molecular coverage, i.e. ∼64 % for the example here. For each coverage data point 25 of these large scale STM images were evaluated, Fig. B.6 shows a full series.

B.6 Complete Measurement Series at 57.5 °C

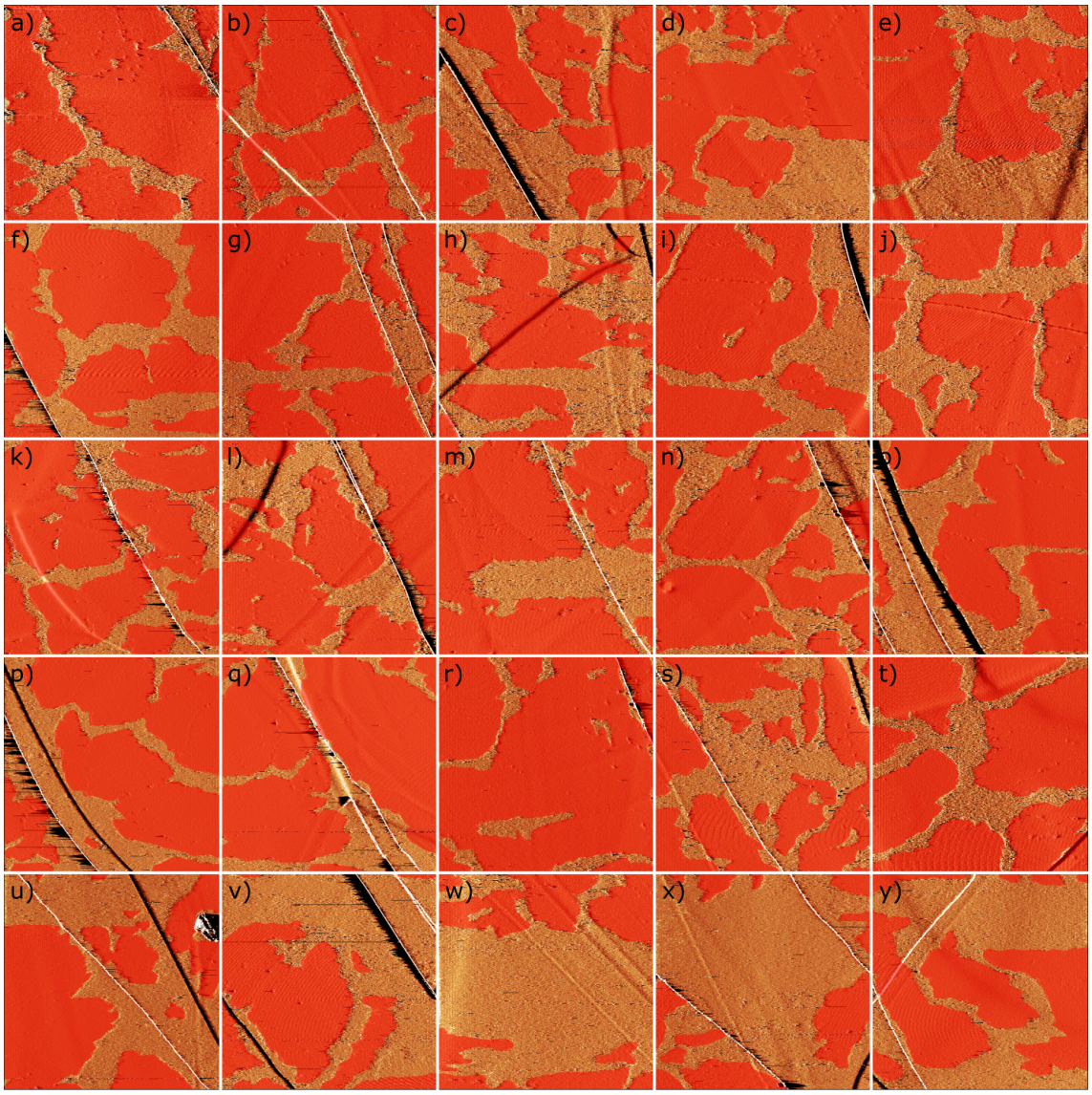

Figure B.6: Complete series of 25 large scale STM images (350 × 350 nm^2, tunneling parameters: 0.59 V, ∼50 pA) evaluated to determine a statistically significant coverage value. These images were acquired at 57.5 °C in ∼77 min. of measurement time and were masked as described in Fig. B.5. Overlap between adjacent images was avoided by leaving a gap of at least 50 nm. Depending on the local topography (e.g. step edges) either forward or backward current images were used whichever provided more clear information.

B.7 NDA Monolayer Desorption Data for $\theta_\infty = 0$

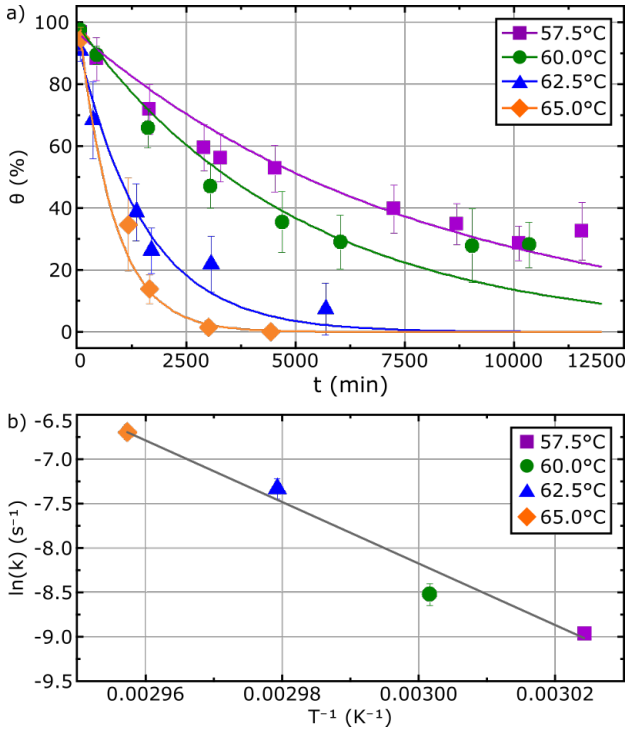

Figure B.7: Summarized results of kinetic measurements on NDA monolayer desorption (same data set as in Fig. 8.2a); (a) Molecular coverage θ vs. time t traces measured by STM at fixed temperatures (purple squares: 57.5 $°C$; green dots: 60.0 $°C$; blue triangles: 62.5 $°C$; orange diamonds: 65.0 $°C$); Vertical error bars correspond to standard deviations, and (invisibly small) horizontal error bars reflect the measurement duration of ~90 min. Solid lines represent fits with single exponential decays to zero (i.e. $\theta_\infty = 0$ % set for all desorption traces) (cf. Table B.1 for a summary of the fitting results). (b) Arrhenius plot of the rate constants. The solid line represents a linear fit, with a slope corresponding to an activation energy of +289 $kJ\ mol^{-1}$. Fitting uncertainties account for vertical error bars. Fitting the desorption traces with single exponential decays, i.e. neglecting finite partial coverages, results in a significantly higher activation barrier.

B.8 Rate Constants for $\theta_\infty = 0$

Table B.1: Rate constants k as obtained from fitting desorption traces in Fig. B.7a acquired at temperatures T with single exponential decays to zero; fitting uncertainties are stated in parenthesis;

T ($^\circ C$)	**k** ($10^{-4}\ min^{-1}$)
57.5	1.27 ($\pm$0.09)
60.0	1.98 ($\pm$0.24)
62.5	6.56 ($\pm$0.74)
65.0	12.44 ($\pm$1.04)

List of Figures

List of Tables

References

[1] Lehn, J.-M. Supramolecular chemistry. *Science* **1993**, *260*, 1762–1763.

[2] Lehn, J.-M. Supramolecular Chemistry–Scope and Perspectives Molecules, Supermolecules, and Molecular Devices (Nobel Lecture). *Angew. Chem. Int. Ed. Engl.* **1988**, *27*, 89–112.

[3] Whitesides, G. M.; Mathias, J. P.; Seto, C. T. Molecular self-assembly and nanochemistry: a chemical strategy for the synthesis of nanostructures. *Science* **1991**, *254*, 1312–1319.

[4] Whitesides, G. M.; Grzybowski, B. Self-Assembly at All Scales. *Science* **2002**, *295*, 2418–2421.

[5] Mendes, A. C.; Baran, E. T.; Reis, R. L.; Azevedo, H. S. Self-assembly in nature: using the principles of nature to create complex nanobiomaterials. *WIREs Nanomed. Nanobiotechnol.* **2013**, *5*, 582–612.

[6] Hemsley, A. R.; Collinson, M. E.; Kovach, W. L.; Vincent, B.; Williams, T. The role of self-assembly in biological systems: evidence from iridescent colloidal sporopollenin in *Selaginella* megaspore walls. *Phil. Trans. R. Soc. Lond. B, Biol. Sci.* **1994**, *345*, 163–173.

[7] Whitesides, G. M.; Kriebel, J. K.; Mayers, B. T. In *Nanoscale Assembly: Chemical Techniques. Self-Assembly and Nanostructured Materials*; Huck, W. T. S., Ed.; Springer US: Boston, MA, 2005; pp 217–239.

[8] Nie, Z.; Petukhova, A.; Kumacheva, E. Properties and emerging applications of self-assembled structures made from inorganic nanoparticles. *Nat. Nanotechnol.* **2010**, *5*, 15–25.

[9] Thiruvengadathan, R.; Korampally, V.; Ghosh, A.; Chanda, N.; Gangopadhyay, K.; Gangopadhyay, S. Nanomaterial processing using self-assembly-bottom-up chemical and biological approaches. *Rep. Prog. Phys.* **2013**, *76*, 066501.

[10] Binnig, G.; Rohrer, H.; Gerber, C.; Weibel, E. Surface Studies by Scanning Tunneling Microscopy. *Phys. Rev. Lett.* **1982**, *49*, 57–61.

[11] Binnig, G.; Rohrer, H. Scanning tunneling microscopy. *Surface Science* **1983**, *126*, 236–244.

[12] Eigler, D. M.; Schweizer, E. K. Positioning single atoms with a scanning tunnelling microscope. *Nature* **1990**, *344*, 524–526.

[13] Binnig, G.; Rohrer, H. Scanning Tunneling Microscopy–from Birth to Adolescence (Nobel Lecture). *Angew. Chem. Int. Ed. Engl.* **1986**, *26*, 606–614.

[14] Eichhorn, J.; Nieckarz, D.; Ochs, O.; Samanta, D.; Schmittel, M.; Szabelski, P. J.; Lackinger, M. On-Surface Ullmann Coupling: The Influence of Kinetic Reaction Parameters on the Morphology and Quality of Covalent Networks. *ACS Nano* **2014**, *8*, 7880–7889.

[15] Galeotti, G. et al. Synthesis of mesoscale ordered two-dimensional π-conjugated polymers with semiconducting properties. *Nat. Mater.* **2020**, *19*, 874–880.

[16] Miranda, R.; García, N.; Baró, A. M.; García, R.; Peña, J. L.; Rohrer, H. Technological applications of scanning tunneling microscopy at atmospheric pressure. *Appl. Phys. Lett.* **1985**, *47*, 367–369.

[17] Madueno, R.; Räisänen, M. T.; Silien, C.; Buck, M. Functionalizing hydrogen-bonded surface networks with self-assembled monolayers. *Nature* **2008**, *454*, 618–621.

[18] McIntyre, B. J.; Salmeron, M. B.; Somorjai, G. A. A scanning tunneling microscope that operates at high pressures and high temperatures (430 K) and during catalytic reactions. *Catal. Letters* **1992**, *14*, 263–269.

[19] Sonnenfeld, R.; Hansma, P. K. Atomic-Resolution Microscopy in Water. *Science* **1986**, *232*, 211–213.

[20] Drake, B.; Sonnenfeld, R.; Schneir, J.; Hansma, P. K. Scanning tunneling microscopy of processes at liquid-solid interfaces. *Surf. Sci.* **1987**, *181*, 92–97.

[21] Schneir, J.; Marti, O.; Remmers, G.; Gläser, D.; Sonnenfeld, R.; Drake, B.; Hansma, P. K.; Elings, V. Scanning tunneling microscopy and atomic force microscopy of the liquid–solid interface. *J. Vac. Sci. Technol.* **1988**, *6*, 283–286.

[22] De Feyter, S.; De Schryver, F. C. Self-Assembly at the Liquid/Solid Interface: STM Reveals. *J. Phys. Chem. B* **2005**, *109*, 4290–4302.

[23] Yang, Y.; Wang, C. Solvent effects on two-dimensional molecular self-assemblies investigated by using scanning tunneling microscopy. *Curr. Opin. Colloid Interface Sci.* **2009**, *14*, 135–147.

[24] Gutzler, R.; Sirtl, T.; Dienstmaier, J. F.; Mahata, K.; Heckl, W. M.; Schmittel, M.; Lackinger, M. Reversible Phase Transitions in Self-Assembled Monolayers at the Liquid-Solid Interface: Temperature-Controlled Opening and Closing of Nanopores. *J. Am. Chem. Soc.* **2010**, *132*, 5084–5090.

[25] Blunt, M. O.; Adisoejoso, J.; Tahara, K.; Katayama, K.; Van der Auweraer, M.; Tobe, Y.; De Feyter, S. Temperature-Induced Structural Phase Transitions in a Two-Dimensional Self-Assembled Network. *J. Am. Chem. Soc.* **2013**, *135*, 12068–12075.

[26] Jahanbekam, A.; Vorpahl, S.; Mazur, U.; Hipps, K. W. Temperature Stability of Three Commensurate Surface Structures of Coronene Adsorbed on Au(111) from Heptanoic Acid in the 0 to 60° C Range. *J. Phys. Chem. C* **2013**, *117*, 2914–2919.

[27] Jahanbekam, A.; Mazur, U.; Hipps, K. W. A new variable temperature solution-solid interface scanning tunneling microscope. *Rev. Sci. Instrum.* **2014**, *85*, 103701.

[28] Lackinger, M.; Griessl, S.; Heckl, W. M.; Hietschold, M.; Flynn, G. W. Self-Assembly of Trimesic Acid at the Liquid-Solid Interfacea Study of Solvent-Induced Polymorphism. *Langmuir* **2005**, *21*, 4984–4988.

[29] Heininger, C.; Kampschulte, L.; Heckl, W. M.; Lackinger, M. Distinct differences in self-assembly of aromatic linear dicarboxylic acids. *Langmuir* **2009**, *25*, 968–972.

[30] Fritton, M.; Duncan, D. A.; Deimel, P. S.; Rastgoo-Lahrood, A.; Allegretti, F.; Barth, J. V.; Heckl, W. M.; Björk, J.; Lackinger, M. The Role of Kinetics versus Thermodynamics in Surface-Assisted Ullmann Coupling on Gold and Silver Surfaces. *J. Am. Chem. Soc.* **2019**, *141*, 4824–4832.

[31] Zhu, Z.; Tao, F. F.; Zheng, F.; Chang, R.; Li, Y.; Heinke, L.; Liu, Z.; Salmeron, M.; Somorjai, G. A. Formation of Nanometer-Sized Surface Platinum Oxide Clusters on a Stepped Pt(557) Single Crystal Surface Induced by Oxygen: A High-Pressure STM and Ambient-Pressure XPS Study. *Nano Lett.* **2012**, *12*, 1491–1497.

[32] Meyer, G. A simple low-temperature ultrahigh-vacuum scanning tunneling microscope capable of atomic manipulation. *Rev. Sci. Instrum.* **1996**, *67*, 2960–2965.

[33] Hoshino, T.; Kokubun, K.; Kumamoto, K.; Ishimaru, T.; Ohdomari, I. High-Temperature Scanning Tunneling Microscopy (STM) Observation of Metastable Structures on Quenched Si(111) Surfaces. *Jpn. J. Appl. Phys.* **1995**, *34*, 3346–3350.

[34] Kitamura, S.-i.; Sato, T.; Iwatsuki, M. Observation of surface reconstruction on silicon above 800 °C using the STM. *Nature* **1991**, *351*, 215–217.

[35] Chen, C. J. *Introduction to Scanning Tunneling Microscopy: Second Edition*; Oxford University Press, 2007.

[36] Bardeen, J. Tunnelling from a Many-Particle Point of View. *Phys. Rev. Lett.* **1961**, *6*, 57–59.

[37] Tersoff, J.; Hamann, D. R. Theory and Application for the Scanning Tunneling Microscope. *Phys. Rev. Lett.* **1983**, *50*, 1998–2001.

[38] Meyer, E.; Hug, H.; Bennewitz, R. *Scanning Probe Microscopy: The Lab on a Tip*; Springer-Verlag Berlin Heidelberg, 2004; Vol. 1.

[39] Piezokeramische Materialien und Bauelemente - Grundlagen, Eigenschaften und Anwendungen. Physik Instrumente (PI) GmbH & Co. KG: Auf der Römerstraße 1, 76228 Karlsruhe, 2016 (retrieved on 30.09.2020).

[40] Werkstoffdaten - Piezoelektrische Materialien. Physik Instrumente (PI) GmbH & Co. KG: Lindenstraße, 07589 Lederhose, Germany, 2020.

[41] Pan, P.; Yang, F.; Wang, Z.; Zhong, B.; Sun, L.; Ru, C. *A Review of Stick–Slip Nanopositioning Actuators*; Springer, 2016; pp 1–32.

[42] Besocke, K. An easily operable scanning tunneling microscope. *Surf. Sci.* **1987**, *181*, 145–153.

[43] Pan, S. H.; Hudson, E. W.; Davis, J. C. 3He refrigerator based very low temperature scanning tunneling microscope. *Rev. Sci. Instrum.* **1999**, *70*, 1459–1463.

[44] Piezoceramic Tubes - For Ultra-precise Positioning Applications. EBL Products, Inc.: 22 Prestige Park CircleEast Hartford, CT 06108, Retrieved on 28.09.2020.

[45] Perkampus, *UV-VIS-Spektroskopie und ihre Anwendungen*, 1st ed.; Springer-Verlag Berlin Heidelberg, 1986; Vol. 1.

[46] DH-mini UV-Vis-NIR Deuterium-Halogen Light Source with Shutter - Installation and Operation Manual. Ocean Optics, Inc.: 830 Douglas Ave. Dunedin, FL 34698, USA, 2015.

[47] USB4000 Spectrometer. Ocean Optics, Inc.: 830 Douglas Ave. Dunedin, FL 34698, USA, 2019.

[48] Thermoelectric Module QC-17-1.4-8.5M. Quick-Ohm Küpper & Co. GmbH: Unterdahl 24B, 42349 Wuppertal, 2020.

[49] Datenblatt 5SRTC. OMEGA Engineering GmbH: Daimlerstraße 26, 75392 Deckenpfronn, Germany, 2003.

[50] EA-Elektro-Automatik, EA-PS 3000B 160W-650W DC-Labornetzgeräte. EA-Elektro-Automatik GmbH: Helmholzstr. 31-37, 41747 Viersen, Germany, 2013.

[51] Safe Heating and Mixing - Operation Manual Magnetic Stirrer MR Hei-End. Heidolph Instruments GmbH & Co. KG: Walpersdorfer Str. 12. D-91126 Schwabach, 2017.

[52] Freedman, A.; Kebabian, P. L.; Li, Z.; Robinson, W. A.; Wormhoudt, J. C. Apparatus for determination of vapor pressures at ambient temperatures employing a Knudsen effusion cell and quartz crystal microbalance. *Meas. Sci. Technol.* **2008**, *19*, 125102.

[53] Knudsen, M. Die Molekularströmung der Gase durch Öffnungen und die Effusion. *Ann. Phys.* **1909**, *333*, 999–1016.

[54] Torres, L. A.; Hernandez-Contreras, I.; Guardado, J. A.; Gonzalez, M. G. A quartz crystal microbalance to determine enthalpies of sublimation at intermediate temperatures by the Knudsen effusion method. *Meas. Sci. Technol.* **1994**, *5*, 51–54.

[55] Deakin, M. R.; Buttry, D. A. Electrochemical applications of the quartz crystal microbalance. *Anal. Chem.* **1989**, *61*, 1147A–1154A.

[56] O'Sullivan, C.; Guilbault, G. Commercial quartz crystal microbalances – theory and applications. *Biosens. Bioelectron.* **1999**, *14*, 663 – 670.

[57] Sauerbrey, G. Verwendung von Schwingquarzen zur Wägung dünner Schichten und zur Mikrowägung. *Zeitschrift für Physik* **1959**, *155*, 206–222.

[58] Gutzler, R.; Heckl, W. M.; Lackinger, M. Combination of a Knudsen effusion cell with a quartz crystal microbalance: In situ measurement of molecular evaporation rates with a fully functional deposition source. *Rev. Sci. Instrum.* **2010**, *81*, 015108.

[59] Inficon, Q-pod Quartz Crystal Monitor. Inficon Inc.: Two Technology Place, East Syracuse, NY 13057, USA, 2011.

[60] Wohlfahrt, C. In *Static Dielectric Constants of Pure Liquids and Binary Liquid Mixtures*, 1st ed.; Madelung, O., Ed.; Landolt-Börnstein; Springer-Verlag Berlin Heidelberg, 1991.

[61] Ochs, O.; Hocke, M.; Spitzer, S.; Heckl, W. M.; Martsinovich, N.; Lackinger, M. Origin of Solvent-Induced Polymorphism in Self-Assembly of Trimesic Acid Monolayers at Solid–Liquid Interfaces. *Chem. Mater.* **2020**, *32*, 5057–5065.

[62] Trucano, P.; Chen, R. Structure of graphite by neutron diffraction. *Nature* **1975**, *258*, 136–137.

[63] Batra, I. P.; Ciraci, S. Theoretical scanning tunneling microscopy and atomic force microscopy study of graphite including tip–surface interaction. *J. Vac. Sci. Technol. A* **1988**, *6*, 313–318.

[64] Tománek, D.; Louie, S. G.; Mamin, H. J.; Abraham, D. W.; Thomson, R. E.; Ganz, E.; Clarke, J. Theory and observation of highly asymmetric atomic structure in scanning-tunneling-microscopy images of graphite. *Phys. Rev. B* **1987**, *35*, 7790–7793.

[65] Tománek, D.; Louie, S. G. First-principles calculation of highly asymmetric structure in scanning-tunneling-microscopy images of graphite. *Phys. Rev. B* **1988**, *37*, 8327–8336.

[66] Atkinson, I. M.; Lindoy, L. F. In *Self Assembly in Supramolecular Systems*; Stoddart, J. F., Ed.; Monographs in Supramolecular Chemistry; The Royal Society of Chemistry, 2000.

[67] Zhang, S.; Buschow, K. H. J.; Cahn, R. W.; Flemings, M. C.; Ilschner, B.; Kramer, E. J.; Mahajan, S.; Veyssière, P. *Encyclopedia of Materials: Science and Technology. Molecular Self-assembly*; Elsevier: Oxford, 2001; pp 5822–5828.

[68] Kudernac, T.; Lei, S.; Elemans, J. A. A. W.; De Feyter, S. Two-dimensional supramolecular self-assembly: nanoporous networks on surfaces. *Chem. Soc. Rev.* **2009**, *38*, 402–421.

[69] Barth, J. V. Molecular Architectonic on Metal Surfaces. *Annu. Rev. Phys. Chem.* **2007**, *58*, 375–407, PMID: 17430091.

[70] Otero, R.; Gallego, J. M.; de Parga, A. L. V.; Martín, N.; Miranda, R. Molecular Self-Assembly at Solid Surfaces. *Adv. Mater.* **2011**, *23*, 5148–5176.

[71] Stabel, A.; Heinz, R.; De Schryver, F. C.; Rabe, J. P. Ostwald Ripening of Two-Dimensional Crystals at the Solid-Liquid Interface. *J. Phys. Chem.* **1995**, *99*, 505–507.

[72] Lackinger, M.; Griessl, S.; Kampschulte, L.; Jamitzky, F.; Heckl, W. M. Dynamics of Grain Boundaries in Two-Dimensional Hydrogen-Bonded Molecular Networks. *Small* **2005**, *1*, 532–539.

[73] Conti, S.; Cecchini, M. Predicting molecular self-assembly at surfaces: a statistical thermodynamics and modeling approach. *Phys. Chem. Chem. Phys.* **2016**, *18*, 31480–31493.

[74] Song, W.; Martsinovich, N.; Heckl, W. M.; Lackinger, M. Born-Haber Cycle for Monolayer Self-Assembly at the Liquid-Solid Interface: Assessing the Enthalpic Driving Force. *J. Am. Chem. Soc.* **2013**, *135*, 14854–14862.

[75] Mammen, M.; Shakhnovich, E. I.; Deutch, J.; Whitesides, G. M. Estimating the Entropic Cost of Self-Assembly of Multiparticle Hydrogen-Bonded Aggregates Based on the Cyanuric Acid•Melamine Lattice. *J. Org. Chem.* **1998**, *63*, 3821–3830.

[76] Björk, J. Kinetic and Thermodynamic Considerations in On-Surface Synthesis. On-Surface Synthesis II. Cham, 2018; pp 19–34.

[77] Krissinel, E.; Henrick, K. Inference of Macromolecular Assemblies from Crystalline State. *J. Mol. Biol.* **2007**, *372*, 774 – 797.

[78] Ohkubo, Y. Z.; Brooks, C. L. Exploring Flory's isolated-pair hypothesis: Statistical mechanics of helix–coil transitions in polyalanine and the C-peptide from RNase A. *Proc. Natl. Acad. Sci. U.S.A.* **2003**, *100*, 13916–13921.

[79] Laidler, K. J.; King, M. C. Development of transition-state theory. *J. Phys. Chem.* **1983**, *87*, 2657–2664.

[80] Eyring, H. The Activated Complex in Chemical Reactions. *J. Chem. Phys.* **1935**, *3*, 107–115.

[81] Lackinger, M.; Heckl, W. M. Carboxylic Acids: Versatile Building Blocks and Mediators for Two-Dimensional Supramolecular Self-Assembly. *Langmuir* **2009**, *25*, 11307–11321.

[82] Gutzler, R.; Lappe, S.; Mahata, K.; Schmittel, M.; Heckl, W. M.; Lackinger, M. Aromatic interaction vs.hydrogen bonding in self-assembly at the liquid–solid interface. *Chem. Commun.* **2009**, 680–682.

[83] Sirtl, T.; Song, W.; Eder, G.; Neogi, S.; Schmittel, M.; Heckl, W. M.; Lackinger, M. Solvent-Dependent Stabilization of Metastable Monolayer Polymorphs at the Liquid-Solid Interface. *ACS Nano* **2013**, *7*, 6711–6718.

[84] Zhang, X.; Chen, Q.; Deng, G.-J.; Fan, Q.-H.; Wan, L.-J. Structural Diversity of a Monodendron Molecule Self-Assembly in Different Solvents Investigated by Scanning Tunneling Microscopy: From Dispersant to Counterpart. *J. Phys. Chem. C* **2009**, *113*, 16193–16198.

[85] Ciesielski, A.; Szabelski, P. J.; Rżysko, W.; Cadeddu, A.; Cook, T. R.; Stang, P. J.; Samorì, P. Concentration-Dependent Supramolecular Engineering of Hydrogen-Bonded Nanostructures at Surfaces: Predicting Self-Assembly in 2D. *J. Am. Chem. Soc.* **2013**, *135*, 6942–6950.

[86] Lei, S.; Tahara, K.; De Schryver, F. C.; Van der Auweraer, M.; Tobe, Y.; De Feyter, S. One Building Block, Two Different Supramolecular Surface-Confined Patterns: Concentration in Control at the Solid-Liquid Interface. *Angew. Chem. Int. Ed.* **2008**, *47*, 2964–2968.

[87] Steed, J. W.; Atwood, J. L. *Supramolecular Chemistry*, 2nd ed.; John Wiley & Sons, Ltd, 2009; Chapter Concepts, pp 1–48.

[88] Adair, J.; Suvaci, E.; Sindel, J. In *Encyclopedia of Materials: Science and Technology; Surface and Colloid Chemistry*; Buschow, K. J., Cahn, R. W., Flemings, M. C., Ilschner, B., Kramer, E. J., Mahajan, S., Veyssière, P., Eds.; Elsevier, 2001; pp 1 – 10.

[89] Mali, K. S.; Lava, K.; Binnemans, K.; De Feyter, S. Hydrogen Bonding Versus van der Waals Interactions: Competitive Influence of Noncovalent Interactions on 2D Self-Assembly at the Liquid–Solid Interface. *Chem. Eur. J.* **2010**, *16*, 14447–14458.

[90] Desiraju, G. R. Hydrogen Bridges in Crystal Engineering: Interactions without Borders. *Acc. Chem. Res.* **2002**, *35*, 565–573.

[91] Desiraju, G. R. Chemistry beyond the molecule. *Nature* **2001**, *412*, 397–400.

[92] Jeffrey, G. A.; Saenger, W. *Hydrogen Bonding in Biological Structures*; Springer Berlin Heidelberg, 1991.

[93] Desiraju, G.; Steiner, T. *The Weak Hydrogen Bond: In Structural Chemistry and Biology*; Oxford University Press, 2001.

[94] Grosch, A. A.; van der Lubbe, S. C. C.; Fonseca Guerra, C. Nature of Intramolecular Resonance Assisted Hydrogen Bonding in Malonaldehyde and Its Saturated Analogue. *J. Phys. Chem. A* **2018**, *122*, 1813–1820.

[95] Miliordos, E.; Xantheas, S. S. On the validity of the basis set superposition error and complete basis set limit extrapolations for the binding energy of the formic acid dimer. *J. Chem. Phys.* **2015**, *142*, 094311.

[96] Gilli, G.; Bellucci, F.; Ferretti, V.; Bertolasi, V. Evidence for resonance-assisted hydrogen bonding from crystal-structure correlations on the enol form of the .beta.-diketone fragment. *J. Am. Chem. Soc.* **1989**, *111*, 1023–1028.

[97] Gilli, P.; Bertolasi, V.; Ferretti, V.; Gilli, G. Evidence for resonance-assisted hydrogen bonding. 4. Covalent nature of the strong homonuclear hydrogen bond. Study of the O-H–O system by crystal structure correlation methods. *J. Am. Chem. Soc.* **1994**, *116*, 909–915.

[98] Bordo, V. G.; Rubahn, H. G. *Optics and Spectroscopy at Surfaces and Interfaces*; Wiley, 2008.

[99] Lüth, H. *Solid Surfaces, Interfaces and Thin Films*; Springer International Publishing, 2015; Chapter Adsorption on Solid Surfaces, pp 527–571.

[100] Käfer, D.; Witte, G.; Cyganik, P.; Terfort, A.; Wöll, C. A Comprehensive Study of Self-Assembled Monolayers of Anthracenethiol on Gold: Solvent Effects, Structure, and Stability. *J. Am. Chem. Soc.* **2006**, *128*, 1723–1732.

[101] Ulman, A. Formation and Structure of Self-Assembled Monolayers. *Chem. Rev.* **1996**, *96*, 1533–1554.

[102] Song, W.; Martsinovich, N.; Heckl, W. M.; Lackinger, M. Thermodynamics of 4,4′-stilbenedicarboxylic acid monolayer self-assembly at the nonanoic acid-graphite interface. *Phys. Chem. Chem. Phys.* **2014**, *16*, 13239–13247.

[103] Kampschulte, L.; Lackinger, M.; Maier, A.-K.; Kishore, R. S. K.; Griessl, S.; Schmittel, M.; Heckl, W. M. Solvent Induced Polymorphism in Supramolecular 1,3,5-Benzenetribenzoic Acid Monolayers. *J. Phys. Chem. B* **2006**, *110*, 10829–10836.

[104] Griessl, S.; Lackinger, M.; Edelwirth, M.; Hietschold, M.; Heckl, W. M. Self-Assembled Two-Dimensional Molecular Host-Guest Architectures From Trimesic Acid. *Single Molecules* **2002**, *3*, 25–31.

[105] Takami, T.; Mazur, U.; Hipps, K. Solvent-Induced Variations in Surface Structure of a 2,9,16,23-Tetra-tert-butyl-phthalocyanine on Graphite. *J. Phys. Chem. C* **2009**, *113*, 17479–17483.

[106] Della Pia, A.; Luo, D.; Blackwell, R.; Costantini, G.; Martsinovich, N. Molecular self-assembly of substituted terephthalic acids at the liquid/solid interface: investigating the effect of solvent. *Faraday Discuss.* **2017**, *204*, 191–213.

[107] Fu, C.; Orgiu, E.; Perepichka, D. F. Face-on vs. edge-on: tuning the structure of tetrathiafulvalene monolayers with solvent. *J. Mater. Chem. C* **2018**, *6*, 3787–3791.

[108] Li, Y.; Ma, Z.; Qi, G.; Yang, Y.; Zeng, Q.; Fan, X.; Wang, C.; Huang, W. Solvent Effects on Supramolecular Networks Formed by Racemic Star-Shaped Oligofluorene Studied by Scanning Tunneling Microscopy. *J. Phys. Chem. C* **2008**, *112*, 8649–8653.

[109] Tao, F.; Goswami, J.; Bernasek, S. L. Competition and Coadsorption of Diacids and Carboxylic Acid Solvents on HOPG. *J. Phys. Chem. B* **2006**, *110*, 19562–19569.

[110] Marie, C.; Silly, F.; Tortech, L.; Müllen, K.; Fichou, D. Tuning the Packing Density of 2D Supramolecular Self-Assemblies at the Solid-Liquid Interface Using Variable Temperature. *ACS Nano* **2010**, *4*, 1288–1292.

[111] Einstein, A. Über die von der molekularkinetischen Theorie der Wärme geforderte Bewegung von in ruhenden Flüssigkeiten suspendierten Teilchen. *Ann. Phys.* **1905**, *322*, 549–560.

[112] Meschede, D. *Gerthsen Physik*, 22nd ed.; Springer-Verlag Berlin Heidelberg, 2004.

[113] Ochs, O.; Heckl, W. M.; Lackinger, M. Immersion-scanning-tunneling-microscope for long-term variable-temperature experiments at liquid-solid interfaces. *Rev. Sci. Instrum.* **2018**, *89*, 053707.

[114] Weichlot AuSn 80/20 - Technisches Produktdatenblatt. IPT-Albrecht GmbH: Waldweg 37, D-77963 Schwanau, Germany, 2017 (retrieved on 28.09.2020).

[115] Kupfer-Zink-Legierungen (Messing und Sondermessing) - Informationsdruck i.5. Deutsches Kupferinstitut: Heinrichstraße 24, 40239 Düsseldorf, Germany, 2007 (retrieved on 28.09.2020).

[116] Werkstoffe und ihre Eigenschaften - FPM. Dichtelemente arcus GmbH: Beckedorfer Bogen 16-20, 21218 Seevetal, Germany, Retrieved on 28.09.2020.

[117] Gold und Goldlegierungen. Heimerle + Meule GmbH: Dennigstraße 16, 75179 Pforzheim, Germany, 2016 (retrieved on 30.09.2020).

[118] Produktdatenblatt Kapton HN Polyimidfolie. Synflex Elektro GmbH: Auf den Kreuzen 24, D-32825 Blomberg, Germany, 2018 (retrieved on 28.09.2020).

[119] Cu-OFE. Deutsches Kupferinstitut Berufsverband e.V.: Heinrichstraße 24, 40239 Düsseldorf, Germany, 2005 (retrieved on 28.09.2020).

[120] Technisches Datenblatt, PEEK Polyetheretherketon. König GmbH Kunststoffprodukte: Zeppelinstraße 14, D-82205 Gilching, Germany, 2016 (retrieved on 28.09.2020).

[121] PLATINUM 10% IRIDIUM Material #: 100167. California Fine Wire Co.: 338 S 4th St. Grover Beach, CA 93433, Retrieved from *https://calfinewire.com/datasheets/100167-platinum10iridium/* on 30.09.2020.

[122] Werkstoffdatenblatt - Polytetraflourethylen (PTFE). Auer Kunststofftechnik: Franz-Hagn-Str. 6, D-82140 Olching, Germany, 2020 (retrieved on 28.09.2020).

[123] Einsatzbereich von Material und Beschichtung. HKCM Engineering e.K: Ottestr. 20, D-24340 Eckernfoerde, Germany, 2020 (retrieved on 28.09.2020).

[124] Shapal Hi-M Soft - Machinable Aluminium Nitride Ceramic. Goodfellow GmbH: Alstertwiete 3, D-20099 Hamburg, Deutschland, 2020 (retrieved on 28.09.2020).

[125] Material datasheet: Silver and silver alloys. Heimerle + Meule GmbH: Dennigstraße 16, 75179 Pforzheim, Germany, 2016 (retrieved on 28.09.2020).

[126] Produktinformation - FELDER-ISO-Core "RA" - BLEIHALTIG. FELDER GmbH: Im Lipperfeld 11D-46047 Oberhausen, 2020 (retrieved on 28.09.2020).

[127] Produktinformation - FELDER-ISO-Core "VA" - BLEIFREI. FELDER GmbH: Im Lipperfeld 11D-46047 Oberhausen, 2020 (retrieved on 28.09.2020).

[128] Acidur 4057 - Werkstoffdatenblatt, X17CrNi16-2, 1.4057. Deutsche Edelstahlwerke GmbH: Auestr. 4, 58452 Witten, Germany, 2015 (retrieved on 28.09.2020).

[129] Acidur 4301 - Werkstoffsdatenblatt, X5CrNi18-10, 1.4301. Deutsche Edelstahlwerke GmbH: Auestr. 4, 58452 Witten, Germany, 2015 (retrieved on 28.09.2020).

[130] Acidur 4401 - Werkstoffdatenblatt, X5CrNiMo17-12-2, 1.4401. Deutsche Edelstahlwerke GmbH: Auestr. 4, 58452 Witten, Germany, 2015 (retrieved on 28.09.2020).

[131] Acidur 4571 - Werkstoffdatenblatt, X6CrNiMoTi17-12-2, 1.4571. Deutsche Edelstahlwerke GmbH: Auestr. 4, 58452 Witten, Germany, 2015 (retrieved on 28.09.2020).

[132] Invar 32-5 - Datasheet. Future Alloys LTD: Unit 10,Milland Road,Industrial Estate, Neath, West Glamorgan, SA11 1NJ, 2020 (retrieved on 28.09.2020).

[133] Ceramic Materials - Advanced Ceramics for Mechanical Engineering. CeramTec GmbH: CeramTec-Platz 1-9, 73207 Plochingen, Germany, Retrieved on 28.09.2020.

[134] CuZn5. Deutsches Kupferinstitut Berufsverband e.V.: Heinrichstraße 24, 40239 Düsseldorf, Germany, 2005 (retrieved on 28.09.2020).

[135] EPO-TEK 353ND - Technical Data Sheet. Epoxy Technology, INC.: 14 Fortune Drive, Billerica, MA 01821, 2017 (retrieved on 28.09.2020).

[136] Technical Datasheet - Araldite 2015-1 Two Component Epoxy Paste Adhesive. Huntsman Corporation: 10003 Woodloch Forest Dr, The Woodlands, TX 77380, 2018 (retrieved on 28.09.2020).

[137] Datenblatt Duralco 4460. Polytec PT GmbH: Ettlinger Straße 30, 76307 Karlsbad, Germany, 2019 (retrieved on 28.09.2020).

[138] Polytec Ep 653 - Ungefuellter Epoxidharzklebstoff - Technische Daten. Polytec PT GmbH: Ettlinger Straße 30, 76307 Karsbad, Germany, 2017(retrieved on 28.09.2020).

[139] Polytec EP 655-T - Ungefuellter Epoxidharzklebstoff - Technische Daten. Polytec PT GmbH: Ettlinger Straße 30, 76307 Karlsbad, Germany, 2017 (retrieved on 28.09.2020).

[140] EPO-TEK H74 - Technical Data Sheet. Epoxy Technology, Inc: 14 Fortune Drive, Billerica, MA 01821-3972, 2017 (retrieved on 28.09.2020).

[141] Verarbeitungshinweise für den Klebstoff KGL 130 EP. Klebe- und Giessharztechnik Dr. Ludeck GmbH: Frankfurter Chaussee 56, D-15370 Vogeldirf, Germany, 2018.

[142] Verarbeitungshinweise für den Klebstoff KL 06B. Klebe- und Giessharztechnik Dr. Ludeck GmbH: Frankfurter Chaussee 56, D-15370 Vogeldirf, Germany, 2013.

[143] EP42-2LV Technical Data Sheet. Master Bond Inc.: 154 Hobart Street, Hackensack, NJ 07601 USA, Retrieved on 18.03.2020.

[144] EPO-TEK OD2002 - Technical Data Sheet. Epoxy Technology, Inc: 14 Fortune Drive, Billerica, MA 01821-3972, 2017(retrieved on 28.09.2020).

[145] EPO-TEK PJ1390-1 - Technical Data Sheet. Epoxy Technology, Inc: 14 Fortune Drive, Billerica, MA 01821-3972, 2017 (retrieved on 28.09.2020).

[146] UHU PLUS ENDFEST 300. UHU GmbH & Co. KG: Herrmannstraße 7, D-77815 Bühl (Baden), Germany, 2019 (retrieved on 28.09.2020).

[147] UHU PLUS SCHNELLFEST. UHU GmbH & Co. KG: Herrmannstraße 7, D-77815 Bühl (Baden), Germany, 2018 (retrieved on 28.09.2020).

[148] UHU PLUS SOFORTFEST. UHU GmbH & Co. KG: Herrmannstraße 7, D-77815 Bühl (Baden), Germany, 2019 (retrieved on 28.09.2020).

[149] Instructions for use - X60. Hottinger Baldwin Messtechnik GmbH: Im Tiefen See 45, D-64293 Darmstadt, Germany, 2019 (retrieved on 28.09.2020).

[150] E-870 PIShift Treiberelektronik (E870T0001). Physik Instrumente (PI) GmnH & Co. KG: Physik Instrumente (PI) GmbH & Co. KG, Auf der Römerstraße 1, 76228 Karlsruhe (Germany), 2014 (retrieved on 30.09.2020).

[151] Yasuda, H.; Chun, B. H.; Cho, D. L.; Lin, T. J.; Yang, D. J.; Antonelli, J. A. Interface-Engineered Parylene C Coating for Corrosion Protection of Cold-Rolled Steel. *CORROSION* **1996**, *52*, 169–176.

[152] Kuppusami, S.; Oskouei, R. Parylene Coatings in Medical Devices and Implants: A Review. *Universal Journal of Biomedical Engineering* **2015**, *3(2)*, 9–12.

[153] Liger, M.; Rodger, D. C.; Tai, Y. C. Robust parylene-to-silicon mechanical anchoring. *The Sixteenth Annual International Conference on Micro Electro Mechanical Systems, 2003. MEMS-03 Kyoto. IEEE* **2003**, 602–605.

[154] Gorham, W. F. A New, General Synthetic Method for the Preparation of Linear Poly-p-xylylenes. *Journal of Polymer Science Part A-1: Polymer Chemistry* **1966**, *4*, 3027–3039.

[155] Kramer, P.; Sharma, A. K.; Hennecke, E. E.; Yasuda, H. Polymerization of para-xylylene derivatives (parylene polymerization). I. Deposition kinetics for parylene N and parylene C. *Journal of Polymer Science: Polymer Chemistry Edition* **1984**, *22*, 475–491.

[156] Yamada, M.; Koshiba, Y.; Horike, S.; Fukushima, T.; Ishida, K. Thermophysical properties of the parylene C dimer under vacuum. *Jpn. J. Appl. Phys.* **2020**, *59*, SDDA15.

[157] You, L.; Yang, G.; Lang, C.; Moore, J. A.; Wu, P.; McDonald, J. F.; Lu, T. Vapor deposition of parylene-F by pyrolysis of dibromotetrafluoro-p-xylene. *J. Vac. Sci. Technol. A* **1993**, *11*, 3047–3052.

[158] Kang, D.; Standley, A.; Chang, J. H.; Liu, Y.; Tai, Y. Effects of deposition temperature on Parylene-C properties. *2013 IEEE 26th International Conference on Micro Electro Mechanical Systems (MEMS)* **2013**, 389–390.

[159] Application Guide. Advanced Coating: 10723 Edison Court, Rancho Cucamonga, CA 91730, Retrieved on 28.09.2020.

[160] Braunovic, M.; Myshkin, N. K.; Konchits, V. V. *Electrical contacts: fundamentals, applications and technology*; CRC press, 2006.

[161] Vinaricky, E.; Schröder, K. H.; Weiser, J. *Elektrische Kontakte, Werkstoffe und Anwendungen - Grundlagen, Technologien, Prüfverfahren*; Springer Verlag, 2016.

[162] Goldelektrolyt Midas - Anleitung. Tifoo Marawe GmbH and Co. KG: Donaustufer Str 378, Building 64, 93055 Regensburg, Germany, Retrieved on 28.09.2020.

[163] Goldelektrolyt Flash - Anleitung. Tifoo Marawe GmbH and Co. KG: Donaustufer Str. 378, Building 64, 93055 Regensburg, Germany, Retrieved on 28.09.2020.

[164] Beständigkeitsliste - Elastomere. COG Dichtungstechnik - C. Otto Gehrckens GmbH and Co. KG: Postfach 1453, D-25404 Pinneberg, Germany, Retrieved on 28.09.2020.

[165] Datenblatt LEZ-VITSEAL. AET Lézaud GmbH: Am Hottenwald 8, 66606 St. Wendel, 2017 (retrieved on 28.09.2020).

[166] Wang, X.; Sun, T.; Teja, A. S. Density, Viscosity, and Thermal Conductivity of Eight Carboxylic Acids from (290.3 to 473.4) K. *J. Chem. Eng. Data* **2016**, *61*, 2651–2658.

[167] GOLD 99.99% BE MOD, MATERIAL #: 100542. California Fine Wire Co.: 338 S 4th St. Grover Beach, CA 93433, Retrieved from *https://calfinewire.com/datasheets/100542-gold9999bemod/* on 30.09.2020.

[168] Pierre, A. C.; Pajonk, G. M. Chemistry of Aerogels and Their Applications. *Chemical Reviews* **2002**, *102*, 4243–4266.

[169] Optical Table System - Model: M-INT2-36-8-A. Newport Corporation: 1791 Deere Avenue, Irvine, CA, 92606 USA, Retrieved from *https://www.newport.com/p/M-INT2-36-8-A* on 30.09.2020.

[170] High-performance Vibration Isolation Systems with Steel Honeycomb Top. OptoSigma Europe S.A.S: 3 rue de la Terre de Feu, 91940 Les Ulis, Essonne, France, Retrieved on 28.09.2020.

[171] SPM 1000 Control Electronics User's Guide. RHK Technology, Inc: 1050 East Maple Road, Troy, MI 48083, 1999.

[172] Datasheet LCA-2K-2G - Ultra-Low-Noise Current Amplifier. FEMTO Messtechnik GmbH: Klosterstr. 64, D-10179 Berlin (Germany), 2019 (retrieved on 30.09.2020).

[173] DT3016 High-Speed, Multifunction PCI Data Acquisition Board. Data Translation, Inc: 100 Locke Drive Marlboro, MA 01752, 2017 (retrieved on 30.09.2020).

[174] Model 2416 Process Controller - User Manual. Eurotherm Limited: Faraday Cl, Worthing BN13 3PL, UK, 2014 (retrieved on 30.09.2020).

[175] Datenblatt - Pinnacle Plus Serie. Alpha Technologies GmbH: Hansastr. 8, 91126 Schwabach, Germany, 2006 (retrieved on 30.09.2020).

[176] mvBlueFox-IGC/-MLC. Matrix Vision GmbH: Talstrasse 16, 71570 Oppenweiler, Germany, 2019 (retrieved on 30.09.2020).

[177] CP83 - Schlauchpumpe. Gemke Technik GmbH: Gemke Technik GmbH, Königsfelder Str. 13, D-58256 Ennepetal, Retrieved from *http://www.gemke-schlauchpumpen.com/einbau-schlauchpumpen/cp83-2/index.php* on 05.10.2020.

[178] Datenblatt LEZ-SANSOFT. AET Lézaud GmbH: Am Hottenwald 8, 66606 St. Wendel, 2019 (retrieved on 30.09.2020).

[179] Zhuang, Z. Q.; Haun, M. J.; Jang, S. J.; Cross, L. E. Composition and temperature dependence of the dielectric, piezoelectric and elastic properties of pure PZT ceramics. *IEEE Transactions on Ultrasonics, Ferroelectrics, and Frequency Control* **1989**, *36*, 413 – 416.

[180] Etter, M. C. Encoding and decoding hydrogen-bond patterns of organic compounds. *Acc. Chem. Res.* **1990**, *23*, 120–126.

[181] Shao, X.; Luo, X.; Hu, X.; Wu, K. Solvent Effect on Self-Assembled Structures of 3,8-Bis-hexadecyloxy-benzo[c]cinnoline on Highly Oriented Pyrolytic Graphite. *J. Phys. Chem. B* **2006**, *110*, 1288–1293.

[182] Mamdouh, W.; Uji-i, H.; Ladislaw, J. S.; Dulcey, A. E.; Percec, V.; De Schryver, F. C.; De Feyter, S. Solvent Controlled Self-Assembly at the Liquid-Solid Interface Revealed by STM. *J. Am. Chem. Soc.* **2006**, *128*, 317–325.

[183] Liu, J.; Zhang, X.; Yan, H.-J.; Wang, D.; Wang, J.-Y.; Pei, J.; Wan, L.-J. Solvent-Controlled 2D Host-Guest (2,7,12-Trihexyloxytruxene/Coronene) Molecular Nanostructures at Organic Liquid/Solid Interface Investigated by Scanning Tunneling Microscopy. *Langmuir* **2010**, *26*, 8195–8200.

[184] Xu, L.; Miao, X.; Zha, B.; Deng, W. Self-Assembly Polymorphism: Solvent-Responsive Two-Dimensional Morphologies of 2,7-Ditridecyloxy-9-fluorenone by Scanning Tunneling Microscopy. *J. Phys. Chem. C* **2012**, *116*, 16014–16022.

[185] Silly, F. Selecting Two-Dimensional Halogen–Halogen Bonded Self-Assembled 1,3,5-Tris(4-iodophenyl)benzene Porous Nanoarchitectures at the Solid–Liquid Interface. *J. Phys. Chem. C* **2013**, *117*, 20244–20249.

[186] Wu, Y.; Li, J.; Yuan, Y.; Dong, M.; Zha, B.; Miao, X.; Hu, Y.; Deng, W. Halogen bonding versus hydrogen bonding induced 2D self-assembled nanostructures at the liquid-solid interface revealed by STM. *Phys. Chem. Chem. Phys.* **2017**, *19*, 3143–3150.

[187] Adisoejoso, J.; Tahara, K.; Lei, S.; Szabelski, P.; Rżysko, W.; Inukai, K.; Blunt, M. O.; Tobe, Y.; De Feyter, S. One Building Block, Two Different Nanoporous Self-Assembled Monolayers: A Combined STM and Monte Carlo Study. *ACS Nano* **2012**, *6*, 897–903.

[188] Mazur, U.; Hipps, K. W. Kinetic and thermodynamic processes of organic species at the solution-solid interface: the view through an STM. *Chem. Commun.* **2015**, *51*, 4737–4749.

[189] Gutzler, R.; Cardenas, L.; Rosei, F. Kinetics and thermodynamics in surface-confined molecular self-assembly. *Chem. Sci.* **2011**, *2*, 2290–2300.

[190] Dienstmaier, J. F.; Mahata, K.; Walch, H.; Heckl, W. M.; Schmittel, M.; Lackinger, M. On the Scalability of Supramolecular Networks - High Packing Density vs Optimized Hydrogen Bonds in Tricarboxylic Acid Monolayers. *Langmuir* **2010**, *26*, 10708–10716.

[191] Ishikawa, Y.; Ohira, A.; Sakata, M.; Hirayama, C.; Kunitake, M. A two-dimensional molecular network structure of trimesic acid prepared by adsorption-induced self-organization. *Chem. Commun.* **2002**, 2652–2653.

[192] Dmitriev, A.; Lin, N.; Weckesser, J.; Barth, J. V.; Kern, K. Supramolecular Assemblies of Trimesic Acid on a Cu(100) Surface. *J. Phys. Chem. B* **2002**, *106*, 6907–6912.

[193] Su, G.-J.; Zhang, H.-M.; Wan, L.-J.; Bai, C.-L.; Wandlowski, T. Potential-Induced Phase Transition of Trimesic Acid Adlayer on Au(111). *J. Phys. Chem. B* **2004**, *108*, 1931–1937.

[194] Li, Z.; Han, B.; Wan, L. J.; Wandlowski, T. Supramolecular Nanostructures of 1,3,5-Benzene-tricarboxylic Acid at Electrified Au(111)/0.05 M H2SO4 Interfaces: An in Situ Scanning Tunneling Microscopy Study. *Langmuir* **2005**, *21*, 6915–6928.

[195] Sheerin, G.; Cafolla, A. A. Self-assembled structures of trimesic acid on the Ag/Si(111)-($\sqrt{3}$x$\sqrt{3}$)R30° surface. *Surf. Sci.* **2005**, *577*, 211–219.

[196] Nath, K. G.; Ivasenko, O.; Miwa, J. A.; Dang, H.; Wuest, J. D.; Nanci, A.; Perepichka, D. F.; Rosei, F. Rational Modulation of the Periodicity in Linear Hydrogen-Bonded Assemblies of Trimesic Acid on Surfaces. *J. Am. Chem. Soc.* **2006**, *128*, 4212–4213.

[197] MacLeod, J. M.; Ivasenko, O.; Perepichka, D. F.; Rosei, F. Stabilization of exotic minority phases in a multicomponent self-assembled molecular network. *Nanotechnology* **2007**, *18*, 424031.

[198] Ye, Y.; Sun, W.; Wang, Y.; Shao, X.; Xu, X.; Cheng, F.; Li, J.; Wu, K. A Unified Model: Self-Assembly of Trimesic Acid on Gold. *J. Phys. Chem. C* **2007**, *111*, 10138–10141.

[199] Kampschulte, L.; Werblowsky, T. L.; Kishore, R. S. K.; Schmittel, M.; Heckl, W. M.; Lackinger, M. Thermodynamical Equilibrium of Binary Supramolecular Networks at the Liquid-Solid Interface. *J. Am. Chem. Soc.* **2008**, *130*, 8502–8507.

[200] Ha, N. T. N.; Gopakumar, T. G.; Gutzler, R.; Lackinger, M.; Tang, H.; Hietschold, M. Influence of Solvophobic Effects on Self-Assembly of Trimesic Acid at the Liquid-Solid Interface. *J. Phys. Chem. C* **2010**, *114*, 3531–3536.

[201] Eder, G.; Kloft, S.; Martsinovich, N.; Mahata, K.; Schmittel, M.; Heckl, W. M.; Lackinger, M. Incorporation Dynamics of Molecular Guests into Two-Dimensional Supramolecular Host Networks at the Liquid-Solid Interface. *Langmuir* **2011**, *27*, 13563–13571.

[202] Iancu, V.; Braun, K.-F.; Schouteden, K.; Van Haesendonck, C. Probing the Electronic Properties of Trimesic Acid Nanoporous Networks on Au(111). *Langmuir* **2013**, *29*, 11593–11599.

[203] Zheng, Q.-N.; Liu, X.-H.; Liu, X.-R.; Chen, T.; Yan, H.-J.; Zhong, Y.-W.; Wang, D.; Wan, L.-J. Bilayer Molecular Assembly at a Solid/Liquid Interface as Triggered by a Mild Electric Field. *Angew. Chem. Int. Ed.* **2014**, *53*, 13395–13399.

[204] MacLeod, J. M.; Lipton-Duffin, J. A.; Cui, D.; De Feyter, S.; Rosei, F. Substrate Effects in the Supramolecular Assembly of 1,3,5-Benzene Tricarboxylic Acid on Graphite and Graphene. *Langmuir* **2015**, *31*, 7016–7024.

[205] MacLeod, J. M.; Lipton-Duffin, J.; Fu, C.; Taerum, T.; Perepichka, D. F.; Rosei, F. A 2D Substitutional Solid Solution through Hydrogen Bonding of Molecular Building Blocks. *ACS Nano* **2017**, *11*, 8901–8909.

[206] Spitzer, S.; Helmle, O.; Ochs, O.; Horsley, J.; Martsinovich, N.; Heckl, W. M.; Lackinger, M. What can be inferred from moiré patterns? A case study of trimesic acid monolayers on graphite. *Faraday Discuss.* **2017**, *204*, 331–348.

[207] Lipton-Duffin, J.; Abyazisani, M.; MacLeod, J. Periodic and nonperiodic chiral self-assembled networks from 1,3,5-benzenetricarboxylic acid on Ag(111). *Chem. Commun.* **2018**, *54*, 8316–8319.

[208] Ubink, J.; Enache, M.; Stöhr, M. Bias-induced conformational switching of supramolecular networks of trimesic acid at the solid-liquid interface. *J. Chem. Phys.* **2018**, *148*, 174703.

[209] Acree, W.; Chickos, J. S. Phase Transition Enthalpy Measurements of Organic and Organometallic Compounds. Sublimation, Vaporization and Fusion Enthalpies From 1880 to 2015. Part 1. C1 - C10. *J. Phys. Chem. Ref. Data* **2016**, *45*, 033101.

[210] Shayeganfar, F.; Rochefort, A. Electronic Properties of Self-Assembled Trimesic Acid Monolayer on Graphene. *Langmuir* **2014**, *30*, 9707–9716.

[211] Martsinovich, N.; Troisi, A. Modeling the Self-Assembly of Benzenedicarboxylic Acids Using Monte Carlo and Molecular Dynamics Simulations. *J. Phys. Chem. C* **2010**, *114*, 4376–4388.

[212] Ahn, S.; Matzger, A. J. Six Different Assemblies from One Building Block: Two-Dimensional Crystallization of an Amide Amphiphile. *J. Am. Chem. Soc.* **2010**, *132*, 11364–11371.

[213] Bhattarai, A.; Mazur, U.; Hipps, K. W. A Single Molecule Level Study of the Temperature-Dependent Kinetics for the Formation of Metal Porphyrin Monolayers on Au(111) from Solution. *J. Am. Chem. Soc.* **2014**, *136*, 2142–2148.

[214] Jahanbekam, A.; Chilukuri, B.; Mazur, U.; Hipps, K. W. Kinetically Trapped Two-Component Self-Assembled Adlayer. *J. Phys. Chem. C* **2015**, *119*, 25364–25376.

[215] English, W. A.; Hipps, K. W. Stability of a Surface Adlayer at Elevated Temperature: Coronene and Heptanoic Acid on Au(111). *J. Phys. Chem. C* **2008**, *112*, 2026–2031.

[216] Jäckel, F.; Ai, M.; Wu, J.; Müllen, K.; Rabe, J. P. Solvent Molecules in an Epitaxially Grown Scaffold of Star-Shaped Nanographenes. *J. Am. Chem. Soc.* **2005**, *127*, 14580–14581.

[217] VandeVondele, J.; Krack, M.; Mohamed, F.; Parrinello, M.; Chassaing, T.; Hutter, J. Quickstep: Fast and accurate density functional calculations using a mixed Gaussian and plane waves approach. *Comput. Phys. Commun.* **2005**, *167*, 103–128.

[218] Dion, M.; Rydberg, H.; Schröder, E.; Langreth, D. C.; Lundqvist, B. I. Van der Waals Density Functional for General Geometries. *Phys. Rev. Lett.* **2004**, *92*, 246401.

[219] Goedecker, S.; Teter, M.; Hutter, J. Separable dual-space Gaussian pseudopotentials. *Phys. Rev. B* **1996**, *54*, 1703–1710.

[220] VandeVondele, J.; Hutter, J. Gaussian basis sets for accurate calculations on molecular systems in gas and condensed phases. *J. Chem. Phys.* **2007**, *127*, 114105.

[221] Li, M.; Xie, P.; Deng, K.; Yang, Y.-L.; Lei, S.-B.; Wei, Z.-Q.; Zeng, Q.-D.; Wang, C. A dynamic study of the structural change in the binary network in response to guest inclusion. *Phys. Chem. Chem. Phys.* **2014**, *16*, 8778–8782.

[222] Bellec, A.; Arrigoni, C.; Schull, G.; Douillard, L.; Fiorini-Debuisschert, C.; Mathevet, F.; Kreher, D.; Attias, A.-J.; Charra, F. Solution-growth kinetics and thermodynamics of nanoporous self-assembled molecular monolayers. *J. Chem. Phys.* **2011**, *134*, 124702.

[223] Bhattarai, A.; Mazur, U.; Hipps, K. W. Desorption Kinetics and Activation Energy for Cobalt Octaethylporphyrin from Graphite at the Phenyloctane Solution-Graphite Interface: An STM Study. *J. Phys. Chem. C* **2015**, *119*, 9386–9394.

[224] Bhattarai, A.; Marchbanks-Owens, K.; Mazur, U.; Hipps, K. W. Influence of the Central Metal Ion on the Desorption Kinetics of a Porphyrin from the Solution/HOPG Interface. *J. Phys. Chem. C* **2016**, *120*, 18140–18150.

[225] Kunitake, M.; Akiba, U.; Batina, N.; Itaya, K. Structures and Dynamic Formation Processes of Porphyrin Adlayers on Iodine-Modified Au(111) in Solution: In Situ STM Study. *Langmuir* **1997**, *13*, 1607–1615.

[226] Waldmann, T.; Klein, J.; Hoster, H. E.; Behm, R. J. Stabilization of Large Adsorbates by Rotational Entropy: A Time-Resolved Variable-Temperature STM Study. *ChemPhysChem* **2013**, *14*, 162–169.

[227] Wen, R.; Rahn, B.; Magnussen, O. M. Potential-Dependent Adlayer Structure and Dynamics at the Ionic Liquid/Au(111) Interface: A Molecular-Scale In Situ Video-STM Study. *Angew. Chem. Int. Ed.* **2015**, *54*, 6062–6066.

[228] Gao, Y.; Olsen, K. W. Molecular Dynamics of Drug Crystal Dissolution: Simulation of Acetaminophen Form I in Water. *Mol. Pharmaceutics* **2013**, *10*, 905–917.

[229] Elts, E.; Greiner, M.; Briesen, H. Predicting Dissolution Kinetics for Active Pharmaceutical Ingredients on the Basis of Their Molecular Structures. *Cryst. Growth Des.* **2016**, *16*, 4154–4164.

[230] Parks, C.; Koswara, A.; Tung, H.-H.; Nere, N. K.; Bordawekar, S.; Nagy, Z. K.; Ramkrishna, D. Nanocrystal Dissolution Kinetics and Solubility Increase Prediction from Molecular Dynamics: The Case of α-, β-, and γ-Glycine. *Mol. Pharmaceutics* **2017**, *14*, 1023–1032.

[231] Liu, J. C.; Tan, E. L.; Chien, Y. W. Dissolution Kinetics and Rate-Controlling Mechanisms. *Drug Dev. Ind. Pharm.* **1986**, *12*, 1357–1370.

[232] Clair, S.; Pons, S.; Seitsonen, A. P.; Brune, H.; Kern, K.; Barth, J. V. STM Study of Terephthalic Acid Self-Assembly on Au(111): Hydrogen-Bonded Sheets on an Inhomogeneous Substrate. *J. Phys. Chem. B* **2004**, *108*, 14585–14590.

[233] Zhu, N.; Osada, T.; Komeda, T. Supramolecular assembly of biphenyl dicarboxylic acid on Au(111). *Surf. Sci.* **2007**, *601*, 1789 – 1794.

[234] Giesen, M.; Baier, S. Atomic transport processes on electrodes in liquid environment. *J. Phys.: Condens. Matter* **2001**, *13*, 5009–5026.

[235] Lackinger, M.; Griessl, S.; Markert, T.; Jamitzky, F.; Heckl, W. M. Self-Assembly of Benzene-Dicarboxylic Acid Isomers at the Liquid Solid Interface: Steric Aspects of Hydrogen Bonding. *J. Phys. Chem. B* **2004**, *108*, 13652–13655.

[236] Xiao, W. D.; Jiang, Y. H.; Aït-Mansour, K.; Ruffieux, P.; Gao, H.-J.; Fasel, R. Chiral Biphenyldicarboxylic Acid Networks Stabilized by Hydrogen Bonding. *J. Phys. Chem. C* **2010**, *114*, 6646–6649.

[237] Stepanow, S.; Lin, N.; Vidal, F.; Landa, A.; Ruben, M.; Barth, J. V.; Kern, K. Programming Supramolecular Assembly and Chirality in Two-Dimensional Dicarboxylate Networks on a Cu(100) Surface. *Nano Lett.* **2005**, *5*, 901–904.

[238] Cortés, R.; Mascaraque, A.; Schmidt-Weber, P.; Dil, H.; Kampen, T. U.; Horn, K. Coexistence of Racemic and Homochiral Two-Dimensional Lattices Formed by a Prochiral Molecule: Dicarboxystilbene on Cu(110). *Nano Lett.* **2008**, *8*, 4162–4167.

[239] Baber, A. E.; Tierney, H. L.; Sykes, E. C. H. A Quantitative Single-Molecule Study of Thioether Molecular Rotors. *ACS Nano* **2008**, *2*, 2385–2391.

[240] Kumagai, T.; Hanke, F.; Gawinkowski, S.; Sharp, J.; Kotsis, K.; Waluk, J.; Persson, M.; Grill, L. Thermally and Vibrationally Induced Tautomerization of Single Porphycene Molecules on a Cu(110) Surface. *Phys. Rev. Lett.* **2013**, *111*, 246101.

[241] Marbach, H.; Steinrück, H.-P. Studying the dynamic behaviour of porphyrins as prototype functional molecules by scanning tunnelling microscopy close to room temperature. *Chem. Commun.* **2014**, *50*, 9034–9048.

[242] Jung, L. S.; Campbell, C. T. Sticking Probabilities in Adsorption of Alkanethiols from Liquid Ethanol Solution onto Gold. *J. Phys. Chem. B* **2000**, *104*, 11168–11178.

[243] Hipps, K. W.; Mazur, U. Kinetic and Thermodynamic Control in Porphyrin and Phthalocyanine Self-Assembled Monolayers. *Langmuir* **2018**, *34*, 3–17.

[244] Bickerstaffe, A. K.; Cheah, N. P.; Clarke, S. M.; Parker, J. E.; Perdigon, A.; Messe, L.; Inaba, A. The Crystalline Structures of Carboxylic Acid Monolayers Adsorbed on Graphite. *J. Phys. Chem. B* **2006**, *110*, 5570–5575.

[245] Rossignol, S.; Tinel, L.; Bianco, A.; Passananti, M.; Brigante, M.; Donaldson, D. J.; George, C. Atmospheric photochemistry at a fatty acid–coated air-water interface. *Science* **2016**, *353*, 699–702.

[246] Ponder, J. W.; Richards, F. M. An efficient newton-like method for molecular mechanics energy minimization of large molecules. *J. Comput. Chem.* **1987**, *8*, 1016–1024.

[247] Allinger, N. L.; Yuh, Y. H.; Lii, J. H. Molecular mechanics. The MM3 force field for hydrocarbons. 1. *J. Am. Chem. Soc.* **1989**, *111*, 8551–8566.

[248] Lii, J.-H.; Allinger, N. L. Directional hydrogen bonding in the MM3 force field. I. *J. Phys. Org. Chem.* **1994**, *7*, 591–609.

[249] Lii, J.-H.; Allinger, N. L. Directional hydrogen bonding in the MM3 force field: II. *Journal of Computational Chemistry* **1998**, *19*, 1001–1016.

[250] Allen, G.; Watkinson, J.; Webb, K. An infra-red study of the association of benzoic acid in the vapour phase, and in dilute solution in non-polar solvents. *Spectrochim. Acta* **1966**, *22*, 807 – 814.

[251] Colominas, C.; Teixidó, J.; Cemelí, J.; Luque, F. J.; Orozco, M. Dimerization of Carboxylic Acids: Reliability of Theoretical Calculations and the Effect of Solvent. *J. Phys. Chem. B* **1998**, *102*, 2269–2276.

[252] Nečas, D.; Klapetek, P. Gwyddion: an open-source software for SPM data analysis. *Cent. Eur. J. Phys.* **2012**, *10*, 181–188.

Publications

1. Quantifying the Ultraslow Desorption Kinetics of 2,6-Naphthalenedicarboxylic Acid Monolayers at Liquid–Solid Interfaces
   O. Ochs, N. Martsinovich, W. M. Heckl, and M. Lackinger, *J. Phys. Chem. Lett.* 2020, 11, 17, 7320-7326.

2. Origin of Solvent-Induced Polymorphism in Self-Assembly of Trimesic Acid Monolayers at Solid–Liquid Interfaces
   O. Ochs, M. Hocke, S. Spitzer, W. M. Heckl, N. Martsinovich, and M. Lackinger, *Chem. Mater.* 2020, 32, 12, 5057-5065.

3. Immersion-scanning-tunneling-microscope for long-term variable-temperature experiments at liquid-solid interfaces
   O. Ochs, W. M. Heckl, and M. Lackinger, *Rev. Sci. Instrum.* 2018, 89, 053707.

4. What can be inferred from moiré patterns? A case study of trimesic acid monolayers on graphite
   S. Spitzer, O. Helmle, O. Ochs, J. Horsley, N. Martsinovich, W. M. Heckl, and M. Lackinger, *Faraday Discuss.* 2017, 204, 331-348.

5. On-Surface Ullmann Coupling: The Influence of Kinetic Reaction Parameters on the Morphology and Quality of Covalent Networks
   J. Eichhorn, D. Nieckarz, O. Ochs, D. Samanta, M. Schmittel, P. J. Szabelski, and M. Lackinger, *ACS Nano* 2014, 8, 8, 7880-7889.

Acknowledgements

Es ist mir ein Anliegen mich an dieser Stelle bei allen Personen zu bedanken, die zum Gelingen dieser Doktorarbeit beigetragen haben.

An erster Stelle möchte ich mich bei meinem Doktorvater Markus Lackinger bedanken, der es mir ermöglichte meine Doktorarbeit in seiner Arbeitsgruppe anzufertigen und immer ein offenes Ohr und Rat für mich hatte. Vielen Dank für alles, was Du mir in den Jahren beigebracht hast. Die Zusammenarbeit mit Dir hat mir viel Spaß gemacht.

Mein Dank gilt Prof. Wolfgang Heckl, der mir die Möglichkeit gab an der Technischen Universität München im Fachbereich Physik zu forschen und zu promovieren. Ich danke zudem der Helmut Fischer Stiftung für die finanzielle Unterstützung während meiner Promotionszeit.

Besonderer Dank geht an Stephan Kloft. Danke, für deine stete Hilfsbereitschaft und dass Du mit mir Deinen großen Erfahrungsschatz im Bau von Rastertunnelmikroskopen geteilt hast. Ich danke ganz herzlich Massimo Fritton, Lukas Grossman und Matthias Lischka für Eure fachliche Expertise und die schöne gemeinsame Zeit am Museum. Ein großes Dankeschön geht auch an Johanna Eichhorn, Atena Rastgoo, Manuela Hocke, Eva Ringel, Saskia Spitzer, Gianluca Galeotti und Stefan Sotier. Ohne Euch alle wäre es nur halb so schön gewesen.

Ein großer Dank geht an Günter Hesberg, Ljubi Diklic und Stefan Männl. Ich danke Euch für alles, was Ihr mir in der Werkstatt beigebracht habt und Eure Unterstützung bei der Herstellung von Bauteilen.

Ich danke meiner Mutter und meiner ganzen Familie für Motivation und die Hilfe, die Ihr mir in den letzten Jahren habt zukommen lassen. Zu guter Letzt möchte ich mich bei meiner lieben Freundin Katharina bedanken. Danke, dass Du mich stets bei allem unterstützt und an mich glaubst.